CARDIFF UNIVERSITY

CARDIFF SCHOOL OF BIOSCIENCES

CLAUDIA DI NAPOLI

Label-free multiphoton microscopy of intracellular lipids using Coherent anti-Stokes Raman Scattering (CARS)

A THESIS SUBMITTED TO CARDIFF UNIVERSITY FOR THE DEGREE OF DOCTOR OF PHILOSOPHY

MAY 2014

Declaration and Statements

DECLARATION
This work has not been submitted in substance for any other degree or award at this or any other university or place of learning, nor is being submitted concurrently in candidature for any degree or other award.

Signed .....(candidate) Date .....

STATEMENT 1
This thesis is being submitted in partial fulfillment of the requirements for the degree of Doctor of Philosophy.

Signed .....(candidate) Date .....

STATEMENT 2
This thesis is the result of my own independent work/investigation, except where otherwise stated. Other sources are acknowledged by explicit references. The views expressed are my own.

Signed .....(candidate) Date .....

STATEMENT 3
I hereby give consent for my thesis, if accepted, to be available for photocopying and for inter-library loan, and for the title and summary to be made available to outside organisations.

Signed .....(candidate) Date .....

Abstract

Coherent Antistokes Raman Scattering (CARS) microscopy has emerged in the last decade as a powerful multiphoton microscopy technique to rapidly image lipid droplets (LDs) label-free with intrinsic three-dimensional spatial resolution in cells.

In this thesis I investigate and compare the ability of hyperspectral CARS and dual-frequency/differential CARS (D-CARS) to enable the chemical specificity required to distinguish lipids of different chemical composition. In hyperspectral CARS a series of spatially-resolved images are acquired over a frequency range thus proving high chemical specificity. In D-CARS two vibrational frequencies are simultaneously excited and probed, and the resulting sum and difference CARS intensities are detected by a fast and efficient single photomultiplier. This results in a higher image speed than hyperspectral CARS and in an improved image contrast against the nonresonant CARS background with a straightforward data analysis.

D-CARS and hyperspectral CARS techniques were applied to LDs in model and cellular systems. In model systems made by agarose gel, droplets of pure lipids with different degree of unsaturation (number of carbon-carbon double bonds in the fatty acyl chain) were used as test sample to compare Raman spectra with CARS spectra, and measure D-CARS images at specific chemically-selective wavenumbers. Building from this knowledge, cytosolic droplets induced by loading fatty acids to the culture media of human adipose-derived stem cells (ADSCs)

were distinguished in composition both in fixed cells and in living cells during differentiation into adipocytes. Furthermore, the application of a in-house developed Hyperspectral Image Analysis (HIA) software on hyperspectral data provided spatial distributions and absolute concentrations for the chemical components of the investigated specimens. In particular quantitative information was extracted about the concentration of pure neutral lipid components within cytosolic LDs, and changes over time were inferred in living ADSCs according to the type of pure fatty acid added to the culture media.

Acknowledgements

This work could not have been possible without many people that, with their professional and personal help, took my hand at the beginning of my Ph.D. and guided me through this journey.

I would like to start with my supervisors. I would like to thank Prof. Paola Borri for keeping her office door always open for meetings and discussions, but especially for when I was in need of her support and professional expertise. I would like to thank Dr. Pete Watson for being my biology mentor and for preparing the cell samples at the heart of this work. I would like to thank Prof. Wolfgang Langbein for his thoughtful insights during our meeting discussions.

A special thanks also goes to all the members of the Biophotonics group at Cardiff University, with a particular mention for Dr. Francesco Masia and Dr. Iestyn Pope. I would like to thank Dr. Francesco Masia for his invaluable help in the lab and for providing the HIA software. Francesco, thank you also for your endless calmness and for keeping my Italian alive! I would like to thank Dr. Iestyn Pope for the Raman measurements on model lipid droplets performed with Prof. Wolfgang Langbein and in collaboration with Prof. Cees Otto at the University of Twente, The Netherlands. Iestyn, thank you also for your priceless help and company in the lab, for teaching me everything you knew on rugby and for demonstrating that the Welsh are one of the kindest people in the world!

Then I would like to thank all the past and present members of the E3.19 office, especially Gui Jie, Fliss and Anika. Gui Jie, thank you for being like a second mum to me with your caring attention when I was having a cold, with your spontaneous generosity when I needed to move out in summertime and with your insurmountable cooking skills when I was invited to your house. Fliss, thank you for sharing our reciprocal ups and downs on our life inside and outside the lab, for the unexpected surprises I found on my desk every time I was feeling down and for sharing cat videos when friday afternoon's boredom was about to kick in! Anika, thank you for your biting jokes, the constantly curious questions on CARS and for glimpsing imaginary animals in my images!

Last but not least, I would like to thank two very important families.

One is my family back home – mami, papi and brother Alessandro. Grazie a tutti e tre per aver passato i finesettimana in videochiamata, per tenermi aggiornata su come vanno le cose (familiari, politiche, calcistiche!) a casa, per farmi ridere con delle *monade* e per organizzare insuperabili pranzi/viaggi/rimpatriate ogni volta che torno in Italia.

One is my family in Cardiff – all the girls in Aberdare Hall. From the bottom of my heart, I would like to send a big-as-the-universe thank you to Candace, Erika, Eva, Fatima, Hana, Hannah, Iffah, Irene, Katie, Lucie, Marie Claire, Marlena, Nana, Ragini, Shaneika and Srinidhi (Yingyu, you too!). Thank you for the chats and laughs when eating dinner, watching a movie, visiting places, relaxing in the park, attending the theatre, enjoying freshly-made tiramisù and, above all, for supporting (= bearing with!) me every single day of my Ph.D.! The time we spent together in the past three years has been more valuable than I can explain. I wish to each one of you all the best of this world.

Dedicated to everyone that has successfully made “keep calm and carry on" their life-long motto.

Lori sì che i ga capio tuto dea vita!

Contents

1 Introduction **1**

1.1 Background and Motivation 1

1.2 Thesis Outline 6

2 Theoretical background **8**

2.1 Introduction 8

2.2 Coherent anti-Stokes Raman Scattering 11

2.3 Experimental realization of CARS 15

2.3.1 Phase-matching condition 16

2.3.2 Laser and pulsed excitations 17

2.3.3 Nonresonant background suppression 19

2.3.4 Signal detection 21

3 Material and Methods **23**

3.1 Introduction 23

3.2 Samples 24

3.2.1 Model lipid droplets 24

3.2.2 Cytosolic lipid droplets 25

3.3 CARS and D-CARS set-ups 28

3.3.1 Laser sources 29

3.3.2 Spectral focusing and frequency tuning 30

3.3.3 Dual-frequency differential CARS (D-CARS) 33
3.3.4 Signal collection 35
3.3.5 Data acquisition 36
3.4 Data processing 38
3.5 Data analysis 40
3.5.1 D-CARS and CARS ratio 40
3.5.2 CARS hyperspectral images 42
3.5.3 D-CARS images 45

4 Demonstration of label-free chemical sensitivity of CARS and D-CARS with model lipid droplets 46
4.1 Introduction 46
4.2 Raman characterization 48
4.3 Single-pair CARS spectra 50
4.4 Dual-pair D-CARS spectra and images 54
4.5 Summary 60

5 Quantitative chemical analysis of cytosolic lipid droplets in fixed and live adipocytes 61
5.1 Introduction 61
5.2 Cytosolic lipid droplets in fixed adipocytes 65
5.2.1 Hyperspectral CARS 66
5.2.2 Dual-frequency differential CARS 70
5.2.3 Ratiometric analysis 73
5.2.4 Quantitative chemical analysis using FSC^3 75
5.2.5 Summary 79
5.3 Effects of fixation on adipocytes 80
5.3.1 Fixation with paraformaldehyde 80
5.3.2 Fixation with methanol 83
5.3.3 Summary 84
5.4 Cytosolic lipid droplets in live adipocytes 86
5.4.1 Hyperspectral CARS 87

5.4.2 Dual-frequency differential CARS 96
5.4.3 Ratiometric analysis of FSC^3 lipid components 104
5.4.4 Quantitative chemical analysis using FSC^3: projection into pure lipid components 108
5.4.5 Summary 119
5.5 Explorative studies on protein-lipid interaction processes 120
5.5.1 Effects of Rab18 on adipocytes 120
5.5.2 Effects of Exo2 on adipocytes 123

6 Conclusions **127**
6.1 Thesis summary 127
6.2 Outlook 131

A Appendix **133**

B Appendix **135**

C Appendix **137**

List of acronyms **139**

Bibliography **141**

Publications, Conferences, Proceedings and Academic Achievements **153**

1 Introduction

1.1 Background and Motivation

In 1997 the World Health Organization officially defined obesity as an epidemic disease. Involving nowadays more than 1.5 billion adults all around the world, obesity is seen as consequence of the modern lifestyle that generally imposes a reduced physical activity and an increased food energy intake [1]. The accumulation of body fats originally intended for energy reserve and life survival in periods of nutrient deprivation has now become excessive, posing a threat to human health as a contributing factor in the development of diseases such as type 2 diabetes, atherosclerosis and steatohepatitis [2]. When the food energy intake exceeds the requirements, fats are stored and accumulated as cytosolic lipid droplets in tissues (e.g., artery walls or liver) that are not specialized in fat accumulation, altering hormone levels and signaling pathways.

Lipid droplets have been recently recognized as organelles playing a variety of important roles in the functioning of the cell machinery. For years they have been exclusively considered as inert organelles storing metabolic energy in the form of sterol esters or triglycerides. When highly specific proteins were discovered on the phospholipid monolayer surrounding the triglyceride core, the involvement of lipid droplets in processes such as protein metabolism, membrane biosynthesis and hormone regulation was unveiled, opening new questions on the formation, trafficking and breakdown of lipid droplets in living cells [3].

Optical microscopy is still the only practical tool able to provide the high

spatial and temporal resolution required for the complete understanding of lipid functions within living cells and tissues. For decades fluorescence microscopy has been the main imaging modality with exogenous dyes (e.g., BODIPY, Oil Red O and Nile Red) being used as markers in the identification of lipid-rich structures. As such, this technique is intrinsically invasive and perturbative of the native properties, functions and distribution of the targeted lipids. Besides, it is often prone to labelling artefacts, non-specific binding and photo-bleaching [4]. These problems launched the quest for new microscopy techniques capable to provide contrast without staining the sample with dye labels [5, 6]. Different solutions have been achieved over time which exploit the *linear* or *nonlinear* response of the material (polarization) to an incident electromagnetic field.

Label-free linear optical microscopy techniques include phase contrast and differential interference contrast (DIC) microscopy [7, 8]. They rely on the variations of the thickness and refractive index in a sample, i.e. on the changes of the optical path length experienced by the incident light while crossing the sample, and are effective in providing image contrast. Similarly, optical coherence tomography (OCT) employs interference to extrapolate information on sample depth from the travelled path length, allowing three-dimensional acquisitions at video-rate speed [9]. All these techniques, however, have the disadvantage of being insensitive to the chemically-diversified composition in a sample.

Chemical sensitivity can be gained through another label-free linear optical technique, called vibrational micro-spectroscopy, that exploits the vibrational resonances within a specimen. Vibrational resonances are intrinsically related to the masses of the constituting atoms and to the strengths of their chemical bonds and, as such, they allow the identification and characterization of chemically-different structures in a sample, such as the presence of nucleic acids, proteins and lipid droplets in a cellular environment. Traditionally, a sequence of vibrational resonances (spectrum) is generated through infrared(IR)-light absorption microscopy or Raman scattering microscopy [10, 11]. Because of their label-free chemical specificity, both methods offer promising non-invasive prospects however they do have their own disadvantages that limit their applicability in a biologically rele-

vant context. Specifically, IR microscopy uses long wavelengths for the excitation. As a consequence, it suffers from poor spatial resolution and it is affected by the strong absorption that the aqueous cellular content has in that spectral range. Spontaneous Raman scattering microscopy is able to overcome these problems by employing excitation wavelengths in the visible range. However, the response signal from biological materials is usually weak and easily overwhelmed by the background fluorescence from the sample itself such that high excitation intensities and long acquisition times have to be used. Long acquisition times are not well tolerated by live biological samples, nor are they suited for capturing dynamics within those samples.

Multiphoton microscopy techniques based on nonlinear optical effects have recently started to pave their way in biological research. Label-free multiphoton microscopy techniques include second-harmonic generation (SHG) or third-harmonic generation (THG) processes. In SHG the sample emits a signal at half the wavelength of the exciting light when the molecular organization in the sample does not present inversion symmetry, such as collagen fibres [12]. In THG the response is characterized by a wavelength that is a third of the wavelength of the exciting light and it is generated in presence of discontinuities in the refractive index, e.g., between lipid-rich vesicles and cellular cytosol [13,14]. Because of their nonlinear nature, SHG and THG responses are only efficiently generated at high incident energies found at the focal centre, allowing for three-dimensional spatial resolution without the need for a pin-hole at the detector to reject out-of-focus light as in confocal microscopy. The result is an improved image contrast at the cellular level for thick, scattering specimens. Yet these processes use wavelengths that are well below the vibrational wavelengths range and therefore are not able to provide chemically-specific information.

Chemical contrast can be achieved by using two incident light fields such that their frequency difference matches the frequency at which specific molecules in the sample are vibrating. This is the fundamental concept at the basis of coherent Raman scattering (CRS), which combines the chemical specificity of Raman spectroscopy with the intrinsic optical sectioning of multiphoton microscopy. Impor-

tantly, in CRS identical vibrating bonds in the focal volume are driven coherently and the corresponding Raman scattering fields constructively interfere resulting in a signal enhancement compared to spontaneous Raman [6]. A widely utilized implementation of CRS is Coherent anti-Stokes Raman Scattering (CARS) which, although being a well-known spectroscopy technique in chemistry and material science, was introduced as a multiphoton microscopy technique applicable to cell imaging only in 1999 with the pioneering work by Zumbusch and co-workers [15].

In the last decade, CARS has gradually emerged as a micro-spectroscopy nonlinear technique with high potential in biology-related applications [5, 16, 17]. Its intrinsic chemical specificity, three-dimensional sectioning capability and ability to generate strong signals have made CARS successful in the detection of biologically relevant molecules such as DNA, proteins (in conditions of high concentrations, typically > 1 mM, or strong localisation, e.g., forming aggregates), water and lipids by the excitation of the phosphate, amide I, oxygen-hydrogen and carbon-hydrogen vibrations, respectively [18–21]. Specifically for lipids, the bonds between carbon (C) and hydrogen (H) atoms are so densely organized and well-aligned in the aliphatic fatty chain that an intense CARS signal is generated by the symmetric CH_2 stretch vibration at $2855\,\mathrm{cm}^{-1}$ when the frequency difference between the two incident light fields is tuned to that specific vibrational frequency. This approach has led to the successful mapping of lipid distribution in membranes and vesicles at high imaging speeds [22, 23].

Further technological developments have made it possible to simultaneously excite and probe more than a single vibrational frequency. This technique, called hyperspectral or multiplex CARS microscopy, consists of recording a complete spectral and microscopic dataset as hyperspectral images, i.e. either as a series of spatially-resolved images acquired at different frequencies (commonly referred to as hyperspectral CARS) or as a set of full-range spectra acquired at each different spatial point (multiplex CARS). The amount of information so obtained is significantly richer than that gained through single-frequency CARS as multiple vibrations are addressed. As a result, a higher degree of chemical specificity is achieved allowing one to distinguish different chemical species of a sample on

the basis of their characteristic spectral information [24]. In lipid biology, multiplex CARS has been used to characterize and image the chemical and physical inhomogeneities within lipid droplets of fixed mouse adipocytes (3T3-L1 cells) previously fed with a diversified set of fatty acids [25]. The achievement of such detailed knowledge for intra-cellular lipid droplets marked a first step in the understanding of lipid-type specific metabolic processes occurring at intercellular level. For instance, the development of insulin resistance in the pathogenesis of type 2 diabetes is influenced by the number of C atoms and C-C double bonds constituting the molecular structure of lipids provided through the food diet [26].

Besides the high chemical specificity, multiplex CARS has the advantage of being able to quantify the local concentrations of the lipids and other chemical species present in a sample on a microscopic scale [27]. CARS intensities are in general a complicated function of molecular concentration and therefore creating a distribution map for the different chemical components is not straightforward. In multiplex CARS the acquisition of spectra on sufficiently wide vibrational ranges allows one to use analytical procedures (e.g., the factorization into susceptibilities and concentrations of the chemical components method, FSC^3 [28]) that can convert CARS vibrational profiles into spectra that are almost equivalent to spontaneous Raman scattering spectra. The Raman-like retrieved spectra so obtained are a linear function of the molecular concentration and therefore permit to quantitatively extract information on the density of each sample component [27].

Multiplex CARS has however the disadvantage of being a low imaging speed technique usually because of the finite light throughput of spectrometers and the limited acquisition speed of charge-coupled device (CCD) cameras [6]. Given that the typical acquisition time for a multiplex CARS spectrum is about 10 ms per pixel, a $100 \times 100\,\mu\text{m}^2$ area ($0.3 \times 0.3\,\mu\text{m}^2$ pixel size) would require a 20-minute long hyperspectral acquisition, which is not compatible with live cell imaging. Notably, hyperspectral CARS can offer an equally effective but faster alternative. By spatially scanning the above area with a dwell time of 1-10 μs per pixel, the multiplex-equivalent time is given by the dwell time multiplied by the number of spectral points, that is 0.1-10 ms per pixel if 100 spectral points are sampled.

Alternatively, dual-frequency differential CARS (D-CARS) microscopy has been recently developed as a technique with the potential to improve and complement multiplex/hyperspectral CARS [29]. In D-CARS, two vibrational frequencies are excited and probed at the same time, and the sum and difference intensities between the corresponding CARS signals are detected by a fast and efficient photomultiplier. As confirmed by proof-of-principle experiments on polystyrene and polymethyl methacrylate beads, this approach maintains the high image speed of single-frequency CARS microscopy and it simultaneously offers an improved chemical specificity and image contrast against the spectrally-constant nonresonant CARS background arising from electronic and off-resonance contributions [29, 30].

The work presented in this thesis aims at demonstrating the applicability of D-CARS and hyperspectral CARS as micro-spectroscopy techniques able to characterize the chemical composition of lipid droplets in fixed and living cells. All data were acquired via home-built CARS microscopes based on femtosecond pulses spectrally focused by glass dispersion. The chemical sensitivity and specificity of the techniques were first demonstrated on lipid droplet model systems and subsequently applied to cytosolic lipid droplets in fixed and living adipocytes fed with saturated and unsaturated fatty acids. A range of quantitative data analysis procedures were applied and compared with state-of-the-art ratiometric methods.

1.2 Thesis Outline

The thesis is organized with the following structure.

Chapter 2 provides the theoretical background for the CARS and D-CARS processes, starting from the description of spontaneous Raman.

Chapter 3 describes the sample preparation, the home-built CARS microscope set-ups used for the experiments and the procedures implemented for the quantitative analysis of the acquired data.

Chapter 4 details the results for the CARS/D-CARS study of micron-sized “mo-

del" lipid droplets consisting of pure triglycerides where the D-CARS capability to distinguish the different compositions in a rapid label-free way is demonstrated.

Chapter 5 discusses the results for the CARS/D-CARS characterization of intracellular lipid droplets in fixed and living human adipose-derived stem cells, respectively; the quantitative description of cellular chemical components is achieved both with a ratiometric analysis of D-CARS and with a phase retrieval procedure of hyperspectral CARS and subsequent FSC^3. Note that Chapter 4 and 5 also include a specific literature overview pertinent to the data analysis discussed, for comparison.

Chapter 6 summarizes the findings in this thesis and provides an outlook for future applications.

2 Theoretical background

2.1 Introduction

When light interacts with matter, it can be absorbed by atoms and converted into internal excitation energy or it can be scattered out with an identical or different energy. Vibrational Raman scattering is a process in which light inelastically collides with a vibrating molecule and it is scattered out with a different frequency. The energy difference between the incident and scattered photon is equal to the vibrational energy gained or lost by the molecule. If the scattered photon has a lower frequency than the incident photon, it is indicated as the Stokes component. If the scattered photon has a higher frequency than the incident photon, it is indicated as the anti-Stokes component [6].

These variations in the photon energy and thus frequency are given by the vibrational frequencies, which are determined by the type of chemical bonds present in molecules.

In a basic description, the nuclear motion of a diatomic molecule can be represented as two masses connected through a spring [31]. According to Hooke's law, when an external force is applied, the system starts to vibrate with a frequency that is defined by the mass of the atoms and the spring constant. Hence, different molecules will have different vibrational frequencies according to the different atomic masses and spring constants. If the molecule has a more complex structure, different types of vibrations, called *vibrational modes*, occur.

In a classical description, a molecule is considered as being composed of two

or more atoms that are covalently bound with each other and surrounded by an inter-nuclei electronic cloud [32, 33]. When a molecule interacts with light, bond electrons are moved away from their equilibrium position and start to follow the oscillations of the electric field component in the incident light. This induces a dipole moment $p(t)$ for the molecule

$$p(t) = \alpha(t) E(t) \tag{2.1}$$

where $\alpha(t)$ is the electric polarizability and $E(t)$ is the electric field amplitude. As a result the molecule becomes polarized (*dipole*), with positive charges in the direction of the electric field and negative charges in the opposite direction. The macroscopic polarization P is obtained by considering the contribution of all N electric dipoles per unit volume

$$P(t) = N p(t). \tag{2.2}$$

If the incident electric field is weaker than the electron-nuclei binding field, the polarization P can be rewritten as

$$P(t) = \varepsilon_0 \chi E(t) \tag{2.3}$$

where ε_0 is the electric permittivity in vacuum and χ is the susceptibility of the material, i.e. a parameter describing how easily a dielectric material polarizes in the presence of an applied field [33].
As the incident electric field becomes stronger, however, the linear relation expressed by Equation 2.3 becomes invalid and the polarization $P(t)$ is expressed as a power series in the electric field $E(t)$

$$\begin{aligned} P(t) &= \varepsilon_0 \left[\chi^{(1)} E(t) + \chi^{(2)} E^2(t) + \chi^{(3)} E^3(t) + ... \right] && (2.4) \\ &= P^{(1)}(t) + P^{(2)}(t) + P^{(3)}(t) + ... && (2.5) \end{aligned}$$

where $\chi^{(n)}$ is the n-th order susceptibility and $P^{(n)}$ is the n-th order contribution

to the polarization [33]. Note that, although the oscillatory motion set by the incident electronic field involves the electronic cloud, it also carries information about the motions of nuclei. Because of the electron-nuclei bond, the motions of the electrons are also affected by nuclear motions. Hence, the polarization $P(t)$ is perturbed by the presence of nuclear modes, i.e. by the symmetric and anti-symmetric stretch motion between two bonded atoms, the bending motion of the bond angle between three atoms and the out-of-plane deformations changing a planar molecular structure into a non-planar one [33].

In general, an N-atomic non-linear molecule has $3N-6$ vibrational normal modes with each normal mode characterized by a well defined frequency. Thus vibrational spectra show a large number of different bands that can be used as the distinctive signature of a molecule [6].

In Raman spectroscopy, a single frequency laser beam is used as incident light source for spontaneous Raman scattering. The result is a characteristic spectrum of frequency-shifted peaks that are generated by the vibrational modes of molecules and can be identified without the use of stains or labels. However, since the scattering cross-section is very small (typically $\sim 10^{-29}\,\mathrm{cm}^2$ per vibrational mode, that is, $\sim 10^{14}$ lower than typical absorption cross-sections of organic fluorophores), Raman scattering is a very weak effect. Consequently, in practical micro-spectroscopy applications high excitation powers ($\sim 100\,\mathrm{mW}$) and long data acquisition times (more than 30 min for a confocal Raman micro-spectroscopy image) are required to generate images with sufficient signal-to-noise, posing serious limitations to biological studies involving live cell experiments [34]. As mentioned previously, a solution is provided by Coherent anti-Stokes Raman scattering (CARS).

2.2 Coherent anti-Stokes Raman Scattering

CARS is a third-order nonlinear process in which two excitation fields, called pump and Stokes, at the corresponding frequencies ω_P and ω_S drive into a coherent oscillation all those chemical bonds that, in the investigated volume, have a vibrational frequency resonant to the frequency difference of the pump-Stokes fields

$$\omega_{vib} = \omega_P - \omega_S. \tag{2.6}$$

Oscillating molecules are probed through a third field, called the probe, of frequency ω_{PB} which is inelastically scattered with an anti-Stokes frequency shift corresponding to the molecular vibration

$$\omega_{AS} = \omega_{vib} + \omega_{PB} \tag{2.7}$$

or, if the same laser field is used for pump and probe,

$$\omega_{AS} = 2\omega_P - \omega_S. \tag{2.8}$$

The intensity I_{CARS} of the anti-Stokes signal generated can be expressed in terms of the induced polarization P in the material. Specifically, CARS is a *four-wave* mixing process (two pump wave fields, one Stokes field and one anti-Stokes field) and I_{CARS} is proportional to the module squared of third-order polarization $P^{(3)}$

$$I_{\mathrm{CARS}} \propto \left| P^{(3)} \right|^2 \tag{2.9}$$

which has a magnitude determined by the strength E_P and E_S of the pump and Stokes field and by the third-order optical susceptibility $\chi^{(3)}$. From Equation 2.3, this leads to:

$$P^{(3)} \propto \chi^{(3)} E_P^2 E_S^*. \tag{2.10}$$

In CARS the susceptibility parameter is expressed in terms of a vibrationally resonant part and a nonresonant part, $\chi_R^{(3)}$ and $\chi_{NR}^{(3)}$ [35]:

$$\chi^{(3)} = \chi_R^{(3)} + \chi_{NR}^{(3)}. \tag{2.11}$$

The resonant part $\chi_R^{(3)}$ is the contribution due to the resonant interaction between the molecular vibrational modes and the pump-Stokes driving term beating at $\omega_P - \omega_S$. The value of $\chi_R^{(3)}$ is a complex number given by the sum over all the vibrational resonances j involved

$$\chi_R^{(3)} = \sum_j \frac{A_j}{\Omega_j - (\omega_P - \omega_S) - i\Gamma_j} \tag{2.12}$$

where A_j is the oscillator strength proportional to the scattering cross-section and to the number of dipoles excited in the focal volume; Γ_j is the half width at half maximum bandwidth of the correspondent spectral line; $\Omega_j - (\omega_P - \omega_S)$ is the frequency difference between the vibrational resonance Ω_j which is at the centre of the spectral line and the driving resonance $\omega_P - \omega_S$.
The nonresonant part $\chi_{NR}^{(3)}$ is a constant contribution due to the electronic response of the material. This induces a polarization effect at the anti-Stokes frequency even when $\omega_P - \omega_S$ is tuned far from vibrational resonance, resulting in a *nonresonant background* independent from the Raman shift. Reformulating Equation 2.9 in terms of the resonant and nonresonant terms of $\chi^{(3)}$ gives

$$\begin{aligned} I_{\text{CARS}} \propto \left|\chi^{(3)}\right|^2 &= \left|\chi_R^{(3)} + \chi_{NR}^{(3)}\right|^2 \\ &= \left|\chi_R^{(3)}\right|^2 + \left|\chi_{NR}^{(3)}\right|^2 + 2\chi_{NR}^{(3)}\,\text{Re}\{\chi_R^{(3)}\} \end{aligned} \tag{2.13}$$

where $\text{Re}\{\chi_R^{(3)}\}$ is the real part of $\chi_R^{(3)}$. The first term carries the information about the resonant vibrating modes; the second term holds the constant contribution from the nonresonant background; the third term is the mixing term between the resonant and the nonresonant contributions and contains the real part of the vibrational response [35]. Figure 2.1 shows the spectral profile for each of these terms and their contribution to construction of the anti-Stokes signal response. The res-

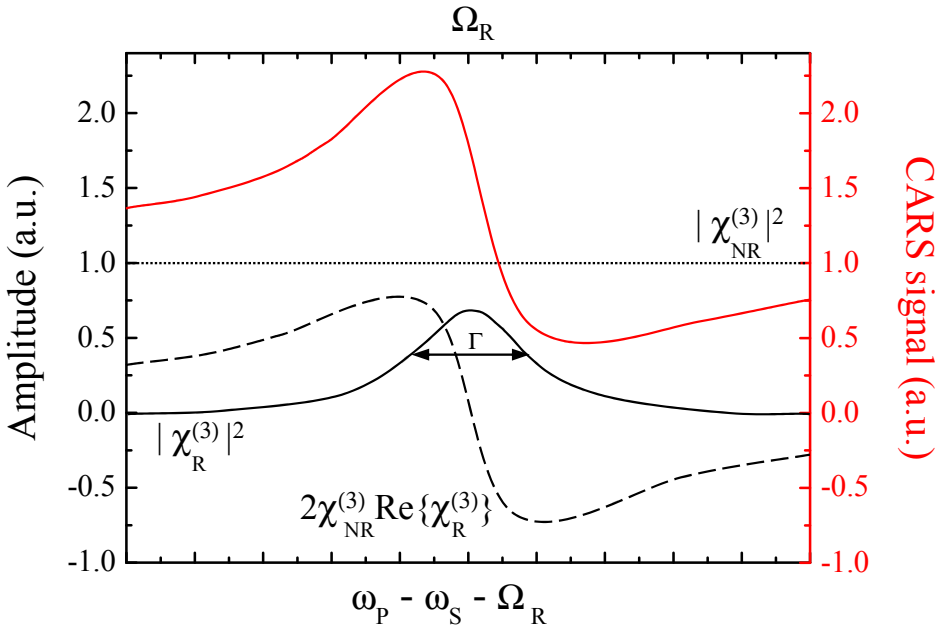

Figure 2.1: SINGULAR AND TOTAL COMPONENTS OF CARS SIGNAL (Adapted from [34]). The resonant term (*black solid line*), the nonresonant term (*black dotted line*), the mixing term (*back dashed line*) and the total CARS signal (*red solid line*) are plotted as function of the Raman shift $\omega_P - \omega_S - \Omega_R$ (Ω_R is the centre frequency of a homogeneously broadened Raman line R) under the condition $\chi^{(3)}_{NR} = 1.2\chi^{(3)}_R$ and $\omega_P - \omega_S - \Omega_R = 0$.

onant term includes the imaginary part $\mathrm{Im}\{\chi^{(3)}_R\}$ which has a Lorentzian profile emulating the spontaneous Raman line. The nonresonant term has a constant, frequency-independent profile. The mixing term presents a dispersive lineshape due to the interference between the resonant and the nonresonant term. The result is a CARS spectral profile with a maximum shifted towards lower frequencies and a dip towards higher frequencies [35].

Understanding the physical basics of the CARS process is fundamental to comprehend the main properties of CARS spectral-microscopy and to exploit CARS as an investigative tool in biology-related contexts [5].

From Equations 2.12 and 2.13 it can be observed that, when the frequency difference $\omega_P - \omega_S$ between the pump and the Stokes field matches the frequency of a molecular vibration Ω_j in the sample, the resonant term $\chi^{(3)}_R$ is maximized and the CARS signal enhanced. Furthermore, since A_j is proportional to the number of dipoles, all the anti-Stokes Raman fields emitted by identical resonantly-driven molecules interfere constructively with each other. This results in a 5 orders-

of-magnitude increase of the CARS intensity with respect to the corresponding spontaneous Raman signal from 10^5 molecules [36]. The vibrational information carried by the term $\chi_R^{(3)}$ can be exploited as a chemically-based contrast mechanism. Specifically, the spatial distribution of a molecule resonant at the vibrational frequency Ω_j can be mapped by tuning the frequency difference $\omega_P - \omega_S$ to Ω_j and by recording the outgoing CARS signal as the focus of the incident fields is scanned over the sample.

Equations 2.9 and 2.10 show that the CARS signal has a quadratic and linear dependence on the pump and Stokes intensity, respectively. Because of this third-order nonlinear relation, CARS signal is only efficiently generated when high excitation intensities are achieved, that is, in the volume where pump and Stokes fields are tightly focused. This provides CARS microscopy with an intrinsic three-dimensional spatial resolution, similarly to other multiphoton techniques such as two-photon microscopy [37].

Another important characteristic is that the CARS signal has a higher frequency than pump and Stokes fields, as follows from Equation 2.8 for $\omega_P > \omega_S$. Contributions from excitation fields, sample fluorescence and spontaneous Raman signal are at lower frequencies and do not interfere with the detection of the CARS signal.

One of the complications of CARS is the presence of a nonresonant background that arises from the contribution of the nonresonant term $\chi_{NR}^{(3)}$ of the susceptibility and it limits both spectral sensitivity and image contrast. On the spectroscopy side, it is responsible for the distortion of spectral lineshapes and the consequent complication in the correct molecular assignment of each present feature. On the microscopy side, it introduces an offset background and a negative contrast for CARS images at the frequencies in the dip of the CARS signal [34].

2.3 Experimental realization of CARS

CARS signal was first observed in laboratory conditions in 1965, when Marker and Terhune performed a series of experiments on nonlinear optical events at the Ford Motor Company. Using a pulsed ruby laser, they investigated the nonlinear distortion (*polarization*) induced by the strong electrical laser fields on the electron clouds of molecules in crystalline and isotropic materials [38]. Their results set the starting point for the use of CARS as a spectroscopic technique for high-resolution studies of gas and condensed phases, with pump and Stokes excitation fields being provided by tunable dye lasers [5].

First applications of CARS as a microscopy technique were attempted 17 years later by Duncan and colleagues who used CARS as a contrast mechanism to image the distribution of heavy water (deuterium oxide, D_2O) in onion-skin cells [39]. Although pioneering in the use of a scanning microscope connected to camera-tube detector, their results were severely limited by a low spatial resolution and the large nonresonant background from off-resonance and electronic transitions [35]. The experimental settings they adopted – two picosecond (ps, 10^{-12} s) visible dye lasers and a noncollinear beam geometry – had been proven suitable only for spectroscopy-based studies but not for microscopy applications, which instead required other types of solutions.

Some of them were found in 1999 when Zumbusch and colleagues successfully imaged chemical and biological samples using a high numerical aperture microscope objective for the excitation geometry and near-infrared sources for the laser beams [15]. Their results demonstrated for the first time the high spatial resolution, sensitivity and three-dimensional sectioning capabilities of CARS as a microscopy technique, reviving the interest in the field and opening the doors to further developments. The most significant advances applied to spectral-microscopy instrumentation in the past years in order to generate a nonlinear, resonant and coherent anti-Stokes signal are summarized below.

2.3.1 Phase-matching condition

In the CARS process energy and momentum conservation rules must apply. The energy conservation dictates the equality in Equation 2.8. The momentum conservation imposes that the sum of the wavevectors of the absorbed photons has to equal the sum of the wavevectors of the emitted photons (*phase-matching condition*)

$$\vec{k}_{AS} = 2\vec{k}_P - \vec{k}_S \tag{2.14}$$

or equivalently

$$\Delta\vec{k} = \vec{k}_{AS} - \left(2\vec{k}_P - \vec{k}_S\right) = \vec{0} \tag{2.15}$$

where $\vec{k}_P$, $\vec{k}_S$ and $\vec{k}_{AS}$ are the wavevectors of pump, Stokes and CARS, respectively and $\Delta\vec{k}$ is the wavevector mismatch [40].

In practice, however, $\Delta\vec{k}$ has a non-zero value. This is due to the different refractive indexes (n_j, $j =$ P, S and AS) that pump, Stokes and anti-Stokes photons experience while propagating through the medium at different velocities (i.e. frequencies).
Since the CARS signal intensity from a homogeneous sample of interaction length L follows the expression [34]

$$I_{\text{CARS}} \propto \left|\chi^{(3)}\right|^2 I_P^2 I_S \,\text{sinc}\left(\frac{\left|\Delta\vec{k}\right| L}{2}\right)^2 \tag{2.16}$$

a strong anti-Stokes signal can still be achieved when

$$\left|\Delta\vec{k}\right| L \ll \pi. \tag{2.17}$$

In order to minimize L, objective lenses with high numerical aperture (> 0.8) are usually adopted [34]. They allow a small focal volume, i.e. an effective axial size of the point spread function that is few micrometers long, to be achieved. This condition, combined with the distribution of $\vec{k}_P$ and $\vec{k}_S$ over a range of forward directions, relaxes the strict requirement of the phase-matching condition of Equation 2.15 [6].

2.3.2 Laser and pulsed excitations

As far as the laser source is concerned, Zumbusch and colleagues chose near-infrared (NIR) lasers. Characterized by a wavelength range between 800 and 1300 nm, this type of excitation source has three main advantages. First, it minimizes the two-photon electronic interaction that contributes towards the enhancement of the nonresonant CARS background, improving the signal-to-noise ratio in image acquisition [15]. Second, it avoids the multiphoton absorption from ultraviolet electronic resonances, decreasing the associated photo-damage [41]. Third, it reduces Rayleigh scattering in thick material, providing a a larger optical penetration depth in samples such as tissues [15].

Besides the wavelength range, the intensity of the excitation sources is another important parameter that has to be taken into account when selecting the most appropriate laser sources for CARS microscopy. As a consequence of its nonlinear nature, the CARS process requires high peak powers. Whilst maintaining moderate average powers, high peak powers are achieved from lasers that emit optical pulses with the ratio between peak power and average power scaling as the ratio of the repetition period between pulses and the pulse duration [15]. When considering femtosecond (fs, 10^{-15} s) pulses, their spectral width is generally much broader than the width of Raman lines (i.e. $10\,\mathrm{cm}^{-1}$ for biomolecules in liquids), hence a large part of their spectral components contributes to the nonresonant background signal, decreasing the chemical contrast [42]. Conversely, picosecond pulses have a spectral width that matches the Raman linewidth of typical biomolecules in liquids and therefore are able to efficiently excite the resonant signal of interest, providing sufficient spectral resolution [42, 43]. Figure 2.2 shows that, as the pulse spectral width increases, the nonresonant signal also increases with a quadratic dependence while the CARS signal remains constant. Therefore the ratio of the resonant signal to the nonresonant background is higher when using picosecond pulses rather than femtosecond pulses.

Laser systems based on this concept are typically realized using two electronically syncronized Titanium:Sapphire (Ti:Sa) oscillators or an optical parametric oscillator pumped by a mode-locked Neodymium:Vanade (Nd:YVO4) laser

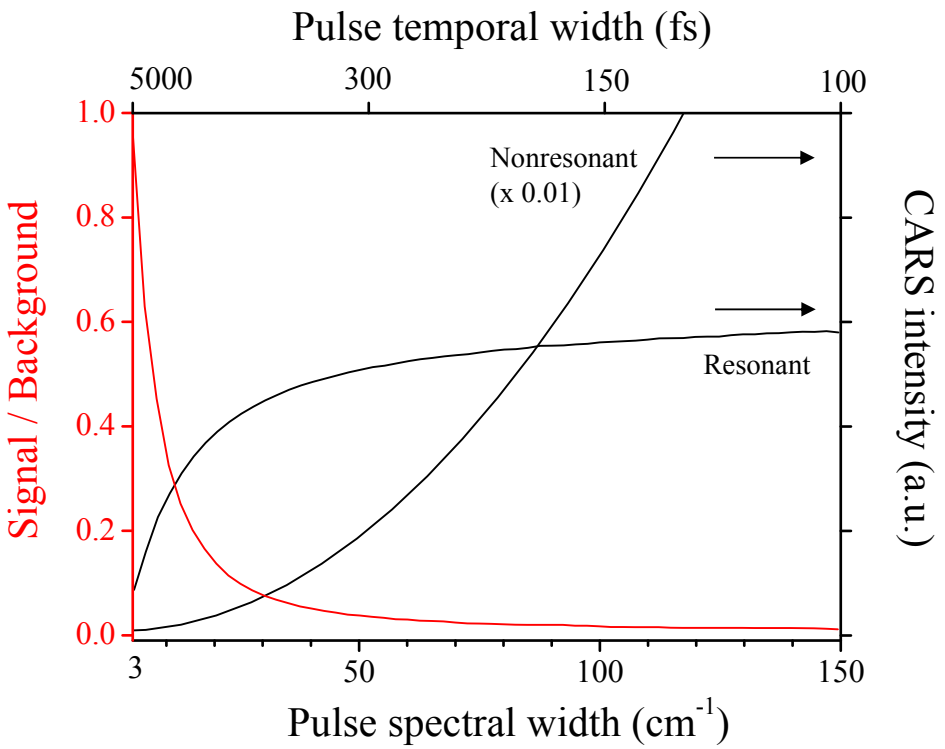

Figure 2.2: DEPENDENCE OF THE RESONANT AND NONRESONANT INTENSITIES ON THE PULSE SPECTRAL WIDTH (Adapted from [42]). The ratio of the signal to background as resonant to nonresonant contribution is also shown for comparison. Note that pump and Stokes pulses are transform-limited with constant energies.

[34, 42]. The greatest disadvantage of picosecond-based equipments is the higher costs and technical expertise required compared to femtosecond sources which are instead cheaper, widespread and more versatile as they also allow efficient multi-photon processes such as the quasi-instantaneous nonlinearities (hence benefiting from shorter pulses) of TPF and SHG that are commonly used in live cell imaging experiments [44]. In the light of this, an alternative approach named *spectral focusing* has been developed to employ femtosecond pulses while overcoming the poor spectral resolution arising from the broad spectral bandwidth [45]. The spectral focusing technique consists of spreading the frequency components of femtosecond pump and Stokes pulses over time (*linear chirp*) with an equal slope. By doing so the overall spectral width of their interference (the vibrational driving term in CARS) is given by the inverse of the chirped pulse duration, which can reach picosecond values (see Figure 3.3 in the next Chapter).

Single- and multiple-frequency excitations

Spectral focusing also provides the opportunity to sequentially excite more vibrational frequencies in a sample and therefore to acquire a broadband vibrational spectrum of the chemical components by changing the delay time between the linearly chirped pump and Stokes pulses (see also Figure 3.3 in the next Chapter). This approach offers faster wavenumber scanning than conventional single frequency CARS and sequential tuning of the laser wavelengths.

In single-frequency CARS, one Raman-active frequency is excited at a time by tuning the pump and Stokes pulse frequency so that the difference $\omega_P - \omega_S$ matches that specific vibrational frequency. When this configuration employs narrow-band laser sources, a high spectral resolution is achieved for every point in the spectrum. However, when multiple frequencies have to be investigated (e.g., in biological samples with many different molecular components), sequentially tuning the laser frequency becomes time-consuming and it is therefore not suitable for dynamic studies that demand for high speed and chemical selectivity [5, 6].

An alternative to sequential tuning is multiplex CARS, where Stokes pulses are characterized by a broader spectral bandwidth than in single-frequency CARS. This allows the simultaneously excitation of molecular vibrations in a wide frequency range and the fast acquisition of the corresponding emitted broadband spectra. Experimentally multiplex CARS have been realized with pico-femto combined schemes and crystal fiber-based laser sources configurations [45–48].

2.3.3 Nonresonant background suppression

As shown in Equation 2.13, the CARS signal is the result of the coherent addition of a resonant $\chi_R^{(3)}$ and a nonresonant term $\chi_{NR}^{(3)}$ with the latter being the main source of background signal in CARS microscopy. Different strategies have been applied to reduce or eliminate the nonresonant contribution and in turn improve the contrast for the signal arising only from targeted vibrating modes [5, 40].

Some methods are based on the different polarization or temporal properties between the resonant and the nonresonant part. In polarization-sensitive detec-

tion, for instance, the polarization of pump and Stokes can be adjusted such that the nonresonant background has a different polarization and it can be blocked by placing a combination of polarization filters in the detection path [18,46]. In time-resolved detection, a tunable time delay is applied between the probe and pump and Stokes pulses in order to distinguish the instantaneous behaviour of the non-resonant signal compared to the finite time response of the resonant signal [49].

Other strategies aim to cancel the nonresonant background through the destructive interference with the pump and Stokes pulses that, by the phase control of the spectral components, have been previously modulated to a function with a period equivalent to the vibrational frequency of selected molecules [50,51]. Others exploit interferometric schemes that mix CARS signal and a local oscillator in order to separate the real part $\mathrm{Re}\{\chi_R^{(3)}\}$ and the imaginary part $\mathrm{Im}\{\chi_R^{(3)}\}$ of the resonant contribution [52–55], where $\mathrm{Im}\{\chi_R^{(3)}\}$ is proportional to the spontaneous Raman intensity [56].

The effectiveness of these methods have been proved successfully on model samples but the technical complexity they required is not compatible with applications to more biologically relevant cases, such as tissues, where phase and polarizations are difficult to control [40]. More feasible methods have been developed considering the intensity difference between the on-resonance frequency and the off-resonance frequency in the CARS vibrational spectrum [57]. Some of them require the pump pulses to be generated by two synchronized pulsed lasers or by an optical parametric oscillator (OPO) forced to oscillate in two modes, which all demand for high technical expertise and expensive equipment [58–60]. Dual-frequency differential CARS (D-CARS) has been recently demonstrated as a simple but still effective technique. Here femtosecond laser pulses that have been linearly chirped by glass elements of known group-velocity dispersion (GVD) are split into two pulse trains. The second pulse train is delayed by half the laser repetition rate and given a small addition amount of chirp so that it probes a slightly different vibrational frequency to the first pulse train. The corresponding intensity difference in the signal generated by the two pulse trains is used to suppress the nonresonant background [29].

2.3.4 Signal detection

The orientation of the CARS radiation pattern depends on the shape of the scattering object under investigation, as shown in Figure 2.3 [61]. When the shape of the object is such that its overall thickness z is small compared to the wavelength of light (e.g., in thin slices), CARS signal is emitted equally in the forward and backward direction. If z is large (e.g., in bulk samples), constructive interference in the forward direction generates forward-propagating CARS (F-CARS) in agreement with the phase-matching condition $\vec{k}_{AS} = 2\vec{k}_P - \vec{k}_S$, while a simultaneous destructive interference in the backward direction prevents the formation of backward-propagating signal (epi-CARS) [61,62].

Epi-CARS has been experimentally observed in different occasions as a consequence of two main mechanisms [34,40]. The first mechanisms involves the size of the scattering dipoles as just discussed, and it leads to an incomplete destructive interference for the epi-CARS when the dipole size is smaller than one-third of the pump wavelength λ_P [42]. Similarly, discontinuities of the susceptibility $\chi^{(3)}$ at one interface that break the symmetry in the focal volume also give rise to epi-CARS [61]. The second mechanism originates from the backward reflection of the F-CARS radiation due to changes in the refractive index and takes place in turbid environments such as biological tissues [63]. Note that this is not proper epi-CARS but F-CARS being back-scattered.

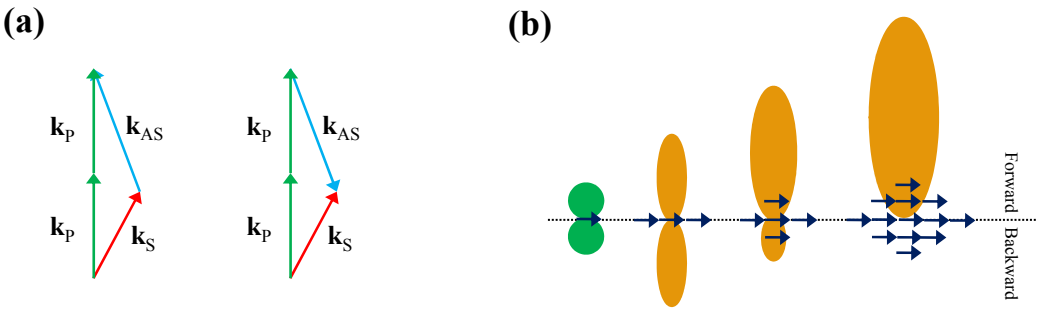

Figure 2.3: FORWARD AND BACKWARD SIGNAL GENERATION IN CARS MICROSCOPY (Adapted from [34]). *Panel (a):* Phase-matching condition for CARS emitted in the forward (left) and backward (right) direction with respect to the phase matching direction. *Panel (b):* Radiation pattern for CARS signal generated by a single vibrating molecule (left), a plane of molecules (left-centre), a three-dimensional group of molecules (centre-right) and a larger three-dimensional group (right) in the focal volume.

F-CARS signal is in general strong in thick samples and therefore detectable against the nonresonant background. Conversely, in the case of thin samples and small objects embedded in a bulk sample, F-CARS is as strong as epi-CARS but epi-CARS is free from the nonresonant background of the bulk-like surrounding medium. Therefore the signal-to-background ratio can be improved through the detection in the backward direction [42, 63–65].

3 Material and Methods

3.1 Introduction

Lipid droplets (LDs) of various chemical compositions were characterized in the spectral and spatial domain through CARS and D-CARS hyperspectral imaging. Two types of samples were investigated: (a) lipid droplet model systems consisting of neutral lipids in micron-size droplets in an agarose-in-water solution, (b) cytosolic lipid droplets as biological components in fixed and living cellular systems.

In order to define and distinguish their intrinsic molecular properties, model and cytosolic LDs were investigated with two home-built set-ups that allowed vibrational sampling in the fingerprint and "CH-stretch" spectroscopic regions. Data were acquired as line spectra and hyperspectral images, and processed in order to eliminate the CARS nonresonant background, to identify different lipid compositions at chemically-discriminant vibrational frequencies and to quantify those compositions spectrally and spatially.

In this chapter, a detailed description of the sample preparation is provided for model and cytosolic LDs. This is followed by the description of the experimental set-ups used to perform CARS/D-CARS microscopy. Finally, the analytical procedures carried out to interpret and quantified the experimental data are explained.

3.2 Samples

Lipids were purchased from Sigma-Aldrich® (Zwinjdrecht, the Netherlands) and from Nu-Chek Prep, Inc (Elysian, Minnesota, USA) in the form of fatty acids and triglycerides. A *fatty acid* is a chain of CH_2 bonds where carbon atoms constitute the central backbone; a *triglyceride* is the combination of three fatty acids and a molecule of alcohol glycerol [66]. Lipids were chosen with physical–chemical characteristics differing in the number of C atoms constituting the fatty acid backbone (lipid length), the absence or presence of double bonds, C=C, between carbon atoms (lipid saturation or unsaturation) and the location of C=C in the fatty acid chains. Major properties are summarized in Table 3.1 and molecular structures are represented in Figure 3.1.

3.2.1 Model lipid droplets

Model LDs were created as an emulsion of micron-sized pure triglyceride droplets in an agarose-in-water solution.

Five triglycerides were used: glyceryl tricaprylate (GTC) with C8:0 fatty acid saturated chains; glyceryl tristearate (GTS) with C18:0 fatty acid saturated chains; glyceryl trioleate (GTO) with C18:1 mono-unsaturated chains with *cis* double bond at the 9th position from the first carbon atom in the chain (*1,2,3-Tri(cis-9-octadecenoyl)glycerol*); α-glyceryl trilinolenate (α-GTL) with C18:3 fatty acid chains and all *cis* double bonds at 9, 12, and 15th position from the 1st carbon atom (*1,2,3-Tri-(cis,cis,cis-9,12,15-octadecatrienoyl)glycerol*); γ-glyceryl trilinolenate (γ-GTL) with C18:3 fatty acid chains all *cis* double bonds at the 6th, 9th and 12th position from the 1st carbon atom (*1,2,3-Tri-(cis,cis,cis-6,9,12-octadecatrienoyl)glycerol*).

For the solution, low melting temperature 65°C agarose powder was purchased from Invitrogen™ (Catalogue number 16520-050, Breda, the Netherlands).

Model LDs were prepared as follows. Agarose powder was dissolved in deionised hot (80°C) water to prepare a 2% mass-volume concentration solution. One of the triglyceride types was then added in a 1% volume-volume concentra-

Lipid Name (abbrev.)	Carbon chain length	Number of double bonds	Position of double bonds	Melting point [°C]
Palmitic Acid (PA)	16	0	-	63
Oleic Acid (OA)	18	1	9	13-14
Linoleic Acid (LA)	18	2	9-12	-5
α-Linolenic Acid (LNA)	18	3	9-12-15	-11
Glyceryl Tricaprylate (GTC)	8	0	-	9-10
Glyceryl Tristearate (GTS)	18	0	-	71-73
Glyceryl Trioleate (GTO)	18	1	9	-5.5
α-Glyceryl Trilinolenate (α-GTL)	18	3	9-12-15	-24
γ-Glyceryl Trilinolenate (γ-GTL)	18	3	6-9-12	-24

Table 3.1: PROPERTIES OF INVESTIGATED LIPIDS. Main physical and chemical properties are summarized for the considered fatty acids and triglycerides (*grey*). The position of C=C bonds is counted from the first carbon atom at the head of the fatty acid chain they are in [67].

tion. While keeping the temperature around the agarose melting point (a heating coil was eventually used), the emulsion was sonicated in an ultrasonic bath (Branson Ultrasonics) for 15 minutes. While still in liquid form, 13 μL of the emulsion was pipetted inside a 120μm thick imaging spacer (Grace^{TM}Bio-Lab SecureSeal^{TM}) glued on a glass coverslip in order to create a chamber, which was sealed by a second coverslip on top (25×40 mm and 25×25 mm #1 Menzel-Gläser® coverslips, Braunschweig, Germany). Once cooled down to room temperature, the agar solution solidified and acted as a matrix where LDs with dimensions in the order of micrometers were evenly suspended throughout. Note from Table 3.1 that at room temperature GTS is in solid phase, while the other lipids are in liquid phase.

Samples were stored at 4°C with 100% humidity conditions in order to prevent the agar emulsion from drying out.

3.2.2 Cytosolic lipid droplets

Cytosolic LDs were investigated in human adipose-derived stem cells (ADSCs) differentiated into adipocytes and cultured in lipid-enriched media. Specifically, four fatty acids were used: palmitic acid (PA), a saturated 16-carbon chain (*hex-*

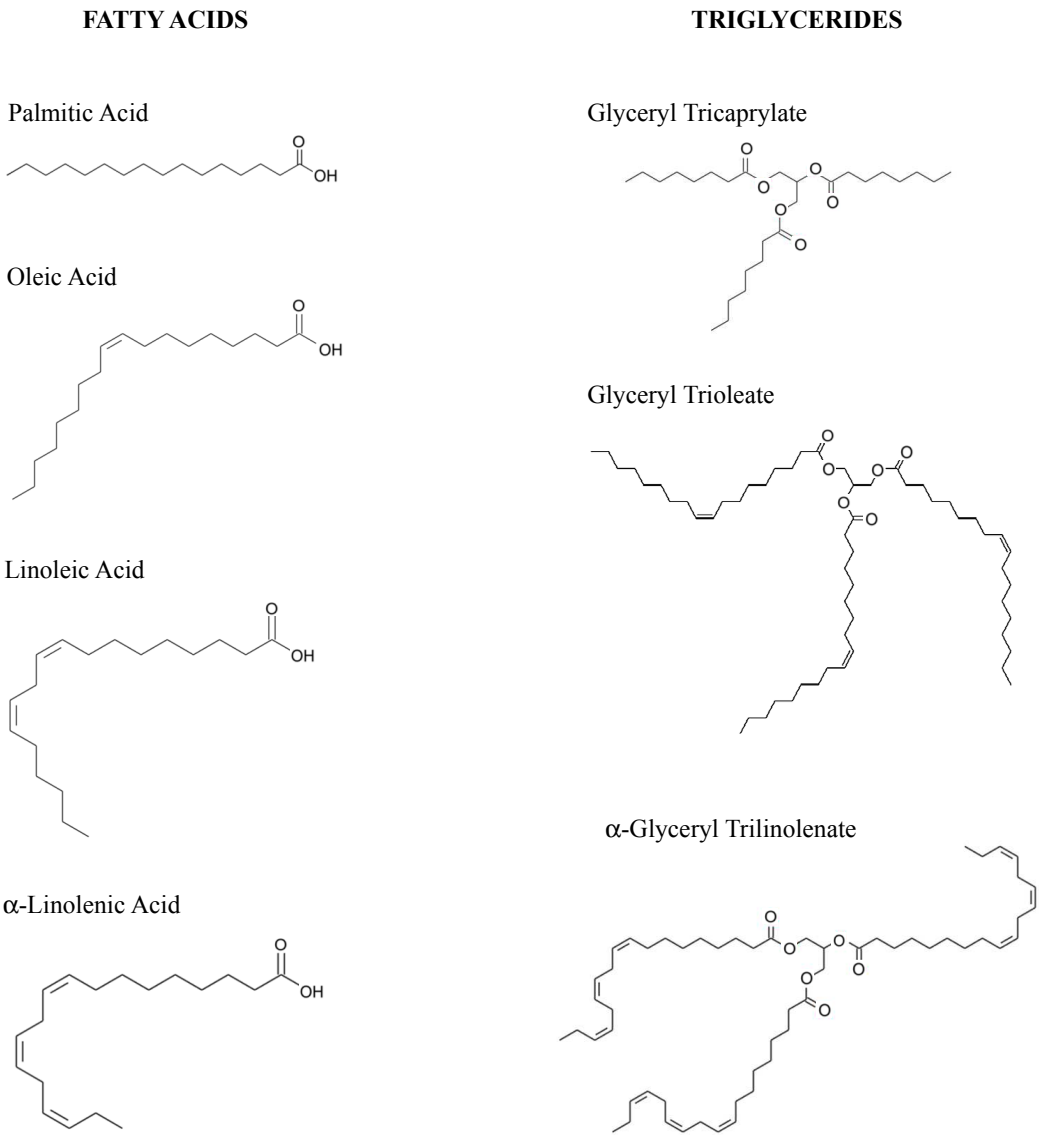

Figure 3.1: STRUCTURES OF INVESTIGATED LIPIDS. Chemical structures are reported for some of the considered fatty acids and triglycerides, as indicated. MolView was used as molecule editor to represent them.

adecanoic acid); oleic acid (OA), a mono-unsaturated 18-carbon chain with a *cis* double bonds at the 9th position from the first carbon atom (*cis-9-octadecenoic acid*); linoleic acid (LA), a bi-unsaturated 18-carbon chain with two *cis* double bonds at the 9th and 12th position (*cis,cis-9,12-octadecadienoic acid*); α-linolenic acid (LNA), a tri-unsaturated 18-carbon chain with *cis* double bonds at 9, 12, and 15th position (*cis,cis,cis-9,12,15-octadecatrienoic acid*).

Cell samples were prepared as follows. ADSCs purchased from Invitrogen (Carlsbad, CA, USA) were grown in low glucose DMEM and GlutaMAX^{TM} me-

dia supplemented with 10% mesenchymal stem cells qualified FBS, 75 μg/mL Gentamicin and 37.5 μg/mL Amphotericin. In order to induce differentiation into adipocytes, they were cultured in StemPro® adipogenic differentiation media as indicated by the manufacturer's protocol. For experimental purposes, cell cultures were grown directly on glass coverslips (thickness no. 1.5, $\varnothing$25, PA, VWR International, USA). After 3 days, media were supplemented with fatty acid-BSA complex (9.4 μg/mL fatty acid concentration). From this moment on (day 0) cells were treated differently according to the experiment intended to be performed.

For live cell experiments, the cell seeded coverslips were mounted in custom-made stainless steel imagining chambers (in which they remained for the duration of the experiment) and were observed directly from day 0. The initial set of human ADSCs was fed with oleic acid, linoleic acid, α-linolenic acid and a 1:1 volume:volume mixture of oleic acid and α-linolenic acid. A fifth sample was left in the normal differentiation media and used as a control. On day 3, the oleic acid-supplemented media was substituted with α-linolenic acid-supplemented media and *viceversa*. Live cell imaging measurements were performed daily up to day 9. Whilst undergoing imaging cells were kept at 37°C in a 5% CO_2 air blend atmosphere. In between measurements samples were kept in a tissue culture incubator, again with a 5% CO_2 air blend atmosphere at 37°C. Alignment marks on the exterior of the imaging chambers ensured their precise repositioning on the microscope stage, enabling specific cells to be tracked throughout the course of the experiment.

For experiments with fixed cells, after day 0 human ADSCs were grown for 3 additional days in the supplemented media and fixed in formaldehyde-phosphate buffered saline (PBS) solution [68]. Specifically, cells were deprived of the culture media, washed with PBS, incubated with 4% paraformaldehyde in PBS for 20 minutes at room temperature and washed again with PBS. In order to study the effects of fixation on cells, cold methanol was also used as fixative and the procedure was as follows [68]. The incubation was with cold methanol (-20°C) in a pre-chilled glass tray kept on dry ice for 5 min and the final wash with cold PBS. For both paraformaldehyde and methanol fixation, coverslips with cells were

mounted onto standard glass slides using 120 μm thick imaging gaskets (Grace^{TM} Bio-lab SecureSeal^{TM}) filled with water or previous culture media.

In order to investigate the effects of the protein Rab18 and the small molecule inhibitor Exo2 on LDs, cells were treated as follows. For the study on Rab18, ADSCs were microinjected with an expression construct containing GFP(green fluorescent protein)-tagged Rab18 [69] using an Eppendorf FemtoJet® injection system. Cells were allowed to express for 16 hours. For the study on Exo2, ADSC cells were incubated in full media containing 150 μM Exo2, before being washed and visualised on the CARS microscope [70].

All samples (both with fixed and living cells) were prepared by Dr. Peter Watson.

3.3 CARS and D-CARS set-ups

Samples were investigated on two different experimental set-ups, one built in the Cardiff School of Physics and Astronomy and the other built in the Cardiff School of Biosciences [29, 71, 72]. A schematic overview of both is shown in Figure 3.2. Four main parts can be distinguished. The first part is related to the generation of the pump and Stokes beams as femtosecond pulsed trains. A second part is dedicated to temporal stretching of laser pulses to the picosecond range by *spectral focusing*. A third part is used for the realisation of the dual-frequency differential (D-CARS) technique which enables simultaneous excitation and detection of 2 vibrational frequencies and in turn better suppression of the CARS nonresonant background. A fourth part is the main microscope assembly used for sample illumination and the collection of the CARS and D-CARS signal emitted by the sample. The two configurations – which will be referred to as "100 fs" and "5 fs" in reference to the temporal duration of the pulses delivered by the laser source – differ in construction in the first and fourth parts of their set-up. They both allow the investigation of molecular CARS vibrations but with different spectroscopic resolutions and vibrational frequency ranges.

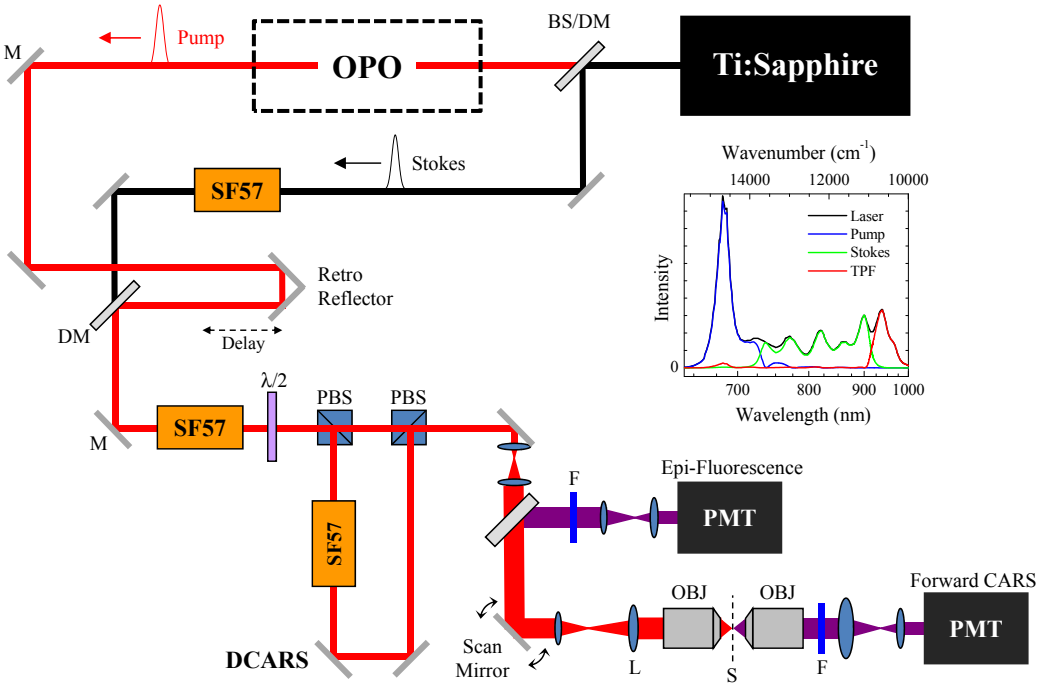

Figure 3.2: OVERALL OPTICAL LAYOUT FOR THE 5 AND 100 FS SET-UPS (Reprinted from [44] with permission from Elsevier). In the 100 fs set-up, the pump beam is generated by an OPO pumped by a 100 fs Ti:Sa laser and, together with the Stokes beam, it is focused on the sample through a home-made microscope. In the 5 fs set-up, the pump beam is provided directly by a < 8 fs Ti:Sa laser as the Stokes beam, and beam collection on/from the sample is incorporated in a commercial microscope. The typical experimental spectra of the laser, pump and Stokes beam is reported for the 5 fs set-up. Legend of optical elements: BS: beam splitter; DM: dichroic mirror; M: mirror; SF57: glass blocks; PBS: polarizing beam splitter; $\lambda/2$: half-wave plate; F: filter; L: lens; S: sample; OBJ: object; PMT: photomultiplier tube.

3.3.1 Laser sources

The data discussed within this thesis were collected with systems equipped with femtosecond laser sources, specifically a 100 fs set-up and a 5 fs set-up.

In the 100 fs set-up, pulses are delivered by a Ti:Sa laser source (Coherent Verdi/Mira) with 100 fs duration at 832.5 nm and with a 76 MHz repetition rate. Using a dichroic splitter, the pulsed beam is then separated into two parts: one part is directly used as the Stokes beam, with 832.5 nm central wavelength and 11 nm full width at half maximum (FWHM); the other part is used to synchronously pump an optical parametric oscillator (OPO, APE PP2) and generate 4 nm-wide pump pulses centred at 670 nm.

In the 5 fs set-up, the main laser source is a Ti:Sa system (Venteon, Pulse:One

PE) delivering < 8 fs pulses with a spectral width at 10% of the maximum of 310 nm (from 660 nm to 970 nm) and a repetition rate of 80 MHz. By an appropriate sequence of beam splitters, the laser spectrum is divided into pump, Stokes and TPF/SHG beams with each of them carrying approximately $1/3$ ($1/6$ for SHG) of the laser power (600 mW on average). Pump and Stokes pulses are centred at 682 nm and 806 nm with a bandwidth at 10% of the maximum of 65 nm and 200 nm, respectively. This allows the excitation of molecular vibrations in the $1200 - 3500\,\mathrm{cm}^{-1}$ range, much wider compared to that achieved with the 100 fs laser system which was limited between $2750 - 3050\,\mathrm{cm}^{-1}$.

3.3.2 Spectral focusing and frequency tuning

It has been already mentioned in Section 2.3.2 that the bandwidth of femtosecond pulses is much larger than the Raman bandwidth. This causes a reduction of spectral selectivity and an increase in the amount of the nonresonant background. This limitation can be overcome by using pump and Stokes pulses which are *chirped*, that is, "stretched" in time so that the temporal interference between them drives vibrations in a narrower frequency range. This process is called *spectral focusing* and it has been implemented in the 100 fs and a 5 fs set-ups by inserting SF57 glass elements (Changchun Fortune Optronic Inc.) of known chromatic dispersion [71, 73].

In optics, chromatic dispersion is a phenomenon in which the refractive index n of a dispersive medium changes with wavelength, $n(\lambda)$, and thus frequency. One example of a dispersive medium is glass. When a laser pulse travels through a piece of glass, its different wavelength components travel at different speeds, with the longer wavelengths moving faster and leaving the glass first (*chirping*) (Figure 3.3). If E_0 is the electric field of a Gaussian-shaped pulse entering a piece of glass of thickness d, the associated electrical field E of the pulse when exiting from the glass may be expressed as

$$E(t) = E_0\, e^{\left(-\left(\frac{t}{\tau_G}\right)^2 + \mathrm{i}\, t(\omega_0 + \beta\, t)\right)} \tag{3.1}$$

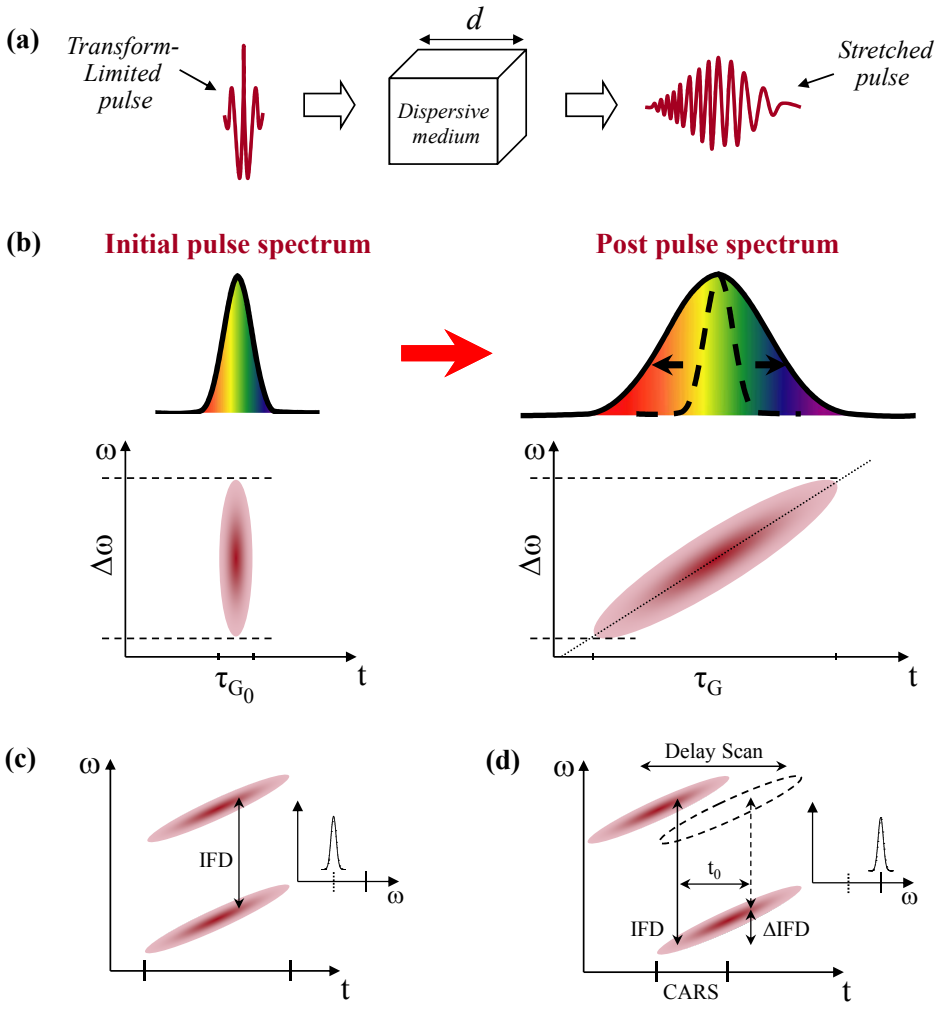

Figure 3.3: VISUAL REPRESENTATION OF SPECTRAL FOCUSING AND TUNING (Reprinted from [44] with permission from Elsevier). When passing through a dispersive medium such as glass, a laser pulse is chirped and the longer wavelengths are the first to emerge (*a*). In this process the spectral range $\Delta\omega$ of the pulse remains constant (*b*). When considering two equally chirped pulses, the IFD between them is constant (*c*) but it can be changed if one pulse is delayed with respect to the second pulse (*d*), allowing sampling of different IFDs.

with

$$\beta = \frac{2k''d}{\tau_{G_0}^2 \tau_G^2} \quad \text{and} \quad k'' = \frac{\lambda^3}{2\pi c^2}\frac{d^2n}{d\lambda^2}$$

where t is time, ω_0 is the frequency at the pulse centre, β is the chirp parameter, c is the speed of light, k'' is the group velocity dispersion, τ_{G_0} is the initial pulse width and τ_G is the pulse width after chirping [71, 73]. From Equation 3.1, the Gaussian pulse has an instantaneous frequency defined as $\omega(t) = \omega_0 + 2\beta t$ with βt being the temporal phase gradient. For spectral focusing in the CARS process,

pump and Stokes pulse have the same linear chirp parameter β, hence

$$\omega_P(t) = \omega_{P_0} + 2\beta t \qquad (3.2)$$
$$\omega_S(t) = \omega_{S_0} + 2\beta t$$

and the instantaneous frequency difference (IFD) between them, $\omega_D = \omega_P(t) - \omega_S(t)$, remains constant over time. Experimentally this concept has been implemented in our set-ups by the addition of extra glass elements in the optical path, where the thickness of the glasses is such that the spectral width of the interference term $E_P E_S^*$ centred at the IFD is given by the Fourier limit of the chirped pulse duration [71]. In particular, in the 100 fs set-up, the Stokes beam is first made to propagate through a block of SF57 glass of thickness $L_1 = 9$ cm; then, when recombined with the pump beam, it is made to go across a second common glass block of thickness $L_2 = 8$ cm in order to account for the different dispersions of pump and Stokes. The chirp introduced by the remaining optics (microscope objective included) was also considered and counted as a SF57 glass of thickness 4 cm. In the 5 fs set-up, $L_1 = 1$ and 3 cm for the fingerprint and the "CH-stretch" region, respectively. No additional glass blocks L_2 were needed since the total amount of glass present in the other optical elements was sufficient to chirp the pulses to the desired picoseconds range.

As a result, pump and Stokes pulses create a beat frequency that is centred at IFD $\omega_{P_0} - \omega_{S_0}$ and has a spectral width determined by the Fourier limit of the temporal envelope of the pulses. Specifically, the spectral resolution and chirped pulse duration were the following: for the 100 fs set-up, 30 cm^{-1} and 0.7 ps, respectively; for the 5 fs set-up, 5 or 10 cm^{-1} and 1.5 ps for the pump pulse (10.6 ps for the Stokes pulse), respectively.

This configuration allows one to resonantly drive one vibrational resonance only. To gain a higher chemical specificity for the samples considered, a multiplex approach is however necessary. This was achieved by changing the arrival time of the pump pulses with respect to the Stokes pulses with a mechanical stage (Physik Intrumente M-403.6DG and M-404.42S for the 100 and 5 fs set-up, respectively).

Specifically, they were made to travel different distances according to the stage position so that pump pulses recombined with Stokes pulses with different delays. By adjusting the delay time (temporal mismatch t_0) between the pump and Stokes pulses it was possible to excite and probe different IFDs sequentially and without the need to tune the laser.

3.3.3 Dual-frequency differential CARS (D-CARS)

After being spectrally focused and tuned, pump and Stokes pulse pairs enter the D-CARS section of the set-ups.

D-CARS is a technique recently developed by our group in Cardiff to eliminate the non-zero contribution to $\chi^{(3)}$ which arises from off-resonance vibrational and electronic transitions (i.e the nonresonant CARS background) that may seriously worsen spectral sensitivity and image contrast [29]. D-CARS works by splitting the pump and Stokes pulse pair beam into two orthogonally polarised pulse pairs using a half-wave plate (CASIX Achromatic waveplate) and a polarising beam splitter (PBS, Lambda Research Optics for the 100 fs set-up and ThorLabs for the 5 fs set-up). These new pulse pairs, Π_1 and Π_2, have the following characteristics (Figure 3.4). The Π_1 pair is transmitted through the PBS at the laser repetition rate T_{rep} and excites resonances at the single frequency ν_{IFD1}. The pair Π_2 is reflected and made to travel a longer distance in order to be delayed by $T_{rep}/2$ with respect to the Π_1 pair. While travelling the additional path, pair Π_2 passes through an additional SF57 glass block that causes the pump pulse to be delayed relative to the Stoke pulse. As a result, the Π_2 pair drives the vibrational resonance at the single shifted frequency $\nu_{\mathrm{IFD2}} = \nu_{\mathrm{IFD1}} - \Delta_{\mathrm{IFD}}$ with Δ_{IFD} being determined by the additional thickness d of the SF57 glass block and ν_{IFD1} being the frequency sampled by Π_1 pair. Specifically, for measurements performed with the 100 fs set-up, $\Delta_{\mathrm{IFD}} = 65\,\mathrm{cm}^{-1}$ was achieved with $d = 4$ mm; for the 5 fs set-up, $\Delta_{\mathrm{IFD}} = 20$ and $34\,\mathrm{cm}^{-1}$ were introduced in fingerprint region with $d = 1$ and 1.4 mm, respectively; $\Delta_{\mathrm{IFD}} = 27$ and $65\,\mathrm{cm}^{-1}$ were used in the "CH-stretch" region with $d = 0.4$ and 4 mm, respectively. Note that for all these cases d was sufficiently small to neglect its effect on the chirp parameter β.

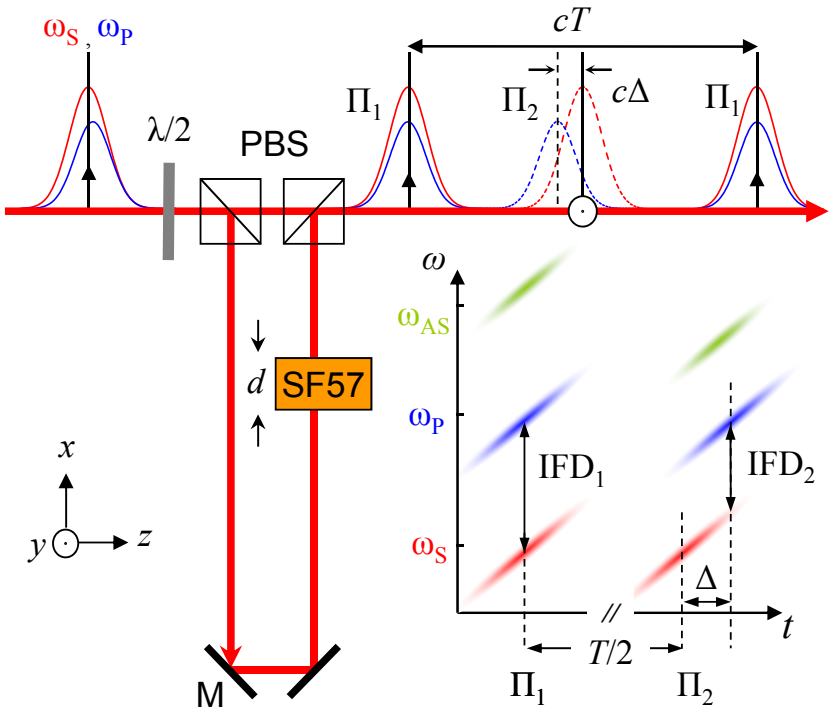

Figure 3.4: OPTICAL LAYOUT FOR THE D-CARS SUBSYSTEM (This figure was published in [29] and is made available as an electronic reprint with the permission of OSA. The paper can be found at the following URL on the OSA website: dx.doi.org/10.1364/OL.34.002258). The main pulse train is divided into two pulse trains, Π_1 and Π_2, with Π_2 delayed in respect to Π_1 and driving resonances at smaller wavenumbers (*bottom right*). Legend of optical elements: $\lambda/2$: half-wave plate; PBS: polarizing beam splitter; M: mirror; SF57: glass blocks.

The signal intensities generated by the Π_1 and Π_2 periodic pulse sequence can be retrieved using an appropriate frequency analysis. The corresponding CARS intensity can be expressed in a laser repetition period $[0, T_{rep})$ as the sum of the intensities from every pump and Stokes pulse pair

$$I(t) = A_1\delta(t) + A_2\delta(t - T_{rep}/2). \tag{3.3}$$

If written as a Fourier series, the former becomes

$$I(t) = a_0/2 + a_1\cos(2\pi t/T_{rep}) + \ldots \tag{3.4}$$

with

$$a_0 = 2(A_1 + A_2)/T_{rep} \text{ and } a_1 = (A_1 - A_2)/T_{rep}$$

where a_0 is the dc Fourier coefficient, proportional to the sum of the CARS signals from Π_1 and Π_2 (sum-CARS) and a_1 is the ac Fourier coefficient, proportional to the difference of the CARS signals from Π_1 and Π_2 (D-CARS). The dc and ac components are simultaneously measured by a lock-in amplifier referenced at the frequency $2\pi/T_{rep}$.

The D-CARS technique can be used to eliminate the nonresonant CARS background and enhance chemical contrast. Note that D-CARS sensitivity is exclusively limited by the shot noise associated to light's inherent nature of photon discreteness. Classical and mechanical fluctuations are suppressed by measuring at the high modulation frequency of the laser beam and by the differential detection of the D-CARS signal, i.e. classical fluctuations from laser intensity instabilities and long term mechanical drifts are overcome [29].

3.3.4 Signal collection

The pump and Stokes periodic pulse train is focused on the sample to drive a selected frequency, and CARS is emitted according to the physical principles of the CARS formation process. The exciting and the emitted beams are handled differently in the 100 fs and the 5 fs set-up.

In the 100 fs set-up, the excitation beam enters a home-built microscope comprising an input microscope objective (Leica HCX PL APO 63x W Corr CS, water immersion, 60× 1.2 NA) which focuses it onto the sample. An identical microscope objective collects the forward emitted sum-CARS and D-CARS signals which are then filtered from the excitation wavelenghts (Semrock FF01-562/40 filter) and detected using a photomultiplier (Hamamatsu H7422-40). The sample is mounted on a motorized/piezoelectric stage and beam-scanned using a single-mirror tip-tilt system (Physik Instrumente PI S-334) controlled using a custom-written software. The resulting CARS spatial resolution (FWHM of the intensity point-spread function) is 0.3 and 0.9 μm in the lateral and axial direction, respectively [73].

In the 5 fs set-up, the excitation beam enters a commercial inverted microscope (Nikon Ti-U), equipped with different objectives and condensers. For the samples

investigated in this thesis, a 20× 0.75 NA dry objective (Nikon CFI Plan Apochromat λ series) and a 0.72 NA dry condenser were used. A pair of galvo mirrors (Eksma Optics and Cambridge Technology) is used to steer the laser beam focus along a sequence of horizontal strips covering the entire sample (*beam scanning*). After passing through appropriate band pass filters (Semrock SP01-633RS and FF01-609/54 filters for the fingerprint region; two Semrock FF01-562/40 filters for the "CH-stretch" region), the forward generated signal is detected by a photomultiplier tube (Hamamatsu H7422-40) around 600 and 560 nm for the fingerprint and the "CH-stretch" region, respectively.

Two dichroic beam splitters (Semrock FF520-Di02 and Chroma t495lp) separate the TPF emission from CARS and SHG emission, and a photomultiplier tube (Hamamatsu H10721-20) collects TPF at around 510 nm. Differential interference contrast (DIC) and epi-fluorescence images can also be acquired. A DIC module is included in the dry condenser. Epi-fluorescence illumination is provided by a metal-halide light source (Prior Lumen 200) and corresponding images are acquired through a monochrome CCD camera (Hamamatsu Orca-285).

Samples are mounted on a stage fully controlled by a Prior ProScan III Control Centre. The resulting CARS spatial resolution is 0.6 and 1.1 μm in the lateral and axial direction, respectively [72].

In order to support live cell imaging, part of the Ti-U stand is enclosed in a larger chamber where temperature, CO_2 levels and humidity are controlled and kept at constant values of 37°C, 5% and 95%, respectively.

3.3.5 Data acquisition

Interesting LDs were first found with the DIC contrast modality incorporated in the microscope. For model-LDs experiments, only droplets with diameters between 3 and 10 μm (i.e. larger than the focal volume but not excessively) were considered in order to guarantee the generation of the CARS/D-CARS signal by the bulk lipid medium and to avoid under-resolution or beam distortion effects (e.g., disturbances from the background signal or the local disalignment of the excitation beams).

On targeted LDs, CARS and D-CARS spectra and images were acquired using a custom-written software called MultiCARS (LabWindows CVI, W. Langbein *et al.*, Cardiff School of Physics and Astronomy) that allows hardware-software interfacing and remote control of the set-up instrumentation. The fingerprint region was investigated with the 5 fs set-up only, the "CH-stretch" region was investigated both with the 100 fs and the 5 fs set-ups. For model LDs, CARS and D-CARS spectra were acquired as two dimensional delay plus line beam scan (so called *x*-IFD scans) crossing a droplet and the surrounding agarose along the transversal direction *x* of the focussed beam; D-CARS images were acquired as *xy* beam raster scans through the droplets' middle section at specific chemically-discriminating wavenumbers. For cytosolic LDs, *x*-IFD line scans were not acquired to avoid prolonged sample heating by repeatedly addressing the same line, and consequent cell damage. Instead CARS hyperspectral images were recorded as collections of *xy* images over a specific range of wavenumbers, namely $1200-2000\,\mathrm{cm}^{-1}$ ($5\,\mathrm{cm}^{-1}$ step) for the fingerprint region and $2600-3200\,\mathrm{cm}^{-1}$ ($5\,\mathrm{cm}^{-1}$ step) for the "CH-stretch" region. In order to optimise the imaging of the lipid content in the cytosolic LDs' core, *xy* images were taken at the depth *z* for which medium-sized droplets (i.e., with diameter between 3 and 5 μm) are equatorially cut. Specific settings, such laser power on the sample and image dwell time, will be specified in the next Chapters.

In order to avoid saturation in the detection and amplification electronics, the photoelectron flux and corresponding current from the photomultiplier as well as the voltage amplitude of the alternating component detected by the high-frequency lock-in electronics were kept below saturation values (2μA is the limit for the photomultipliers).

In all measurement sessions, CARS spectra from a solid layer of polystyrene and from glass were also recorded. The polystyrene was used as standard to calibrate wavenumbers against its well known vibrational spectrum. Conversely, glass was used as a material with no vibrational resonances in the investigated range, hence as a measure of the temporal overlap of pump and Stokes pulses and in turn to normalize measured CARS intensities to achieve a CARS ratio independent of

excitation/detection parameters [28, 74].
Background contributions from set-up electronics or cellular auto-fluorescence were quantified through measurements where pump and Stokes pulses are so delayed relative to each other that time overlap does not occur between them and no CARS/D-CARS signal is therefore generated. For hyperspectral imaging, for instance, background images were acquired at nominal $1000\,\mathrm{cm}^{-1}$ for the fingerprint region and at $5000\,\mathrm{cm}^{-1}$ for the "CH-stretch" region, which corresponded to a delay time with pump and Stokes out of time overlap.

Experiments on model LDs and fixed cytosolic LDs were performed at room temperature; experiments on cytosolic LDs in living cells were performed in a temperature-controlled environmental chamber.

3.4 Data processing

Acquired images and spectra were analysed in three main steps. These steps are: data regularization to a processing-suitable format; extrapolation of raw intensity CARS/D-CARS values as function of wavenumbers; data analysis via software-implemented methods.

Regularization was performed through MultiCARS software (W. Langbein *et al.*, Cardiff School of Physics and Astronomy).
As an example of regularization, let's suppose that a hyperspectral CARS *xy* image is acquired in the "CH-stretch" region. It carries spatial and spectral information in every single scan channel in the scan output, namely in the scan channel along the x dimension, in the scan channel along the y dimension and in the scan channel in the IFD dimension. In order to be interpreted, this information has to be converted into a multi-dimensional Cartesian data cube of equal sized voxels (a *voxel* is a volumetric picture element representing a signal intensity value in a three dimensional space). This means for the considered example that the hyperspectral CARS *xy* image is regularized into a 3-dimensional cube where x and y are the orthogonal coordinates at the bottom sides and IFD is the height. A fourth coordinate might be added if the hyperspectral image is measured for different

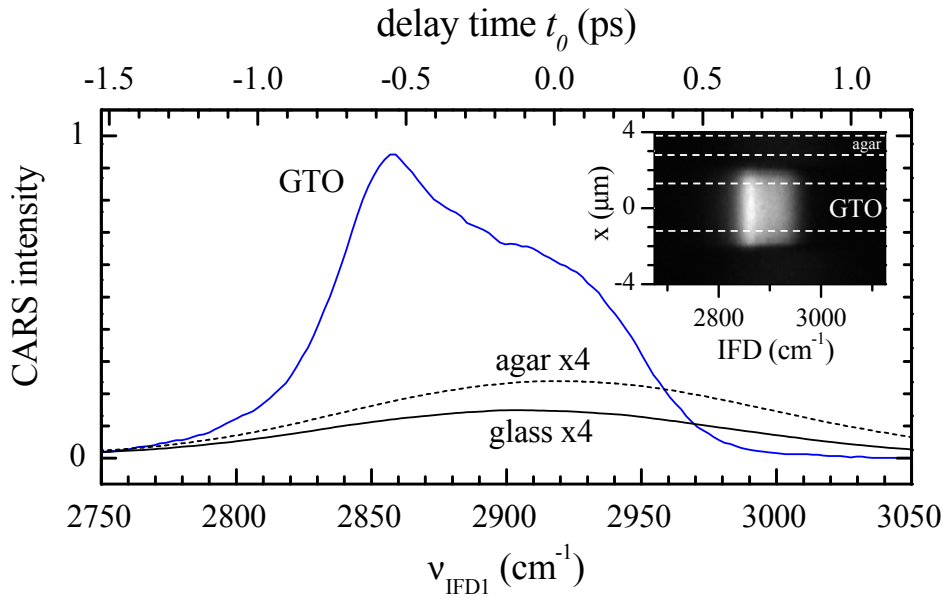

Figure 3.5: EXAMPLE OF CARS SPECTRA IN THE "CH-STRETCH" REGION AS MEASURED WITH THE 100 FS SET-UP (Adapted from [74]). Measured spectra of a GTO-made model LD, of the surrounding agarose gel and of the glass coverslip as a function of the delay time t_0 between pump and Stokes pulses and corresponding wavenumbers. The inset shows the line-scan at the center of the LD, with dotted lines indicating the x positions of GTO and agar. Pump power on the sample 7 mW, Stokes power 2 mW, objective 60x 1.2NA, 0.1 ms pixel dwell time, 75 nm pixel size.

positions in the field of view or by moving the axial coordinate z.

Regularization also allows one to correct for the response of the scanning mirror and of the sample stage so that the actual position (read by sensors) can be used in the data cube. Regularized data can be exported as ASCII files and/or bitmap images for further data analysis.

After regularization, the second step is the extrapolation of raw CARS and D-CARS information from line-scan spectra and hyperspectral images. For the spectra of model LDs, a small range in the x position was selected so that only the vibrational emission from a targeted droplet was considered, and the CARS intensities in that range were averaged through MultiCARS in order to maximize the signal-to-noise ratio. Contribution from the surrounding agarose was similarly estimated by averaging on a wider region above or below the droplet's emission band (see an example in Figure 3.5). For IFD-stacked images, lipid and agar contributions were extrapolated through specifically-designed programmes for more data quantitative analysis which will be discussed in the next Section.

3.5 Data analysis

Data analysis was applied to line-scan spectra and images in order to remove the background offset and to define CARS ratios independent from experimental settings. In addition, CARS hyperspectral images were processed through an imaging analysis software for noise reduction, but also to retrieve correspondent Raman-like spectra and to determine the absolute concentration of chemical components in the sample [28].

3.5.1 D-CARS and CARS ratio

Let S and D be the measured intensities of the sum-CARS and D-CARS signals emitted by the molecular bonds excited in the focal volume. If A_1 and A_2 are the intensities created respectively by Π_1 and Π_2 pulse trains in the D-CARS design, S and D can be expressed as

$$\begin{cases} S = A_1 + A_2 \\ a \times D = A_2 - A_1 \end{cases} \tag{3.5}$$

where the coefficient a represents the proportionality factor in the detection of CARS from the two channels. In fact the CARS channel measures a continuous current converted into a voltage and digitised by a digital-analog converter, which is then given in calibrated units of photoelectron/sec corresponding to the photon flux at the photomultiplier cathode. Conversely in the D-CARS channel, the high frequency component of the current is converted into voltage and detected by high frequency electronics in Volt units. The value of a was empirically deduced through single-pair measurements where $A_2 = 0$. As a consequence,

$$\begin{cases} S_{agar} = A_{1,agar} \\ a \times D_{agar} = -A_{1,agar} \end{cases} \Rightarrow \; a = -\frac{S_{agar}}{D_{agar}} \tag{3.6}$$

where the subscript "agar" signifies that CARS was measured in the agarose gel, and peak values were considered for S_{agar} and D_{agar}.

The introduction of a is a necessary step in order to take experimental settings

into account. To find out A_1 and A_2, the equation system 3.5 was inverted as

$$\begin{cases} A_{1,agar} = \frac{1}{2}\left(S_{agar} - a \times D_{agar}\right) \\ A_{2,agar} = \frac{1}{2}\left(S_{agar} + a \times D_{agar}\right) \end{cases} \tag{3.7}$$

for agar-emitted signal and as

$$\begin{cases} A_{1,lipid} = \frac{1}{2}\left(S_{lipid} - a \times D_{lipid}\right) \\ A_{2,lipid} = \frac{1}{2}\left(S_{lipid} + a \times D_{lipid}\right) \end{cases} \tag{3.8}$$

for lipid-emitted signal.

Note that the simultaneous acquisition of CARS signal from the lipid material and the surrounding agar-in-water gel guarantees that the excitation/detection conditions under which the measurement was acquired are exactly the same. However the presence of vibrational resonances from the water component in the "CH-stretch" region makes the agar response not spectrally constant at those wavenumbers. As a consequence, any CARS intensity normalized with respect to agar would be slightly spectrally deformed. In order to overcome this, the nonresonant spectrum from a medium such as the coverslip glass was measured. Specifically, the water-to-glass intensity ratio was measured separately and multiplied to the lipid-to-agar ratio so that the CARS intensity ratio is defined as the ratio between the A_1 (resp. A_2) component of the lipid droplet targeted for investigation and the A_1 (resp. A_2) correspondent nonresonant component measured in glass under the same conditions of laser excitation and detection

$$\begin{cases} \text{CARSratio}_1 = \frac{A_{1,lipid}}{A_{1,glass}} \\ \text{CARSratio}_2 = \frac{A_{2,lipid}}{A_{2,glass}}. \end{cases} \tag{3.9}$$

As a result, CARS ratios become independent from the laser intensity and its variations when changing pump-Stokes time overlap.

The D-CARS spectrum is retrieved as the difference between the two previous terms

$$\text{DCARSratio} = \text{CARSratio}_2 - \text{CARSratio}_1. \tag{3.10}$$

All the introduced quantities have to be meant as background-subtracted. In the 100 fs set-up, the numerical value corresponding to the background was evaluated from the terminal parts of the measured signal in the $2400-3400\,\mathrm{cm}^{-1}$ range. In the 5 fs set-up it was estimated from the signal acquired in the $1000-4000\,\mathrm{cm}^{-1}$ range.

3.5.2 CARS hyperspectral images

CARS hyperspectral images were processed via Hyperspectral Imaging Analysis (HIA) software written by Masia *et al.* [28]. HIA is an analytical tool that allows the extrapolation of noise-filtered, quantitative information on chemical components from hyperspectral images. It also removes background contributions through the subtraction of images acquired at 1000 or $5000\,\mathrm{cm}^{-1}$ according to the vibrational region of interest. HIA consists of three main steps each of which are computed through the following mathematical methods: a singular value decomposition (SVD) algorithm, a phase-corrected Kramers-Kronig (PCKK) retrieval method and a blind factorization into susceptibilities and concentrations of chemical components (FSC^3) method.

SVD is a factorization procedure that was implemented by Masia *et al.* [28] in order to allow for an unsupervised noise filtering. Without entering too much into the details of the procedure (it can be found in [28]) let us briefly recall the main points.

Let D be a $s \times p$ matrix containing the dataset from the considered hyperspectral image where s are the measured spectral points for each of the spatial points p in the image. D can be expressed as

$$D = U \Sigma V' \tag{3.11}$$

with U being a $s \times s$ unitary matrix containing a new set of spectra (spectral basis) with which D is represented, Σ being a $s \times s$ diagonal matrix expressing the importance or *weight* (singular values) of the new spectral basis, and V' (transpose of V) being a $s \times p$ matrix containing the spatial distribution of the new spectral

basis.

For large photon numbers, CARS intensity I shows a shot-noise behaviour and scales proportionally to $\sqrt{I}$. As a consequence, $I/\sqrt{I}$ has an intensity independent noise. In order to remove spectral components dominated by this spatially and spectrally uncorrelated noise, D is expressed as $I/\sqrt{I}$. Noise filtering can be achieved by removing the SVD components associated to the noise, namely by limiting the number of singular values (the diagonal elements of Σ). Specifically, a new index, $i_{\max}$, is defined in order to select non-noise-dominated components in the spectra basis and D is expressed as a new noise-free matrix D_{nf}

$$D_{nf} = U_{s\times i\max}\ \Sigma_{i\max\times i\max}\ V'_{i\max\times p}. \tag{3.12}$$

Note that $i_{\max}$ is determined by fitting linearly Σ_i for $i > s/2$ (the Gaussian noise has a linear dependence on Σ_i for large i) and by considering the components with singular values larger than $\sqrt{2}$ times the fit. For the study on fixed (resp. living) cells, $i_{\max}$ was set equal to 14 (resp. 10) to denoise hyperspectral images acquired in the "CH-stretch" region and as 12 (resp. 10) for hyperspectral images acquired in the fingerprint region.

PCKK is a phase-retrieval method based on Kramers-Kronig relations that was used to extrapolate the CARS third-order susceptibility $\chi^{(3)}$ normalized with respect to the glass response. Specifically, by estimating the phase ϕ of the CARS field from the CARS intensity ratio I_{ratio} (with respect to the glass response) as

$$\phi = \mathrm{Im}\left(\mathcal{F}\left(\theta(t)\,\mathcal{F}^{-1}\left(\ln\left(I_{ratio}\right)\right)\right)\right) \tag{3.13}$$

with $\mathcal{F}$ being the Fourier transform operator and $\theta(t)$ the Heaviside function [28], the real and imaginary part of the susceptibility are given by

$$\mathrm{Re}\{\chi_R^{(3)}\} = \sqrt{I_{ratio}}\sin\phi \tag{3.14}$$

$$\mathrm{Im}\{\chi_R^{(3)}\} = \sqrt{I_{ratio}}\cos\phi. \tag{3.15}$$

The retrieval of the imaginary part from measured data is particularly important

because $\mathrm{Im}\{\chi_R^{(3)}\}$ is chemically specific (it is part of $\chi_R^{(3)}$, Equation 2.13) and it has a linear dependence with respect the concentration of the imaged chemical components, as the Raman intensity does [75]. This allows a direct comparison between the PCKK-retrieved spectra and the corresponding Raman spectra from the literature, for peak assignments and quantitative analyses. Further details on the PCKK method can be found in [28].

FSC^3 is a procedure to obtain from the phase-retrieved $\chi^{(3)}$ spectra the corresponding spectra and absolute volume concentrations of chemical components. It applies the non-negative matrix factorization (NNMF) algorithm [76] on a matrix that is composed by two parts. One part is related to the imaginary part $\mathrm{Im}\{\chi_R^{(3)}\}$ and it has the form of a matrix D_{Im} of measured spectral points

$$D_{\mathrm{Im}} = CS + E \tag{3.16}$$

where $C > 0$ is the $n \times p$ matrix of absolute volume concentrations (with n being the number of chemical components indicated to be present in the image), $S > 0$ is the $s \times n$ matrix of absolute spectra and E is the $s \times p$ matrix of concentration error residuals. The other part is related to the real part $\mathrm{Re}\{\chi_R^{(3)}\}$ and it has the form a spectral point with value given by the spectral average of $\mathrm{Re}\{\chi_R^{(3)}\}$ multiplied by $\sqrt{s}$. This guarantees for $\mathrm{Re}\{\chi_R^{(3)}\}$ the same weight as $\mathrm{Im}\{\chi_R^{(3)}\}$.
The NNMF algorithm finally finds the matrices C and S which minimize E in an iterative way with the condition that the deviation from unity is minimum for the sum of the volume concentrations.

The application of HIA to CARS hyperspectral images of ADSCs shows the full spatial distribution of CARS intensity ratios and the retrieved spectra $\mathrm{Im}\{\chi_R^{(3)}\}$ for the lipid content of cytosolic LDs, with the corresponding spatial maps of other cellular components such as water and proteins.
Mean spectra have been calculated for cytosolic LDs by averaging spectra over more than 100 LDs for each group of cells fed with the same fatty acids (each group containing at least 6 differentiated cells). In this case only LDs with a diameter above 2 μm were considered, and the spectrum of each LD was taken by

averaging over the LD core spatial region of constant CARS intensity, to take into account only regions completely filled with lipids.

3.5.3 D-CARS images

D-CARS images were processed via source codes written and compiled in MATLAB® environment.

As for CARS images, background images at 1000 and 5000 cm^{-1} were subtracted from D-CARS images. In order to obtain normalized-to-glass values, formula described in Section 3.5.1 were implemented as follows. Let $I_{\text{D-CARS}}$ and $I_{\text{Sum-CARS}}$ be the D-CARS and the Sum-CARS images acquired at ν_{IFD2} with a Δ_{IFD} shift between the two pulse trains Π_1 and Π_2. According to Equations 3.7 and 3.8, the corresponding single-pulse CARS images at $\nu_{\text{IFD2}} = \nu_{\text{IFD1}} - \Delta_{\text{IFD}}$ and ν_{IFD2} can be deduced as

$$\begin{cases} I_{\nu_{\text{IFD1}}} = \frac{1}{2}\left(I_{\text{Sum-CARS}} - a \times I_{\text{D-CARS}}\right) \\ I_{\nu_{\text{IFD2}}} = \frac{1}{2}\left(I_{\text{Sum-CARS}} + a \times I_{\text{D-CARS}}\right). \end{cases} \tag{3.17}$$

In order to correct with respect to the laser pulse correlation (Equation 3.9), each images is divided by the value of glass signal at the corresponding wavenumber

$$\begin{cases} \text{CARSratio}_{\nu_{\text{IFD1}}} = \frac{I_{\nu_{\text{IFD1}}}}{glass_{\nu_{\text{IFD1}}}} \\ \text{CARSratio}_{\nu_{\text{IFD2}}} = \frac{I_{\nu_{\text{IFD2}}}}{glass_{\nu_{\text{IFD2}}}}. \end{cases} \tag{3.18}$$

As in Formula 3.10, the D-CARS image at ν_{IFD2} is therefore retrieved as independent from experimental parameters if calculated as

$$\text{DCARSratio}_{\nu_{\text{IFD1}}} = \text{CARSratio}_{\nu_{\text{IFD2}}} - \text{CARSratio}_{\nu_{\text{IFD1}}}. \tag{3.19}$$

Mean D-CARS spectra have been calculated for cytosolic LDs by averaging spectra over the same of set of droplets chosen for CARS hyperspectral images.

4

Demonstration of label-free chemical sensitivity of CARS and D-CARS with model lipid droplets

4.1 Introduction

Lipids are one of the most investigated samples in CARS micro-spectroscopy [34]. Either in form of thin polar membranes (*bilayers*) or condensed spherical volumes (*droplets*), they posses an intrinsic chemical structure which corresponds to a well characterized Raman spectrum and gives rise to a strong CARS signal. For these reasons, model systems consisting of lipids of known chemical composition have proved useful in the characterization of the imaging and spectroscopic properties of home-built CARS microscopes [17, 22]. Strong vibrational resonances are particularly present in the "CH-stretch" region (2600 to 3400 cm^{-1}) by the modes of methine (CH), methylene (CH_2), methyl (CH_3) and vinyl (=CH-) groups [77]. Because of the presence of so many spectral contributions, however, significant overlaps might occur preventing a straightforward assignment for most molecular functional groups. The "CC-stretch" region or fingerprint region (1200 to 2000 cm^{-1}) provides complementary information with the presence of vibrational peaks that are more easily recognizable. On the other hand, the CARS signal in the fingerprint region is typically one order of magnitude weaker than in the CH stretch region and thus suffers from the interference with the nonresonant CARS background, resulting in a vibration spectrum with distorted line shapes [78].

As pointed out in previous chapters, D-CARS microscopy has been recently

shown to be a very helpful technique for the improvement of the chemical specificity and the suppression of the nonresonant background. Measurements performed on a test sample made of a mixture of 3 μm polysterene (PS) beads and 2 - 4 μm polymethyl methacrylate (PMMA) beads showed that the chemical sensitivity to a specific material can be enhanced against the nonresonant background [29]. In D-CARS the choice of an appropriate frequency difference Δ_{IFD} between the two pump-Stokes pulse pairs is fundamental and must be defined on the basis of the CARS spectral profile of the sample under investigation. For instance, in the "CH-stretch" region the CARS spectrum of PMMA differs from the spectrum of PS because the peaks associated to CH aromatic vibrations are absent. With the introduction of $\Delta_{\mathrm{IFD}} = 145\,\mathrm{cm}^{-1}$ between the pulse pairs Π_1 and Π_2, D-CARS can be used to distinguish the two bead types on the basis of their contrast, which is positive for PS beads and negative for PMMA beads. For $\Delta_{\mathrm{IFD}} = 60\,\mathrm{cm}^{-1}$, the D-CARS contribution is suppressed for the PMMA and only PS beads remain visible.

In order to demonstrate the capability of D-CARS as chemically-discriminative micro-spectroscopy technique in a more relevant biological context, test samples made of micron-sized lipid droplets and agorose solution gel were used as simplified version of intracellular lipid droplets submerged in cytosol. In this chapter, model droplets characterized by different triglyceride contents are shown to be distinguished in composition through the acquisition of CARS and D-CARS spectra and images. Using Raman spectral information as reference, specific D-CARS spectral features were identified in the fingerprint and "CH-stretch" vibrational regions as able to discern droplets made of disordered poly-unsaturated triglycerides from droplets made of more ordered saturated triglycerides. D-CARS images acquired at corresponding wavenumbers with rapid scans distinctly showed the different triglyceride types, confirming this technique as an effective tool for fast chemically-selective imaging for the observation and study of intracellular droplets.

4.2 Raman characterization

Raman spectroscopy is a reliable tool to characterize chemical substances in general (triglycerides in this case) on the basis of the photon energy shift occurring from the scattering of incident photons with molecular bonds. The result is a red shifted (Stokes) spectrum of the scattered light that gives an insight into the intrinsic chemical-physical structure of triglycerides. Lipid Raman spectra are known from the scientific literature and therefore provide a reference for the interpretation of CARS intensity spectra $I_{\mathrm{CARS}}(\nu_{\mathrm{IFD}})$, in which molecular bands are conversely more difficult to assign because of the interference between the resonant and the nonresonant terms of the susceptibility $\chi^{(3)}$, as described in the Theoretical Background chapter [56].

Spontaneous Raman spectra were measured by Dr. Iestyn Pope and Prof. Wolfgang Langbein for all model LDs and for an additional sample of droplets made of OA [74]. They are shown in Figure 4.1 where the fingerprint and "CH-stretch" vibrational regions can be recognized. Note that all spectra had been normalized so that the area in the "CH-stretch" region – which is related to the total lipid concentration [25] – is the same.

The fingerprint region presents well identified vibrational bands [79, 80]: the ν(C-C) stretching band between 1050 and 1150 cm^{-1}, the $\delta(CH_2)$ twist band at around 1290 cm^{-1}, and the $\delta(CH_2)$ and $\delta(CH_3)$ deformation band between 1400 cm^{-1} and 1500 cm^{-1}. The presence and the intensity of each band is linked to the intrinsic chemical-physical properties of the correspondent lipid. The $\delta(CH_2)$ band at 1290 cm^{-1} appears with one peak for saturated lipids (GTC and GTS) and it divides into two peaks at 1260 cm^{-1} and 1300 cm^{-1} attributed to δ(=CH) and $\delta(CH_2)$ deformations respectively, for unsaturated lipids (OA, GTO and GTL). In particular, the δ(=CH) band gets stronger with respect to the $\delta(CH_2)$ band as the number of carbon-carbon double bonds increases in the lipid acyl chain. Similar trend is shown by the peak at 1660 cm^{-1} associated to the ν(C=C) stretch: it is missing in the spectra of saturated lipids and appears for unsaturated lipids with an intensity proportional to their degree of unsaturation. The band at 1740 cm^{-1}

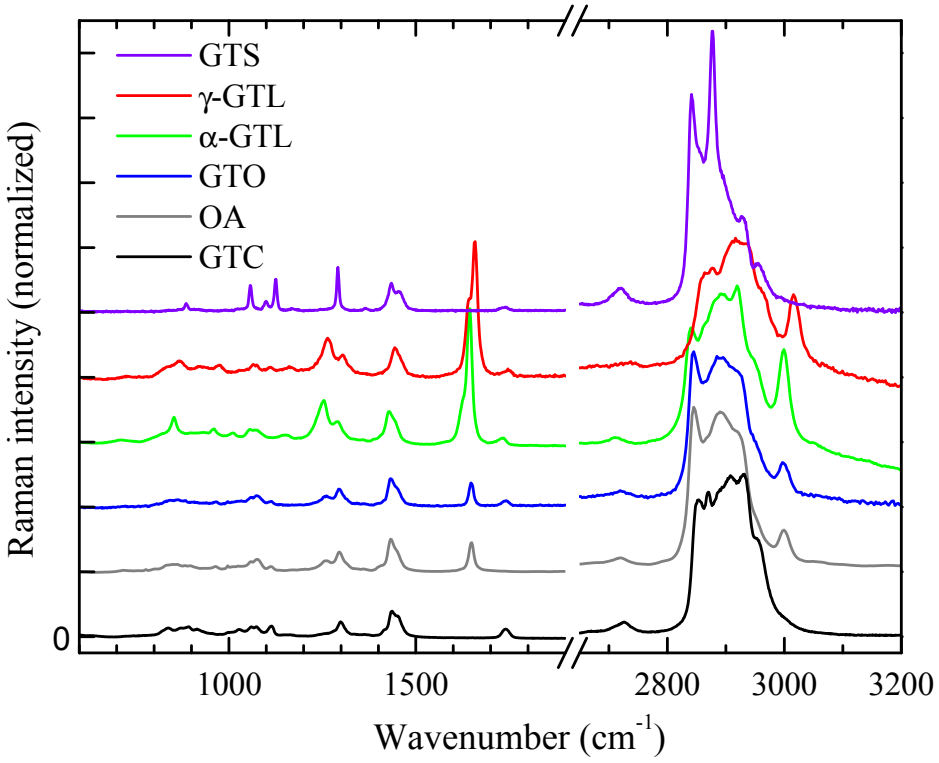

Figure 4.1: RAMAN SPECTRA FOR INVESTIGATED TRIGLYCERIDES [74]. Spectra are vertically shifted in respect to each other in order to avoid overlap. Legend. GTC: glyceryl tricaprylate. GTO: glyceryl trioleate. OA: oleic acid. α(γ)-GTL: α(γ)-glyceryl trilinolenate, GTS: glyceryl tristearate.

is generated by the ν(C=O) stretch of the ester bonds between the acyl chains and the glycerol molecule present in the triglyceride configuration and it is missing in the OA spectrum.

The "CH-stretch" region is characterized by bands that are more difficult to attribute because generated by the overlap of several vibrational resonances. The band at 2855 cm^{-1} is attributed to the CH_2 symmetric stretch and shifts at about 2840 cm^{-1} for saturated lipids in the solid phase, as shown in the spectrum of GTS. The band at 2880 cm^{-1} is a combination between the CH_2 asymmetric stretch vibrations and the Fermi resonance interactions with the overtones originated by CH_2 and CH_3 deformations; it has higher intensity for lipids in the solid phase rather than for lipids in liquid phase and its relative intensity with respect to the 2855 cm^{-1} band can be therefore used as indicator of the acyl chain order [25]. The band at 2930 cm^{-1} is generated by the overlap between CH_3 stretch vibrations and CH_2 asymmetric stretch vibrations, which are both intensified for

Wavenumber [cm^{-1}]	Assignment
1050 - 1150	ν(C-C) stretch
1260	δ(=CH) deformation
1290	δ(CH_2) twist
1300	δ(CH_2) deformations
1400 - 1500	δ(CH_3) deformation
1660	ν(C=C) stretch
1740	ν(C=O) stretch
2730	overtones of CH_2 scissor-like and wag-like deformations, and Fermi resonances with CH_2 stretch vibrations
2840 - 2855	CH_2 asymmetric stretch, Fermi resonance interactions with overtones from CH_2 and CH_3 deformations
2930	CH_3 stretch and CH_2 asymmetric stretch
3010	ν(=CH) stretch

Table 4.1: SUMMARY OF RAMAN RESONANCES FOR THE INVESTIGATED LIPIDS. Both fingerprint and "CH-stretch" regions are considered. References are given in the main text.

lipids in liquid phase by the broadening and shift of the CH deformations; therefore, as for the 2880 cm^{-1} band, the relative intensity of the 2930 cm^{-1} band also provides a measure of molecular order. The band at 3010 cm^{-1} is attributed to the =CH stretch and its intensity increases as the number of carbon-carbon double bonds increases, getting its maximum value for GTL. Finally, the weak band at 2730 cm^{-1} arises from the combined overtones of CH_2 scissor-like and wag-like deformations, enhanced by the proximity of the Fermi resonance with the CH_2 stretch vibrations [81, 82].

Main resonances are summarized for the considered lipids in Table 4.1.

4.3 Single-pair CARS spectra

Model LDs were investigated with the 100 fs and 5 fs laser set-ups described in the Materials and Methods chapter. Starting from the measurements performed with the 100 fs set-up with Π_1 pulse pair only, corresponding CARS spectra are shown as ratio to the nonresonant glass CARS intensity in Figure 4.2. Corresponding spontaneous Raman spectra in the same vibrational range are also plotted for comparison.

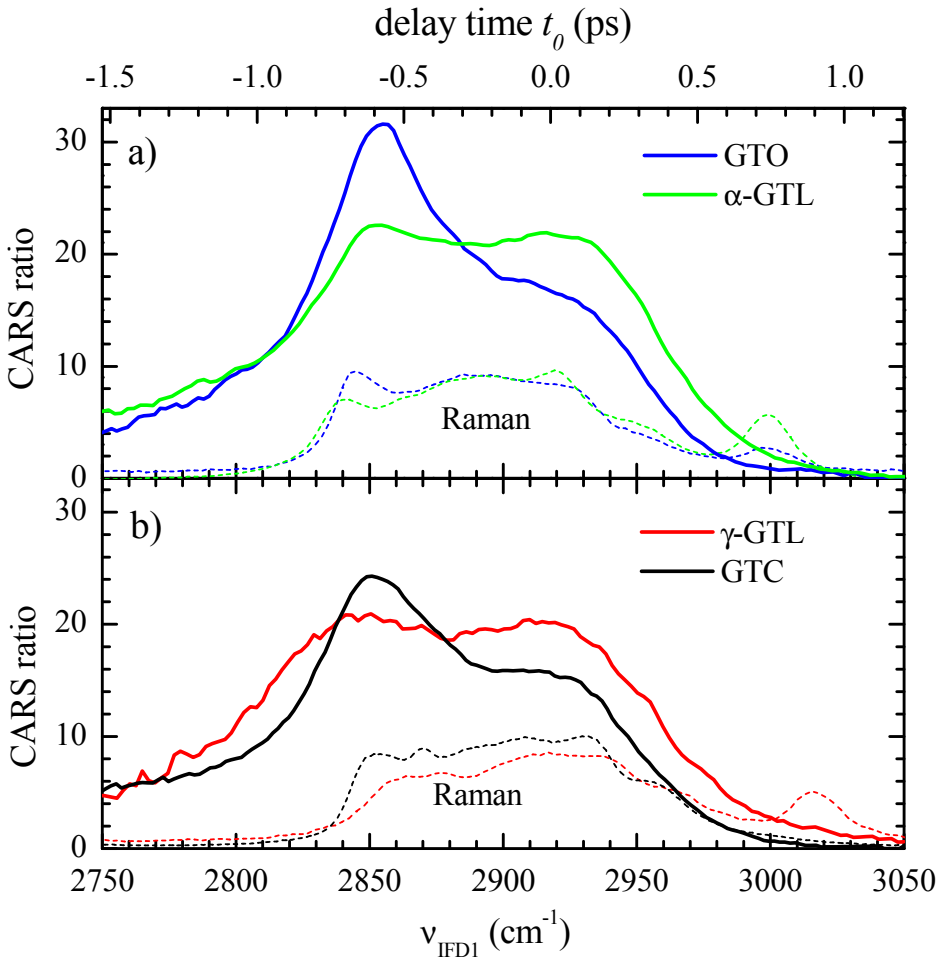

Figure 4.2: CARS SPECTRA FOR TRIGLYCERIDES INVESTIGATED WITH THE 100 FS SET-UP (Adapted from [74]). CARS ratios $\bar{I}_{CARS}$ with respect to glass for model LDs made of GTO and α-GTL (a), and GTC and γ-GTL (b). Note that the corresponding intensity spectrum for GTO droplets is reported as experimentally measured in Figure 3.5. Raman spectra (dotted lines) are also shown. Pump power on the sample 7 mW, Stokes power 2 mW, objective 60x 1.2NA.

In the "CH-stretch" region the CH_2 symmetric stretch band at 2855 cm^{-1} is clearly recognizable in the CARS spectra. It is characterized by a higher intensity relative to the broad band around 2930 cm^{-1} than what shown in Raman spectra due to the nonlinear dependence of the CARS intensity on the number of chemical bonds as well as the interference between the resonant vibrational contribution and the nonresonant electronic contribution to the CARS susceptibility $\chi^{(3)}$. Qualitatively the multi-overlapped vibrational band at 2930 cm^{-1} has a relative intensity with respect to the band at 2855 cm^{-1} that shows the same trend as in Raman, that is, it increases as the degree of acyl chain unsaturation increases from the more

ordered saturated GTS and mono-unsaturated GTO to the more disordered poly-unsaturated GTLs. CARS spectra acquired with the 5 fs laser system in the same vibrational range (Figure 4.3, right panels) confirmed these findings for a broader range and a higher spectral resolution.

In the fingerprint region, CARS spectra were measured with the 5 fs set-up only and are shown in Figure 4.3 (left panels). They present S-shaped features at about 1450, 1660 and 1740 cm^{-1} due to the weak resonant CARS contribution and the high nonresonant background. As explained in the Theoretical Background chapter, at these wavenumbers the interference term $2\chi_{\mathrm{NR}}^{(3)}\mathrm{Re}\{\chi_{\mathrm{R}}^{(3)}\}$ between the resonant part of the third-order susceptibility $\chi_{\mathrm{R}}^{(3)} = R/(-\omega_\delta - i\Gamma)$ and the real nonresonant part $\chi_{\mathrm{NR}}^{(3)}$ (with ω_δ being the difference between vibrational excitation and resonance frequency and Γ being the vibrational dephasing rate) becomes important, dominating the entire spectral lineshape [5,30,73]. In particular the term $\mathrm{Re}\{\chi_{\mathrm{R}}^{(3)}\} = -R\omega_\delta/(\omega_\delta^2+\Gamma^2)$ is responsible for generating a dispersive feature, the tails of which extend proportionally to ω_δ^{-1}. The result is a spectrum that differs substantially from that of a spontaneous Raman profile where features have peaked lineshapes proportional to $\mathrm{Im}\{\chi_{\mathrm{R}}^{(3)}\} = R\Gamma/(\omega_\delta^2+\Gamma^2)$. It is therefore characterized by less vibrational contrast and it makes a correct molecular attributions more challenging. The C=C stretch band at 1660 cm^{-1} can however be recognized in the spectra of unsaturated GTO and GTLs and it is missing in the spectra of saturated GTC and GTS.

In Figure 4.3 the CARS intensity measured in a completely nonresonant medium such as glass can be compared with the corresponding intensity measured in an aqueous buffer (the agar solution is 98% made of water), which resembles the surrounding medium for living cells. The CARS ratio of agar to glass changes depending on the spectral range considered. In the fingerprint region, the agar-to-glass ratio is a constant value. In the "CH-stretch" region, the ratio has a spectral band with a maximum at 3200 cm^{-1} due to the H_2O-stretching vibrations of water [34]. Therefore at high wavenumbers it is particularly important to divide measured CARS spectra of lipids with the nonresonant response in glass in order to correct for the pump-Stokes intensity cross-correlation. A ratio relative to water

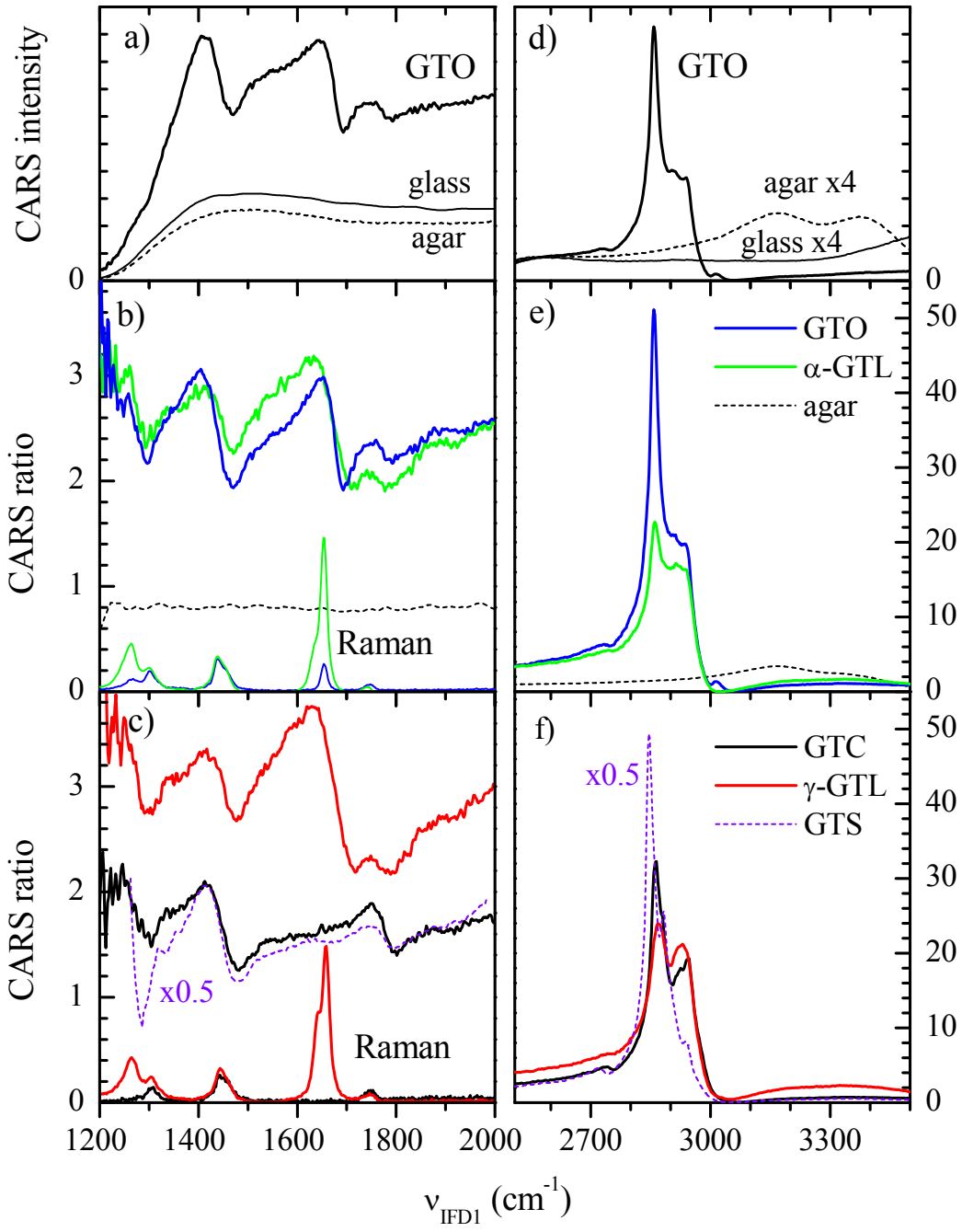

Figure 4.3: CARS SPECTRA FOR TRIGLYCERIDES INVESTIGATED WITH THE 5 FS SET-UP [74]. CARS ratios to glass are shown for the fingerprint region (a, b, c) and in the CH-stretch region (d, e, f). *Panels a, d:* CARS intensity I_{CARS} as measured in a $> 2\mu$m droplet of GTO, in the surrounding agarose gel and in the glass coverslip. *Panels b, c:* CARS ratio $\bar{I}_{CARS}$ for different triglycerides and agar as indicated, together with corresponding Raman spectra in the fingerprint region. *Panels e, f:* as b) and c), but for the CH-stretch region. Pump power on the sample 16 mW, Stokes power 8 mW, objective 20x 0.75NA.

(agar) would introduce spectral distortions in the high-frequency tail.

4.4 Dual-pair D-CARS spectra and images

When a single-pair CARS spectrum is probed for a given triglyceride with Π_1 pulse train at ν_{IFD1} frequencies, the corresponding D-CARS spectrum $\bar{I}_{DCARS} = \bar{I}_{CARS}(\nu_{IFD2}) - \bar{I}_{CARS}(\nu_{IFD1})$ can be calculated from the CARS ratio of Π_1 as

$$\bar{I}_{CARS}(\nu_{IFD2}) = \bar{I}_{CARS}(\nu_{IFD1} - \Delta_{IFD})$$

with Π_2 being the pulse pair exciting vibrational resonance at smaller frequencies $\nu_{IFD2} = \nu_{IFD1} - \Delta_{IFD}$, as described in the Material and Methods chapter. This procedure is visualized in Figure 4.4 where the Π_1-pair CARS spectra measured in the "CH-stretch" region with the 100 fs set-up on GTO and α-GTL droplets (panels a and d) are used to numerically simulate D-CARS ratio spectra for values of Δ_{IFD} ranging from 20 to 80 cm^{-1} in 10 cm^{-1}steps (panels c and f). Changes in colour intensities show for GTO that the corresponding D-CARS has a minimum at about 2855 cm^{-1} and two maxima at 2930 and 2980 cm^{-1} circa, with the latter achieving higher absolute values as Δ_{IFD} increases. Also for α-GTL D-CARS presents a minimum at 2855 cm^{-1} and maximum at 2980 cm^{-1} with a similar trend, but the peak at 2930 cm^{-1} is almost absent. This is due to the different shape of CARS ratios for the two triglycerides: the CARS ratio of GTO has a pronounced peak at around 2855 cm^{-1} and a shoulder around 2930 cm^{-1}, and α-GTL has a "flat-hat" lineshape with both bands equally intense.

Let's consider the D-CARS ratios simulated for $\Delta_{IFD} = 65\,cm^{-1}$ and shown as a function of ν_{IFD1} in Figure 4.4 (panels b and c). In the GTO case, the D-CARS value at 2855 cm^{-1} is given by the difference between the CARS intensity $\bar{I}_{CARS}(2790\,cm^{-1})$ at the lower frequency wavenumber of 2855 cm^{-1} and the CARS intensity $\bar{I}_{CARS}(2855\,cm^{-1})$ of the peak; the D-CARS value at 2930 cm^{-1} is given by the difference between the CARS intensity $\bar{I}_{CARS}(2865\,cm^{-1})$ near the peak and the CARS intensity $\bar{I}_{CARS}(2930\,cm^{-1})$ at the shoulder; the D-CARS

value at $2925\,\mathrm{cm}^{-1}$ is given by the difference between the CARS intensity $\bar{I}_{\mathrm{CARS}}(2925\,\mathrm{cm}^{-1})$ near the shoulder and the CARS intensity $\bar{I}_{\mathrm{CARS}}(2990\,\mathrm{cm}^{-1})$ at the high frequency tail. In the α-GTL case, CARS ratio has a flatter trend with no evident peaks and therefore, according to the above definitions, the corresponding simulated D-CARS ratio has an almost null value at $2930\,\mathrm{cm}^{-1}$.

Experimentally, the value $\Delta_{\mathrm{IFD}} = 65\,\mathrm{cm}^{-1}$ represents a compromise in the "CH-stretch" region between achieving a difference in $\bar{I}_{\mathrm{DCARS}}$ that is large enough to distinguish GTO and GTLs, and maintaining a temporal overlap of pump and Stokes that is sufficient to guarantee CARS excitation capability for both pulse pairs. Considering the limited bandwidth of the 100 fs laser system, this means that, in the Π_2 pulse train, Stokes pulses are temporally shifted by 550 fs circa compared to pump pulses (see Figure 3.5 where the pump-Stokes cross-correlation from the nonresonant contribution in glass is decreased by about 30% at 550 fs compared to time-overlap).

Measured D-CARS spectra using both the 100 fs set-up and the 5 fs set-up are shown for the "CH-stretch" region in Figure 4.5 (upper panel, top and bottom graph respectively). They confirm the expected behaviour from the simulations: all the triglycerides have a negative D-CARS at around $2855\,\mathrm{cm}^{-1}$ and a positive D-CARS at around $2990\,\mathrm{cm}^{-1}$ but α-GTL and γ-GTL exhibit $\bar{I}_{\mathrm{DCARS}}(2930\,\mathrm{cm}^{-1}) \approx 0$ while GTC and GTO show $\bar{I}_{\mathrm{DCARS}}(2930\,\mathrm{cm}^{-1}) > 0$. The bottom panels in Figure 4.5 show the corresponding $\bar{I}_{\mathrm{DCARS}}(x,y)$ images measured on LDs, which reveal that D-CARS can be used to distinguish poly-unsaturated disordered lipids from more ordered unsaturated or mono-saturated ones by simply looking at $\bar{I}_{\mathrm{DCARS}}$ at a specific $\nu_{\mathrm{IFD1,2}}$. Note also the suppression of the nonresonant CARS background from the agarose gel surrounding each LD in D-CARS [29].

Measured D-CARS spectra are shown in Figure 4.6 in the fingerprint range using the 5 fs system with a $\Delta_{\mathrm{IFD}} = 20\,\mathrm{cm}^{-1}$. Such a value is comparable to the spectral resolution and to the Raman linewidth of the resonances for this range. As a consequence, $\bar{I}_{\mathrm{DCARS}}$ can be considered as the spectral derivative of $\bar{I}_{\mathrm{CARS}}$, which for small resonant contributions is given by $\partial_{\omega_\delta}\mathrm{Re}\{\chi_{\mathrm{R}}^{(3)}\} = R(\omega_\delta^2 - \Gamma^2)/(\omega_\delta^2 +$

$\Gamma^2)^2$, and thus recover a lineshape similar to that of spontaneous Raman [30]. The C=C stretch band at around $1660\,\mathrm{cm}^{-1}$ is absent in $\bar{I}_{\mathrm{DCARS}}(\nu_{\mathrm{IFD1}})$ of GTC and present for all other unsaturated triglycerides, as expected.

Correspondent D-CARS images (Figure 4.6, bottom panels) measured on LDs at the C=C stretch frequency also show the difference between the saturated GTC lipid ($\bar{I}_{\mathrm{DCARS}} \approx 0$) and the unsaturated ones ($\bar{I}_{\mathrm{DCARS}} > 0$), demonstrating that D-CARS at specific wavenumbers is a valuable tool to chemically distinguish between these two categories of triglycerides. We note however that the values of $\bar{I}_{\mathrm{DCARS}}$ from resonant contributions in the fingerprint wavenumber region are much lower than those in the "CH-stretch" region and small alignment artifacts due, for example, to the non-perfect spatial overlap of Π_1 and Π_2 become therefore critical. This is for example the case in the images shown for GTL where a spatial differential is visible. We also note that although GTL has three double bonds, GTLs show a peak at around $1660\,\mathrm{cm}^{-1}$ with a $\bar{I}_{\mathrm{DCARS}}$ that is comparable to that of GTO even when scaled to the $1450\,\mathrm{cm}^{-1}$ resonance for relative comparison [25]. This is attributed to the larger linewidth of the C=C resonance for GTL compared to GTO (see Figure 4.1) considering that at resonance $\bar{I}_{\mathrm{DCARS}}$ is scaling as I_{R}/Γ (I_{R} refers to the Raman intensity spectra).

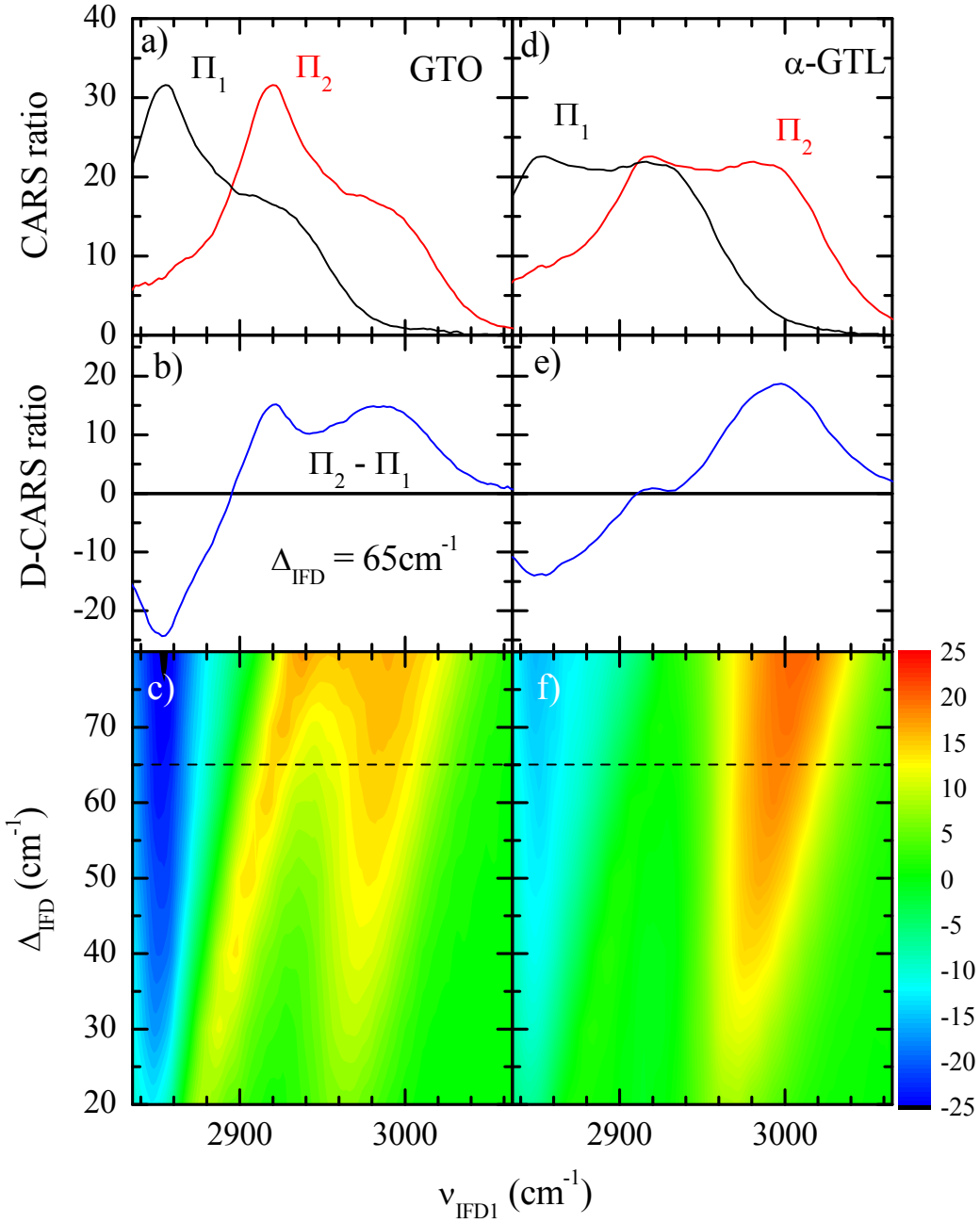

Figure 4.4: D-CARS RATIO SIMULATED FOR DIFFERENT WAVENUMBER SHIFT FROM SINGLE-PAIR CARS SPECTRA [74]. CARS and D-CARS ratio as calculated from the measured Π_1 CARS for GTO (a, b, c) and α-GTL (d, e, f). *Panels a and d*: CARS ratio $\bar{I}_{\mathrm{CARS}}$ of the two pairs $\Pi_{1,2}$ for $\Delta_{\mathrm{IFD}} = 65\,\mathrm{cm}^{-1}$. *Panels b and e*: D-CARS ratio $\bar{I}_{\mathrm{DCARS}}$ for $\Delta_{\mathrm{IFD}} = 65\,\mathrm{cm}^{-1}$. *Panels c and f*: D-CARS ratio $\bar{I}_{\mathrm{DCARS}}$ as function of Δ_{IFD} on a color scale as indicated; dashed line is for the D-CARS ratio correspondent to $\Delta_{\mathrm{IFD}} = 65\,\mathrm{cm}^{-1}$.

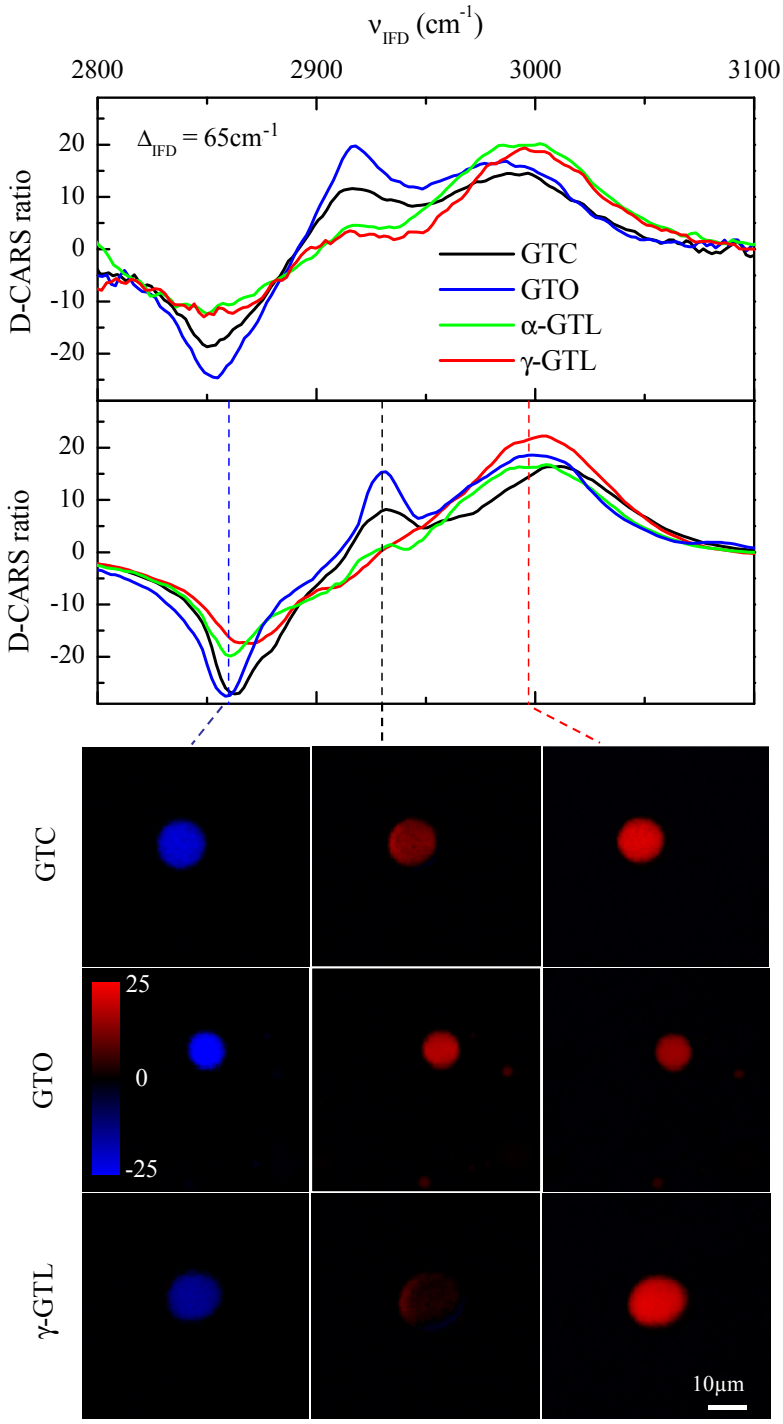

Figure 4.5: D-CARS SPECTRA AND IMAGES AS MEASURED WITH THE 100 FS AND 5 FS SET-UP FOR $\Delta_{\mathrm{IFD}} \sim 65\,\mathrm{CM}^{-1}$ IN THE "CH-STRETCH" REGION [74]. *Upper panels:* Measured $\bar{I}_{\mathrm{DCARS}}$ spectra for different lipids as indicated using the 100 fs laser system (top) and the 5 fs system (bottom). *Lower panels:* $\bar{I}_{\mathrm{DCARS}}(x,y)$ images through the center of LDs at ν_{IFD1}, indicated by corresponding dashed lines (blue 2860 cm^{-1}, black 2930 cm^{-1}, red 2997 cm^{-1}) on a color scale as shown. Pump power on each pair 16 mW, Stokes power on each pair 8 mW, objective 20x 0.75NA, 10 μs pixel dwell time, 0.3 μm pixel size.

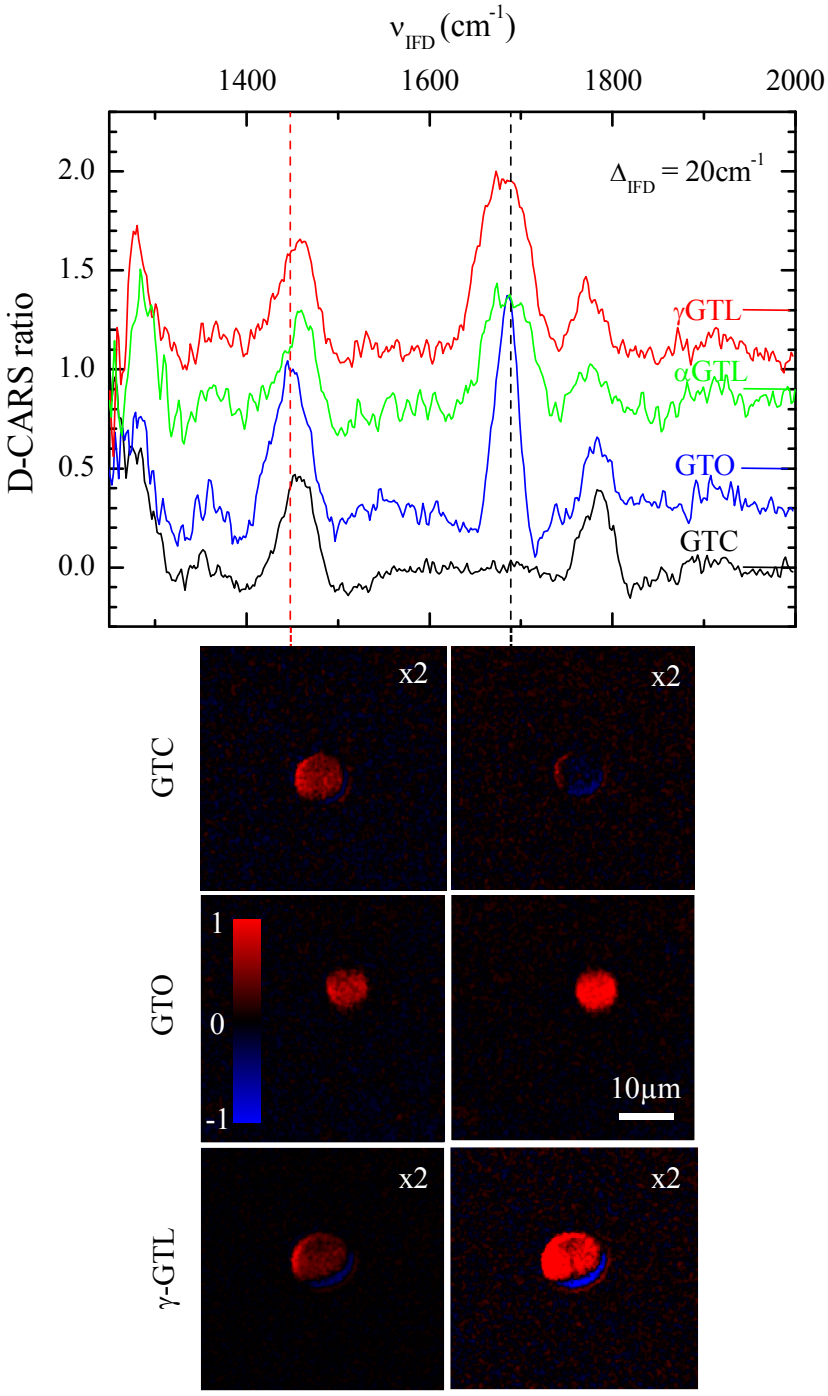

Figure 4.6: D-CARS SPECTRA AND IMAGES AS MEASURED WITH THE 5 FS SETUP FOR $\Delta_{\mathrm{IFD}} \sim 20\,\mathrm{cm}^{-1}$ IN THE FINGERPRINT REGION [74]. *Upper panel:* Measured $\bar{I}_{\mathrm{DCARS}}$ spectra for different lipids as indicated using the 5 fs system. Curves are vertically displaced for clarity, as indicated by offset lines. *Lower panels:* $\bar{I}_{\mathrm{DCARS}}(x,y)$ images of LDs on a color scale at the two ν_{IFD1} indicated by corresponding dashed lines (red 1448 cm^{-1}, black 1689 cm^{-1}). $\bar{I}_{\mathrm{DCARS}}$ has been multiplied by two in the images for GTC and γ-GTL as indicated, in order to have comparable values at 1448 cm^{-1}. Pump power on each pair 16 mW, Stokes power on each pair 8 mW, objective 20x 0.75NA, 10 μs pixel dwell time, 0.3 μm pixel size.

4.5 Summary

In this chapter D-CARS spectral-microscopy has been demonstrated as able to distinguish poly-unsaturated triglicerides (GTLs) from more ordered mono-unsaturated and saturated triglycerides (GTO, GTC and GTS respectively) without the need of complicated CARS multiplex acquisition and analysis.

The spectral signatures of molecular disorder appearing in the “CH-stretch” region of Raman spectra at around $2930\,\mathrm{cm}^{-1}$ correlate well with D-CARS values measured as CARS intensity difference between the bands at $2930\,\mathrm{cm}^{-1}$ and $2855\,\mathrm{cm}^{-1}$. Specifically, poly-unsaturated GTLs exhibit a "flat-hat" CARS spectrum with equally intense bands and hence zero D-CARS, while all other lipids exhibit a positive D-CARS. As a proof-of principle, D-CARS images were acquired on micron-sized lipid droplets at specific wavenumbers to directly distinguish GTLs from the other triglycerides on the basis of their D-CARS contrast. Similarly, spectral signatures of acyl chain unsaturation appearing in the fingerprint region of Raman spectra at $1660\,\mathrm{cm}^{-1}$ correlate with D-CARS spectra and images and enabled us to distinguish the saturated GTC from unsaturated triglycerides. With such a chemical specificity in distinguishing different lipid types, D-CARS has therefore the potential to become a rapid label-free tool for the measurement of lipid composition of cytosolic droplets in cells, overcoming the slow and complex image acquisition and analysis of hyperspectral CARS. The next chapter is dedicated to the demonstration of the D-CARS applicability in a biological context and in comparison with hyperspectral CARS.

5 Quantitative chemical analysis of cytosolic lipid droplets in fixed and live adipocytes

5.1 Introduction

Model LDs provide a reliable platform to test CARS and D-CARS capabilities since the *a priori* knowledge of their pure contents and concentrations simplifies the spectral interpretation of experimental data. However, the ultimate purpose of developing these spectral-microscopy techniques is to use them as chemically-quantitative imaging tools to investigate more complicated samples such as cellular systems, where numerous components with different vibrational spectra are present in unknown concentrations.

So far CARS microscopy has been proved successful in a variety of applications, many of which addressed tissues and model organisms characterized by a high lipid content [6, 16, 40, 83]. The combination of the very intense anti-Stokes signal from lipid molecules with CARS intrinsic optical sectioning and penetration capability has allowed the visualization of myelin sheaths in the nerve tissue of guinea pigs and the imaging of ear-skin layers, brain structures and atherosclerotic plaques in mice [63, 84–86]. Recent multimodal studies involving CARS, TPF and SHG have demonstrated the application of these techniques to clinically-relevant samples, i.e. the monitoring of drug delivery and the diagnosis of cancer, coronary artery diseases, neurodegenerative processes, skin and retinal dysfunctions [87–91].

In order to understand the triggering events leading to the development of these disorders, it is however necessary to move from the tissue to the cellular level where a series of metabolic and trafficking processes involving lipids in the form of *cytosolic* droplets takes place. With a diameter changing from 0.1 μm to 100 μm according to the cell type, cytosolic LDs have been the target of several CARS studies that revealed their bidirectional motion along the microtubules of adrenocortical cells' cytoskeleton, monitored changes in LDs' size and number in starved yeasts, and witnessed variations in LDs' structure and dynamics in liver cells infected by hepatitis C virus [92–94].

Among the varied pool of cell types, adipocytes are cells rich in lipid content that largely contribute to the composition of a highly-specialized connective tissue, called adipose tissue [95]. Because of their physiological role, adipocytes have drawn particular interest from the CARS community. The accumulation of cytosolic LDs in human adipocytes has been recently investigated via CARS-based systems to assess the differentiation process from unspecialised stem cells to mature fat cells [96–98]. The biogenesis of LDs in differentiated murine (3T3-L1) adipocytes has also been the subject of several CARS studies that aimed to find evidences on the formation process of LDs in cells [99].

LD formation is still an open topic in cell biology and so far several models have been proposed. One of these sets the starting point of the formation process in micro-lipid droplets (mLD) which have been originated from the fragmentation of large perinuclear LDs in order to increase the overall droplets' surface/volume ratio and thus achieve a more efficient breakdown of stored triglycerides (*lipolysis*) for metabolic uses [100, 101]. However, time-lapse studies performed with CARS microscopy revealed that mLDs are not located in the proximity of large LDs, as it would be expected from a fission-based process, but they are scattered in all areas of the cytoplasm [102]. Moreover, mLDs have been observed to form *de novo* as defence response to the toxic overflow of fatty acids into the cell [99]. Other investigations performed with multiplex CARS systems have indicated the endoplasmic reticulum (ER) as possible formation site where esterification processes tranform fatty acids into triglycerides, the major component of cytosolic

LDs' core [103]. This result might provide a confirmation for the so-called "budding" model in which triglycerides accumulate in lens-shaped structures enclosed by ER phospholipids leaflets until they are pinched off as LDs [3, 104, 105].

In order to gain further evidence in support to these or other formation models, current studies are focussing on the identification and characterization of the proteins enriching the LD coat surface [106]. Some of these belong to the PAT-family – perilipin, adipophilin, and TIP47 protein – which has been discovered to play a significant role in managing the storage and use of lipids, especially in adipocytes [107, 108]. Interestingly, the distribution of PAT-family proteins differs greatly when physiological changes take place in the cellular environment. In a recent study on 3T3-L1 adipocytes, it has been shown that LDs at rest conditions are mostly coated by perilipin. However, after a few hour incubation in oleic-acid loaded media, perilipin is found only around central and large LDs, while small LDs at the periphery are layered only by TIP47 and medium-sized LDs at intermediate positions are covered only by TIP47 and adipophilin [109]. It is not clear why PAT-family proteins localize to different subsets within the droplet population but possible explanations include size, location and composition of the single LD [105, 110].

These findings suggest that chemical composition is another aspect that has to be taken into consideration in order to understand the connections between LDs and coat proteins, and the possible consequences on lipid storage and metabolism within cells and tissues [111, 112]. Long-chain poly-unsaturated fatty acids introduced through diet are known to have positive effects on human health, i.e. they strengthen the immune system and increase insulin signaling [113, 114]. However, the mechanisms by which dietary fats induce these effects remain undiscovered [115]. Possible explanations can be found by investigating the composition of LDs in cells fed under different dietary conditions. Historically chromatographic methods have been used for the purpose, providing information about the type and amount of specific lipids in cytosolic droplets. Nevertheless such information is obtained by the extraction of LDs, which is time-consuming and expensive, and it is representative of the overall lipid content in the sample [112]. The sensitivity

required to analyse singular droplet composition can be achieved with CARS microscopy. CARS intensities measured for specific vibrational bands can be used to visualize lipids with different degree of unsaturation or order. For instance, the intensity of the carbon-deuterium bond in isotope-labelled palmitic acid has been used to deduce the amount of that lipid in the single LDs of pre-differentiated 3T3-L1 cells accordingly fed [116]. Another CARS study on the same cell line allowed to distinguish palmitic acid from poly-unsaturated linolenic acid in individual droplets through the intensity ratio between C=C and CH_2 vibrations [25].

In this chapter the applicability of CARS and D-CARS as quantitative chemical imaging techniques is demonstrated for saturated and unsaturated lipid droplets developed in human stem-cell-derived adipocytes previously cultured in fatty acids-enriched media. Differently from previous studies which mostly employed mice adipocyte-like cells, the use of human adipocytes from human ADSCs (in turn extracted by liposuction) provides a more relevant *in vitro* model for understanding lipid absorption and incorporation in cytosolic LDs under different dietary conditions, in relation to human lipid metabolism.

In our work D-CARS images of human adipocytes were rapidly acquired at the chemically-selective wavenumbers identified in the model lipid droplets experiment. For comparison, hyperspectral CARS images were collected in the fingerprint and "CH-stretch" vibrational regions and provided quantitative information on the composition and concentration of chemical components through the application of unsupervised phase-retrieval and factorization methods. Both fixed and living ADSCs were investigated. In the case of living cells, individual pre-adipocytes were imaged during differentiation over several days.

5.2 Cytosolic lipid droplets in fixed adipocytes

Adipocytes represent the majority of cells in adipose tissue which is divided into two subtypes, brown adipose tissue and white adipose tissue [95]. Brown adipose tissue is scarcely present in adults and has the primary function to provide body heat, especially for newborn babies. White adipose tissue is more widespread and, besides offering also thermal insulation, it serves as primary site for fat metabolism and storage [95].

The cells of white adipose tissue usually contain a single large LD (*unilocular adipocytes*) where triglycerides are stored during periods of energy excess by the esterifications of hydroxyl heads in glycerol molecules with fatty acids. If energy deprivation occurs, triglycerides are hydrolysed to free fatty acids by the action of the enzyme lipase; through the bloodstream, fatty acids are then transferred to other cells where oxidation takes place and the long fatty carbon chains are split into fatty acyl CoA molecules; these eventually enter a series of chemical reactions (Krebs cycle) that generate energy in form of adenosine triphosphate (ATP) [66].

In this process, the triglyceride turnover in the adipose tissue has been measured to take approximately one year. Because of such a slow cycle, the composition of the adipose tissue well represents dietary fatty acids, i.e. fatty acids incorporated through the food diet [117].

The triglyceride composition of the adipose tissue has been the object of many studies over the years. A comprehensive review by Hodson *et al.* indicates mono-unsaturated oleic acid as the major component (43.5%) for subcutaneous adipose tissue. The next abundant fatty acids are the saturated palmitic acid (21.5%) and bi-unsaturated linoleic acid (13.9%). Poly-unsaturated fatty acids, such as tri-unsaturated α-linolenic acid (0.8%), are far less common and their concentration significantly decreases as their chains length increases [117].

We have therefore investigated human pre-adipocytes cultured during differentiation in media loaded with palmitic acid and α-linolenic acid in different concentration ratios in order to induce *in vitro* fatty acid intake by the cells.

Adipocytes were then fixed on coverslips and mounted onto microscope slides as described in the Materials and Methods chapter (Section 3.2.2). CARS and D-CARS measurements as hyperspectral images were performed with the 5 fs set-up in order to assess spectrally and microscopically the composition of cytosolic LDs. Results from data processing and HIA analysis are detailed below [118].

5.2.1 Hyperspectral CARS

Hyperspectral images of CARS intensities as ratios relative to the nonresonant glass response are shown in Figure 5.1 (lower panel) for human adipocytes grown in media supplemented with either pure saturated (PA) or pure unsaturated (LNA) fatty acids. Corresponding phase-retrieved images of the imaginary part $\mathrm{Im}\{\chi_R^{(3)}\}$, obtained by the method described in Chapter 3 (Section 3.5.2), are shown in Figure 5.2 (lower panels). Images are shown at characteristic wavenumbers in both fingerprint and "CH-stretch" regions.

In both Figures (upper panels) spectra are also reported as averages over more than 100 LDs of resolved size, i.e. with diameter $> 2\,\mu$m hence greater than the spatial resolution of the set-up. As for model LDs, CARS ratio spectra are affected by the interference term $2\chi_{NR}^{(3)}\mathrm{Re}\{\chi_R^{(3)}\}$ and are consequently characterized by a spectral shape that is dispersive in the fingerprint region and are only qualitatively similar to spontaneous Raman spectral shapes in the "CH-stretch" region. On the contrary, retrieved $\mathrm{Im}\{\chi_R^{(3)}\}$ spectra well recover Raman-like shapes and exhibit the characteristic vibrational bands of neutral lipids described in the study in model LDs [74].

In comparative terms, cytosolic LDs within cells fed with poly-unsaturated LNA have on average much more prominent bands at $1660\,\mathrm{cm}^{-1}$, $2930\,\mathrm{cm}^{-1}$ and $3010\,\mathrm{cm}^{-1}$ that specifically suggest the presence of many carbon-carbon double bonds for this type of LDs rather than for LDs of cells fed with PA. Furthermore, their retrieved spectrum $\mathrm{Im}\{\chi_R^{(3)}\}$ has a shape similar to the Raman spectrum of pure α-glyceryl trilinolenate (especially in the relative amplitude between the $1660\,\mathrm{cm}^{-1}$ and $1450\,\mathrm{cm}^{-1}$ bands [74]). This is a clear indication that human ADSCs have efficiently uptaken and accumulated LNA, which is consistent with

other findings in the literature where the different fatty-acid composition in the media has been shown to change the chemical composition of LDs in cells [25]. Conversely, cytosolic LDs within cells fed with PA show the presence of carbon-carbon double bonds despite PA being a saturated lipid. In particular, the average lipid spectrum is similar to that measured for oleic acid [28, 74] which appears to be the main fatty acid component of the differentiation media (cells grown in a media supplemented with oleic acid also showed very similar spectra, see Appendix A). This suggests that, for the considered experimental conditions, human ADSCs incorporate LNA much more efficiently than PA as it will be discussed in detail in the following section.

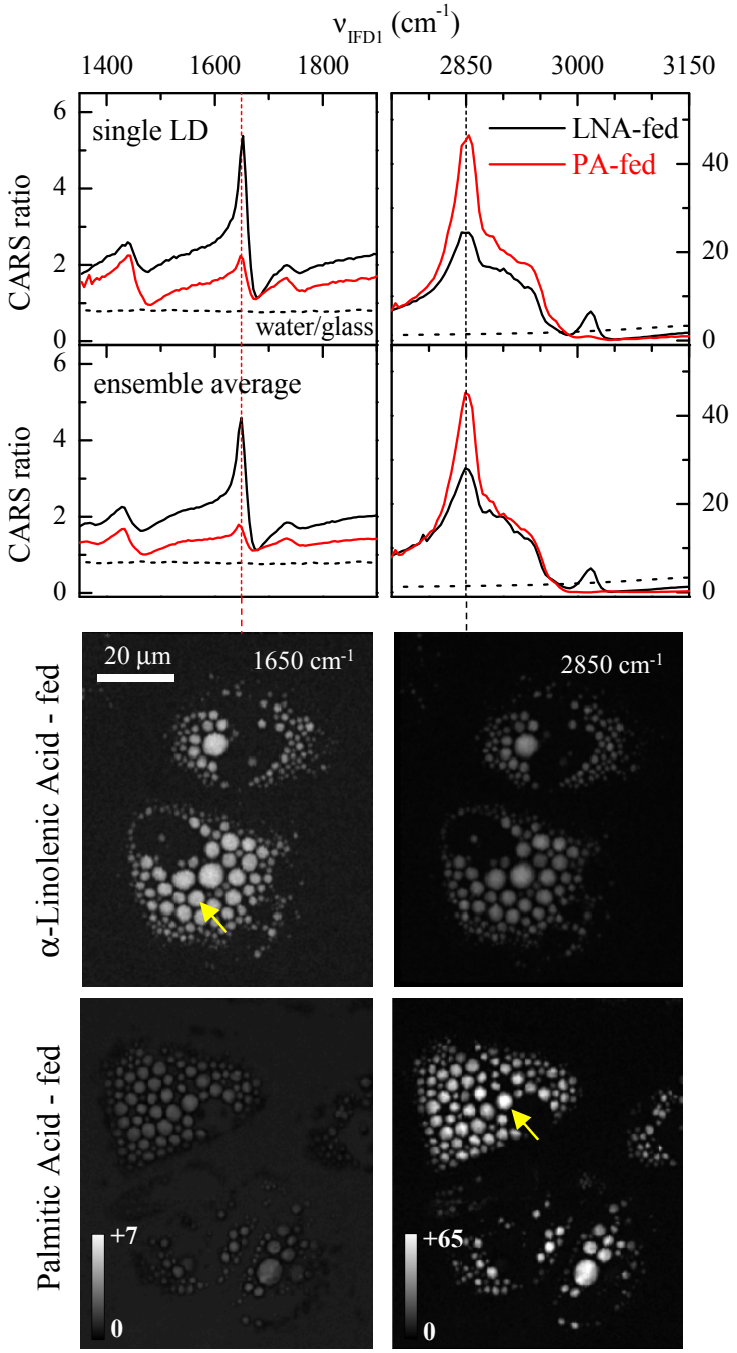

Figure 5.1: CARS SPECTRA AND CORRESPONDING IMAGES FOR ADIPOCYTES FED WITH SATURATED AND POLY-UNSATURATED FATTY ACIDS [118]. *Upper panels:* CARS intensity ratio for human ADSCs fed with palmitic acid (PA) and α-linolenic acid (LNA). Spectra for the individual droplets indicated by the yellow arrow and as averaged over more than 100 LDs. The spectrum of the water to glass ratio is also shown. *Lower panels:* Images of the CARS intensity ratio at 1650 cm^{-1} and 2850 cm^{-1}, as indicated by the vertical dotted lines in the spectra. Linear grey scales as indicated. The pump power on the sample was 20 mW (14 mW) and the Stokes power was 10 mW (7 mW) for the fingerprint region ("CH-stretch" region); 10 μs pixel dwell time, 0.3 μm pixel size.

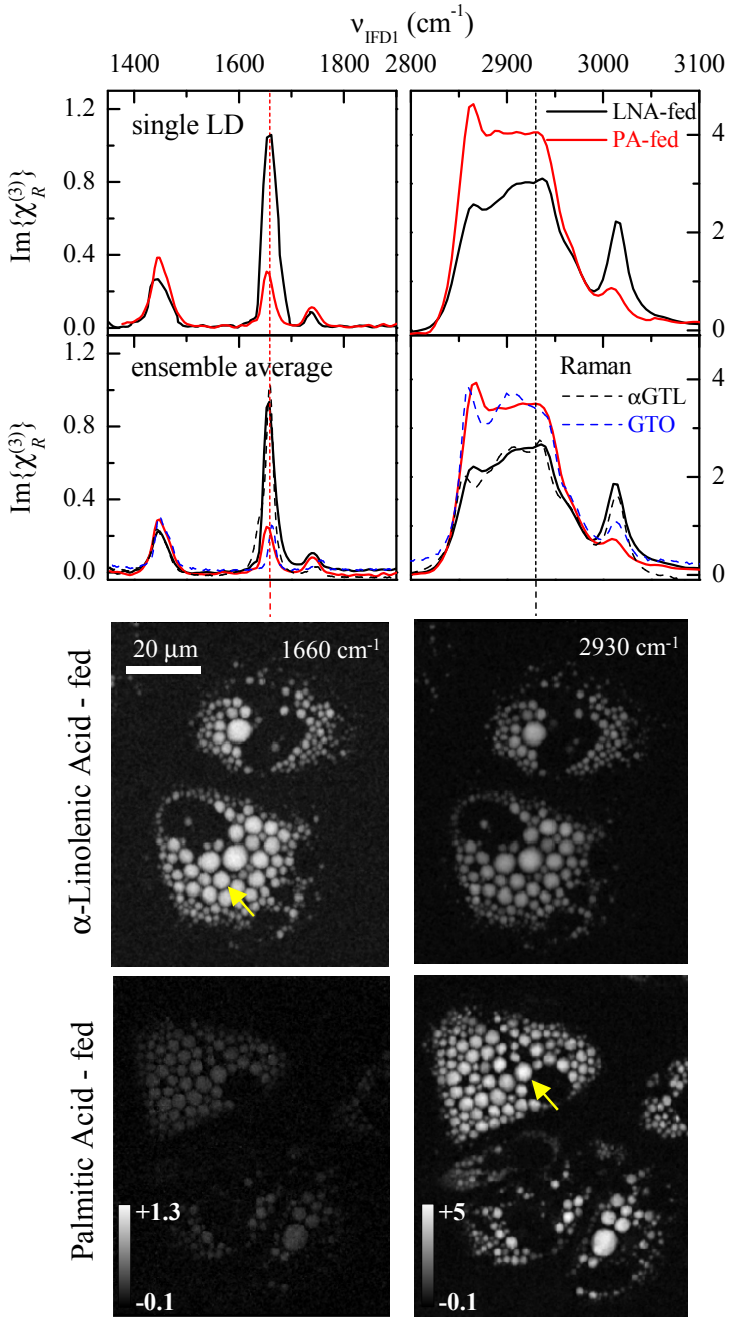

Figure 5.2: PHASE-RETRIEVED SPECTRA AND CORRESPONDING IMAGES FOR ADIPOCYTES FED WITH SATURATED AND POLY-UNSATURATED FATTY ACIDS [118]. *Upper panels:* Phase-retrieved imaginary part $\mathrm{Im}\{\chi_R^{(3)}\}$ of the normalized susceptibility for human ADSCs fed with palmitic acid (PA) and α-linolenic acid (LNA). Spectra of the individual droplets indicated by the yellow arrow and as averaged over more than 100 LDs. Raman spectra of α-glyceryl trilinolenate (αGTL) and glyceryl trioleate (GTO) are shown for comparison (dashed lines). *Lower panels:* Images of the imaginary part of the normalized susceptibility at $1660\,\mathrm{cm}^{-1}$ and $2930\,\mathrm{cm}^{-1}$. Linear grey scales as indicated. The pump power on the sample was 20 mW (14 mW) and the Stokes power was 10 mW (7 mW) for the fingerprint region ("CH-stretch" region); 10 μs pixel dwell time, 0.3 μm pixel size.

5.2.2 Dual-frequency differential CARS

D-CARS spectra and images following the same criteria as for Figure 5.1 are given in Figure 5.3 and 5.4 for the fingerprint and the "CH-stretch" region, respectively. The upper panels show simulated D-CARS spectra constructed as described in the model LDs study (Section 4.4), using the single-pair CARS intensity ratio of Figure 5.1 and the experimental value of the wavenumber shift Δ_{IFD}. They agree well with the experimentally measured D-CARS spectra from model LDs. The lower panels show experimental D-CARS images acquired at selected wavenumbers [118].

In the fingerprint region, D-CARS images were measured for $\Delta_{\mathrm{IFD}} = 34\,\mathrm{cm}^{-1}$. This value is comparable to the peak-dip distance in the dispersive CARS lineshapes centred at around $1450\,\mathrm{cm}^{-1}$ and $1660\,\mathrm{cm}^{-1}$, and therefore it provides the maximum D-CARS contrast. Simulated D-CARS spectra present maxima at $1470\,\mathrm{cm}^{-1}$ and $1680\,\mathrm{cm}^{-1}$, at which corresponding D-CARS images were acquired. The peak at $1680\,\mathrm{cm}^{-1}$ is a measure of the abundance of C=C stretch band in LDs of cells fed with LNA [118].

In the "CH-stretch" region, D-CARS images were measured for $\Delta_{\mathrm{IFD}} = 65\,\mathrm{cm}^{-1}$. As in the model LD study, this value enables us to distinguish saturated from poly-unsaturated triglycerides according to the different CARS intensity lineshapes, i.e. the relative importance of the peak at $2850\,\mathrm{cm}^{-1}$ and the broad shoulder at $2930\,\mathrm{cm}^{-1}$. Simulated D-CARS spectra present an absolute maximum at $2920\,\mathrm{cm}^{-1}$ which is more pronounced for cells fed with PA, where the presence of saturated or mono-unsaturated lipids is more significant compared to cells fed with LNA. D-CARS images acquired at $2920\,\mathrm{cm}^{-1}$ and $2990\,\mathrm{cm}^{-1}$ are shown for relative comparison, with D-CARS at $2990\,\mathrm{cm}^{-1}$ representing the amplitude of the broad shoulder in the CARS ratio spectrum (Figure 5.4, upper panel, sketch) [118]. D-CARS images were also measured for $\Delta_{\mathrm{IFD}} = 27\,\mathrm{cm}^{-1}$ to investigate the CARS intensity peak at $3010\,\mathrm{cm}^{-1}$ characteristic of the =CH bond. Simulated D-CARS spectra present a maximum at $3045\,\mathrm{cm}^{-1}$ proportional to the amplitude of the =CH peak. Corresponding D-CARS images acquired at that wavenumber show the presence of that bond for cells fed with LNA [118].

Note that the choice of Δ_{IFD} value is not straightforward if the spectral profile of the substance under investigation is not known a priori. A "rule-of-thumb" approach that can be however for D-CARS imaging is to use a Δ_{IFD} value comparable to the bandwidth of the resonance [118].

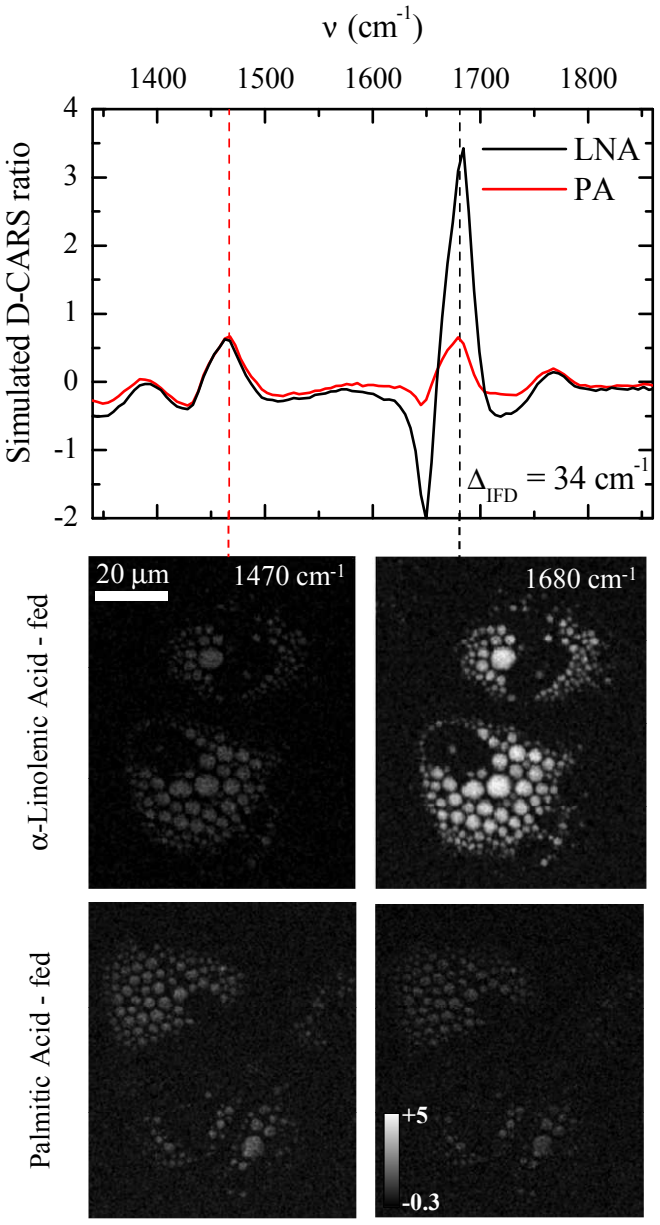

Figure 5.3: D-CARS IMAGING IN THE FINGERPRINT REGION OF HUMAN ADSCS FED WITH DIFFERENT FATTY ACIDS [118]. *Upper panels:* D-CARS spectra calculated from the measured CARS intensity ratios shown in Figure 5.1 with Δ_{IFD} as indicated. *Lower panels:* D-CARS images of adipocytes measured at the wavenumbers indicated by corresponding dotted lines (1470 and 1680 cm^{-1}). Grey scale as shown. Pump power on each pair 16 mW, Stokes power on each pair 8 mW, 10 μs pixel dwell time, 0.3 μm pixel size.

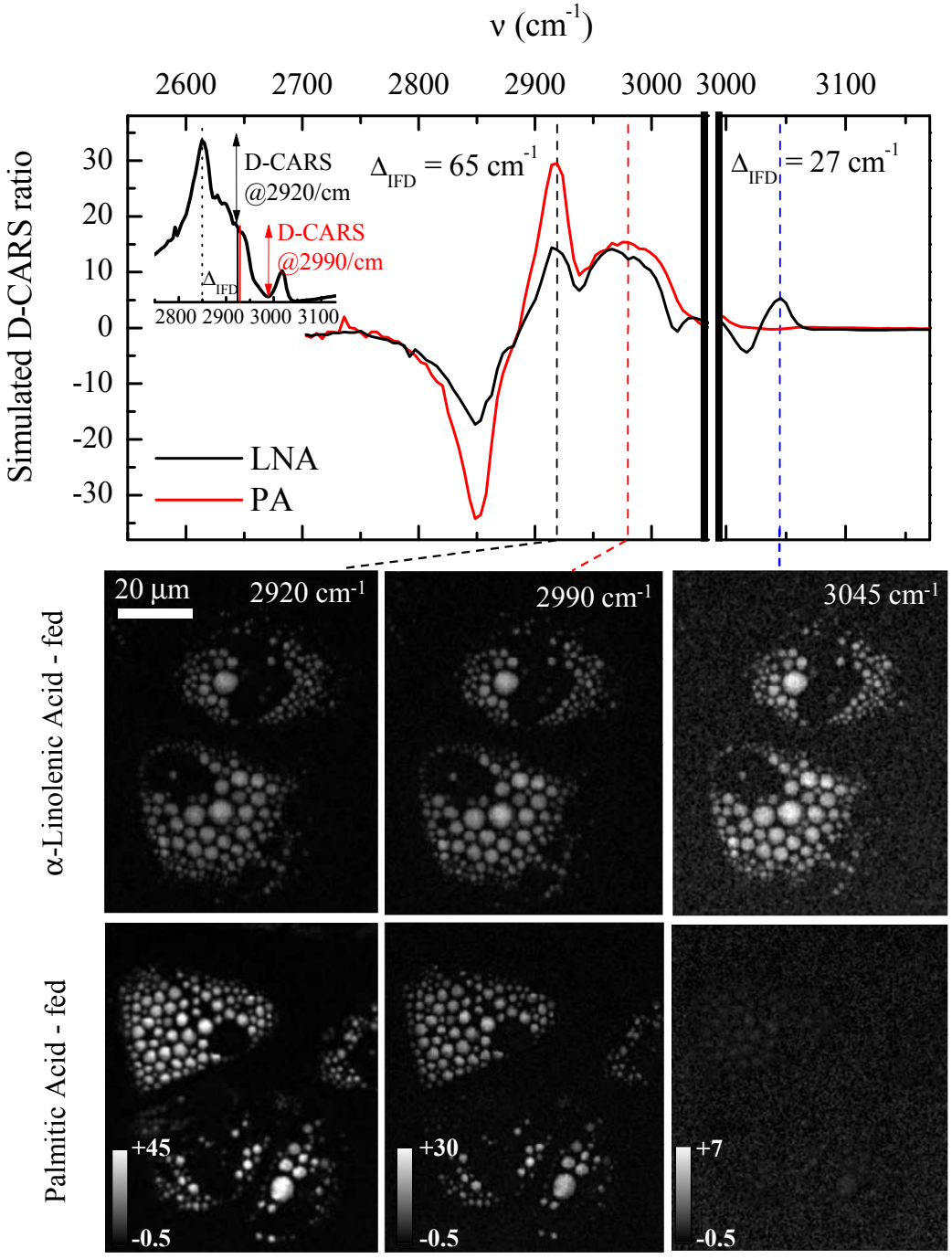

Figure 5.4: D-CARS IMAGING IN THE "CH-STRETCH" REGION OF HUMAN ADSCS FED WITH DIFFERENT FATTY ACIDS [118]. *Upper panels:* D-CARS spectra calculated from the measured CARS intensity ratios shown in Figure 5.1 with Δ_{IFD} as indicated. The inset schematically shows D-CARS amplitudes (vertical arrows) at 2920 cm^{-1} and 2990 cm^{-1} in relation to the CARS intensity lineshape. *Lower panels:* D-CARS images of adipocytes measured at the wavenumbers indicated by corresponding dotted lines (2920, 2990 and 3045 cm^{-1}). Grey scale as shown. Pump power on each pair 16 mW, Stokes power on each pair 8 mW, 10 μs pixel dwell time, 0.3 μm pixel size.

5.2.3 Ratiometric analysis

The degree of C=C poly-unsaturation and the acyl-chain order of lipids (i.e. their fluidity) in cytosolic LDs can be determined from the ratios between CARS intensities that refer to specific vibrational bands [25]. With this procedure, called *ratiometric analysis*, the ratio of the phase-retrieved $\mathrm{Im}\{\chi_R^{(3)}\}$ between $1660\,\mathrm{cm}^{-1}$ and $1450\,\mathrm{cm}^{-1}$ bands can provide a quantitative measure for the degree of unsaturation. Similarly, the ratio of $\mathrm{Im}\{\chi_R^{(3)}\}$ between the $2930\,\mathrm{cm}^{-1}$ band and the $2850\,\mathrm{cm}^{-1}$ CH_2 symmetric stretch resonance can be used as a measure of molecular disorder within LDs. Figure 5.5 shows the results of the ratiometric analysis for D-CARS and phase-retrieved $\mathrm{Im}\{\chi_R^{(3)}\}$ values for human ADSCs fed with media supplemented with PA, LNA and mixtures. Note that for each group of cells fed with one type of lipid-supplemented media, the ratio was calculated as average among more than 100 LDs of resolved diameter. The corresponding standard deviation is shown as error bar for each case [118].

In the fingerprint region, the ratio measured using D-CARS coincides within errors with the ratio measured using $\mathrm{Im}\{\chi_R^{(3)}\}$ and it scales proportionally to the volume fraction of LNA used in the experiments, as indicated by the dashed line in Figure 5.5 (upper panel). Considering that $\mathrm{Im}\{\chi_R^{(3)}\}$ is linear in the concentration of chemical components [75], this result allows us to make two conclusions. First, the cellular uptake of LNA in the droplets of ADSCs follows on average the relative concentration of LNA in the culture media. Second, the D-CARS ability to quantitatively determine the degree of C=C poly-unsaturation is as effective as the CARS analysis on hyperspectral measurements, which can be thus circumvented [118].

In the "CH-stretch" region, $\mathrm{Im}\{\chi_R^{(3)}\}$ ratios scale linearly with the volume fraction of LNA (Figure 5.5, middle and low panel, dashed lines), as expected from the linearity of the phase-retrieved imaginary part of the susceptibility. On the contrary, D-CARS ratios show a trend which is only qualitatively similar to $\mathrm{Im}\{\chi_R^{(3)}\}$. This is because in the "CH-stretch" region D-CARS retains the CARS nonlinear dependence with concentration [118].

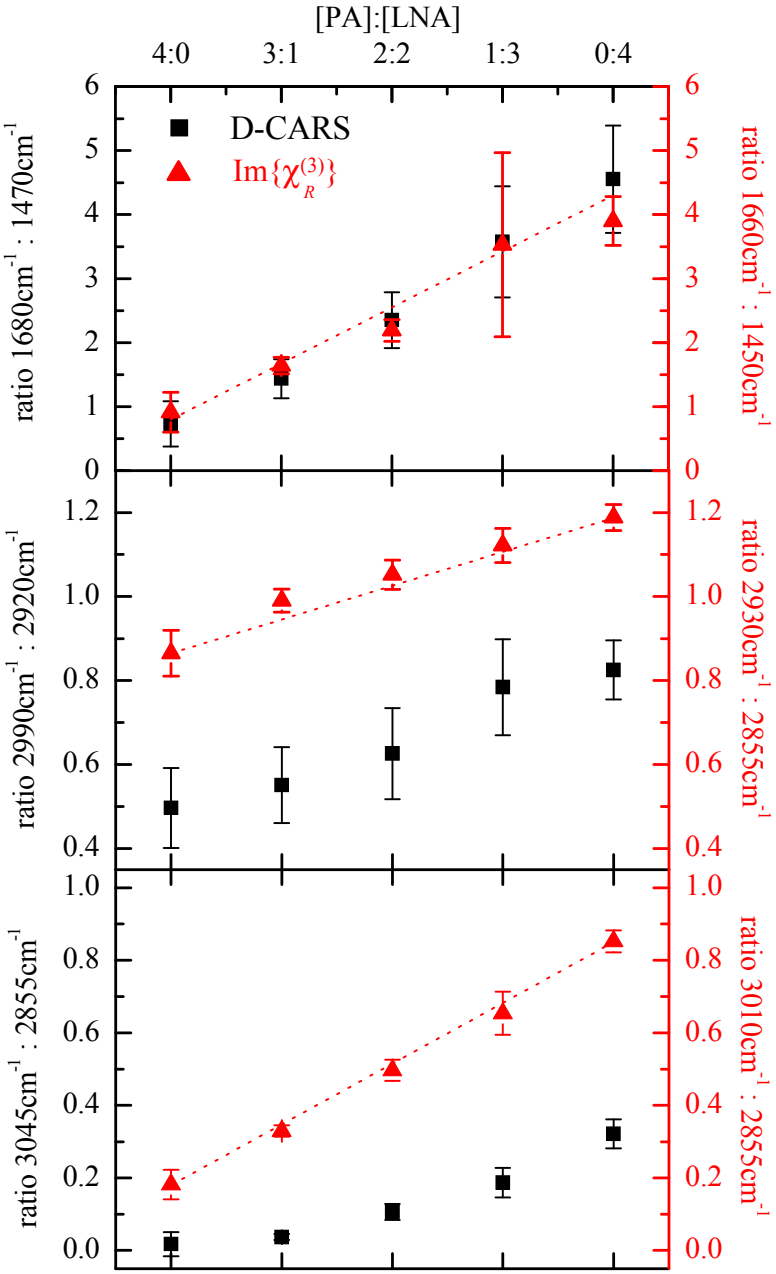

Figure 5.5: RATIOMETRIC ANALYSIS OF MEASURED D-CARS RATIO AND PHASE-RETRIEVED IM$\{\chi_R^{(3)}\}$ IN FIXED HUMAN ADSCS FED WITH MIXTURES OF PALMITIC ACID AND α-LINOLENIC ACID WITH A VOL:VOL RATIO AS INDICATED [118]. Black squares represent average D-CARS intensity ratios, red triangles indicate average ratios of Im$\{\chi_R^{(3)}\}$. Errors bars show the standard deviation over the analysed droplets ensemble. Dotted lines are the calculated linear dependencies from the values with pure PA and LNA. *Upper panel:* D-CARS ratio between 1680 cm^{-1} and 1470 cm^{-1} and corresponding ratio of Im$\{\chi_R^{(3)}\}$ at 1660 cm^{-1} and 1450 cm^{-1}. *Middle panel:* D-CARS intensity ratio between 2990 cm^{-1} and 2920 cm^{-1} and corresponding ratio of Im$\{\chi_R^{(3)}\}$ at 2930 cm^{-1} and 2855 cm^{-1}. *Lower panel:* D-CARS intensity ratio between 3045 cm^{-1} and 2855 cm^{-1} and corresponding ratio of Im$\{\chi_R^{(3)}\}$ at 3010 cm^{-1} and 2855 cm^{-1}.

5.2.4 Quantitative chemical analysis using FSC^3

In Figure 5.5 the error bars of $\mathrm{Im}\{\chi_R^{(3)}\}$ ratios provide a measure of the variation for the degree of poly-unsaturation and the acyl-chain order within cells fed with one type of lipid, suggesting a fairly homogeneous distribution in most cases. However, a key point in CARS micro-spectroscopy is to spatially resolve the distribution of the lipid content and of other chemical components within the cellular environment. We have evaluated this point in detail using the FSC^3 method discussed in the Materials and Methods chapter (Section 3.5.2) [28].

FSC^3 results for human ADSCs fed with PA, LNA and an equal volume mixture of both are shown in Figure 5.6. For all samples, the overall cellular chemical composition has been represented in terms of 5 chemical species. Their spectral profiles and spatial distributions (volume concentration units) are also shown.

Water, indicated as component 1, is the most abundant constituent in all samples in terms of volume fraction. It is shown in Figure 5.6 for cells fed with LNA only. The main lipid component for medium-large sized cytosolic LDs is indicated as component 4 and it shows the same characteristic spectrum as in Figure 5.1. In the red-green-blue (RGB) overlay of Figure 5.6 its spatial distribution is color-coded in red.

A chemical component, indicated as component 3 and color-coded in blue, is spatially located in the cytosol and in the nucleus. Its spectrum has a pronounced band at around $2930\,\mathrm{cm}^{-1}$ which is characteristic of proteins and nucleic acids. Note that it partially mixes with lipid resonances for cells fed with LNA [28].

Another chemical component, indicated as component 5, is located at or near LDs. It shows a spectrum that is not easily interpretable and might be caused by image artefacts introduced by LDs. In particular, spatial distributions of the refractive index can cause distortions in the excitation fields which result into a modulation of the CARS intensity and into artefacts for the corresponding retrieved concentrations [119]. Factorization errors in the FSC^3 analysis are quantified by the relative spectral error E_S and the relative concentration error E_C, which are shown in Figure 5.7 for the FSC^3 results reported in Figure 5.6.

The relative spectral error E_S provides a measure of the residual generated when

the phase-retrieved dataset is factorized as the product between a matrix of concentration and a non-negative matrix of spectra for the chemical components (see Materials and Methods chapter, Equation 3.16). For the investigated samples E_S achieves a maximum value of 30% and it is localized at large LDs as shown in Figure 5.7.

The relative concentration error E_C is defined as

$$E_C = \left(\sum_{k=1}^{K} c_p^{\{k\}} \right) - 1 \tag{5.1}$$

where $c_p^{\{k\}}$ is the non-negative relative volume concentration of the k-th chemical component at voxel p [28]. The spatial distribution of E_C shown in Figure 5.7 shows that largest relative errors are located at the large lipid droplets and spatially correlate with component 5, supporting the hypothesis that excitation fields might have been distorted by the presence of spatial refractive index structures [119]. Conversely, spatial-spectral coupling effects due to the phase shift between the resonant and nonresonant components of $\chi_R^{(3)}$ [120] are expected to be weak since the resonant CARS contribution in the "CH-stretch" region is much larger than the nonresonant one for droplets that have a comparable or larger size than the focal volume.

Another chemical component, indicated as component 2 and color-coded in green, is identified for cells fed with PA in correspondence to small, peripheral LDs and presents a spectrum resembling the profile of a saturated lipid such as PA. It is interesting to note that in this sample larger, internal LDs appear to be filled with the lipids from the differentiation media (i.e. mostly oleic acid). A possible explanation might be that, because of its low fluidity, PA is not easily transported across LDs during cell differentiation and therefore tends to be located in the outer cellular periphery. A study performed with Raman spectroscopy and gas chromatography on human liver carcinoma cells (HepG2) has shown that, when treated with equal concentrations of PA and oleic acid, the latter is present in cells at twice the amount of PA. This finding has also been interpreted as due to PA being solid at room temperature, which complicates the creation of mixtures

with more fluid fatty acids such as oleic acid [112].

For cells fed with the PA:LNA mixture, the main lipid component is well reproduced by an equally weighted combination of LD spectra from cells fed with PA and LNA, respectively. As described above, the main lipid component in medium-large LDs of cells fed with PA has a spectral profile similar to oleic acid. Since LNA and oleic acid are both liquid at room temperature (see Table 3.1), it is reasonable to hypothesize that they mix into a spatially homogeneous compound which is recognized as a single substance in the FSC^3 analysis.
Furthermore, a more saturated lipid component can be identified in smaller peripheral LDs, similarly to what observed in cells fed with PA only [118]. For cells fed with LNA only, such component is not present and the overall chemical composition is fully described by the FSC^3 analysis by 4 components only [118].

These results allow us to make some initial considerations on the biology of ADSCs [118]. Firstly, as previously mentioned, in human adipose tissue oleic acid is the most abundant fatty acid, followed by palmitic acid and, at much lower percentage, by α-linolenic acid [117]. Our data suggest that, despite being not so common, α-linolenic acid is efficiently incorporated and stored in human adipocytes. Secondly, the protein-like component 3 appears more pronounced around LDs of cells fed with LNA, suggesting that LDs of different compositions might present different protein coatings possibly because proteins might target LDs with mechanisms that are lipid specific. How this process occurs is however still unclear, as discussed in the Introduction of this chapter, and more detailed studies are needed. Finally, the lower part of Figure 5.6 shows the spatial distribution of the LD chemical content that is obtained when performing a ratiometric analysis according to the method described by Rinia *et al.* [25]. Specifically, we considered the $\mathrm{Im}\{\chi_R^{(3)}\}$ ratio between $2930\,\mathrm{cm}^{-1}$ and $2855\,\mathrm{cm}^{-1}$ as representative of the lipid chemical composition through the degree of lipid disorder (which is correlated with the degree of poly-unsaturation). The analysis shows that the lipid disorder increases going from cells fed with PA to cells fed with LNA. However, the spatially-resolved chemical contrast is far worse than the one obtained with FSC^3 [118].

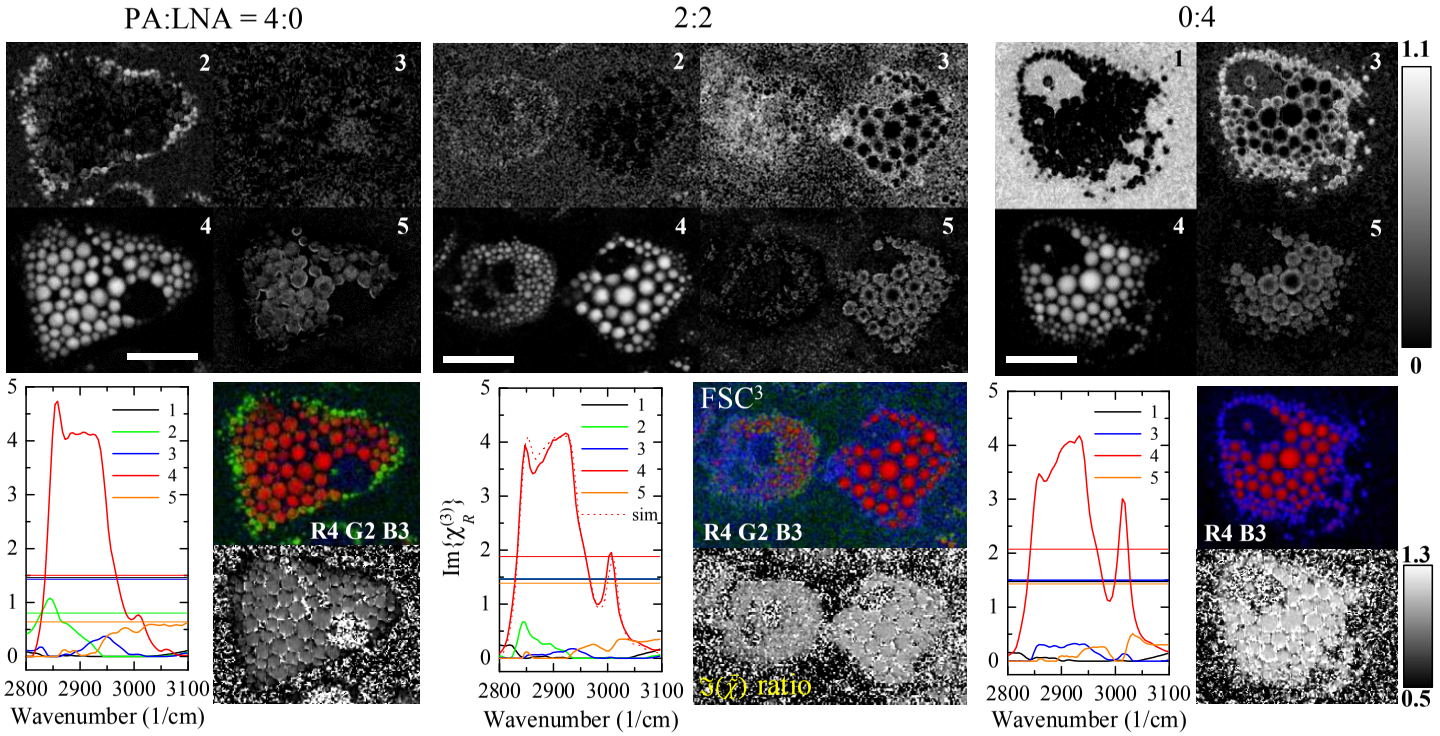

Figure 5.6: RESULTS OF FSC^3 ON THE PHASE-RETRIVED IM$\{\chi_R^{(3)}\}$ IN HUMAN ADSCS FED WITH PA, LNA AND AN EQUAL MIXTURE (VOL:VOL) OF PA AND LNA [118]. *Upper panels:* Spatial distributions of the volume concentration on a gray scale from 0 (black) to 1.1 (white) for the 5 components considered in the analysis. *Lower panels:* Spectra of Im$\{\chi_R^{(3)}\}$ and its real part (horizontal lines) for the corresponding components. In the spectra for the PA:LNA mixture the thin dotted line is an equally weighted superposition from component 4 of cells fed with PA and LNA only. RGB overlays show the spatial distribution of the concentration for specific components as indicated. Below the RGB overlays, the spatial distribution of the Im$\{\chi_R^{(3)}\}$ ratio between 2930 cm^{-1} and 2855 cm^{-1} is shown on a gray scale, as indicated. The scale bars indicate 20 μm.

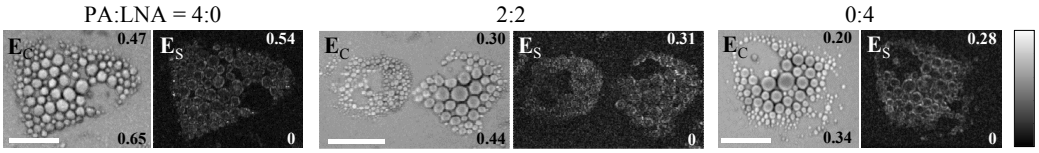

Figure 5.7: RELATIVE SPECTRAL ERROR E_S AND RELATIVE CONCENTRATION ERROR E_C FOR THE SAME CELLS ANALYZED WITH FSC^3 IN FIGURE 5.6 [118]. The grey scale is as indicated, with the range given for each image. Scale bars are 20 μm.

5.2.5 Summary

Fixed human stem-cell derived adipocytes fed with saturated (palmitic acid) and poly-unsaturated (α-linolenic acid) fatty acids have been investigated in order to compare dual-frequency CARS and hyperspectral CARS ability to provide quantitative chemical imaging. D-CARS enables fast acquisition, as for single-frequency CARS, and requires minimal data analysis. Hyperspectral CARS enables better chemical specificity and quantitative analysis, but requires phase-retrieval. We also used a novel unsupervised factorization into concentrations of chemical components (FSC^3) method to quantitatively analyze phase-retrived hyperspectral CARS images.

We find that D-CARS and hyperspectral CARS are equally able to quantify the degree of poly-unsaturation when applied to the fingerprint vibrational region. In the "CH-stretch" region, D-CARS is less quantitative due to its non-linear dependence on the concentration of chemical components but still provides results that are qualitatively similar to those achieved through hyperspectral CARS. Furthermore, hyperspectral CARS has been proven powerful when combined with FSC^3 because it able to extract the spatial distribution of chemical components within a cellular environment with superior contrast compared to other ratiometric methods described in literature.

5.3 Effects of fixation on adipocytes

The results presented in the previous section refer to cells that had been fixed with paraformaldehyde (PFA) according to the procedure described in the Materials and Methods chapter. Fixation of cells with PFA is one of the several chemical methods used to preserve cell structures so that optical microscopy can capture the localization of the different cellular components present in the cell at the time of fixation [68]. In this section we report our study on the effect of PFA by investigating ADSCs just before and after the fixation process through the FSC^3 analysis of CARS hyperspectral images. The effect of fixation with methanol, another commonly used cell fixative, has been also addressed for comparison on the same cell line. In both cases, ADSCs were cultured in normal differentiation media. Fixation was performed as indicated in the Materials and Methods chapter (Section 3.2.2).

5.3.1 Fixation with paraformaldehyde

PFA is widely considered as an ideal fixative for studies on cytosolic lipids. The cross-linking with protein molecules via methylene bridges does not affect the overall cellular lipid content or the lipid droplet structure, which remains preserved in shape and size [68, 121]. So far, PFA suitability for lipid studies have been demonstrated in non-human cellular systems (e.g., 3T3-L1 cells) via labeling methods or destructive techniques. Fluorescence microscopy, for example, has been used to visualize dye-stained lipids inside cytosolic droplets. Similarly, chromatography has been utilized to extract the total lipid content from cells, with different lipid types quantified by densitometry at a later stage [68].

We have used CARS as a minimally invasive tool to investigate the effect of PFA on human adipocytes. Specifically, hyperspectral CARS images have been acquired in the "CH-stretch" vibrational region on adipocytes just before and after they had been fixed with PFA. Quantitative FSC^3 analysis has been applied simultaneously on both datasets and the overall cellular chemical composition has been represented in terms of 5 chemical species. Results as spectral profiles and spatial

distributions are shown in Figure 5.8.

Water, indicated as component 1, is the most abundant constituent. The main lipid component for cytosolic LDs is indicated as component 3 and it is color-coded in red in the RGB overlay. A chemical component, indicated as component 2 and color-coded in blue, is spatially located in the nuclei, in the cytosol and at the periphery of the LD ensemble and it has a spectral profile interpretable as a mixture of nucleic acids and proteins. Another chemical component, indicated as component 4 and color-coded in green, shows a widespread distribution across cells and an association to proteins is plausible on the basis of its spectral profile (peak at $2950\,\mathrm{cm}^{-1}$ circa). Furthermore a component, indicated as component 5 and color-coded in orange, is also present in the cells; it is weak in intensity and it is likely due to artefact effects, as described in the case of fixed ADSCs (Section 5.2.4).

The comparison of FSC^3 spatial distributions before and after fixation reveals that the lipid-type component 3 remain almost unchanged, confirming the role of PFA as an ideal fixative for cytosolic LDs. Red-green overlay of the lipid spatial distribution before and after fixation shows however that small differences are present (non-yellow areas) and they are possibly due to the time interval between CARS observation and the fixation treatment. Conversely, component 2 and 4 show changes in their intensities before and after fixation with a decrease and slight increase, respectively. For component 4 this could be due to the effect of PFA as fixative, i.e. to the crosslink of the carbon-hydrogen-oxygen bonds in the protein structures of the cells with the analogous bonds in the PFA structure. Note also that the spectrum of component 4 does not present peaks at $2850\,\mathrm{cm}^{-1}$ hence it is well distinguished from the lipid component by FSC^3.

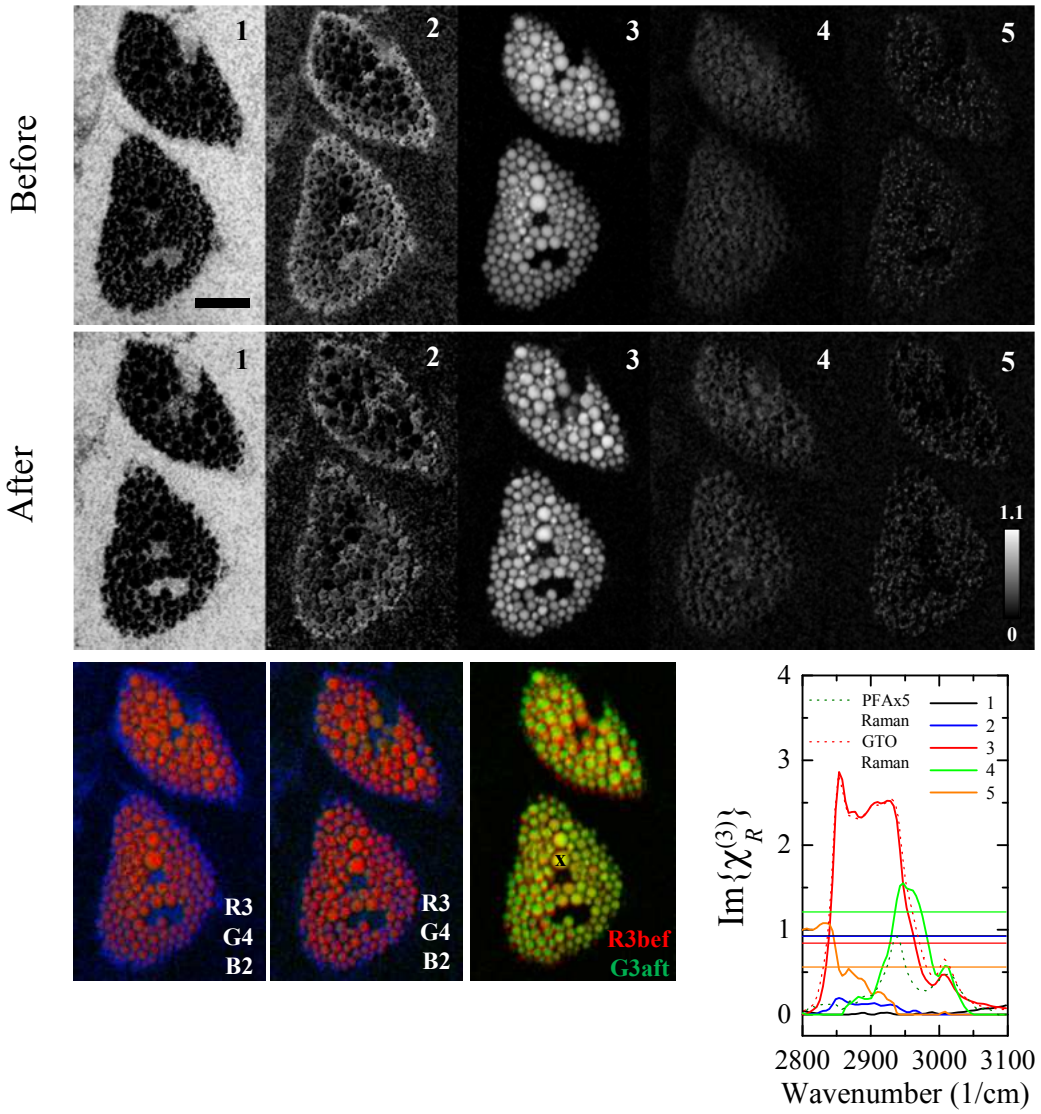

Figure 5.8: RESULTS OF FSC^3 ON THE PHASE-RETRIVED IM$\{\chi_R^{(3)}\}$ IN HUMAN ADSCS BEFORE AND AFTER FIXATION WITH PARAFORMALDEHYDE. *Upper panels:* Spatial distributions of the volume concentration on a gray scale from 0 (black) to 1.1 (white) for the 5 components considered in the analysis. Note that cell medium was kept after fixation. *Lower panels:* RGB overlays showing the spatial distribution of the concentration for specific components as indicated (*left*). RG overlay showing the spatial distribution of the lipid component before and after fixation (*centre*); *x* indicates where images were made to perfectly superimpose. Spectra of Im$\{\chi_R^{(3)}\}$ and its real part (horizontal lines) for the corresponding components (*right*). The red dotted line is the Raman spectrum of glyceryl trioleate scaled to match at 2855 cm^{-1} the phase-retrieved intensity of the main lipid component within LDs; the green dotten line is the phase-retrieved intensity of paraformaldehyde (4% concentration in phosphate buffered saline solution) multiplied by 4. The scale bar indicates 20 μm. For acquisitions before (resp. after) fixation, pump power on each pair 13 mW (resp. 30 mW), Stokes power on each pair 6.5 mW (resp. 15 mW), 10 μs pixel dwell time, 0.3 μm pixel size.

5.3.2 Fixation with methanol

Fixation of cells with methanol is also performed and it is effective at maintaining the structure of cytoskeletal elements such as microtubules. Despite being faster than the fixation with PFA (5 minutes instead of 20 minutes), this method is not compatible with studies on lipids droplets because it damages the structural integrity of cellular organelles. Specifically, it extracts the majority of cellular phospholipids, including the phospholipid monolayer surrounding the core of LDs. This generally results in the promotion of fusion among adjacent LDs at the moment of fixation [68].

Figure 5.9 shows the effect of methanol fixation as measured by hyperspectral CARS on the LDs of differentiated adipocytes. Comparison between FSC^3 images of CARS hyperspectral dataset acquired before and after fixation with methanol (100%) reveals that LDs were severely affected by the methanol fixation, with the lipid content being almost completely absent after fixation (Figure 5.9, component 4, color-coded in red). A possible explanation is that the extraction of phospholipids by methanol was so severe that LD phospholipid monolayers had been dissolved and the core lipid content released into the surrounding media. Note that the spectrum of the lipid component resembles in its profile the spectrum of pure glyceryl trioleate, thus supporting the hypothesis that cell differentiation media has this type of lipid. Conversely, the protein component (Figure 5.9, component 3, color-coded in green) is visible in the cytoplasm and in the nucleus before and after cell fixation, showing a more concentrated presence in the second case. In the FSC^3 after-fixation image the structure of cell nuclei is well defined with the nuclear envelope and nucleoli clearly visible. This is due to the nature of methanol as precipitating fixative that reduces the solubility of protein molecules and nucleic acids, and immobilizes them by precipitation [122]. The water component (component 1, color-coded in black) has a more uniform appearance in after-fixation cells and this is likely due to the combined action of methanol as fixative of cytoskeletal elements and destroyer of lipid elements (that are washed out during the fixation procedure). The artefact component (component 2, color-coded in orange) is visible in pre-fixation cells only where the presence of LDs

causes distortions in the excitation fields, especially in correspondence of the borders.

5.3.3 Summary

These results show that the choice of fixative is critical in studies of LDs and that the fixation with PFA essentially preserves the LD chemical content and structure while the fixation with methanol is completely disruptive. However, because of its inherit nature, cell fixation provides only a stop-motion of the continuously working cellular machinery. A better understanding on how a cell system reacts when incorporating a new fatty acid can be achieved only by observing that process while it is taking place. This is the main purpose of CARS and D-CARS live imaging on adipocytes as it will be described in the next section.

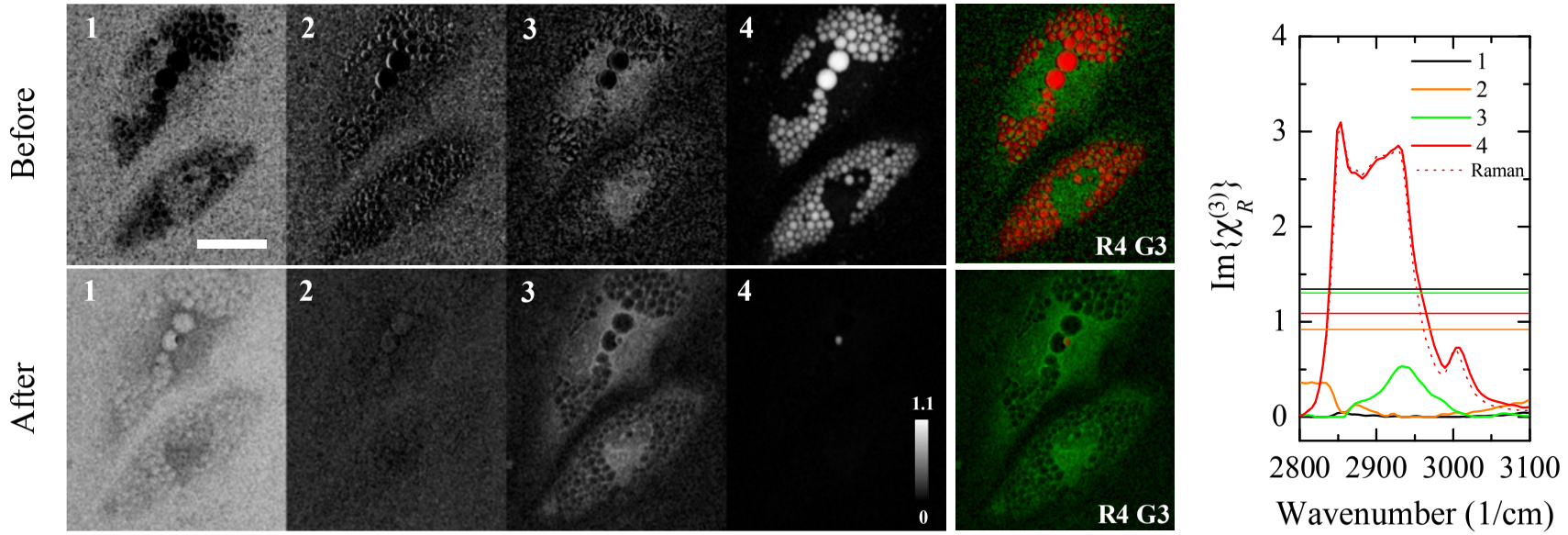

Figure 5.9: RESULTS OF FSC^3 ON THE PHASE-RETRIVED IM$\{\chi_R^{(3)}\}$ IN HUMAN ADSCS BEFORE AND AFTER FIXATION WITH METHANOL. *Left:* Spatial distributions of the volume concentration on a gray scale from 0 (black) to 1.1 (white) for the 4 components considered in the analysis. RGB overlays show the spatial distribution of the concentration for specific components as indicated. *Right:* Spectra of Im$\{\chi_R^{(3)}\}$ and its real part (horizontal lines) for the corresponding components. The red dotted line is the Raman spectrum of glyceryl trioleate scaled to match at 2855 cm^{-1} the phase-retrieved intensity of the main lipid component within LDs. The scale bar indicates 20 μm. For acquisitions before (resp. after) fixation, pump power on each pair 13 mW (resp. 30 mW), Stokes power on each pair 6.5 mW (resp. 15 mW), 10 μs pixel dwell time, 0.3 μm pixel size.

5.4 Cytosolic lipid droplets in live adipocytes

In recent years CARS microscopy has become a promising tool for real-time studies on living cells, especially for adipocytes due to the large number of LDs in these cell. Some studies, for instance, have addressed the morphological changes occurring to LDs when stem cells are converted into adipocytes with the ultimate aim to prevent the differentiation into an unwanted cell lineage [96–98]. Proving CARS as label-free assessment tool of adipogenic differentiation would also allow the circumvention of conventional methods (e.g., cell surface markers) that are intrusive and provide information averaged over the entire cell population [98]. Time course studies of ADSCs induced towards adipocytes have been performed at different stage post-inductions with one- and multi-frequency CARS acquisitions. CARS images at the CH_2 stretch frequency $2855\,cm^{-1}$ have revealed that, two days after induction, LDs are present as small bright spots around cell nuclei but, as adipogenesis takes place, they become bigger, numerous and better structured [97]. Hyperspectral CARS images have complemented this information with maps of specific biochemical species and have been used to characterize adipocytes from other lineage groups [98].

Other CARS studies were performed on living ADSCs in order to investigate how the number and size of LDs increases during differentiation and how this may lead to one large unilocular LD occupying most of the cell volume once reached the maturation stage [99, 123]. By monitoring ADSCs at different time points via 3-dimensional CARS stacks tuned at $2855\,cm^{-1}$, LDs have been observed to grow by the absorption of smaller LDs (*donors*) in a several-hour-long process during which lipid content is transferred to larger droplets (*acceptors*) by a fusion pore. Parallel immunofluorescence studies on 3T3-L1 cells have shown that Fsp27, a protein of the CIDE (cell death-inducing DNA fragmentation factor 45-like effector) family, localizes at the contact site between the two LDs and there it interacts with the LD-coat protein perilipin1 (Plin1) [124, 125]. It has been hypothesized that the cooperative action between Fsp27 and Plin1 is responsible for the opening of the fusion pore [125, 126].

Within this context, however, no CARS studies have been dedicated so far to the study in real time of lipid composition in ADSCs. As mentioned in the previous section, human adipose tissue is characterized by a heterogeneous pool of fatty acids. How this heterogeneity influences adipocytes is still unclear. The application of CARS spectral-microscopy on live ADSCs while being cultured in media loaded with different types of fatty acids can provide a better understanding on LD formation and composition under these circumstances.

We have therefore investigated differentiated human adipocytes cultured in a cell media previously enriched with oleic acid or linoleic acid or α-linolenic acid or an equal-volume mixture of oleic acid and α-linolenic acid. D-CARS and hyperspectral CARS measurements were performed with the 5 fs set-up in the fingerprint and "CH-stretch" vibrational regions. Acquisitions were taken at different time points in order to characterize the LD content while cells are in a culture medium loaded with exogenous fatty acids. Results from data processing and HIA analysis are reported below.

5.4.1 Hyperspectral CARS

Hyperspectral images of CARS intensities as ratios relative to the nonresonant glass response are shown in Figures 5.10, 5.11, 5.12, 5.13, 5.14 (left panels) for human adipocytes grown over time in medium supplemented with fatty acids. As described in the Materials and Methods chapter (Section 3.2.2), three days after induction to adipogenesis (day 0) cells were fed with oleic acid (OA), linoleic acid (LA), α-linolenic acid (LNA) and an equal volume mixture of OA and LNA (MIX). Images refer to time points before (0 hours) and after lipid addition (24, 48, 72, 144 and 216 hours) with exchange on day 3 for OA- and LNA-treated cells to LNA- and OA-enriched culture media, respectively. A control sample, where cells were left in normal differentiation media, was also considered.
Corresponding phase-retrieved images of the imaginary part $\mathrm{Im}\{\chi_R^{(3)}\}$, obtained by the method described in Chapter 3 (Section 3.5.2), are shown in the same Figures (right panels). Images are shown at characteristic wavenumbers in both fingerprint and "CH-stretch" regions.

In all Figures CARS and phase-retrieved spectra (upper panels) are reported as averages between two medium/large sized LDs in different fields of view, where LDs were selected with a diameter between 2 and 15 μm in order to avoid under-resolution or beam-distortion effects. LDs considered in the field of view are indicated by yellow arrows.

As for model and fixed cytosolic LDs, CARS spectra show dispersive spectral shapes in the fingerprint region and peak-shoulder profiles in the "CH-stretch" region. Retrieved $\mathrm{Im}\{\chi_R^{(3)}\}$ spectra, with their Raman-like shapes, exhibit the characteristic vibrational bands of neutral lipids, e.g., the C=C stretch band at $1660\,\mathrm{cm}^{-1}$, the C=O stretch band at $1740\,\mathrm{cm}^{-1}$, the multiple-stretch band at $2930\,\mathrm{cm}^{-1}$ and the =CH stretch band at $3010\,\mathrm{cm}^{-1}$. As for fixed cytosolic LDs, the presence of these peaks suggests that ADSCs have uptaken fatty acids from the culture media and they have accumulated them in form of LDs. Through the hyperspectral observation of living ADSCs, this information can be completed and extended by monitoring the changes in intensity and spectral shape of the characteristic vibrational bands over time.

For cells cultured in standard media (Figure 5.10), images show the increase in size for cytosolic LDs which is consistent with cells approaching the mature stage as adipocytes. Lipid phase-retrieved spectra exhibit a time-dependent increase in their amplitude reaching saturation 144 hours after day 0. The overall lineshape of the spectra remains mostly unaltered as the relative amplitudes between significant vibrational bands stay approximately constant overtime. This suggests that no major changes occur in the chemical composition of LDs.

For cytosolic LDs of cells fed with bi-unsaturated LA (Figure 5.11), relative amplitudes do change, particularly for the bands at $1660\,\mathrm{cm}^{-1}$ and $3010\,\mathrm{cm}^{-1}$. Already 24 hours after the replacement of the control media, the amplitude of the $3010\,\mathrm{cm}^{-1}$ band has increased more than the amplitude of the $2850\,\mathrm{cm}^{-1}$ band, indicating the presence of more carbon-carbon double bonds within LDs. The higher relative amplitude of the $1660\,\mathrm{cm}^{-1}$ band with respect to the $1450\,\mathrm{cm}^{-1}$ band in that time interval also confirms the LD content change to a more poly-unsaturated lipid. In the following hours the relative amplitudes of $3010\,\mathrm{cm}^{-1}$

and 1660 cm^{-1} bands increase further. After 72 hours the overall lineshape seems to remain unaltered with vibrational bands increasing their amplitudes simultaneously.

Images are consistent with the intensities at the spectral peaks. Interestingly, we observe especially in the fingerprint region an intensity background in the surrounding medium which is more significant compared to the case with fixed cells. This might be due to the presence of fatty acids in the differentiation media, which was instead washed away for the measurements with fixed cells (see Section 5.2.1). Conversely, before measurements on live cells, each cell sample was prepared by replacing the old media with fresh media with the same compositional characteristics. Because of this, a higher amount of unprocessed fatty acid suspended in the media contributed to the overall CARS signal from the lipids. As mentioned, this type of noise has not being observed in fixed ADSCs where the culture medium was substituted by water.

Similar considerations for spectra and images apply to cytosolic LDs within cells fed with MIX (Figure 5.12). The relative amplitudes of 1660 cm^{-1} and 3010 cm^{-1} bands increase 24 hours after the media switch as a response to the higher degree of poly-unsaturation in MIX. As for the cells fed with LA, no changes in the relative amplitudes seem to occur after 72 hours. Note that the peak at 2930 cm^{-1} shows a higher intensity than the peak at 2855 cm^{-1} at any time point. This is due to the CH_2 asymmetric vibrations in the acyl chains that arise as consequence of the carbon-carbon double bonds.

Cytosolic LDs within cells fed with OA for 48 hours from day 0 also an increase for the absolute amplitudes of the 1660 cm^{-1} and 3010 cm^{-1} bands over time (Figure 5.13). When the media is changed to LNA-supplemented media, the shape of the spectral profile also varies and differences can be noticed already after 24 hours from the switch. Specifically, the relative amplitude of 1660 cm^{-1} and 3010 cm^{-1} bands increase significantly due to the greater number of carbon-carbon double bonds introduced via the poly-unsaturated LNA. The relative amplitude of the 2930 cm^{-1} band also grows in intensity as consequence of the asymmetric stretches in the acyl chains, that are more numerous in the disordered LNA

than in the ordered mono-unsaturated LA. After 48 and 96 hours from the switch, the relative amplitude of the 3010 cm^{-1} band has slightly increased, and the intensity of the peak at 2930 cm^{-1} is higher than that of the peak at 2855 cm^{-1}. This indicates a significant presence of carbon-carbon double bonds within cytosolic LDs and a more disordered packing in their molecular composition.

Cytosolic LDs within cells fed with LNA for 48 hours from day 0 show an increase in relative amplitudes for the band at 1660 cm^{-1} and 3010 cm^{-1} which is consistent with the high degree of poly-unsaturation of LNA (Figure 5.14). The peak at 2855 cm^{-1} becomes less intense compared to the peak at 2930 cm^{-1} in agreement with the increase of molecular disorder within LDs compared the control case. When the media is changed to OA-supplemented media, the intake of a less unsaturated fatty acids translates after 24 hours into an intensity reduction of the C=C-related peaks. After 48 hours from the switch, the relative amplitude of the 2855 cm^{-1} band increases consistently with the higher degree of molecular order introduced by the OA. In the following 48 hours, the relative amplitude of the 3010 cm^{-1} band decreases and the spectral shape resembles that from cytosolic LDs fed exclusively with OA. This suggests that a change in the lipid content from poly-unsaturated to mono-unsaturated fatty acids is detectable 96 hours after the media replacement.

These findings suggest that, for the considered experimental conditions, human ADSCs efficiently incorporate fatty acids and are sensitive to changes in the lipid-content of the culture media with time scales in the range of 24 hours to 96 hours depending on the lipid type.

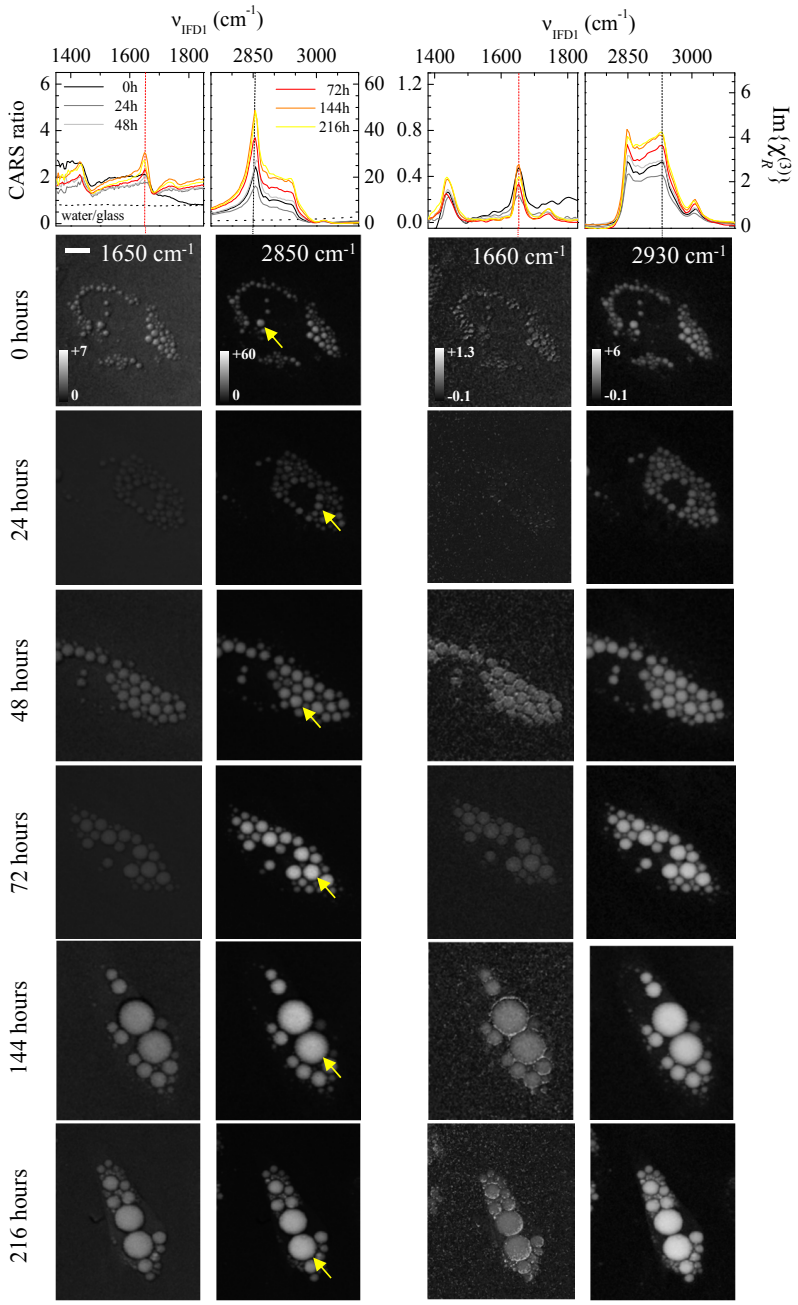

Figure 5.10: CARS SPECTRA, PHASE-RETRIEVED SPECTRA AND CORRESPONDING IMAGES FOR LIVING ADSCS FED IN CONTROL DIFFERENTIATION MEDIA. *Upper panels:* CARS intensity ratio relative to the nonresonant intensity in glass (left) and corresponding spectrum of the retrieved susceptibility (right) at 24, 48, 72, 144 and 216 hours after day 0 for human ADSCs cultured in control media. Spectra are obtained by averaging over two LDs from cells in two different field of views. For the shown field of view, the corresponding LD is indicated by the yellow arrow and as average over two LDs. The spectrum of the water to glass ratio is also shown. *Lower panels:* Images of the CARS intensity ratio (left) and corresponding susceptibilities (right) at different time points and wavenumbers, as indicated by the vertical dotted lines in the spectra. Linear grey scales as indicated. The pump power on the sample was 30 mW (18 mW) and the Stokes power was 15 mW (9 mW) for the fingerprint region ("CH-stretch" region); 10 μs pixel dwell time, 0.3 μm pixel size, 20 μm scale bar.

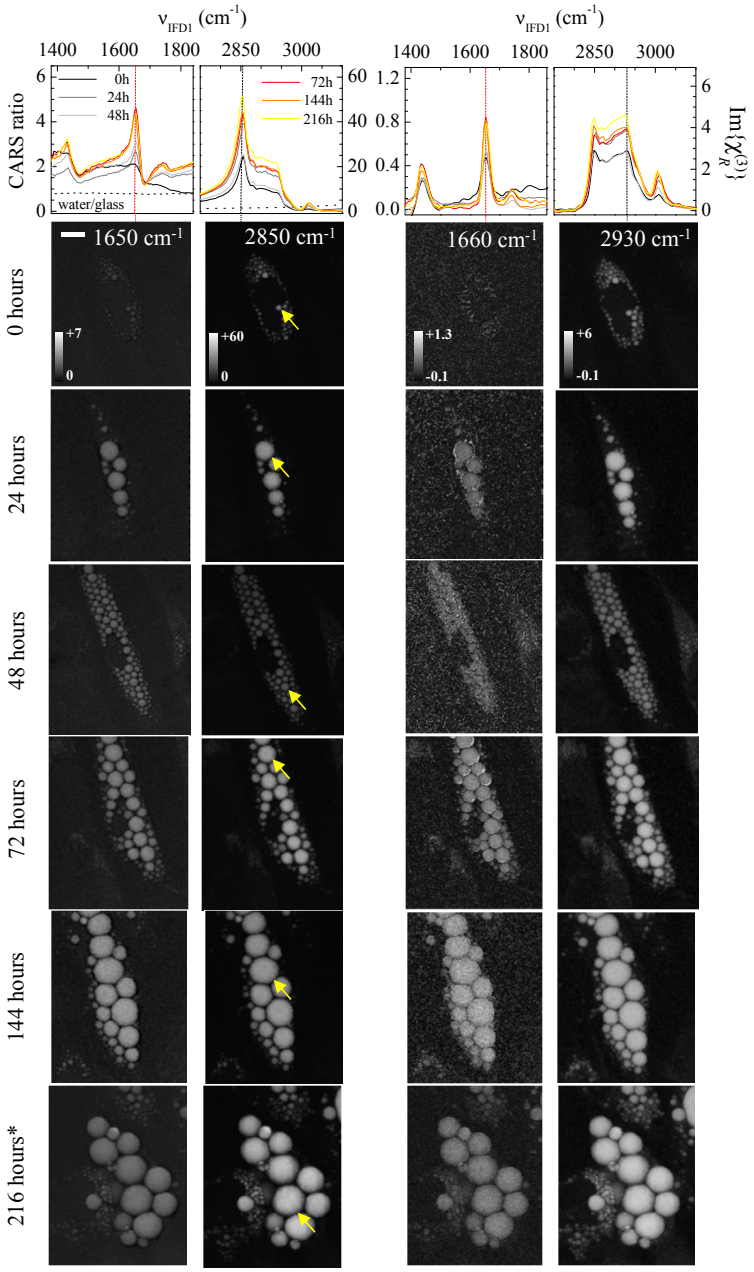

Figure 5.11: CARS SPECTRA, PHASE-RETRIEVED SPECTRA AND CORRESPONDING IMAGES FOR LIVING ADSCS FED IN LINOLEIC ACID-SUPPLEMENTED MEDIA. *Upper panels:* CARS intensity ratio relative to the nonresonant intensity in glass (left) and corresponding spectrum of the retrieved susceptibility (right) at 24, 48, 72, 144 and 216 hours after day 0 for human ADSCs cultured in control media. Spectra are obtained by averaging over two LDs from cells in two different field of views. For the shown field of view, the corresponding LD is indicated by the yellow arrow and as average over two LDs. The spectrum of the water to glass ratio is also shown. *Lower panels:* Images of the CARS intensity ratio (left) and corresponding susceptibilities (right) at different time points and wavenumbers, as indicated by the vertical dotted lines in the spectra. Linear grey scales as indicated. Asterisk at the time point indicates a different field of view from the one considered previously. The pump power on the sample was 30 mW (18 mW) and the Stokes power was 15 mW (9 mW) for the fingerprint region ("CH-stretch" region); 10 μs pixel dwell time, 0.3 μm pixel size, 20 μm scale bar.

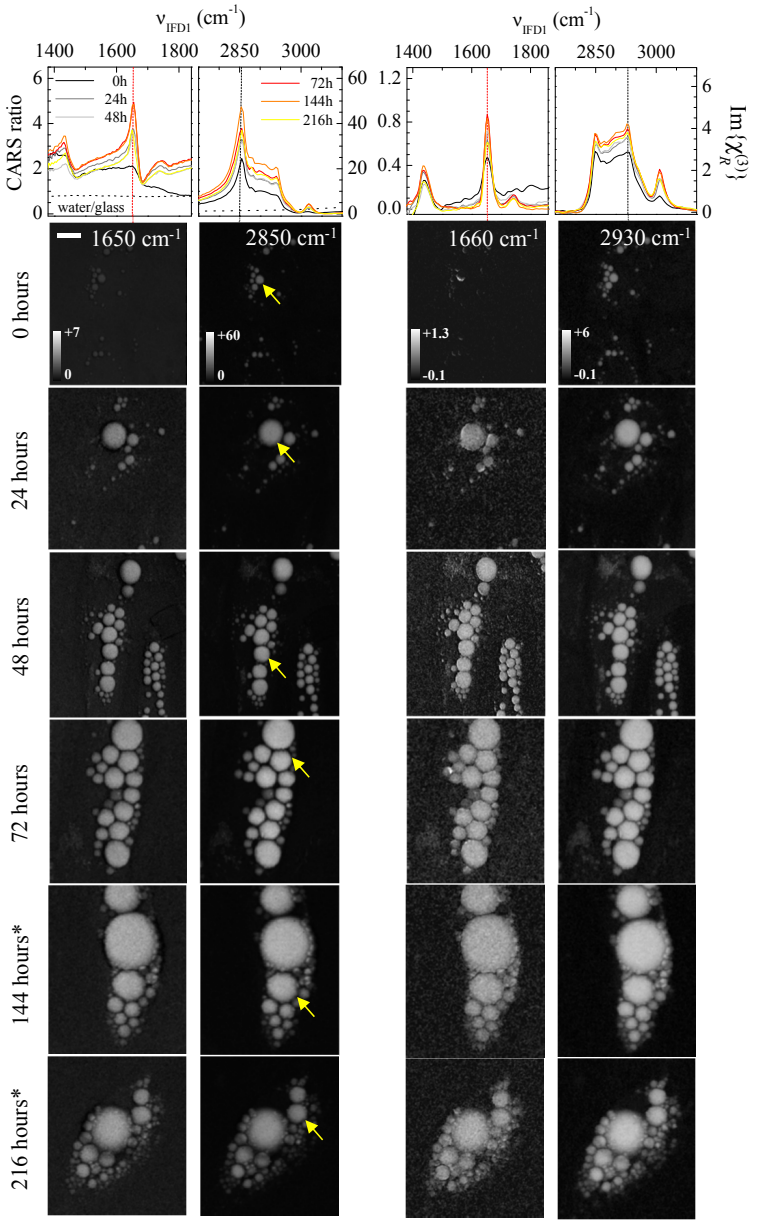

Figure 5.12: CARS SPECTRA, PHASE-RETRIEVED SPECTRA AND CORRESPONDING IMAGES FOR LIVING ADSCS FED IN A MEDIA SUPPLEMENTED WITH AN EQUAL VOLUME MIXTURE OF OLEIC ACID AND α-LINOLENIC ACID. *Upper panels:* CARS intensity ratio relative to the nonresonant intensity in glass (left) and corresponding spectrum of the retrieved susceptibility (right) at 24, 48, 72, 144 and 216 hours after day 0 for human ADSCs cultured in control media. Spectra are obtained by averaging over two LDs from cells in two different field of views. For the shown field of view, the corresponding LD is indicated by the yellow arrow and as average over two LDs. The spectrum of the water to glass ratio is also shown. *Lower panels:* Images of the CARS intensity ratio (left) and corresponding susceptibilities (right) at different time points and wavenumbers, as indicated by the vertical dotted lines in the spectra. Linear grey scales as indicated. Asterisks at the time points indicate a different field of view from the one considered previously. The pump power on the sample was 30 mW (18 mW) and the Stokes power was 15 mW (9 mW) for the fingerprint region ("CH-stretch" region); 10 μs pixel dwell time, 0.3 μm pixel size, 20 μm scale bar.

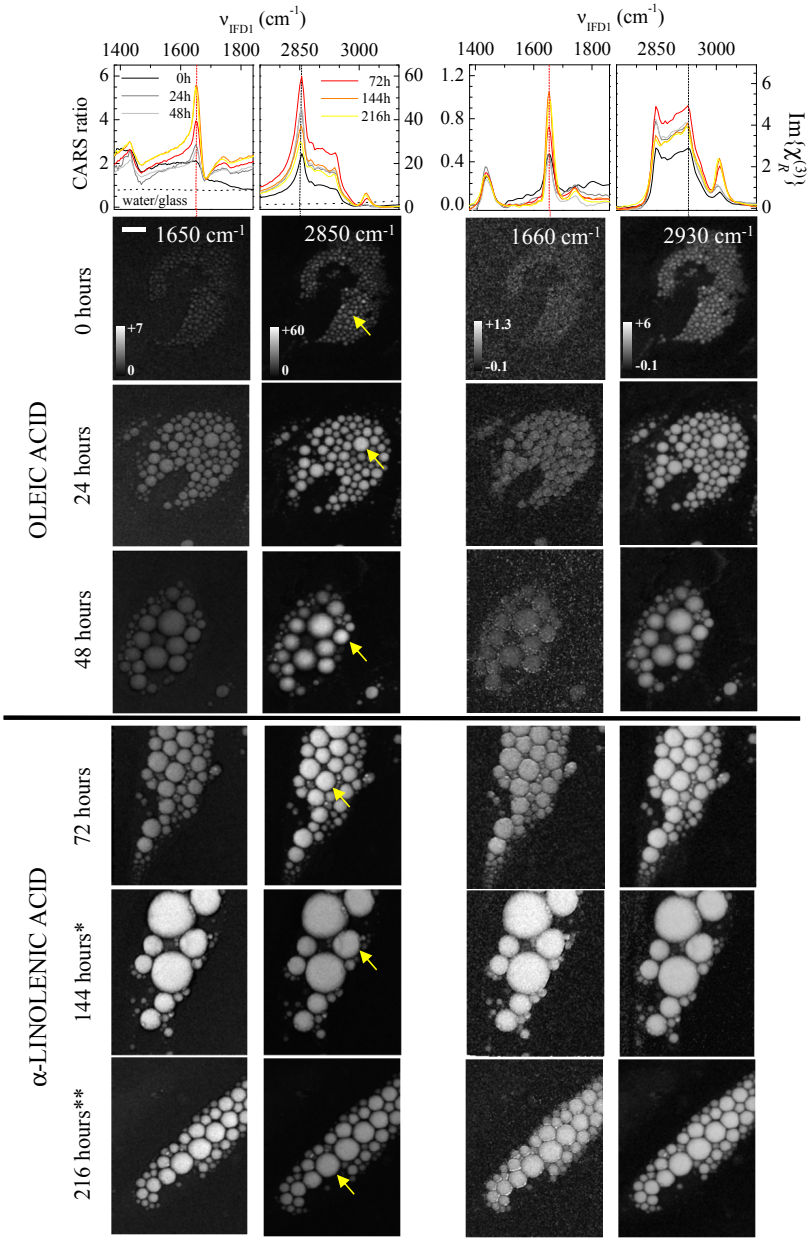

Figure 5.13: CARS SPECTRA, PHASE-RETRIEVED SPECTRA AND CORRESPONDING IMAGES FOR LIVING ADSCS FED IN MEDIA SUPPLEMENTED INITIALLY WITH OLEIC ACID FIRST AND THEN WITH α-LINOLENIC ACID. *Upper panels:* CARS intensity ratio relative to the nonresonant intensity in glass (left) and corresponding spectrum of the retrieved susceptibility (right) at 24, 48, 72, 144 and 216 hours after day 0 for human ADSCs cultured in control media. Spectra are obtained by averaging over two LDs from cells in two different field of views. For the shown field of view, the corresponding LD is indicated by the yellow arrow and as average over two LDs. The spectrum of the water to glass ratio is also shown. *Lower panels:* Images of the CARS intensity ratio (left) and corresponding susceptibilities (right) at different time points and wavenumbers, as indicated by the vertical dotted lines in the spectra. Linear grey scales as indicated. Asterisks at the time points indicate different fields of view from the one considered previously. The pump power on the sample was 30 mW (18 mW) and the Stokes power was 15 mW (9 mW) for the fingerprint region ("CH-stretch" region); 10 μs pixel dwell time, 0.3 μm pixel size, 20 μm scale bar.

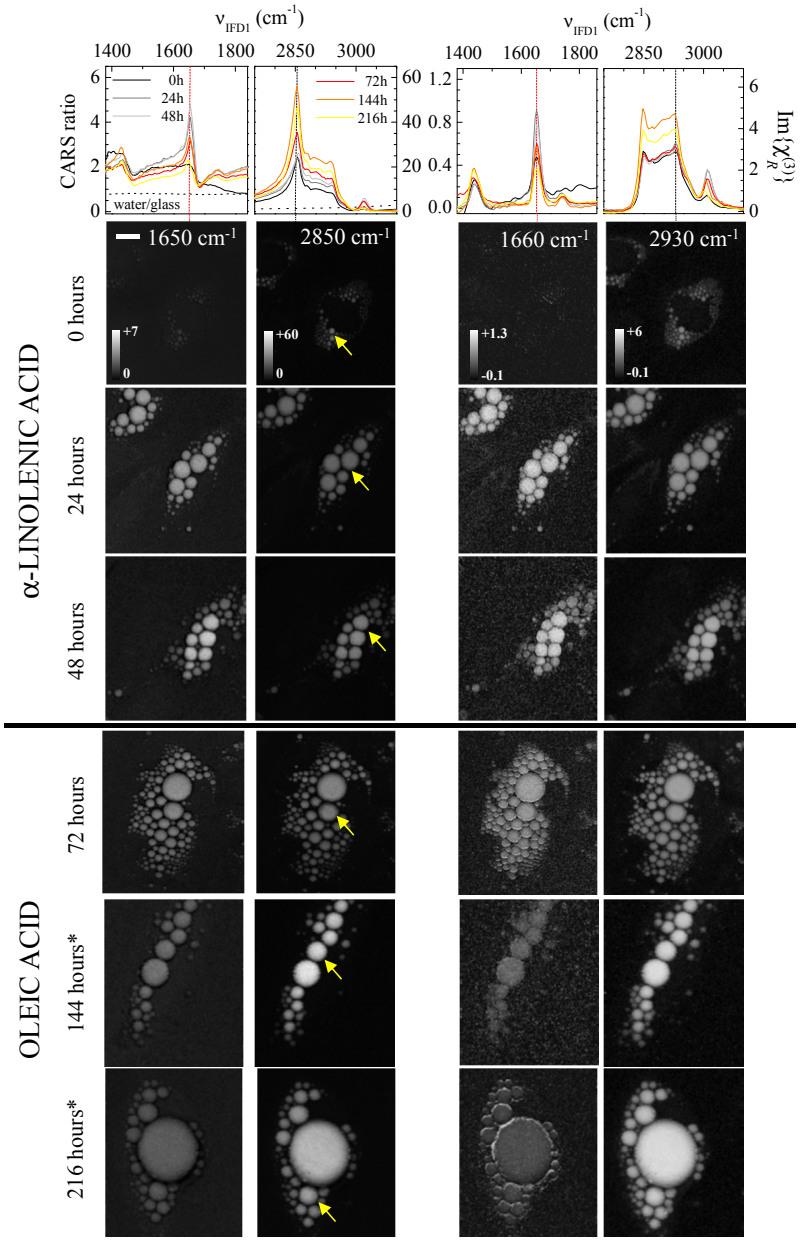

Figure 5.14: CARS SPECTRA, PHASE-RETRIEVED SPECTRA AND CORRESPONDING IMAGES FOR LIVING ADSCS FED IN MEDIA SUPPLEMENTED INITIALLY WITH α-LINOLENIC ACID FIRST AND THEN WITH OLEIC ACID. *Upper panels:* CARS intensity ratio relative to the nonresonant intensity in glass (left) and corresponding spectrum of the retrieved susceptibility (right) at 24, 48, 72, 144 and 216 hours after day 0 for human ADSCs cultured in control media. Spectra are obtained by averaging over two LDs from cells in two different field of views. For the shown field of view, the corresponding LD is indicated by the yellow arrow and as average over two LDs. The spectrum of the water to glass ratio is also shown. *Lower panels:* Images of the CARS intensity ratio (left) and corresponding susceptibilities (right) at different time points and wavenumbers, as indicated by the vertical dotted lines in the spectra. Linear grey scales as indicated. Asterisks at the time points indicate a different field of view from the one considered previously. The pump power on the sample was 30 mW (18 mW) and the Stokes power was 15 mW (9 mW) for the fingerprint region ("CH-stretch" region); 10 μs pixel dwell time, 0.3 μm pixel size, 20 μm scale bar.

5.4.2 Dual-frequency differential CARS

D-CARS spectra and images following the same criteria as for the Figures in the previous Section are given in Figures 5.15, 5.16, 5.17, 5.18 and 5.19 for the fingerprint (left panels) and the "CH-stretch" region (right panel). Simulated D-CARS spectra (upper panels) are also reported and, as for the studies on fixed cytosolic LDs, they were constructed using the corresponding single-pair CARS intensity ratio from the previous Section and the experimental value of the wavenumber shift Δ_{IFD}, i.e. $34\,\mathrm{cm}^{-1}$ for the fingerprint region and $27\,\mathrm{cm}^{-1}$ and $65\,\mathrm{cm}^{-1}$ for the "CH-stretch" region. D-CARS images acquired at chemically- discriminating wavenumbers are also shown (bottom panels). Note that the fields of view chosen for D-CARS spectral-imaging are different from the fields of view considered for CARS hyperspectral imaging. This was done in order to limit laser-induced stress on cells.

For cytosolic LDs of cells fed with standard media (Figure 5.15), the lineshape of the D-CARS spectra is mostly unchanged. Despite showing a time-dependent increase in amplitude, the relative intensities of D-CARS bands at 1680, 2920 and $3045\,\mathrm{cm}^{-1}$ remain the same, indicating no changes in the LD composition.

Conversely, for cytosolic LDs of cells fed with LA (Figure 5.16) D-CARS relative amplitudes are affected by the switch to a media with different lipid content. As demonstrated in the study on model LDs, the D-CARS intensity at selected wavenumbers is able to provide information on LD composition as it is defined as difference between CARS ratios of chemically-specific lineshape. For instance, the D-CARS intensity ratio at $2920\,\mathrm{cm}^{-1}$ reflects the peak-shoulder amplitude in the CARS profile and it decreases as the degree of lipid poly-unsaturation increases. As shown in the study on fixed cells, D-CARS is able to provide quantitative results in the fingerprint region where the ratiometric analysis of the D-CARS ratio at $1680\,\mathrm{cm}^{-1}$ relative to the D-CARS ratio at $1470\,\mathrm{cm}^{-1}$ is indicative of the concentration of carbon-carbon double bonds within LDs. For cells fed with LA the intensity of the $1680\,\mathrm{cm}^{-1}$ band increases relatively to the $1470\,\mathrm{cm}^{-1}$ band already after 24 hours from the switch. This can be inferred also by comparing the corresponding D-CARS images. Conversely, this does not apply to

the "CH-stretch" region where the D-CARS ratios at $2920\,cm^{-1}$, $2990\,cm^{-1}$ and $3045\,cm^{-1}$ are only qualitative indicators of the number of C=C and associated molecular disorder, even when they are ratiometrically analysed.

Similar considerations for spectra and images apply to cytosolic LDs in cells fed with MIX (Figure 5.17). With time, the D-CARS intensity at $1680\,cm^{-1}$ increases relatively to the D-CARS intensity at $1470\,cm^{-1}$. This is in agreement with the high degree of unsaturation in MIX and it is qualitatively confirmed by the higher relative amplitude of the D-CARS band at $3045\,cm^{-1}$.

Cytosolic LDs within cells fed with OA for 48 hours from day 0 (Figure 5.18) show an increase in the overall D-CARS intensity over time with no significant changes in the lineshape, confirming once again the presence of an oleic-like lipid in the standard differentiation media. When cells are changed to LNA-supplemented media, D-CARS intensities change accordingly to the new lipid environment. Because of the greater number of carbon-carbon double bonds in the poly-unsaturated LNA, the relative amplitudes of the D-CARS bands at $1680\,cm^{-1}$ and $3045\,cm^{-1}$ increase in intensity. After 24 hours from the switch, the band at $2920\,cm^{-1}$ starts to decrease as expected for a highly-disordered lipid until it matches in intensity the band at $2990\,cm^{-1}$.

The opposite trend is observed in cells fed initially with LNA (Figure 5.19). In consistency with the high degree of poly-unsaturation and disorder of LNA, cytosolic LDs show in the first 48 hours an intensity increase for the $1680\,cm^{-1}$ band relative to the $1470\,cm^{-1}$ band and for the $3045\,cm^{-1}$ band relative to the $2850\,cm^{-1}$ band; the intensity of the band at $2920\,cm^{-1}$ is instead similar to that of the band at $2990\,cm^{-1}$. When the media is changed to OA-supplemented media, the less abundance of carbon-carbon double bonds causes the related band peaks to decrease and the $2920\,cm^{-1}$ band to gain more intensity.

D-CARS images are in good agreement with the intensities from the D-CARS simulated spectra. Despite being not completely noise-free (especially in the fingerprint region and at $3045\,cm^{-1}$), they allow us to efficiently track compositional changes within LDs over time. Furthermore, the results are consistent with the outcomes from the CARS hyperspectral analysis. Importantly death induced

by laser irradiation has been less frequent in measurements with D-CARS than in measurements with hyperspectral CARS. Specifically, for D-CARS measurements, the same set of cells was monitored over 216 hours in 3 cases out of 5 and over 144 hours in 5 cases out of 5; for CARS hyperspectral measurements, only one set of cells was successfully monitored over 216 hours, another set over 144 and three sets over 72 hours. The higher cell survival to laser-induced apoptosis in D-CARS is mostly likely due to the fast acquisition enabled with this technique. Combined with its chemical selectivity and the minimum data analysis required, D-CARS is therefore as an effective and valuable technique for studies of living cells.

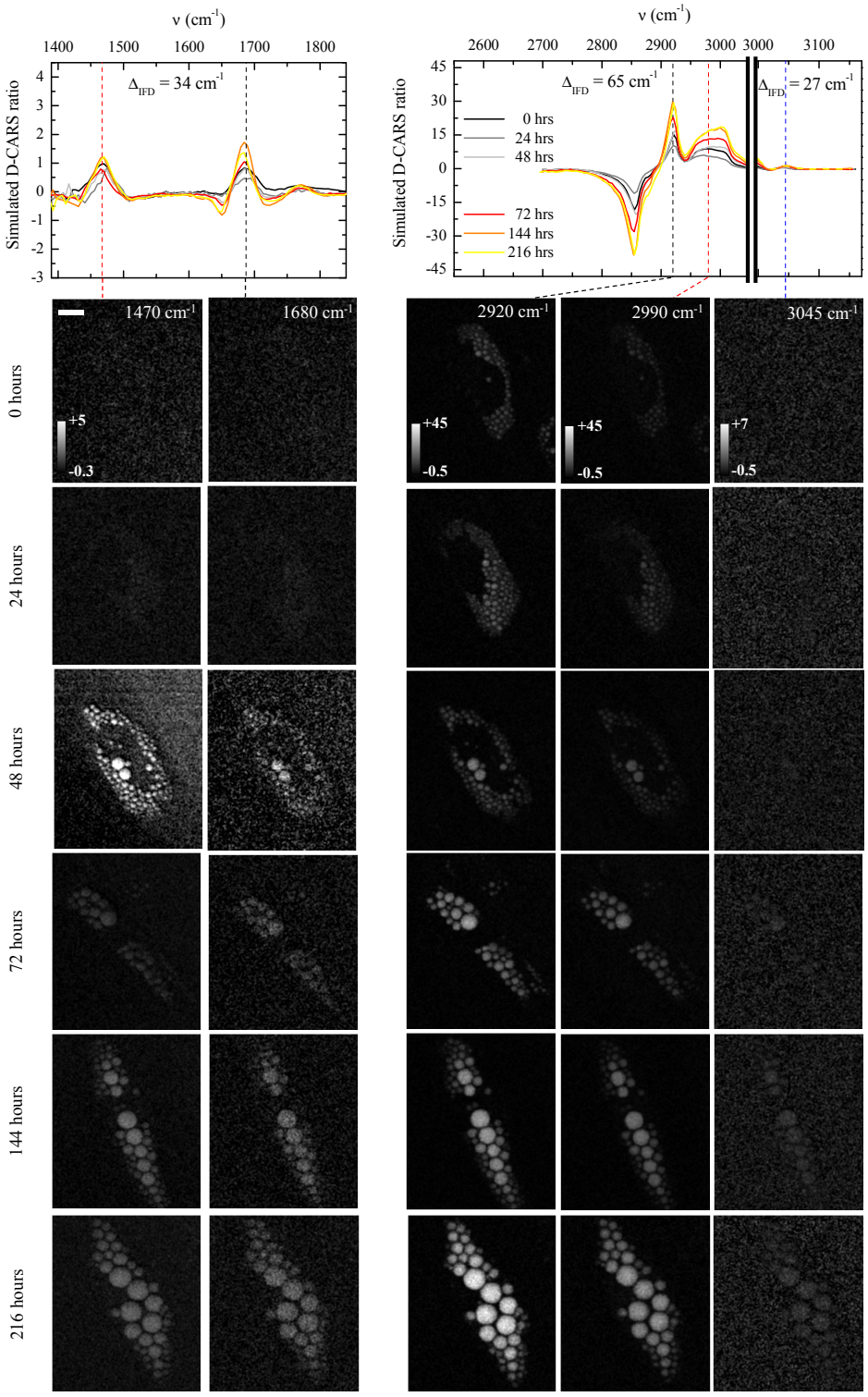

Figure 5.15: D-CARS IMAGING OF LIVING ADSCs CULTURED IN CONTROL DIFFERENTIATION MEDIA. *Upper panels:* D-CARS spectra calculated from the measured CARS intensity ratios shown in Figure 5.10 with Δ_{IFD} as indicated. *Lower panels:* D-CARS images of adipocytes measured at the wavenumbers indicated by corresponding dotted lines at different time points. Grey scale as shown. Pump power on each pair 32 mW (20 mW), Stokes power on each pair 16 mW (10 mW) for the fingerprint region ("CH-stretch" region); 10 μs pixel dwell time, 0.3 μm pixel size; 20 μm scale bar.

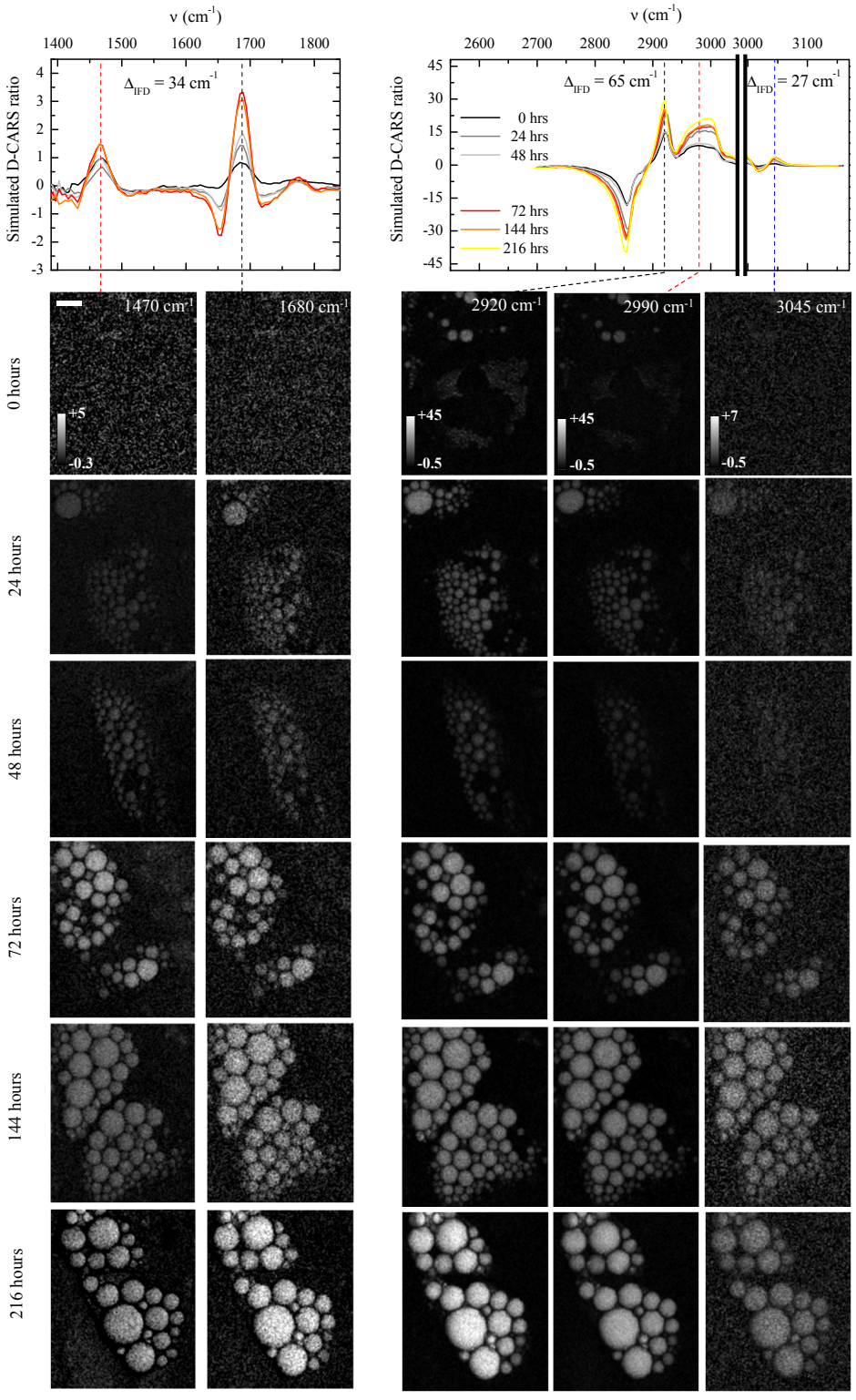

Figure 5.16: D-CARS IMAGING OF LIVING ADSCs FED WITH LINOLEIC ACID-ENRICHED MEDIA. *Upper panels:* D-CARS spectra calculated from the measured CARS intensity ratios shown in Figure 5.11 with Δ_{IFD} as indicated. *Lower panels:* D-CARS images of adipocytes measured at the wavenumbers indicated by corresponding dotted lines at different time points. Grey scale as shown. Pump power on each pair 32 mW (20 mW), Stokes power on each pair 16 mW (10 mW) for the fingerprint region ("CH-stretch" region); 10 μs pixel dwell time, 0.3 μm pixel size; 20 μm scale bar.

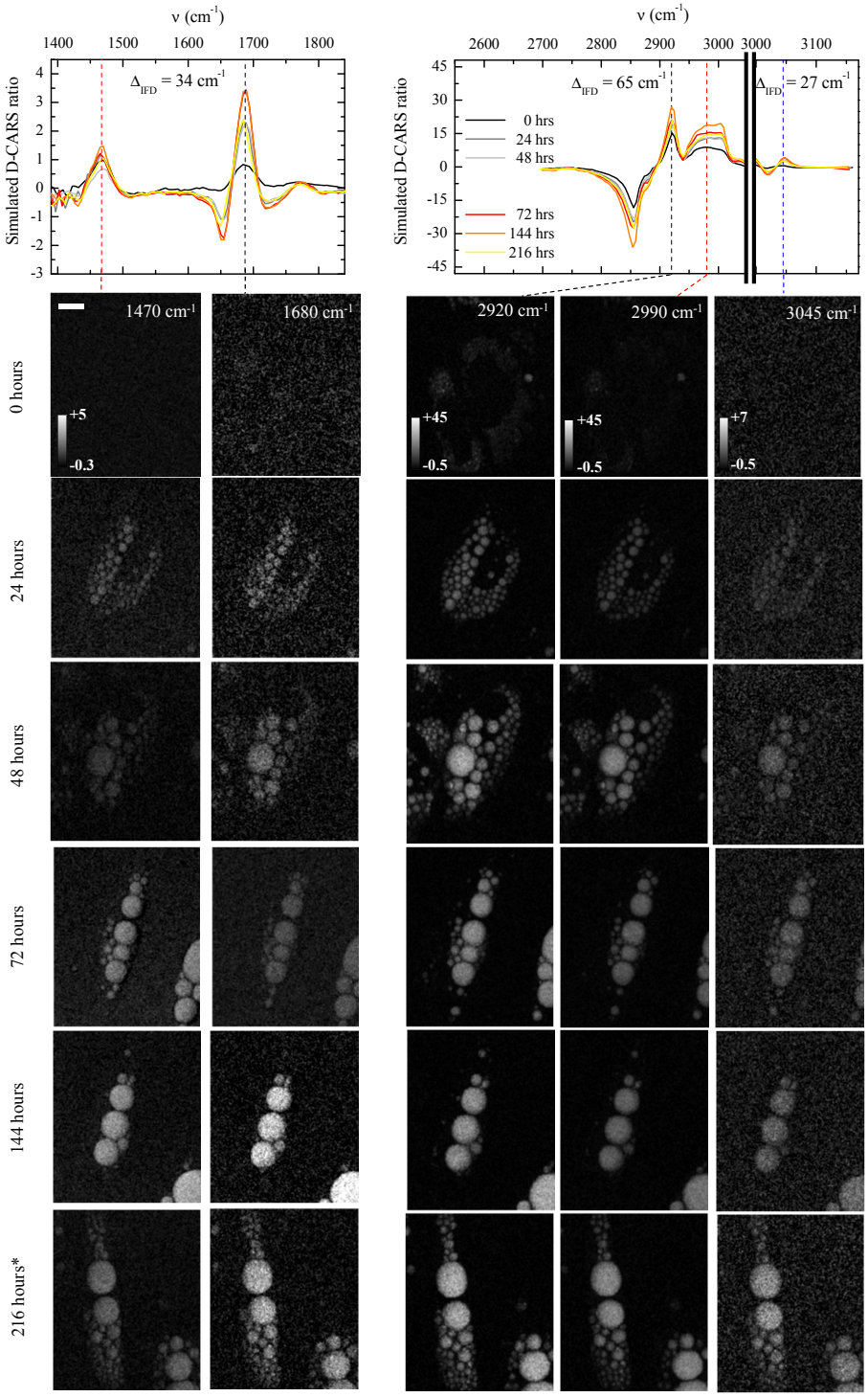

Figure 5.17: D-CARS IMAGING OF LIVING ADSCS CULTURED IN A MEDIA LOADED WITH AN EQUAL VOLUME MIXTURE OF OLEIC ACID AND α-LINOLENIC ACID. *Upper panels:* D-CARS spectra calculated from the measured CARS intensity ratios shown in Figure 5.12 with Δ_{IFD} as indicated. *Lower panels:* D-CARS images of adipocytes measured at the wavenumbers indicated by corresponding dotted lines at different time points. Grey scale as shown. Asterisk indicates different field of view from the previous one. Pump power on each pair 32 mW (20 mW), Stokes power on each pair 16 mW (10 mW) for the fingerprint region ("CH-stretch" region); 10 μs pixel dwell time, 0.3 μm pixel size; 20 μm scale bar.

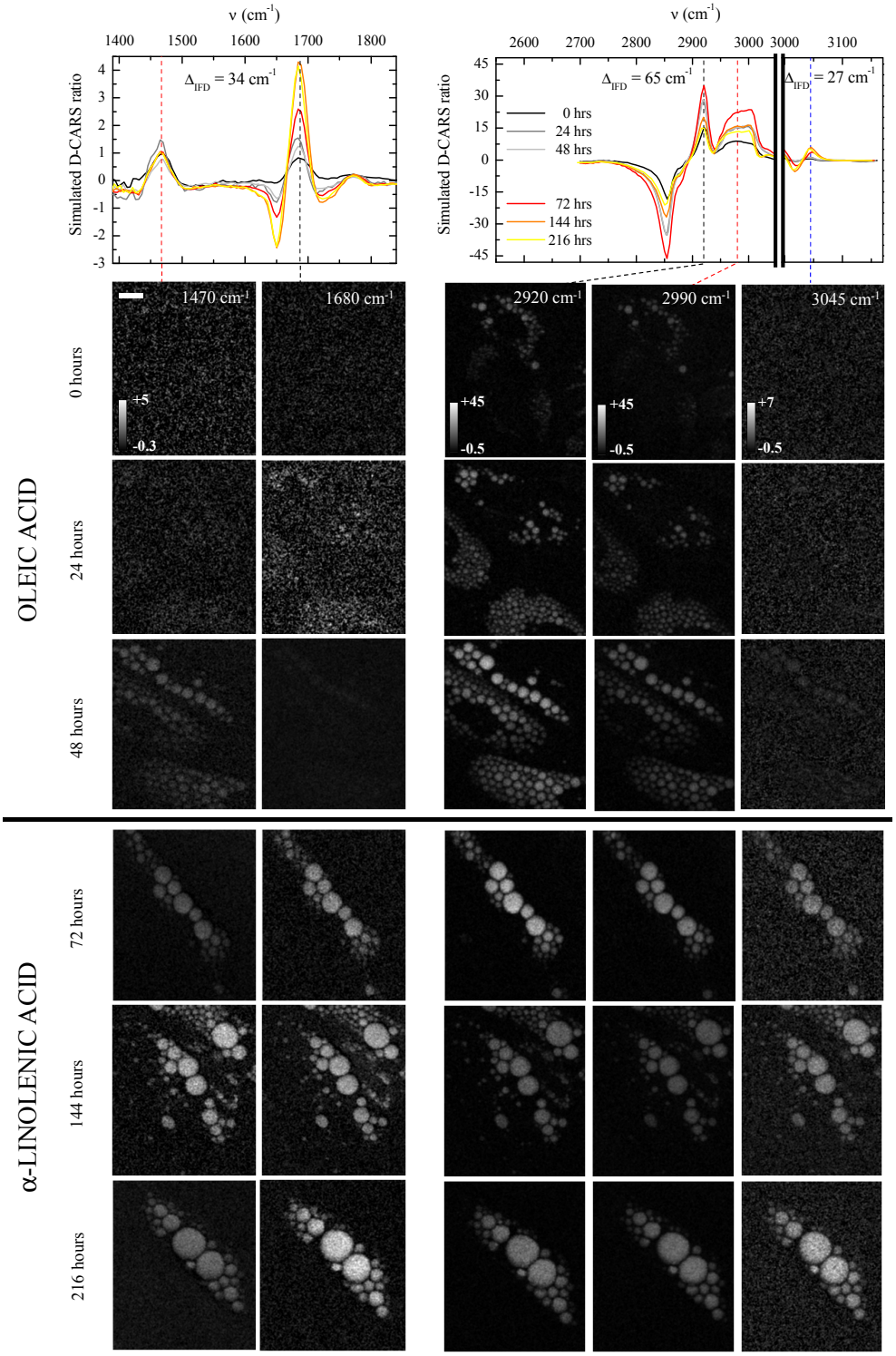

Figure 5.18: D-CARS IMAGING OF LIVING ADSCs FED INITIALLY WITH OLEIC ACID FIRST AND LATER WITH α-LINOLENIC ACID. *Upper panels:* D-CARS spectra calculated from the measured CARS intensity ratios shown in Figure 5.13 with Δ_{IFD} as indicated. *Lower panels:* D-CARS images of adipocytes measured at the wavenumbers indicated by corresponding dotted lines at different time points. Grey scale as shown. Pump power on each pair 32 mW (20 mW), Stokes power on each pair 16 mW (10 mW) for the fingerprint region ("CH-stretch" region); 10 μs pixel dwell time, 0.3 μm pixel size; 20 μm scale bar.

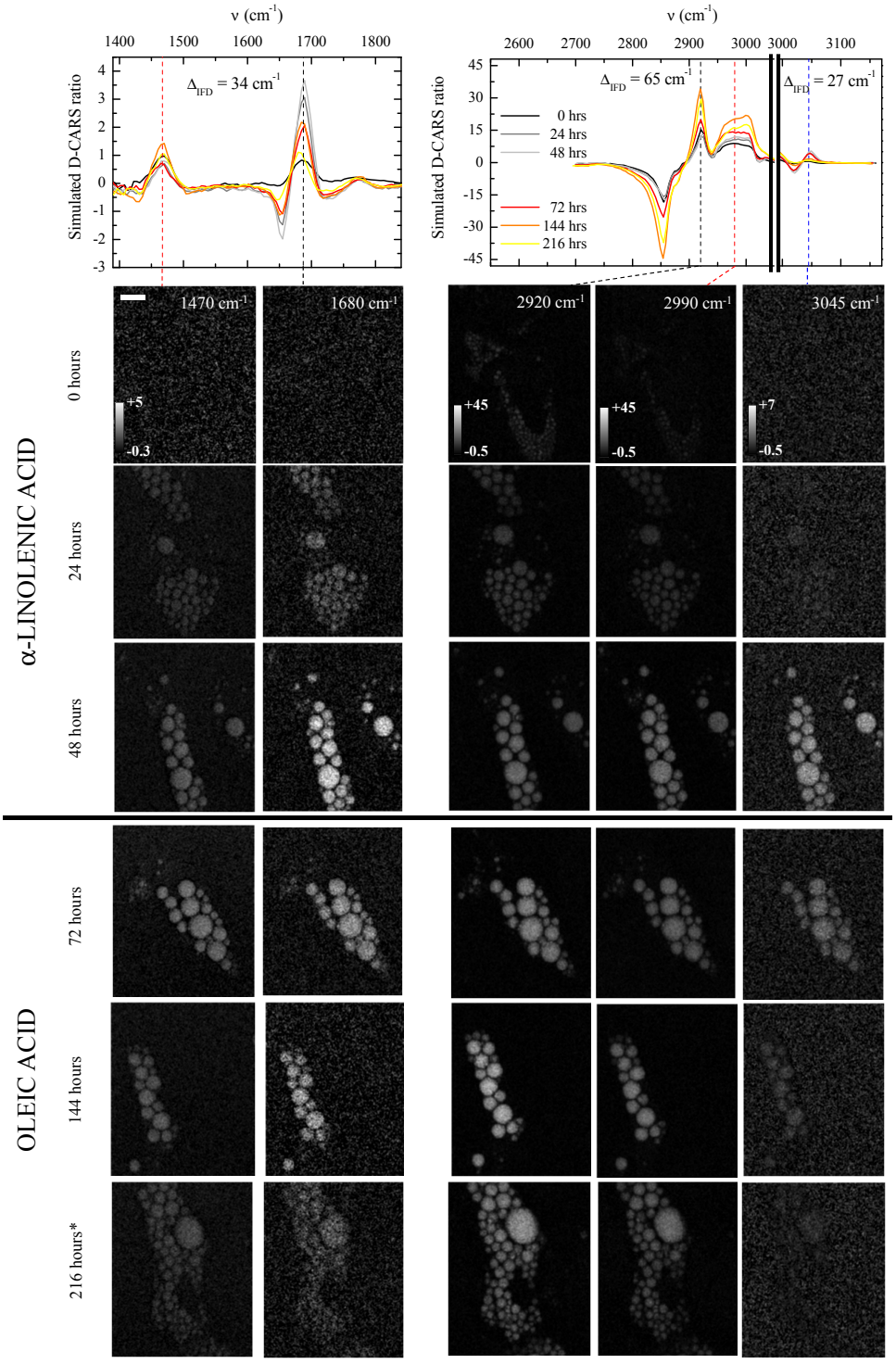

Figure 5.19: D-CARS IMAGING OF LIVING ADSCS FED INITIALLY WITH α-LINOLENIC ACID FIRST AND LATER WITH OLEIC ACID. *Upper panels:* D-CARS spectra calculated from the measured CARS intensity ratios shown in Figure 5.14 with Δ_{IFD} as indicated. *Lower panels:* D-CARS images of adipocytes measured at the wavenumbers indicated by corresponding dotted lines at different time points. Grey scale as shown. Asterisk indicates different field of view from the previous one. Pump power on each pair 32 mW (20 mW), Stokes power on each pair 16 mW (10 mW) for the fingerprint region ("CH-stretch" region); 10 μs pixel dwell time, 0.3 μm pixel size; 20 μm scale bar.

5.4.3 Ratiometric analysis of FSC^3 lipid components

As shown in the study on fixed ADSCs, the degree of unsaturation and molecular disorder within cytosolic LDs can be quantified through a ratiometric analysis. For living ADSCs we have therefore investigated how these parameters change over time. For each group of cells fed with a given set of lipid-supplemented media, we first determined the main lipid spectral component via the unsupervised FSC^3 analysis and then performed a ratiometric analysis on this component. Note that in the ratiometric analysis presented for fixed ADSCs we retrieved the susceptibility spectra and calculated spectral ratios as averages over more than 100 LDs. However this averaging procedure (which was manually done) is rather lengthy. Hence, here we chose to work directly with the main lipid component that has been extracted from the FSC^3 analysis and it represents the lipid spectrum overall without the need for spatial averaging.

For all samples, the overall cellular chemical composition has been represented via the unsupervised FSC^3 analysis in terms of 4 chemical species, namely the water-like culture media, the cell proteins, the lipid content and the image-artefact component. Their spectral profiles and spatial distributions (volume concentration units) are shown in Appendix B for the exemplifying case of a human ADSC that has been fed with linoleic acid-loaded media for 72 hours.
The FSC^3 spectral profiles for the lipid content only are shown in Figure 5.20 for each group of living cells cultured in the same conditions of lipid-supplemented media. Results in the fingerprint and in the "CH-stretch" region (left and right panels, respectively) confirm that the overall lipid content of cytosolic LDs changes with time and accordingly to the fatty acid type in the media. Changes in these spectral profiles over time are generally consistent with the observed changes in the spectral profiles of the retrieved susceptibilities on typical LDs as shown in the Figures of Section 5.4.1.

In order to quantitatively characterize these changes, a ratiometric analysis was applied to the FSC^3 values of each lipid profile at the $1450\,\mathrm{cm}^{-1}$, $1660\,\mathrm{cm}^{-1}$, $2855\,\mathrm{cm}^{-1}$, $2930\,\mathrm{cm}^{-1}$ and $3010\,\mathrm{cm}^{-1}$ bands. Results are shown in Figure 5.21 for each group of cells and each time point. Ratios of FSC^3 values between

1660 cm^{-1} and 1450 cm^{-1} bands reveal a change in the degree of unsaturation within LDs already within 24 hours from the addition of exogenous fatty acids to the media. The greatest variations are observed for cells fed with lipids with a high number of carbon-carbon double bonds (LA, LNA and MIX), while cells fed with oleic-acid supplemented media show a trend similar to the control cells, supporting the hypothesis of an oleic-acid-like component in the common differentiation media. After 48 hours, the degree of unsaturation remains very similar to that of the previous time point. After 72 hours, two different situations can be identified. For ADSCs that have been fed with the same lipid-supplemented media (LA, MIX and Control), the ratio remains constant within 8% percent for the next time points. For ADSCs that have been fed initially with one type of lipid and later with another, the ratio varies as a consequence. Specifically, cells originally fed with oleic acid-supplemented media show an increase in the ratio already after being incubated for 24 hours with α-linolenic acid. In the next time points, the ratio continues to increase but its value remains below the one achieved by ADSCs fed initially with α-linolenic acid. This suggests that LDs still retain an oleic acid content 168 hours after the lipid switch. Similarly, cells originally fed with α-linolenic acid-supplemented media show a decrease in the ratio after 24 hour incubation with oleic acid. The decrease continues in the next time points and, differently from the previous case, it reaches after 168 hours the same value as those cells that have been fed with oleic acid only. Ratios of FSC^3 values between 3010 cm^{-1} and 2850 cm^{-1} show trends over time for the degree of C=C unsaturation that are in agreement with the ones previously described. Similar observations can be deduced from the ratios of FSC^3 values between 2930 cm^{-1} and 2850 cm^{-1}. Time trends of molecular disorder within LDs are in general consistent with time trends for the degree of unsaturation.

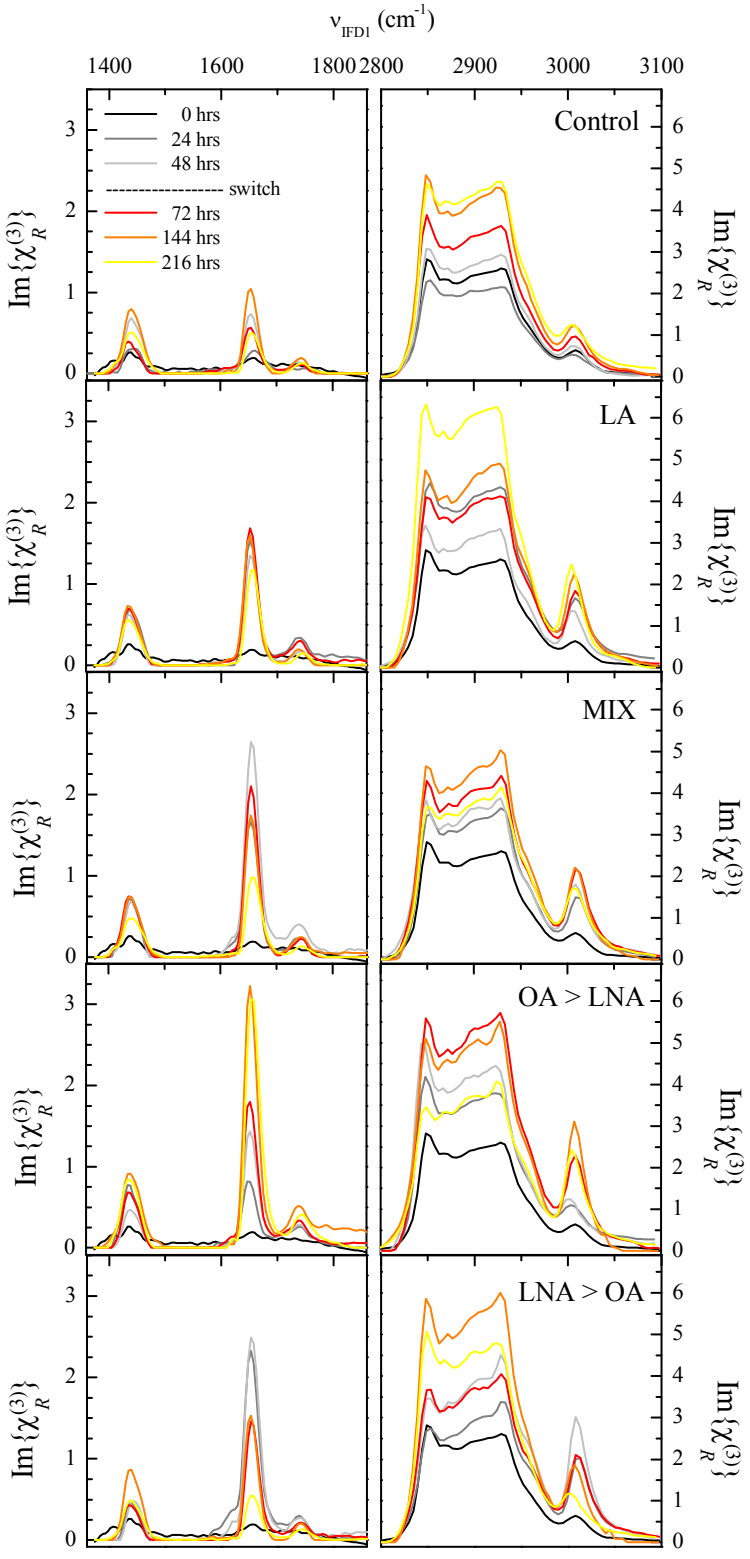

Figure 5.20: FSC^3 LIPID COMPONENTS FOR LIVING HUMAN ADSCS FED WITH FATTY ACIDS AS INDICATED. Components were obtained via FSC^3 analysis on single cell samples for 4 indicated components in the fingerprint (left panels) and in the "CH-stretch" (right panels) region.

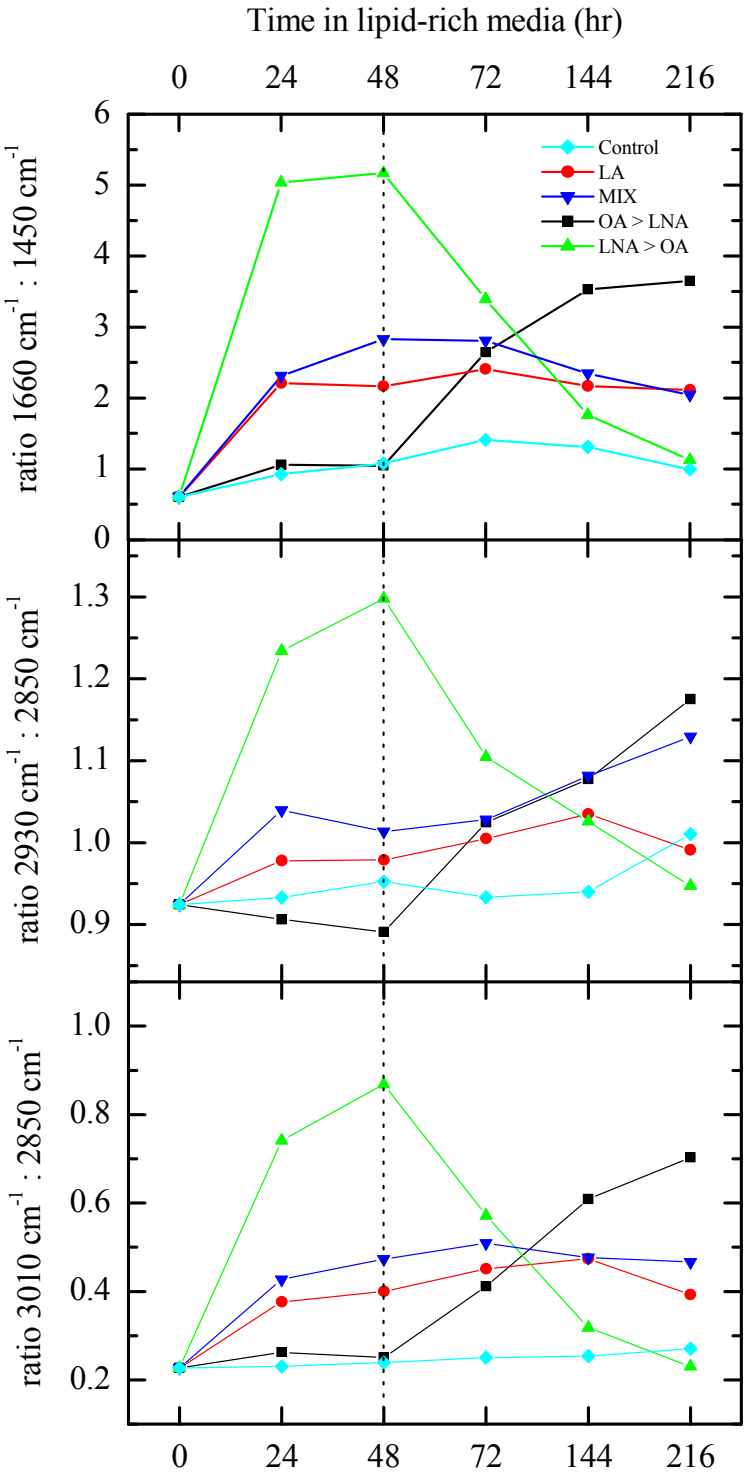

Figure 5.21: RATIOMETRIC ANALYSIS OF FSC^3 LIPID COMPONENT FOR LIVING HUMAN ADSCS FED WITH FATTY ACIDS AS INDICATED. Light blue rhombuses refer to control sample, red circles to LA samples, blue triangles to MIX samples, black squares to OA-LNA samples and green triangles to LNA-OA samples. *Upper panel:* Ratios of FSC^3 lipid components at 1660 cm^{-1} and 1450 cm^{-1}. *Middle panel:* Ratios of FSC^3 lipid components at 2930 cm^{-1} and 2850 cm^{-1}. *Lower panel:* Ratios of FSC^3 lipid components at 3010 cm^{-1} and 2850 cm^{-1}.

5.4.4 Quantitative chemical analysis using FSC^3: projection into pure lipid components

As shown in the previous Section, the FSC^3 method provides the susceptibility spectra of the lipid content within living ADSCs for each single time point. Similarly to the analysis performed on fixed ADSCs, it can be used to spatially resolve the distribution of the lipid content within the cellular environment at the corresponding single time point. The FSC^3 method can be also applied to temporal sets of hyperspectral data simultaneously. This has the advantage to visualize the changes affecting the lipid distribution over time on the basis of a common intensity scale and to track variations in the absolute volume concentrations of the lipid component.

The FSC^3 analysis has been therefore applied to the phase-retrieved temporal datasets of living cells cultured in the same conditions of lipid-supplemented media. Differently from the previous Section, the phase-retrieved hyperspectral information of the pure lipid component has also been included and accordingly weighed so that its statistical importance in the analysis is sufficiently high to identify that lipid type in the cellular environments. In the fingerprint region the overall cellular chemical composition has been represented in terms of 4 chemical species, namely the water-based media, two lipid contents (i.e. the lipid content in the cells before the addition of the lipid-supplemented media and the lipid content in the cells after the addition of the lipid-supplemented media) and a fourth component for image artefacts. In the "CH-stretch" region the overall chemical composition has been represented in terms of 3 chemical species, namely the water-based media and two lipid components. The analysis with 4 chemical species for this vibrational region showed that considering a fourth component either does not provide further relevant information to the chemical-quantitative analysis (see Appendix C) or it causes instabilities and lack of reproducible convergence in the FSC^3 algorithm.

FSC^3 results for living ADSCs fed with LA are shown in Figure 5.22 and 5.23 for the "CH-stretch" and the fingerprint region, respectively. The spectral profiles

and spatial distributions are shown for each chemical species and for each time point; time plots are also reported for the LA and GTO volume:volume concentrations taken at significant LDs as indicated in Figure 5.11. In the "CH-stretch" region, data show a progressive increase in the LA content of cytosolic LDs at the expense of the GTO content that, originally being the only lipid component at 0 hour, decreases in concentration in the following time points until it reaches a *plateau* at 72 hours after lipid addition. In the fingerprint region, images and plots confirm the increasing trend from 0 to 0.6 for the LA concentration. GTO concentration trend in the 24–216 hour interval is similar to the one from the "CH-stretch" region with the major difference being at the first time point. The very low lipid content and signal-to-noise ratio at 0 hour might be responsible for this discrepancy. As far as the fourth "free" component is concerned, we believe that it might account for spatial-spectral artefacts of the type described by Barlow *et al.*, considering its spectral profile and spatial distribution [120].

FSC^3 results for living ADSCs fed with an equal volume of oleic acid and α-linolenic acid (MIX) are shown in Figure 5.24 and 5.25 for the "CH-stretch" and the fingerprint region, respectively. Including in the analysis the single contribution of oleic acid and α-linolenic acid as pure lipids has permitted to discern these components in MIX and to investigate their concentration trends individually. In the "CH-stretch" region, data indicate an overall constant concentration at 0.4 for GTO and a significant increase in the concentration of α-GTL in the first 24 hours followed by a settlement around at 0.4. In the fingerprint region, results are in general in agreement with the trends in the "CH-stretch" region. However they seem affected by the low signal-to-noise ratio of this vibrational region, particularly in the first 48 hours when the GTO concentration shows the highest variations and the α-GTL concentration deviates from the 0.4 value at 24 hours.

FSC^3 results for living ADSCs fed initially with oleic acid and later with α-linolenic acid are shown in Figure 5.26 and 5.27 for the "CH-stretch" and the fingerprint region, respectively. In the "CH-stretch" region, data show a high concentration (0.7 circa) for GTO and a null concentration for α-GTL within LDs as expected from the type of lipid-supplemented media. After the switch to α-

linolenic acid, its presence as α-GTL starts to increase and it reaches a maximum concentration (0.6) after 168 hours. Simultaneously, GTO concentration decreases and it reaches a minimum at 0.2. Interestingly, this value is not null and it can be explained by presence of an oleic acid-like component in the normal differentiation media. Note also that with FSC^3 spatial dishomogeneities in the LD lipid content can be visually identified 24 hours after the media replacement (yellow dashed box showing different LDs in the same cell having different concentrations of GTO and α-GTL). In the fingerprint region, the time trend for the α-GTL concentration agrees with the results from the "CH-stretch" region. The GTO concentration also follows a consistent trend but it shows major deviations in the last two time points. This might be due to the lower intensity of GTO signal compared to the α-GTL signal which can complicate the FSC^3 retrieval of the GTO component.

FSC^3 results for living ADSCs fed initially with α-linolenic acid and later with oleic acid are shown in Figure 5.28 and 5.29 for the "CH-stretch" and the fingerprint region, respectively. As for the previous sample, changes in the lipid component according to the media are evident. In the "CH-stretch" region, the high GTO concentration at time point 0 is rapidly substituted by an equally high α-GTL concentration which increases in the next 24 hours and, after the switch to oleic acid-loaded media, it drops down until it becomes almost null. Note that, also in this sample, LDs with different lipid content are visible at the cell periphery 24 hours after the lipid replacement (yellow dashed box). In the fingerprint region, concentration trends are in good agreement with the above results although they are characterized by less high values.

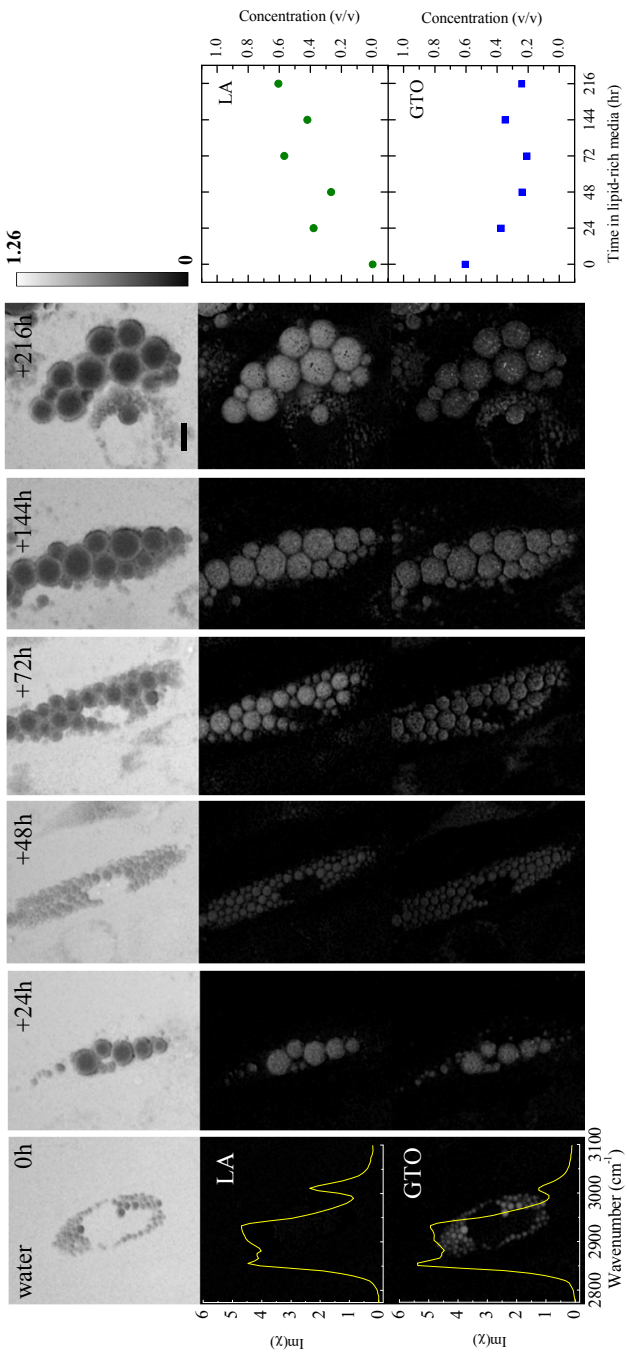

Figure 5.22: RESULTS OF FSC^3 ON THE PHASE-RETRIVED IM$\{\chi_R^{(3)}\}$ IN LIVING ADSCS FED WITH LINOLEIC ACID FOR THE "CH-STRETCH" REGION. *Left:* Spatial distributions of the volume concentration at different time points for the 3 components considered in the analysis. Gray scale as indicated. Scale bar is 20 μm. Spectra of Im$\{\chi_R^{(3)}\}$ also reported for the lipid content. *Right:* Absolute concentrations of LA and GTO over time taken at a specific LD as indicated in Figure 5.11.

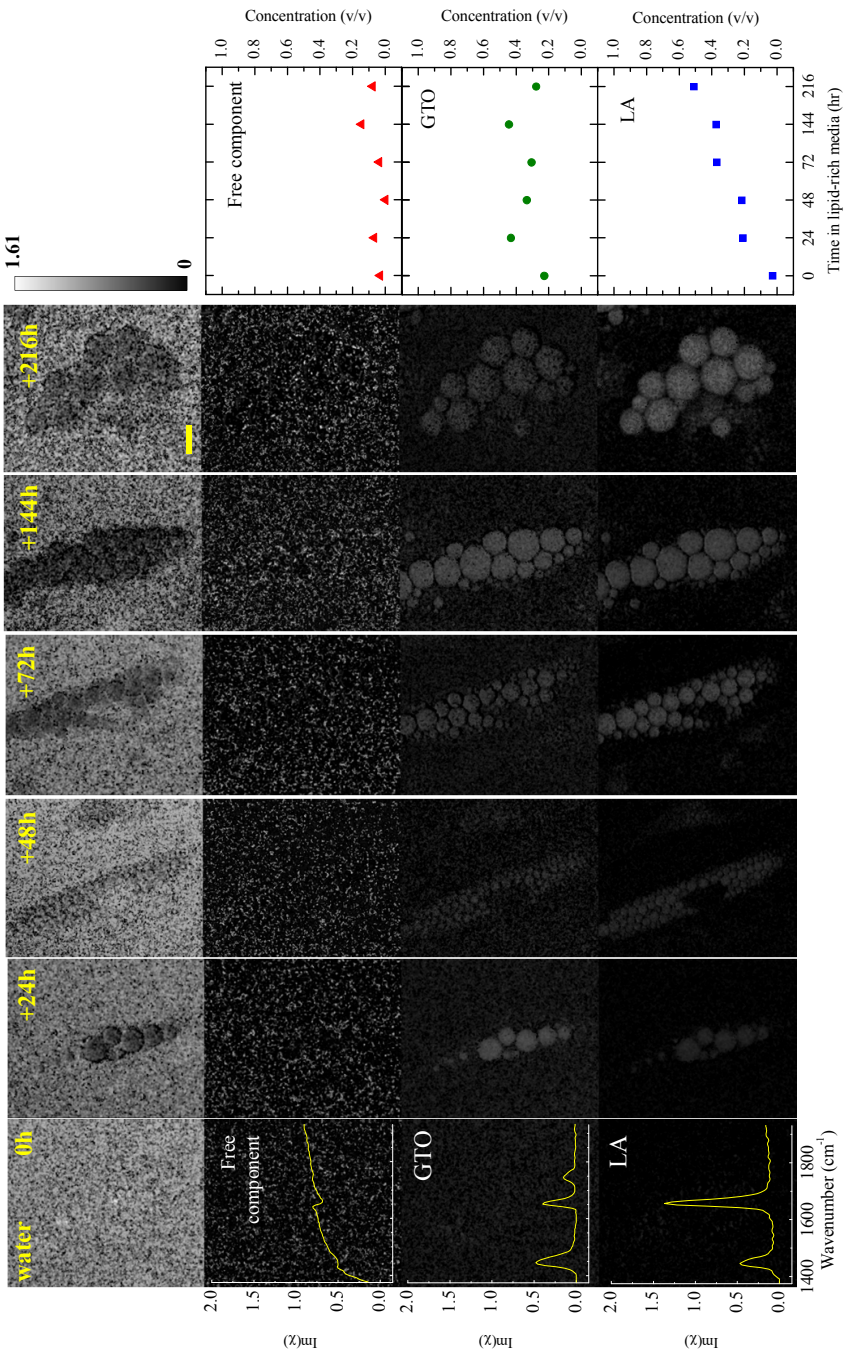

Figure 5.23: RESULTS OF FSC^3 ON THE PHASE-RETRIVED IM$\{\chi_R^{(3)}\}$ IN LIVING ADSCS FED WITH LINOLEIC ACID FOR THE FINGERPRINT REGION. *Left:* Spatial distributions of the volume concentration at different time points for the 4 components considered in the analysis. Gray scale as indicated. Scale bar is 20 μm. Spectra of IM$\{\chi_R^{(3)}\}$ also reported for the lipid content. *Right:* Absolute concentrations of LA and GTO over time taken at a specific LD as indicated in Figure 5.11.

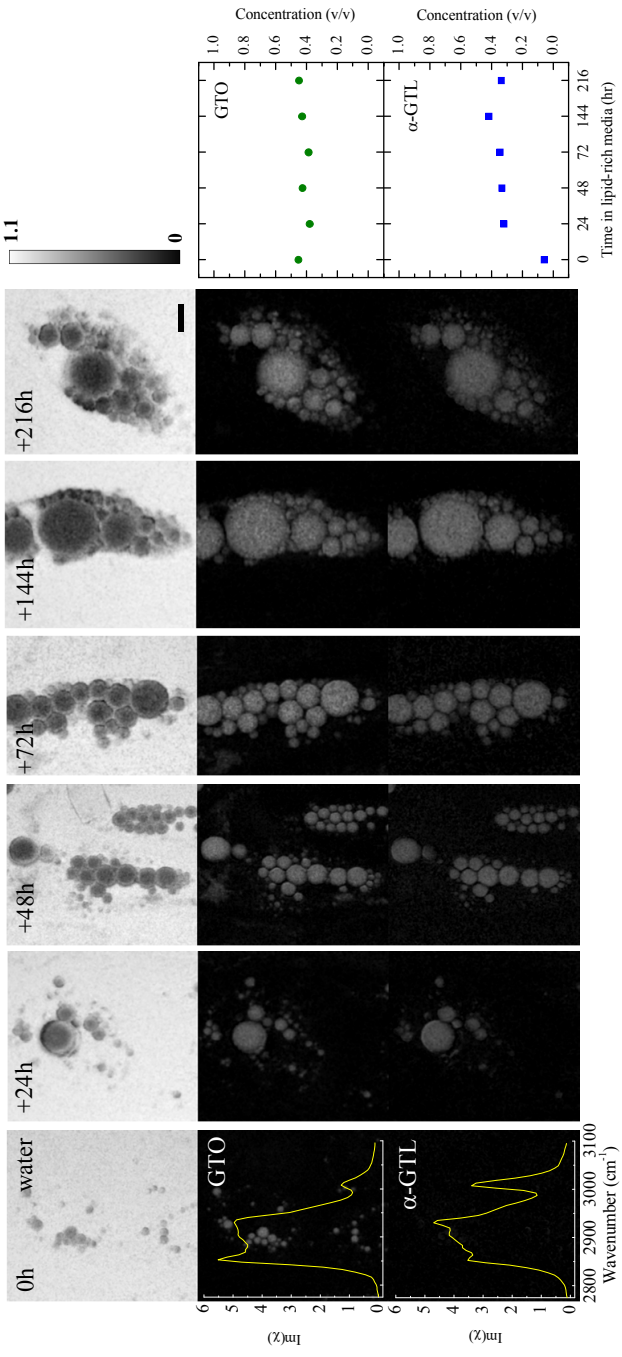

Figure 5.24: RESULTS OF FSC^3 ON THE PHASE-RETRIVED IM$\{\chi_R^{(3)}\}$ IN LIVING ADSCS FED WITH AN EQUAL VOLUME MIXTURE OF OLEIC AND α-LINOLENIC ACID FOR THE "CH-STRETCH" REGION. *Left:* Spatial distributions of the volume concentration at different time points for the 3 components considered in the analysis. Gray scale as indicated. Scale bar is 20μm. Spectra of Im$\{\chi_R^{(3)}\}$ also reported for the lipid content. *Right:* Absolute concentrations of GTO and α-GTL over time taken at a specific LD as indicated in Figure 5.12.

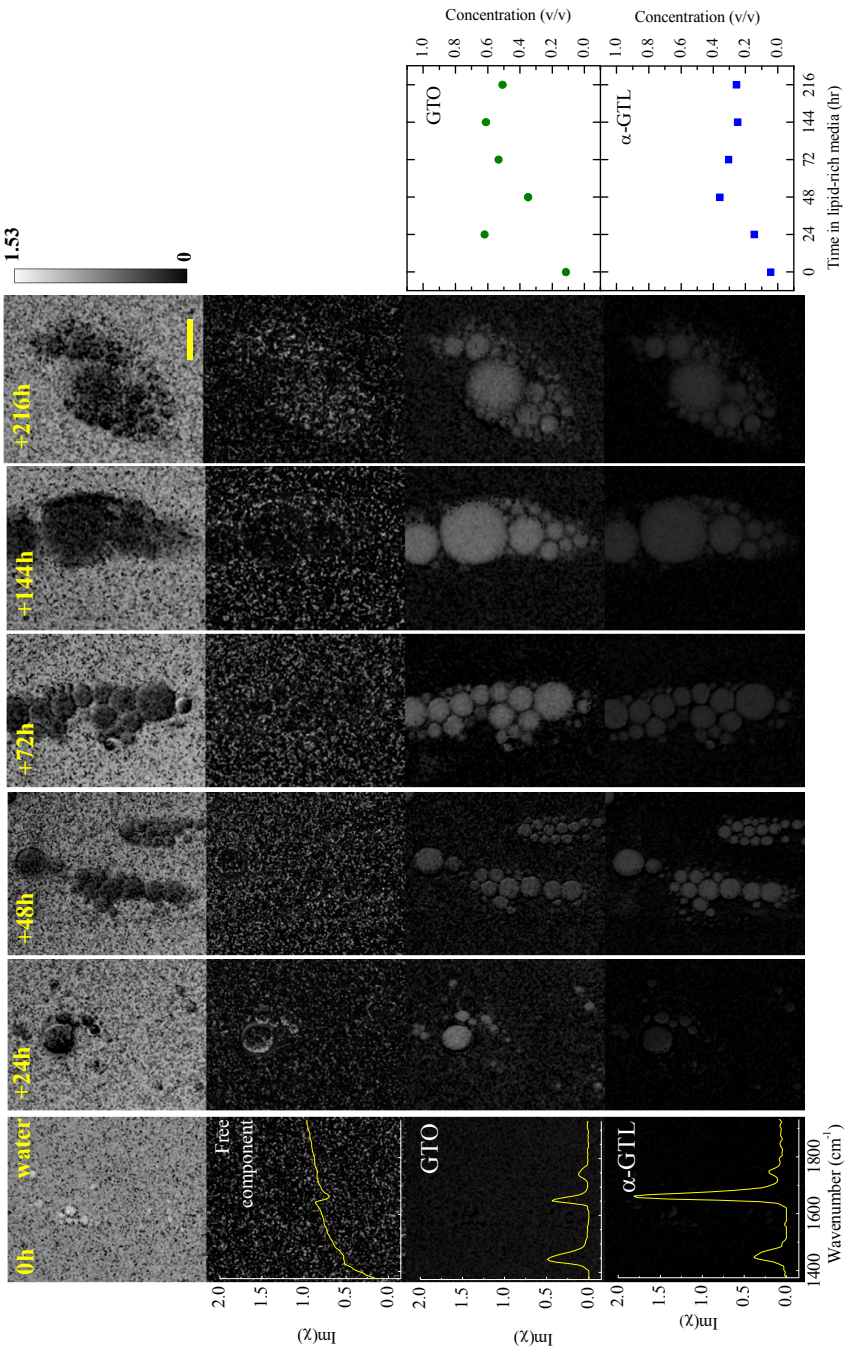

Figure 5.25: RESULTS OF FSC^3 ON THE PHASE-RETRIVED IM$\{\chi_R^{(3)}\}$ IN LIVING ADSCS FED WITH AN EQUAL VOLUME MIXTURE OF OLEIC AND α-LINOLENIC ACID FOR THE FINGERPRINT REGION. *Left:* Spatial distributions of the volume concentration at different time points for the 4 components considered in the analysis. Gray scale as indicated. Scale bar is 20μm. Spectra of Im$\{\chi_R^{(3)}\}$ also reported for the lipid content. *Right:* Absolute concentrations of GTO and α-GTL over time taken at a specific LD as indicated in Figure 5.12.

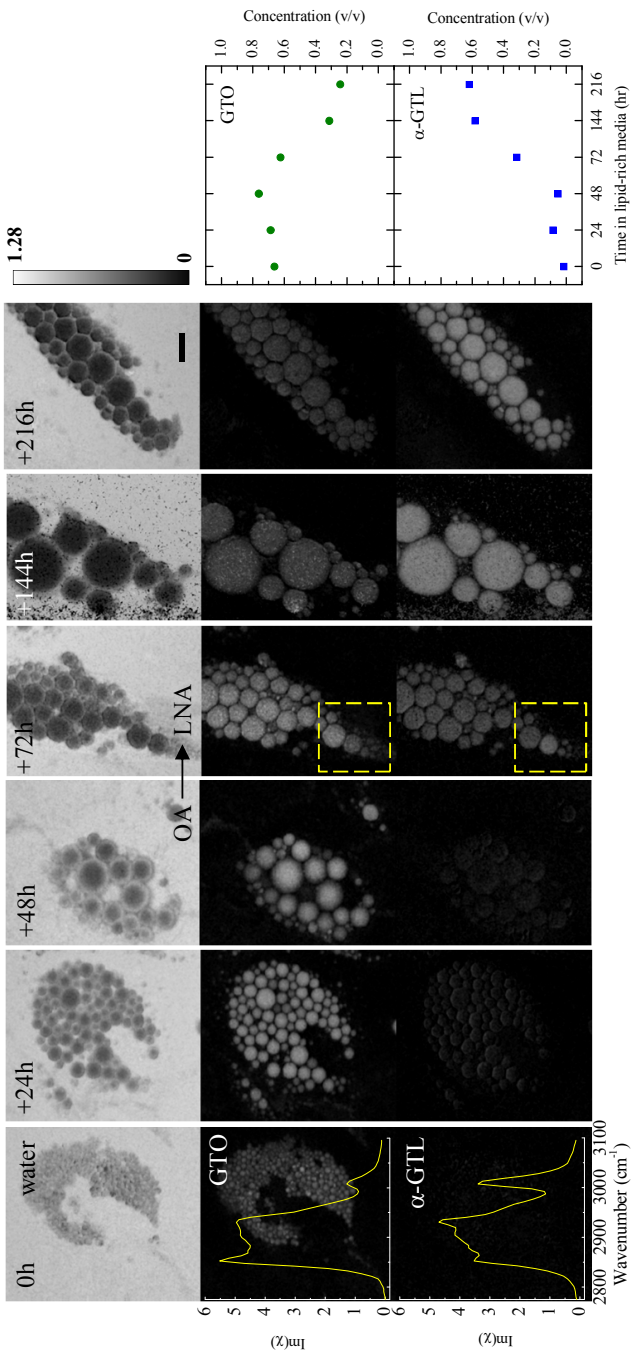

Figure 5.26: RESULTS OF FSC^3 ON THE PHASE-RETRIVED Im$\{\chi_R^{(3)}\}$ IN LIVING ADSCS FED INITIALLY WITH OLEIC ACID AND LATER WITH α-LINOLENIC ACID FOR THE "CH-STRETCH" REGION. *Left:* Spatial distributions of the volume concentration at different time points for the 3 components considered in the analysis. Regions with different lipid content in the same field of view are enclosed in yellow dotted boxes. Gray scale as indicated. Scale bar is 20 μm. Spectra of Im$\{\chi_R^{(3)}\}$ also reported for the lipid content. *Right:* Absolute concentrations of GTO and α-GTL over time taken at a specific LD as indicated in Figure 5.13.

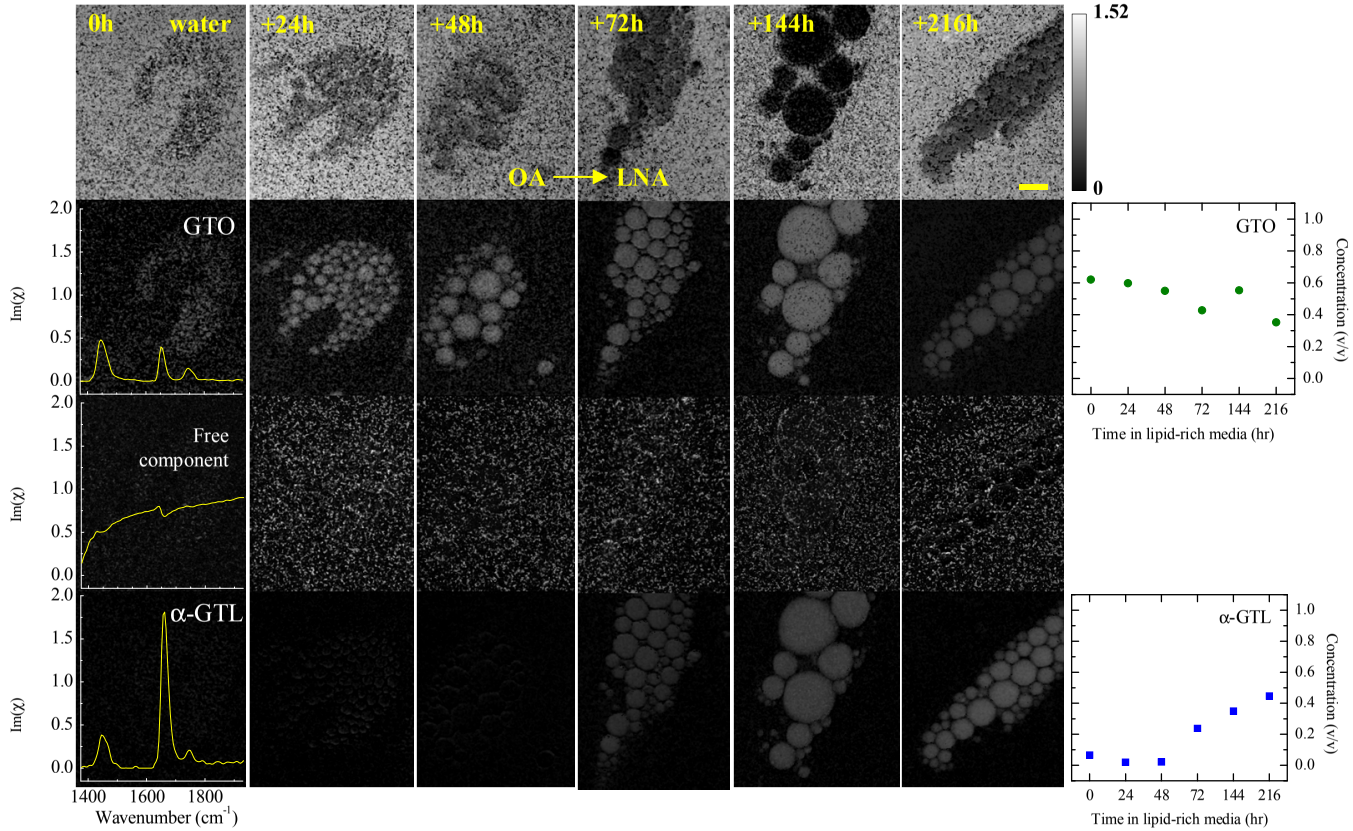

Figure 5.27: RESULTS OF FSC^3 ON THE PHASE-RETRIVED IM$\{\chi_R^{(3)}\}$ IN LIVING ADSCS FED INITIALLY WITH OLEIC ACID AND LATER WITH α-LINOLENIC ACID ACID FOR THE FINGERPRINT REGION. *Left:* Spatial distributions of the volume concentration at different time points for the 4 components considered in the analysis. Regions with different lipid content in the same field of view are enclosed in yellow dotted boxes. Gray scale as indicated. Scale bar is 20 μm. Spectra of Im$\{\chi_R^{(3)}\}$ also reported for the lipid content. *Right:* Absolute concentrations of GTO and α-GTL over time taken at a specific LD as indicated in Figure 5.13.

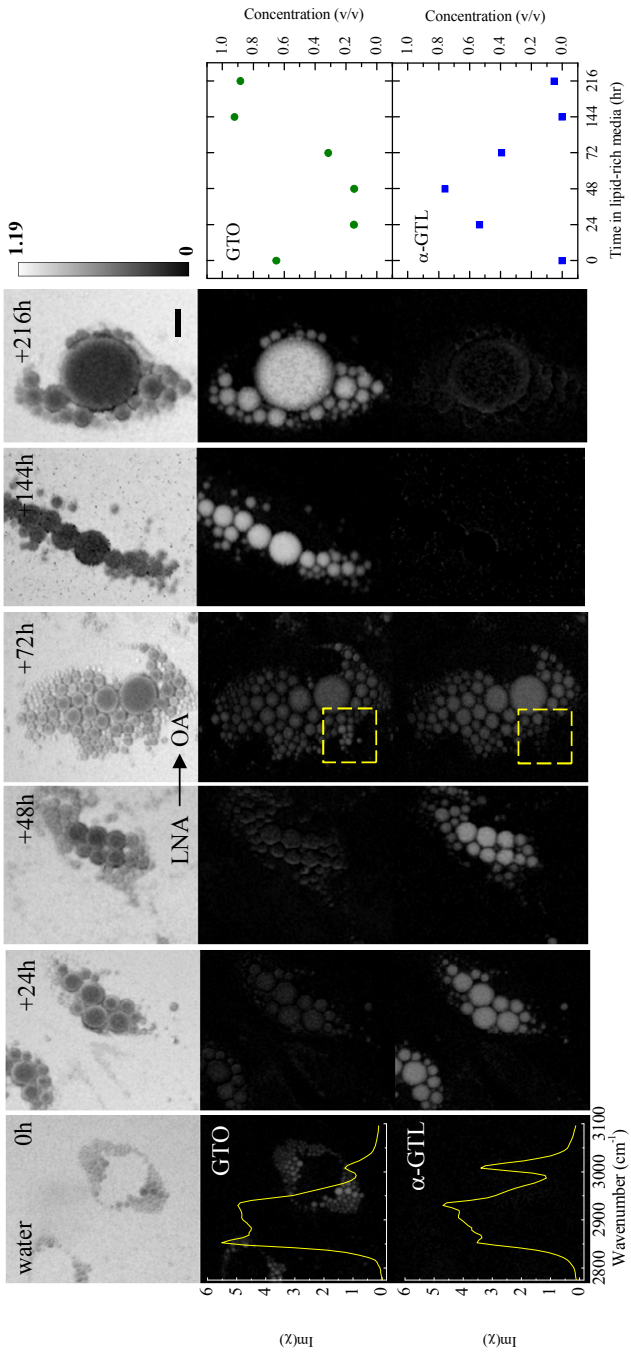

Figure 5.28: RESULTS OF FSC^3 ON THE PHASE-RETRIVED IM$\{\chi_R^{(3)}\}$ IN LIVING ADSCS FED INITIALLY WITH α-LINOLENIC ACID AND LATER WITH OLEIC ACID FOR THE "CH-STRETCH" REGION. *Left:* Spatial distributions of the volume concentration at different time points for the 3 components considered in the analysis. Regions with different lipid content in the same field of view are enclosed in yellow dotted boxes. Gray scale as indicated. Scale bar is 20 μm. Spectra of Im$\{\chi_R^{(3)}\}$ also reported for the lipid content. *Right:* Absolute concentrations of GTO and α-GTL over time taken at a specific LD as indicated in Figure 5.14.

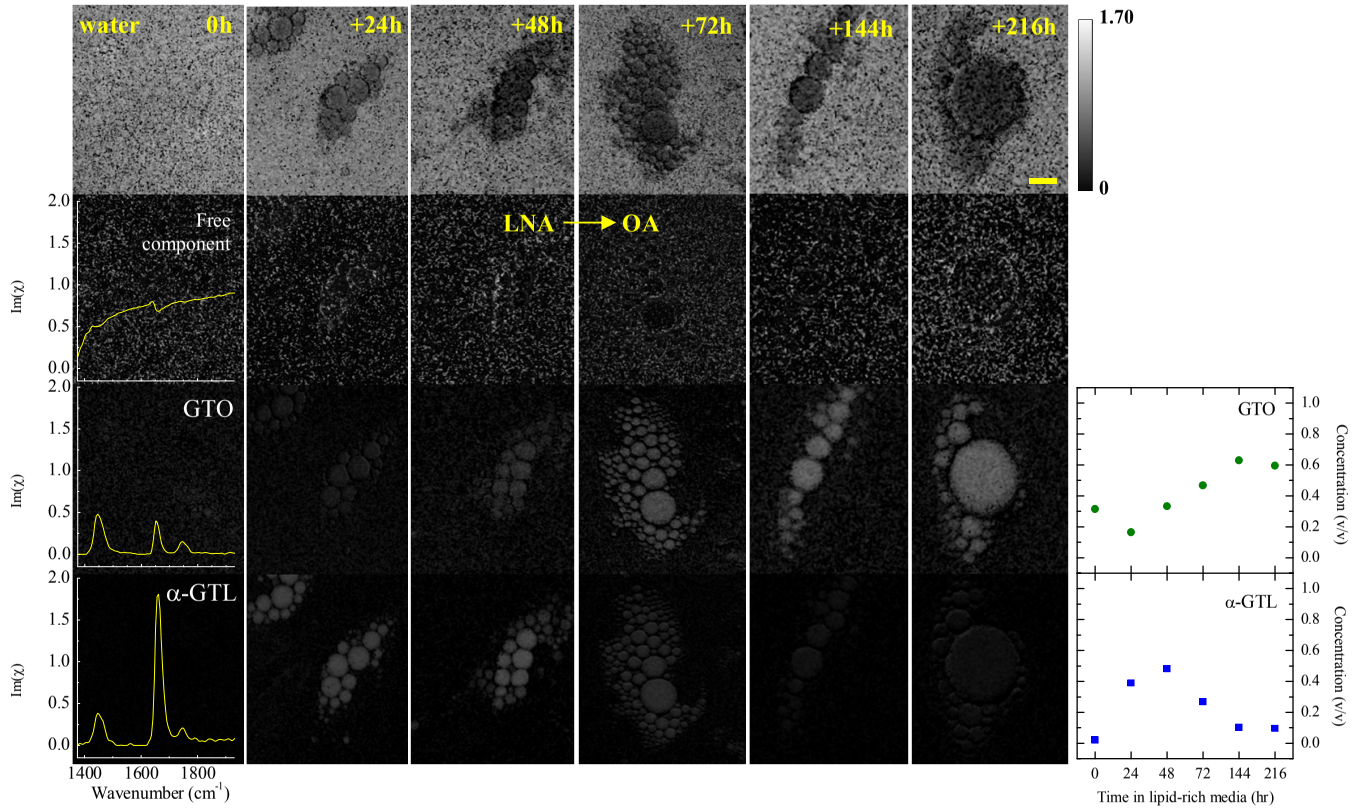

Figure 5.29: RESULTS OF FSC^3 ON THE PHASE-RETRIVED IM$\{\chi_R^{(3)}\}$ IN LIVING ADSCS FED INITIALLY WITH α-LINOLENIC ACID AND LATER WITH OLEIC ACID ACID FOR THE FINGERPRINT REGION. *Left:* Spatial distributions of the volume concentration at different time points for the 4 components considered in the analysis. Regions with different lipid content in the same field of view are enclosed in yellow dotted boxes. Gray scale as indicated. Scale bar is 20 μm. Spectra of Im$\{\chi_R^{(3)}\}$ also reported for the lipid content. *Right:* Absolute concentrations of GTO and α-GTL over time taken at a specific LD as indicated in Figure 5.14.

5.4.5 Summary

Live human stem-cell derived adipocytes cultured in media enriched with fatty acids (oleic acid, linoleic acid, α-linolenic acid and an equal volume mixture of oleic acid and α-linolenic acid) have been investigated. We verified the ability of CARS and hyperspectral CARS to discriminate different lipid contents over time in cytosolic LDs developed in living cellular environments. Moreover, phase-retrieved hyperspectral CARS images have been analysed via the factorization into concentrations of chemical components (FSC^3) method to extrapolate quantitative information on the lipid content within LDs.

Results indicate that, as in the study on fixed ADSCs, different lipid compositions can be distinguished in live cells by fast D-CARS images or long CARS hyperspectral images with the latter being more disrupting to cell survival. However, when analysed with the FSC^3 method, CARS hyperspectral images enabled us to derive the spatial distribution and the volume concentration of individual chemical components. In particular it permitted to extrapolate time-dependent trends for the lipid content of LDs in live cells and to study how these trends change in relation to the fatty acids loaded into the culture media.

5.5 Explorative studies on protein-lipid interaction processes

The results presented in the previous Section provide interesting insights on the response of human ADSC to the presence of lipid-loaded differentiation media. Specifically, the application of the FSC^3 method has allowed the quantification of the concentration values and spatial distribution of chemically-different lipid components for cytosolic LDs in live cellular environments. An important next step in the study of lipid intake and accumulation would be the identification of the mechanisms responsible for the regulation of these processes. For instance, a recent study indicates that Rab18, a membrane-trafficking protein, is likely to be involved in mobilizing the fatty acids stored in LDs [69]. Another study shows that Exo2, a small-molecule inhibitor, stimulates Golgi-ER fusion in mammalian cells [70]. Since LDs seem to originate from the ER, the presence of Exo2 might affect lipid accumulation in LDs.

In this section an initial exploratory study on the effects of Rab18 and Exo2 on live ADSCs is reported. CARS hyperspectral images were acquired in the "CH-stretch" region before and after transfection, and they were analysed by the FSC^3 method. ADSCs were prepared as indicated in the Materials and Methods chapter (Section 3.2.2).

5.5.1 Effects of Rab18 on adipocytes

Rab18 is a member of the Rab GTPase family which plays a fundamental role in the membrane trafficking between intracellular compartments as it manages the formation, motility, targeting and fusion of membrane-bound secretory cargo carriers [127]. In particular, Rab18 is involved in many cellular processes such as lipid storage/breakdown in LDs and membrane trafficking between ER and Golgi complex. It has been shown, for instance, that Rab18 brings LDs into the proximity of ER-derived membranes and it might be therefore involved in lipid transportation processes between the two organelles [69]. There are also

evidences that Rab18 association to LDs increases when lipolysis is stimulated, suggesting a connection with the metabolic state of single LDs [128]. Furthemore, Rab18-LD association has been shown to be selective, i.e. Rab18 is expressed in sub-populations of the LD assembles, and this might be due to the different LD regulations and/or functions within the cellular environment [129].

Fluorescence and electron microscopy studies on 3T3-L1 revealed that Rab18 directly associates with the exterior monolayer of LDs [129]. Figure 5.30 confirms this association for human ADSCs that had been cultured in standard differentiation media for 12 days and had been transfected with GFP(green fluorescent protein)-tagged Rab18 on day 12. Simultaneous TPF (of the GFP-tagged protein) and CARS image acquisition across cell mid-plane is shown with CARS acquired using pair Π_1 tuned at the $2855\,\mathrm{cm}^{-1}$ frequency (left panel). Small cytosolic LDs are visible from the CARS image and are color-coded as red dots; the presence of Rab18 is identifiable from the TPF image and is color-coded as green circles. This is due to the image acquisition through the middle plane of the cells. Figure 5.30 also shows the results of the unsupervised FSC^3 analysis (centre and right panel) on hyperspectral CARS images that have been acquired in the "CH-stretch" region and in correspondence of cells' middle plane.

This study proves the correlative CARS/TPF ability of our set-up on live cell samples and sets a starting point for future research of this kind. For instance, cells overexpressing GFP-tagged Rab18 could be tracked over time via TPF and quantitatively characterized in their lipid component through the acquisition of hyperspectral CARS images at specific time points. This would help to reveal whether and eventually how the LD content is influenced by Rab18 overexpression.

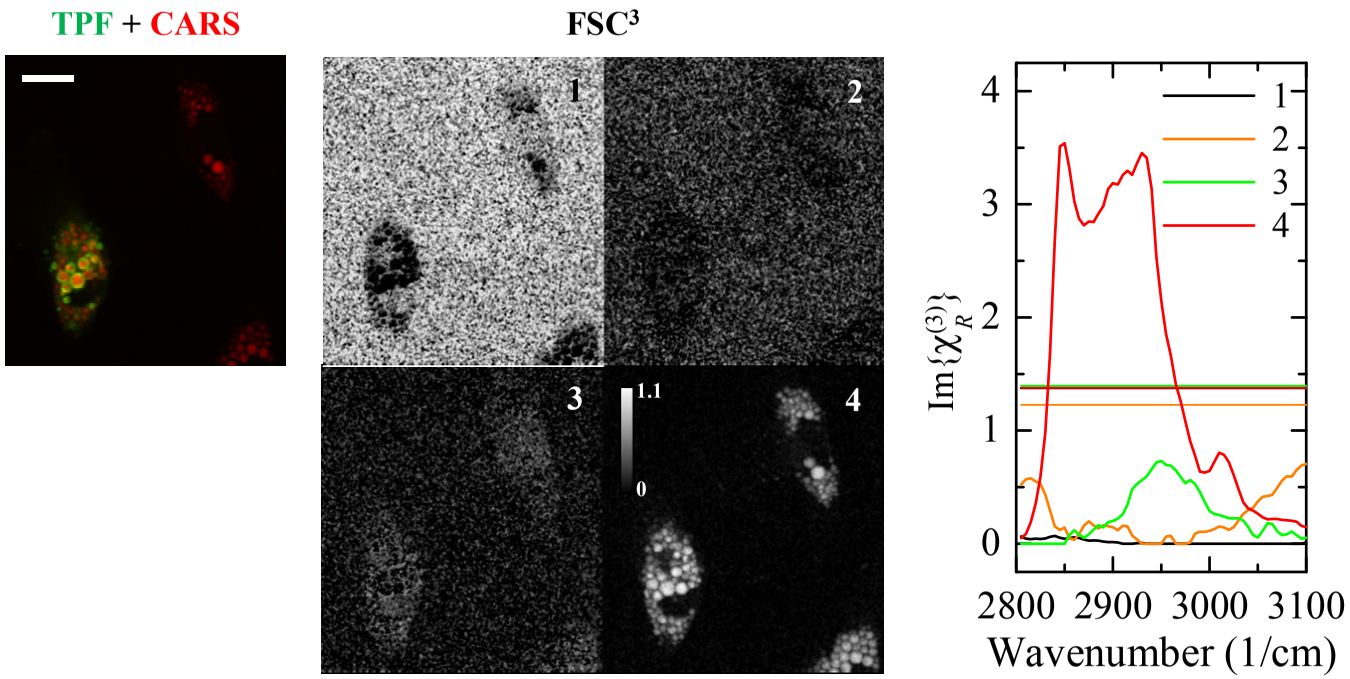

Figure 5.30: TPF AND CARS OF GFP-TAGGED RAB18 MEMBRANE-TRAFFICKING PROTEIN ON LIVE HUMAN ADSCS CULTURED IN CONTROL DIFFERENTIATION MEDIA. *Left:* False colour image of TPF from green-fluorescent-labelled Rab18 protein (green) and CARS from cytosolic LDs at 2850 cm^{-1} (red). The scale bar indicates 20 μm. *Centre:* FSC^3 spatial distributions of the volume concentration on a gray scale from 0 (black) to 1.1 (white) for the 4 components considered in the analysis. *Right:* Spectra of $\mathrm{Im}\{\chi_R^{(3)}\}$ and its real part (horizontal lines) for the corresponding components. TPF, pump and Stokes power on the sample were 7 mW, 16 mW and 8 mW, respectively; 20x 0.75NA objective, 10 μs pixel dwell time and 0.3 μm pixel size.

5.5.2 Effects of Exo2 on adipocytes

Exo2 (4-hydroxy-3-methoxy-(5,6,7,8-tetrahydrol[1]benzothieno[2,3-d]pyrimidin-4-yl)hydraz-one benzaldehyde) is a molecule that severely affects the endomembrane system [70]. Specifically, Exo2 has been reported to inhibit the secretory pathway in mammalian cells as it prevents secretory cargos from leaving the ER and it disrupts the *trans*-Golgi network, not directing proteins to the appropriate cellular destination. The precise target of Exo2 is still to be identified [70].

Studies on normal rat kidney (NRK) epithelial cells incubated in oleic acid-loaded media and treated with Exo2 showed that the disruption of the Golgi apparatus does not affect the number or size of LDs [130]. Contrary to this result, previous work done within our lab (Dr. Peter Watson and co-workers) suggests that Exo2 at high concentrations (150 μM) can induce LD fusion. In both cases, the effects of Exo2 were assessed via fluorescent microscopy. In this preliminary study, instead, hyperspectral CARS has been employed as non-invasive quantitative technique to confirm LD fusion at high Exo2 concentration and to identify possible changes in the lipid composition. Samples of human ADSCs had been cultured in standard differentiation media and linoleic acid-enriched media for 12 days after induction to differentiation, and had been treated with Exo2 on day 12.

Figures 5.31 and 5.32 show correspondently an unsupervised FSC^3 analysis in terms of 4 chemical species, namely the water-based medium, the main lipid component, the protein content and a component likely due to image artefacts. Comparison between images before and after the treatment with Exo2 reveals that the droplets' lipid composition has not changed but their number has decreased after treatment, respectively both in the control case and in cells cultured with media supplemented with linoleic acid. This result confirms that a fusion process occurs among LDs. The reason behind it however is still unknown. Different scenarios are possible. For example, the disruption of the Golgi apparatus due to Exo2 might prevent protein(s) delegated in the control of LD volume from reaching LD surface and therefore preventing droplet fusion. Alternatively, Exo2 might have a destabilising effect on the LD membrane, i.e. it directly disrupts the phospholipid coating or it deactivates a protein that has a critical role in maintaining

LD volume.

Moreover, the effect of Exo2 does not seem to depend on the type of lipid stored in the LDs. In order to gain further insights on this point, the effect of Exo2 could be investigated on ADSCs where a lipid-enriched medium has been switched with a medium of different lipid composition and LDs with mixed and inhomogeneous lipid compositions are present within the same cell (as described in Section 5.4.4). Combined with the FSC^3 method, these studies could help to reveal whether fusion may occur between LDs of different content and what composition may result from it.

Figure 5.31: RESULTS OF FSC^3 ON THE PHASE-RETRIVED IM$\{\chi_R^{(3)}\}$ IN LIVE HUMAN ADSCS CULTURED IN STANDARD DIFFERENTIATION MEDIA BEFORE AND AFTER TREATMENT WITH EXO2. *Left:* Spatial distributions of the volume concentration on a gray scale from 0 (black) to 1.1 (white) for the 4 components considered in the analysis. RGB overlays show the spatial distribution of the concentration for specific components as indicated. *Right:* Spectra of Im$\{\chi_R^{(3)}\}$ and its real part (horizontal lines) for the corresponding components. The red dotted line is the Raman spectrum of OA scaled to overlay the phase-retrieved intensity of the main lipid component within LDs. The scale bar indicates 20 μm. Pump power on each pair 10 mW, Stokes power on each pair 5 mW, 10 μs pixel dwell time, 0.3 μm pixel size.

Figure 5.32: RESULTS OF FSC^3 ON THE PHASE-RETRIVED IM$\{\chi_R^{(3)}\}$ IN HUMAN ADSCS CULTURED IN LINOLEIC ACID-LOADED CONTROL MEDIA BEFORE AND AFTER TREATMENT WITH EXO2. *Left:* Spatial distributions of the volume concentration on a gray scale from 0 (black) to 1.1 (white) for the 4 components considered in the analysis. RGB overlays show the spatial distribution of the concentration for specific components as indicated. *Right:* Spectra of Im$\{\chi_R^{(3)}\}$ and its real part (horizontal lines) for the corresponding components. The red dotted line is the Raman spectrum of OA scaled to overlay the phase-retrieved intensity of the main lipid component within LDs. The scale bar indicates 20 μm. Pump power on each pair 10 mW, Stokes power on each pair 5 mW, 10 μs pixel dwell time, 0.3 μm pixel size.

6 Conclusions

6.1 Thesis summary

In this thesis the applicability of two specific implementations of Coherent Anti-Stokes Raman scattering microscopy, namely dual-frequency/differential CARS and hyperspectral CARS micro-spectroscopy, has been demonstrated for the label-free chemically sensitive rapid imaging of lipid droplets (LDs).

In **Chapter 1** the scientific motivation of the thesis is presented. LDs, the main site of fats storage in cells, are nowadays recognized as active organelles within the cellular machinery. Beyond their role as pure energy reservoir, the recently-discovered involvement in lipid metabolism, cell signaling and inflammation has set a fresh start to the research in LD dynamics and interaction. In fact several questions are waiting to be answered, especially about the biogenesis and the composition of LDs in cells. Regarding the composition, LDs are known to include a core full of triglycerides and be enclosed by a phospholipid monolayer and a protein coating. The type of triglycerides within LDs is highly diverse and, for cells in the adipose tissue (the main fat reservoir in the human body), is characterized by fatty acids of different lengths and of different degree of unsaturation. Although the main lipid components of the adipose tissue have been quantified by means of biochemical methods on cell extracts, it is still unknown if and how individual LDs inside living cells spatially partition different lipid types and how this relates to their metabolic function. It is within this context that the CARS technique can offer a significant contribution owing to its label-free non-invasiveness,

high-speed imaging capability, the sub-micron three-dimensional spatial resolution and the intrinsic chemical specificity.

In **Chapter 2** the theoretical background of CARS is explained. CARS is a four-wave mixing process where three photons (the pump, the Stokes and the probe photons) interact with a sample, and a fourth photon (the anti-Stokes photon) is emitted as a result. The generated CARS signal is resonantly enhanced when the frequency of a molecular vibration in the sample is matched by the frequency difference of pump and Stokes incoming photons. Since lipids are abundant in carbon-hydrogen groups (CH_2) that vibrate symmetrically at $2855\,cm^{-1}$, tuning the frequency difference at that vibrational frequency results in the generation of a very strong CARS signal that can be exploited to identify and characterize the presence of lipids in a specimen.
An overview of the experimental implementations possible for CARS is also presented. For the excitation, laser sources delivering femtosecond pulses are more advantageous for cost and widespread use than laser sources delivering picosecond pulses. However, because their spectral bandwidth is not matched to typical Raman linewidths, the corresponding spectral resolution is poor unless specific strategies are adopted, such as the temporal stretching of both pump and Stokes femtosecond pulses to picosecond pulses with equal linear chirp (*spectral focusing*). For the suppression of the nonresonant background that always accompanies CARS processes, D-CARS offers a simple and effective solution as it exploits the intensity difference between two CARS signals simultaneously generated by two pump-Stokes pulse pairs. For background-free signal detection, CARS collection in the backward (epi) direction can also be advantageous over the forward direction.

In **Chapter 3** details are provided for the preparation of all the samples, for the home-built CARS systems used in the experiments and for the procedures implemented in the quantitative analysis of acquired data. The aim of this work was to investigate two types of samples, namely LDs as pure neutral lipids in an agarose-in-water solution (*model LDs*) and LDs as biological organelles in fixed and living cellular systems (*cytosolic LDs*). In order to define and distinguish their

lipid content spectroscopically and microscopically, samples were investigated via home-built CARS set-ups based on femtosecond pulses spectrally focused by glass dispersion. These allowed the acquisition of chemically-specific information either as line spectra or as hyperspectral images in the fingerprint (1200 – 2000 cm^{-1}) and in the "CH-stretch" (2600 – 3200 cm^{-1}) vibrational regions. Experimental data were processed with analytical procedures in order to subtract the background offset, to define the CARS signal with respect to the resonance-free glass response and, for hyperspectral images, to retrieve quantitative information on the degree of lipid disorder and unsaturation within LDs. Specifically, quantitative results were obtained via the HIA software that allowed for noise reduction (singular value decomposition algorithm), Raman-like spectra retrieval from CARS spectra (phase-corrected Kramers-Kronig method) and spatial-spectral determination of absolute concentrations for the chemical components in the investigated samples (factorization into susceptibilities and concentrations of chemical components, FSC^3, method) [28].

In **Chapter 4** D-CARS has been confirmed as technique capable to suppress the CARS nonresonant background in the spectral-microscopy characterization of model LD systems. Furthermore, it was demonstrated that D-CARS is able to distinguish LDs with a disordered poly-unsaturated lipid content (α- and γ-glyceryl trilinolenate, GTLs) from LDs with a more ordered mono-unsaturated (glyceryl trioleate) or saturated lipid content (glyceryl caprilate, GTC) without the need of lengthy CARS hyperspectral measurements and analysis. We have reported that, in the "CH-stretch" region, the D-CARS values measured as CARS intensity difference between the bands at 2930 cm^{-1} and 2855 cm^{-1} well correlate with the Raman lineshape that is representative of molecular disorder. Specifically, LDs made of poly-unsaturated GTLs exhibit a "flat-hat" CARS spectrum with equally intense bands and hence nearly zero D-CARS, while LDs made of the other lipids exhibit a positive D-CARS. Similarly, in the fingerprint region, despite the CARS differential lineshape the D-CARS values measured as CARS intensity difference between the wavenumbers at 1690 cm^{-1} and 1670 cm^{-1} well correlate with the amplitude of the Raman band at 1660 cm^{-1} that is representative of acyl chain

unsaturation. In fact LDs made of saturated GTC do not exhibit a D-CARS peak at 1690 cm^{-1} which is instead present in the spectra of unsaturated lipids. On the basis of their different D-CARS values, D-CARS images were directly acquired on model LDs providing a fast technique to visually discriminate saturated and unsaturated triglycerides. Notably, the main findings shown in this Chapter were accepted for publication in the international peer-reviewed Journal of Biophotonics [74].

In **Chapter 5** the D-CARS chemical sensitivity and specificity has been applied to cytosolic LDs that had been induced in human adipose-derived stem cells (ADSCs) by the addiction of exogenous saturated and unsaturated fatty acids to the culture media. Furthermore, D-CARS has been compared with hyperspectral CARS on the capability to provide quantitative chemical imaging, i.e. spatially resolved information for the chemical constituents of the investigated sample. Chapter 5 is divided into two main sections.

In the first section, fixed human stem-cell derived adipocytes fed with saturated fatty acid (palmitic acid), poly-unsaturated fatty acid (α-linolenic acid) and their mixtures have been investigated. We found that D-CARS is effective in distinguishing LDs of different contents in fixed cell environments at the chemically-selective wavenumbers identified in the model LD study. Moreover, D-CARS is able to quantify the degree of lipid unsaturation when the D-CARS band at 1680 cm^{-1} is ratiometrically compared with D-CARS band at 1470 cm^{-1}. In the "CH-stretch" region, however, D-CARS is less quantitative because of its non-linear dependence on the concentration of chemical components and results are to be considered more qualitatively. Conversely, hyperspectral CARS provides quantitative information for the lipid unsaturation and disorder both in the fingerprint and in the "CH-stretch" region, where the vibrational bands at 2930 and 3010 cm^{-1} are ratiometrically compared with the vibrational band at 2855 cm^{-1}. Furthermore, the FSC^3 analysis of hyperspectral CARS data has been shown to provide the absolute volume:volume concentrations of chemical components in cells and to map their spatial distribution with greater contrast than ratiometric methods described in literature. Notably, these results were accepted for publica-

tion in the international peer-reviewed journal Biomedical Optics Express [118]. In the second section, a similar procedure has been applied to investigate LDs in live ADSCs cultured in media loaded with fatty acids including mono-unsaturated oleic acid, bi-unsaturated linoleic acid, tri-unsaturated α-linolenic acid and an equal volume mixture of oleic acid and α-linolenic acid. As in the study on fixed ADSCs, D-CARS spectral-imaging has been proved successful in rapidly discriminating lipid contents between differently-fed cells and within the same cell over time. Despite being more disrupting to cells, long CARS hyperspectral images were able to show different lipid compositions and they were used to singularly quantify the spatial distribution and volume concentrations in the samples during differentiation over time, via the FSC^3 method. This permitted to define time-dependent trends for the lipid concentration within LDs and to investigate their changes according to the fatty acids added to the culture media. Publication of these results in an international peer reviewed journal is planned in the near future. Furthermore, preliminary experiments on proteins (Rab18) and inhibitors (Exo2) transfected into live ADSCs confirmed the capability for our set-up to perform CARS/TPF studies and to visualize LD dynamic phenomena such as droplet fusion.

6.2 Outlook

The results achieved in this Ph.D. project contribute to a more in depth understanding of LD-related processes in the cellular machinery, especially regarding the cell intake of lipids from the media and the consequent accumulation in the form of LDs. For instance, our results suggest that long-chain poly-unsaturated fatty acids are efficiently stored in ADSCs (Sections 5.2 and 5.4). This would seem in agreement with the current literature that indicates this type of lipids as beneficial for the human health [113, 114]. However, human adipose tissue has been reported to contain a small percentage of poly-unsaturated lipids [117]. In order to investigate this apparent discrepancy, future work could be directed to adipocytes at a more mature stage. Since human adipose tissue is composed of

mature adipocytes, it would be interesting to investigate how these cells, compared to differentiating ADSCs, store exogenous fatty acids when cultured in media with different lipid contents and characterizing them through the acquisition of CARS/D-CARS images. This study could be complementary to the investigation of differentiating ADSC cultured for longer time in fatty acid supplemented media. Mature adipocytes could be obtained either from ADSCs or directly from human adipose tissue. So far adipose tissue has been investigated in animal models such as *Drosophila* flies and mice with CARS microscopy and Raman spectroscopy [131, 132], but there are no reported studies on human adipose tissue and CARS-based hyperspectral techniques.

The application of CARS and D-CARS spectral-microscopy to non-adipose tissues would provide insights on lipid composition and distribution in organs that are not specialized in storing lipids, such as liver tissue. In normal human liver, cholesterol, triglycerides and phospholipids are stored in small LDs (diameter below 10 μm) with a total concentration that is well known in the literature [133, 134]. In human fatty liver, however, triglycerides are stored in much larger vacuoles as cells start to retain an abnormal quantity of fats (*steatosis*) [135]. Current studies in the field are trying to determine the composition and concentration of lipids in livers affected by this pathology. Hyperspectral CARS can offer an important contribution from this point of view. Similarly to the procedure followed for living ADSCs, the simultaneous FSC^3 analysis of fatty and non-fatty liver specimens can underline spatial and spectral differences between them.

CARS studies at the sub-cellular level and in relation to specific LD-associated proteins deserve equal attention. Our preliminary results on the Exo2 inhibitor indicate the high impact that a small molecule induces on the appearance and organization of cytosolic LDs although the biochemical mechanisms and the cellular components involved (e.g., Exo2 target) are yet to be determined. Proof-of-principle experiments on Rab18 protein have proved that CARS, when used together with correlative and complementary microscopy techniques such as TPF, has the potential to identify Rab18 effects on LD content and to verify Rab18 association to LD sub-populations in terms of the lipid composition.

A

Appendix

Besides saturated and poly-unsaturated fatty acids, we also investigated mono-unsaturated lipids in human adipose-derived stem cells cultured under the same conditions and later fixed as described in the Material and Method chapter. Specifically culture medium was supplemented with an oleic acid-BSA complex (9.4 μg/mL oleic acid concentration) purchased from Sigma-Aldrich®.

As for Figures 5.1 and 5.2, Figure A.1 shows spectra given as averages from more than 100 spatially well-resolved LDs in cells fed with oleic acid-loaded medium. Spectra referring to cells fed with palmitic acid-loaded medium are also reported for comparison. CARS intensity ratios and correspondingly phase-retrieved imaginary part $\mathrm{Im}\{\chi_R^{(3)}\}$ are shown. These average spectra are similar to those measured in cells fed with media containing palmitic acid, as discussed in the main text. Particularly, the relative amplitude between the $1660\,\mathrm{cm}^{-1}$ and $1450\,\mathrm{cm}^{-1}$ bands which indicates the degree of acyl chain unsaturation is very alike.

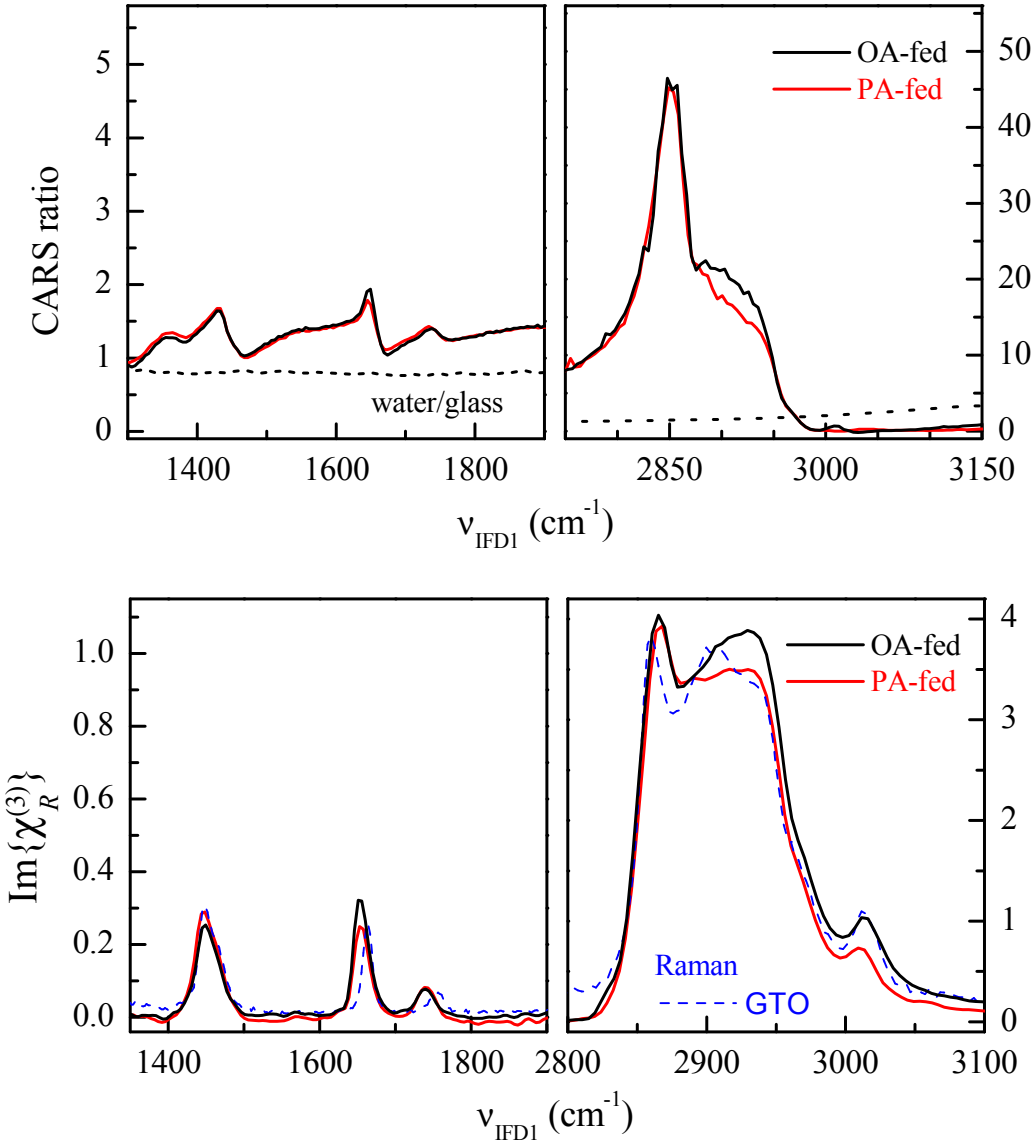

Figure A.1: CARS AND PHASE-RETRIEVED SPECTRA FOR ADIPOCYTES FED WITH SATURATED AND MONO-UNSATURATED FATTY ACIDS [118]. Averaged spectra from more than 100 LDs of human adipose-derived stem cells fed with palmitic acid (PA) and oleic acid (OA). *Upper panels:* CARS intensity ratio spectra in the fingerprint (left) and "CH-stretch" region (right). The spectrum of the water-to-glass ratio is also reported. *Lower panels:* Corresponding phase-retrieved imaginary part of the normalized susceptibility Im$\{\chi_R^{(3)}\}$ (right). The Raman spectrum of glyceryl trioleate (GTO) is shown for comparison (dashed lines). The pump power on the sample was 20 mW (14 mW) and the Stokes power was 10 mW (7 mW) for the fingerprint region (CH region).

B

Appendix

For the ratiometric analysis of lipid content in living ADSCs, FSC^3 analysis was singularly applied to cell samples and the overall chemical composition has been chosen to be represented in terms of 4 chemical species. The result for an ADSC cultured for 72 hours in a media supplemented with linoleic acid is shown in Figure B.1 for the "CH-stretch" region. Spectral profiles and spatial distributions are also shown and their attribution to specific chemical species is as follows.

Water-like culture media is component 1 and, as for fixed ADSCs, it represents the most abundant constituent in the sample. The lipid content is component 4 (color-coded in red in the red-green-blue, RGB, overlay) and it shows a very similar profile to the spectrum of pure LA. The protein content is component 3 (color-coded in green) and it is located in the cytosols and nuclei of the cells in the field of view. Finally, component 2 is attributable to artefacts introduced in the image by beam distortions.

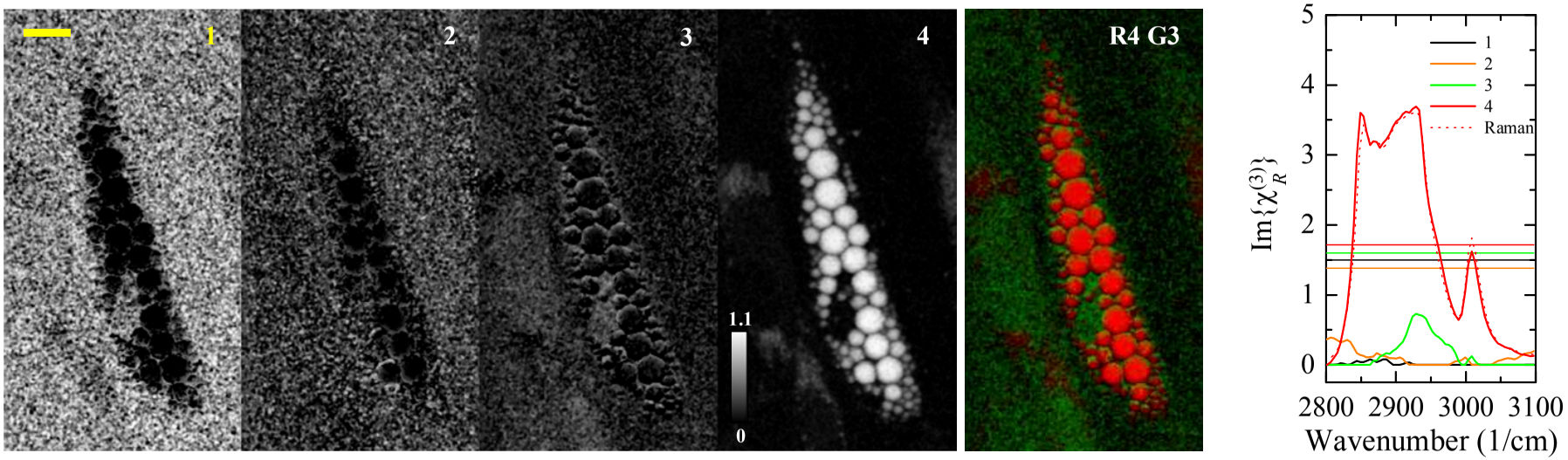

Figure B.1: RESULTS OF FSC^3 ON THE PHASE-RETRIVED IM$\{\chi_R^{(3)}\}$ IN LIVING HUMAN ADSCS FED WITH LINOLEIC ACID. *Left:* Spatial distributions of the volume concentration on a gray scale from 0 (black) to 1.1 (white) for the 4 components considered in the analysis. The scale bars indicate 20 μm. *Centre:* RGB overlay showing the spatial distribution of the concentration for specific components as indicated. *Right:* Spectra of Im$\{\chi_R^{(3)}\}$ and its real part (horizontal lines) for the corresponding components.

C

Appendix

In order to investigate time-dependent changes in the spatial distribution and in the volume concentration of the lipid component in living ADSCs, FSC^3 analysis was simultaneously applied to the phase-retrieved dataset of a group of cells cultured overtime in the same conditions of lipid-loaded differentiation media. The overall chemical composition across the group has been initially represented in terms of 4 chemical species, namely the water-based media, two lipid components (with high statistical weight) and a fourth "free" component. Figure C.1 shows the FSC^3 results for ADSCs cultured in control differentiation media over time for the "CH-stretch" region. Spectral profiles and spatial distributions are as shown. Concentration trends are also reported for the most significant LDs indicated in Figure 5.10.

The lipid content is investigated in terms of GTO and LA. Concentration trends reveal that GTO is present throughout the time span while LA is mainly absent. The only exception is the last time point at 214 hours where high LA concentration is due to errors in the FSC^3 analysis since LA is an *essential fatty acid*, i.e. it cannot be synthesized from other lipids [136].

The "free" component has no spectral profile assigned. In analogous sets of data it shows a non-interpretable spectrum. Therefore, in order to have a consistent analysis, the number of spectral species has been set to 3.

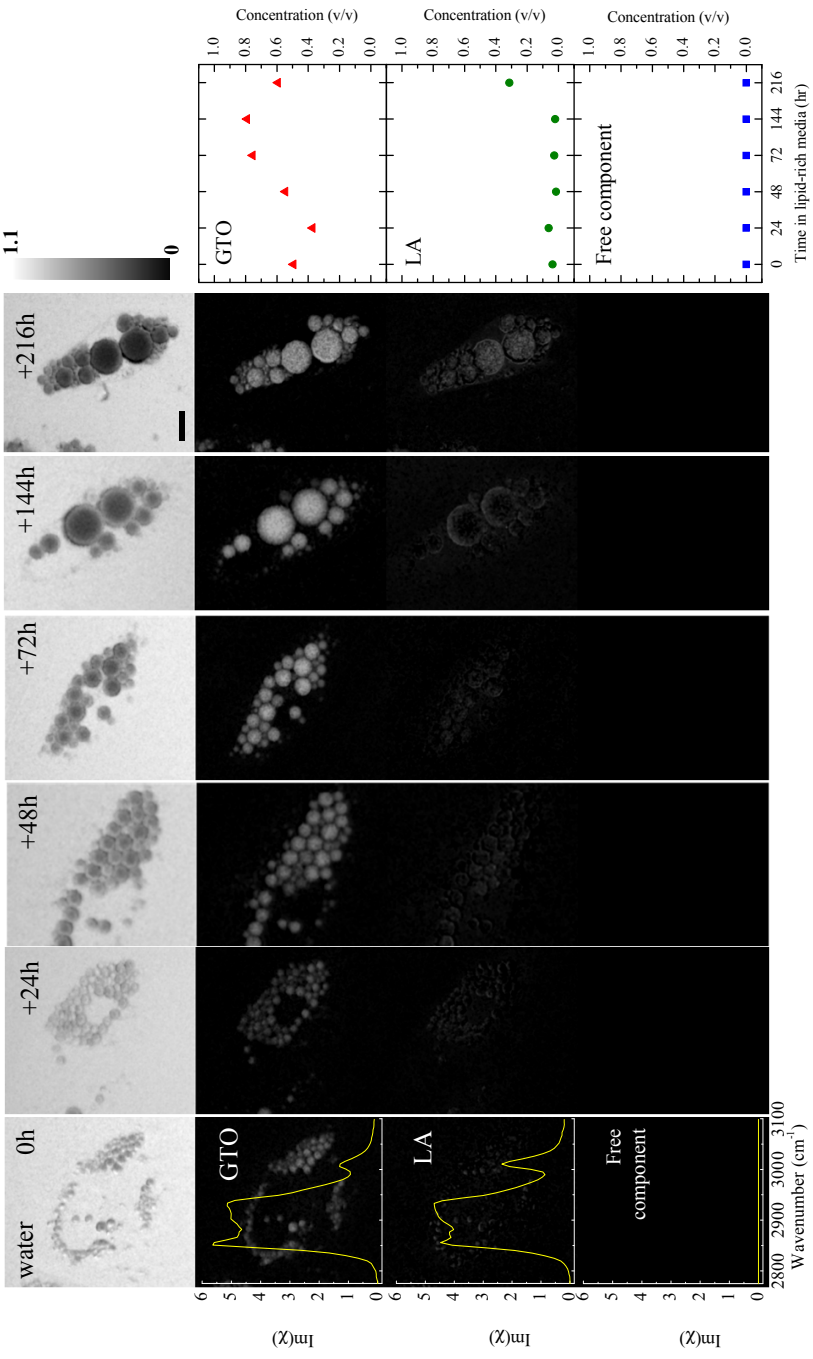

Figure C.1: RESULTS OF FSC^3 ON THE PHASE-RETRIVED IM$\{\chi_R^{(3)}\}$ IN LIVING HUMAN ADSCS CULTURED IN CONTROL DIFFERENTIATION MEDIA. *Left:* Spatial distributions of the volume concentration on a gray scale from 0 (black) to 1.1 (white) for the 4 components considered in the analysis. Grey scale as indicated. The scale bars indicate 20 μm. *Right:* Absolute concentrations of LA and GTO over time taken at a specific LD as indicated in Figure 5.10.

List of acronyms

ADSC	Adipose-Derived Stem Cell
CARS	Coherent anti-Stokes Raman scattering
CRS	Coherent Raman Scattering
D-CARS	Dual-frequency/Differential CARS
DIC	Differential Interference Contrast
Epi-CARS	Backward-propagating CARS
ER	Endoplasmic Reticulum
F-CARS	Forward-propagating CARS
FSC^3	Factorization into Susceptibilities and Concentrations of the Chemical Components
GFP	Green Fluorescent Protein
GTC	Glyceryl Tricaprylate
GTL	Glyceryl Trilinolenate
GTO	Glyceryl Trioleate
GTS	Glyceryl Tristearate
GVD	Group-Velocity Dispersion
HIA	Hyperspectral Imaging Analysis
IR	Infrared
LA	Linoleic Acid
LD	Lipid Droplet
LNA	(α-)Linolenic Acid
MIX	Equal volume mixture of Oleic Acid and (α-)Linolenic Acid
mLD	micro-Lipid Droplet
NIR	Near Infrared
OA	Oleic Acid

OCT	Optical Coherence Tomography
OPO	Optical Parametric Oscillator
PA	Palmitic Acid
PCKK	Phase-Corrected Kramers-Kronig
PFA	Paraformaldehyde
SHG	Second-Harmonic Generation
SVD	Singular Value Decomposition
THG	Third-Harmonic Generation
TPF	Two-Photon Fluorescence
Ti:Sa	Titanium:Sapphire

Bibliography

[1] B. Caballero. The global epidemic of obesity: An overview. *Epidemiologic Reviews*, 29(1):1–5, 2007.

[2] D.W. Haslam and W.P.T James. Obesity. *The Lancet*, 366(9492):1197–1209, 2005.

[3] R.V. Jr Farese and T.C. Walther. Lipid droplets finally get a little R-E-S-P-E-C-T. *Cell*, 139(5):855–860, 2009.

[4] L.L. Listenberger and D.A. Brown. *Current Protocols in Cell Biology*, volume 35, chapter Fluorescent detection of lipid droplets and associated proteins, pages 24.2.1–24.2.11. John Wiley & Sons, Inc., 2007.

[5] M. Müller and A. Zumbusch. Coherent anti-Stokes Raman scattering microscopy. *ChemPhysChem*, 8(15):2156–2170, 2007.

[6] A. Zumbusch, W. Langbein, and P. Borri. Nonlinear vibrational microscopy applied to lipid biology. *Progress in Lipid Research*, 52(4):615–632, 2013.

[7] F. Zernike. How I discovered phase contrast. *Science*, 121(3141):345–349, 1955.

[8] W. Lang. Nomarski differential interference-contrast microscopy. *ZEISS Information*, 70:114–120, 1968.

[9] D. Huang, E.A. Swanson, C.P. Lin, J.S. Schuman, W.G. Stinson, W. Chang, M.R. Hee, T. Flotte, K. Gregory, C.A. Puliafito, and J.G. Fujimoto. Optical coherence tomography. *Science*, 254(5035):1178–1181, 1991.

[10] A. Cricenti, R. Generosi, M. Luce, P. Perfetti, G. Margaritondo, D. Talley, J.S. Sanghera, I.D. Aggarwal, N.H. Tolk, A. Congiu-Castellano, M.A. Rizzo, and D.W. Piston. Chemically resolved imaging of biological cells and thin films by infrared scanning near-field optical microscopy. *Biophysical Journal*, 85(4):2705–2710, 2003.

[11] G. Turrell and J. Corset, editors. *Raman Microscopy: Developments and Applications*. Academic Press, Elsevier, 1996.

[12] P.J. Campagnola and L.M. Loew. Second-harmonic imaging microscopy for visualizing biomolecular arrays in cells, tissues and organisms. *Nature Biotechnology*, 21(11):1356–1360, 2003.

[13] Y. Barad, H. Eisenberg, M. Horowitz, and Y. Silberberg. Nonlinear scanning laser microscopy by third harmonic generation. *Applied Physics Letters*, 70(8):922–924, 1997.

[14] D. Débarre, W. Supatto, Ana-Maria Pena, Aurélie Fabre, Thierry Tordjmann, Laurent Combettes, Marie-Claire Schanne-Klein, and Emmanuel Beaurepaire. Imaging lipid bodies in cells and tissues using third-harmonic generation microscopy. *Nature Methods*, 3(1):47–53, 2006.

[15] A. Zumbusch, G.R. Holtom, and S. Xie. Three-dimensional vibrational imaging by coherent anti-Stokes Raman scattering. *Physical Review Letters*, 82(20):4142–4145, 1999.

[16] T.T. Le, S. Yue, and J.X. Cheng. Shedding new light on lipid biology with coherent anti-Stokes Raman scattering microscopy. *Journal of Lipid Research*, 51(11):3091–3102, 2010.

[17] J.P. Pezacki, J.A. Blake, D.C. Danielson, D.C. Kennedy, R.K. Lyn, and R. Singaravelu. Chemical contrast for imaging living systems: Molecular vibrations drive CARS microscopy. *Nature Chemical Biology*, 7(3):137–145, 2011.

[18] J.X. Cheng, L.D. Book, and X.S. Xie. Polarization coherent anti-Stokes Raman scattering microscopy. *Optics Letters*, 26(17):1341–1343, 2001.

[19] T. Ichimura, N. Hayazawa, M. Hashimoto, Y. Inouye, and S. Kawata. Tip-enhanced coherent anti-Stokes Raman scattering for vibrational nanoimaging. *Physical Review Letters*, 92(22):220801–1–4, 2004.

[20] J.X. Cheng, S. Pautot, D.A. Weitz, and X.S. Xie. Ordering of water molecules between phospholipid bilayers visualized by coherent anti-Stokes Raman scattering microscopy. *Proceedings of the National Academy of Sciences U.S.A.*, 100(17):9826–9830, 2003.

[21] X. Nan, W.Y.Y. Yang, and X.S. Xie. CARS microscopy lights up lipids in living cells. *Biophotonics International*, 11:44–47, 2004.

[22] E.O. Potma and X.S. Xie. Detection of single lipid bilayers with coherent anti-Stokes Raman scattering (CARS) microscopy. *Journal of Raman Spectroscopy*, 34:642–650, 2003.

[23] G.W.H. Wurpel, H.A. Rinia, and M. Müller. Imaging orientational order and lipid density in multilamellar vesicles with multiplex CARS microscopy. *Journal of Microscopy*, 218(Pt 1):37–45, 2005.

[24] G.W.H. Wurpel, J.M. Schins, and M. Müller. Chemical specificity in three-dimensional imaging with multiplex coherent anti-Stokes Raman scattering microscopy. *Optics Letters*, 27(13):1093–1095, 2002.

[25] H.A. Rinia, K.N.J. Burger, M. Bonn., and M. Müller. Quantitative label-free imaging of lipid composition and packing of individual cellular lipid droplets using multiplex CARS microscopy. *Biophysical Journal*, 95(10):4908–4914, 2008.

[26] M.P. Corcoran, S. Lamon-Fava, and R.A. Fielding. Skeletal muscle lipid deposition and insulin resistance: effect of dietary fatty acids and exercise. *American Journal of Clinical Nutrition*, 85(3):662–667, 2007.

[27] J.P.R. Day, K.F. Domke, G. Rago, H. Kano, H. Hamaguchi E.M. Vartiainen, and M. Bonn. Quantitative coherent anti-Stokes Raman scattering (CARS) microscopy. *Journal of Physical Chemistry B*, 115(24):7713–7725, 2011.

[28] F. Masia, A. Glen, P. Stephens, P. Borri, and W. Langbein. Quantitative chemical imaging and unsupervised analysis using hyperspectral coherent anti-Stokes Raman scattering microscopy. *Analytical Chemistry*, 85(22):10820–10828, 2013.

[29] I. Rocha-Mendoza, W. Langbein, P. Watson, and P. Borri. Differential coherent anti-Stokes Raman scattering microscopy with linearly chirped femtosecond laser pulses. *Optics Letters*, 34(15):2258–2260, 2009.

[30] W. Langbein, I. Rocha-Mendoza, and P. Borri. Single source coherent anti-Stokes Raman microspectroscopy using spectral focusing. *Applied Physics Letters*, 95(8):081109, 2009.

[31] I.W. Schie and T. Huser. Label free analysis of cellular biochemistry by Raman spectroscopy and microscopy. *Comprehensive Physiology*, 3(3):941–956, 2013.

[32] L.G. Rodriguez, S.J. Lockett, and G.R. Holtom. Coherent anti-Stokes Raman scattering microscopy. a biological review. *Cytometry Part A*, 69A:779–791, 2006.

[33] J.X. Cheng and X.S. Xie. *Coherent Raman Scattering Microscopy*, chapter Theory of Coherent Raman Scattering, pages 3–11. CRC Press, 2012.

[34] C.L. Evans and X.S. Xie. Coherent anti-Stokes Raman scattering microscopy: Chemical imaging for biology and medicine. *Annual Review of Analytical Chemistry*, 1:883–909, 2008.

[35] J.X. Cheng and X.S. Xie. Coherent anti-Stokes Raman scattering microscopy: Instrumentation, theory, and application. *Journal of Physical Chemistry B*, 108(3):827–840, 2004.

[36] F. Ganikhanov, C.L. Evans, B.G. Saar, and X.S. Xie. High-sensitivity vibrational imaging with frequency modulation coherent anti-Stokes Raman scattering (FM CARS) microscopy. *Optics Letters*, 31(12):1872–1874, 2006.

[37] W. Denk, J.H. Strickler, and W.W. Webb. Two-photon laser scanning fluorescence microscopy. *Science*, 248(4951):73–76, 1990.

[38] P.D. Maker and R.W. Terhune. Study of optical effects due to an induced polarization third order in electric field strength. *Physical Review*, 137(3A):A801–A818, 1965.

[39] M.D. Duncan, J. Reintjes, and T.J. Manuccia. Scanning coherent anti-Stokes Raman microscope. *Optics Letters*, 7(8):350–352, 1982.

[40] J.X. Cheng. Coherent anti-stokes raman scattering microscopy. *Applied Spectroscopy*, 61(9):197–208, 2007.

[41] Y. Fu, H.W., R.S., and J.X. Cheng. Characterization of photodamage in coherent anti-stokes raman scattering microscopy. *Optics Express*, 14(9):3942–3951, 2006.

[42] J.X. Cheng, A. Volkmer, L.D. Book, and X.S. Xie. An epi-detected coherent anti-Stokes Raman scattering (E-CARS) microscope with high spectral resolution and high sensitivity. *The Journal of Physical Chemistry B*, 105(7):1277–1280, 2001.

[43] M. Hashimoto, T. Araki, and S. Kawata. Molecular vibration imaging in the fingerprint region by use of coherent anti-stokes raman scattering microscopy with a collinear configuration. *Optics Letters*, 25(24):1768–1770, 2000.

[44] I. Pope, W. Langbein, P. Borri, and P. Watson. Live cell imaging with chemical specificity using dual frequency CARS microscopy. In P. Michael Conn, editor, *Imaging and Spectroscopic Analysis of Living Cells – Optical and Spectroscopic Techniques*, volume 504 of *Methods in Enzymology*, pages 273–291. Elsevier, 2012.

[45] T. Hellerer, A.M.K. Enejder, and A. Zumbusch. Spectral focusing: High spectral resolution spectroscopy with broad-bandwidth laser pulses. *Applied Physics Letters*, 85(1):25–27, 2004.

[46] J.X. Cheng, A. Volkmer, L.D. Book, and X.S. Xie. Multiplex coherent anti-Stokes Raman scattering microspectroscopy and study of lipid vesicles. *The Journal of Physical Chemistry B*, 106(34):8493–8498, 2002.

[47] M. Müller and J.M. Schins. Imaging the thermodynamic state of lipid membranes with multiplex CARS microscopy. *The Journal of Physical Chemistry B*, 106(14):3715–3723, 2002.

[48] E.R. Andresen, H.N. Paulsen, V. Birkedal, J. Thøgersen, and S.R. Keiding. Broadband multiplex coherent anti-Stokes Raman scattering microscopy employing photonic-crystal fibers. *Journal of the Optical Society of America B*, 22(9)(9):1934–1938, 2005.

[49] A. Volkmer, L.D. Book, and X.S. Xie. Time-resolved coherent anti-Stokes Raman scattering microscopy: Imaging based on Raman free induction decay. *Applied Physics Letters*, 80(9):1505–1507, 2002.

[50] N. Dudovich, D. Oron, and Y. Silberberg. Single-pulse coherently controlled nonlinear Raman spectroscopy and microscopy. *Nature*, 418:512–514, 2002.

[51] D. Oron, N. Dudovich, and Y. Silberberg. Femtosecond phase-and-polarization control for background-free coherent anti-Stokes Raman spectroscopy. *Physical Review Letters*, 90(21):213902, 2003.

[52] C.L. Evans, E.O. Potma, and X. S. Xie. Coherent anti-Stokes Raman scattering spectral interferometry: determinationof the real and imaginary components of nonlinear susceptibility $\chi^{(3)}$ for vibrational microscopy. *Optics Letters*, 29(24)(24):2923–2925, 2004.

[53] D.L. Marks and S.A. Boppart. Nonlinear interferometric vibrational imaging. *Physics Review Letters*, 92:123905, 2004.

[54] T.W. Kee, H. Zhao, and M.T. Cicerone. One-laser interferometric broadband coherent anti-Stokes Raman scattering. *Optics Express*, 14(8):3631–3640, 2006.

[55] E.O. Potma, C.L. Evans, and X.S. Xie. Heterodyne coherent anti-Stokes Raman scattering (CARS) imaging. *Optics Letters*, 31(2):241–243, 2006.

[56] E.M. Vartiainen, H.A. Rinia, M. Müller, and M. Bonn. Direct extraction of Raman line-shapes from congested CARS spectra. *Optics Express*, 14(8):3622–3630, 2006.

[57] L. Li, H. Wang, and J.X. Cheng. Quantitative coherent anti-Stokes Raman scattering imaging of lipid distribution in coexisting domains. *Biophysical Journal*, 89(5):3480–3490, 2005.

[58] F. Ganikhanov, S. Carrasco, X.S. Xie, M. Katz, W. Seitz, and D. Kopf. Broadly tunable dual-wavelength light source for coherent anti-Stokes Raman scattering microscopy. *Optics Letters*, 31(9):1292–1294, 2006.

[59] O. Burkacky, A. Zumbusch, C. Brackmann, and A. Enejder. Dual-pump coherent anti-Stokes-Raman scattering microscopy. *Optics Letters*, 31(24):3656–3658, 2006.

[60] Y.S. Yoo, D.H. Lee, and H. Cho. Differential two-signal picosecond-pulse coherent anti-Stokes Raman scattering imaging microscopy by using

a dual-mode optical parametric oscillator. *Optics Letters*, 32(22):3254–3256, 2007.

[61] J.X. Cheng, A. Volkmer, and X.S. Xie. Theoretical and experimental characterization of coherent anti-Stokes Raman scattering microscopy. *Journal of the Optical Society of America B*, 19(6):1363–1375, 2002.

[62] E.O. Potma, W.P. de Boeij, and D.A. Wiersma. Nonlinear coherent four-wave mixing in optical microscopy. *Journal of the Optical Society of America B*, 17(10):1678–1684, 2000.

[63] C.L. Evans, E.O. Potma, M. Puoris'haag, D. Côté, C.P. Lin, and X.S. Xie. Chemical imaging of tissue in vivo with video-rate coherent anti-Stokes Raman scattering microscopy. *Proceedings of the National Academy of Sciences of the United States of America*, 102(46):16807–16812, 2005.

[64] A. Volkmer, J.X. Cheng, and X.S. Xie. Vibrational imaging with high sensitivity via epidetected coherent anti-Stokes Raman scattering microscopy. *Physical Review Letters*, 87(2):023901, 2001.

[65] T.B. Huff and J.X. Cheng. In vivo coherent anti-Stokes Raman scattering imaging of sciatic nerve tissue. *Journal of Microscopy*, 225(2):175–182, 2007.

[66] B. Alberts, A. Johnson, J. Lewis, M. Raff, K. Roberts, and P. Roberts. *Molecular Biology of the Cell*. Taylor & Francis Ltd., Garland Science, New York, USA, 5th edition, 2008.

[67] The LIPID MAPS Lipidomics Gateway. http://www.lipidmaps.org/.

[68] D. DiDonato and D.L. Brasaemle. Fixation methods for the study of lipid droplets by immunofluorescence microscopy. *Journal of Histochemistry & Cytochemistry*, 51(6):773–780, 2003.

[69] S. Ozeki, J. Cheng, K. Tauchi-Sato, N. Hatano, H. Taniguchi, and T. Fujimoto. Rab18 localizes to lipid droplets and induces their close apposition to the endoplasmic reticulum-derived membrane. *Journal of Cell Science*, 118(12):2601–2611, 2005.

[70] R.A. Spooner, P. Watson, D.C. Smith, F. Boal, M. Amessou, L. Johannes, G.J. Clarkson, J.M. Lord, D.J. Stephens, and L.M. Roberts. The secretion inhibitor Exo2 perturbs trafficking of Shiga toxin between endosomes and the trans-Golgi network. *Biochemical Journal*, 414(3):471–484, 2008.

[71] I. Rocha-Mendoza, W. Langbein, and P. Borri. Coherent anti-Stokes Raman microspectroscopy using spectral focusing with glass dispersion. *Applied Physics Letters*, 93(20):201103, 2008.

[72] I. Pope, W. Langbein, P. Watson, and P. Borri. Simultaneous hyperspectral differential-CARS, TPF and SHG microscopy with a single 5 fs Ti:Sa laser. *Optics Express*, 21(6):7096, 2013.

[73] W. Langbein, I. Rocha-Mendoza, and P. Borri. Coherent anti-Stokes Raman micro-spectroscopy using spectral focusing: Theory and experiment. *Journal of Raman Spectroscopy*, 40(7):800–808, 2009.

[74] C. Di Napoli, F. Masia, I. Pope, C. Otto, W. Langbein, and P. Borri. Chemically-specific dual/differential CARS micro-spectroscopy of saturated and unsaturated lipid droplets. *Journal of Biophotonics*, 7(1–2):68–76, 2014.

[75] H.A. Rinia, M. Bonn, M. Müller, and E.M. Vertiainem. Quantitative CARS spectroscopy using the maximum entropy method: The main lipid phase transition. *ChemPhysChem*, 8(2):279–287, 2007.

[76] J. Kim and H. Park. Fast nonnegative matrix factorization: An active-set-like method and comparisons. *SIAM Journal on Scientific Computing*, 33(6):3261–3281, 2011.

[77] C.Y. Chung, J. Boik, and E.O. Potma EO. Biomolecular imaging with coherent nonlinear vibrational microscopy. *Annual Review of Physical Chemistry*, 64:77–99, 2013.

[78] B.C. Cheng, J. Sung, X. Wu, and S.H. Lim. Chemical imaging and microspectroscopy with spectral focusing coherent anti-Stokes Raman scattering. *Journal of Biomedical Optics*, 16(2):021112, 2011.

[79] J. De Gelder, K. De Gussem, P. Vandenabeele, and L. Moens. Reference database of Raman spectra of biological molecules. *Journal of Raman Spectroscopy*, 38(9):1133–1147, 2007.

[80] S.P. Verma and D.F.H. Wallach. Raman spectra of some saturated, unsaturated, and deuterated C18 fatty acids in the HCH-deformation and CH-stretching regions. *Biochimica et Biophysica Acta*, 486(2):217–227, 1977.

[81] R.N. Jones and R.A. Ripley. The Raman spectra of deuterated methyl laurates and related compounds. *Canadian Journal of Chemistry*, 42(2)(2):305–325, 1964.

[82] J. Sebek, L. Pele, E.O. Potma, and R.B. Gerber. Raman spectra of long chain hydrocarbons: anharmonic calculations, experiment and implications for imaging of biomembranes. *Physical Chemistry Chemical Physics*, 13(28):12724–12733, 2011.

[83] I.I. Patel, C. Steuwe, S. Reichelt, and S. Mahajan. Coherent anti-Stokes Raman scattering for label-free biomedical imaging. *Journal of Optics*, 15(9):094006, 2013.

[84] C.L. Evans, X. Xu, S. Kesari, X.S. Xie, S.T.C. Wong, and G.S. Young. Chemically-selective imaging of brain structures with CARS microscopy. *Optics Express*, 15(19):12076–12087, 2007.

[85] S.H. Kim, E.S. Lee, J.Y. Lee, E.S. Lee, B.S. Lee, J.E. Park, and D.W. Moon. Multiplex coherent anti-Stokes Raman spectroscopy images intact atheromatous lesions and concomitantly identifies distinct chemical profiles of atherosclerotic lipids. *Circulation Research*, 106(8):1332–1341, 2010.

[86] H. Wang, Y. Fu, P. Zickmund, R. Shi, and J.X. Cheng. Coherent anti-stokes Raman scattering imaging of axonal myelin in live spinal tissues. *Biophysical Journal*, 89(1):581–591, 2005.

[87] R. Mouras, G. Rischitor, A. Downes, S. Salter, and A. Elfick. Nonlinear optical microscopy for drug delivery monitoring and cancer tissue imaging. *Journal of Raman Spectroscopy*, 41(8):848–852, 2010.

[88] H.W. Wang, I.M. Langohr, M. Sturek, and J.X. Cheng. Imaging and quantitative analysis of atherosclerotic lesions by CARS-based multimodal nonlinear optical microscopy. *Arteriosclerosis, Thrombosis, and Vascular Biology*, 29(9):1342–1348, 2009.

[89] Y. Fu, H. Wang, T.B. Huff, R. Shi, and J.-X. J.X. Cheng. Coherent anti-Stokes Raman scattering imaging of myelin degradation reveals a calcium-dependent pathway in lyso-PtdCho-induced demyelination. *Journal of Neuroscience Research*, 85(13):2870–2881, 2007.

[90] S. Heuke, N. Vogler, T. Meyer, D. Akimov, F. Kluschke, H.-J. Röwert-Huber, J. Lademann, B. Dietzek, and J. Popp. Multimodal mapping of human skin. *British Journal of Dermatology*, 169(4):794–803, 2013.

[91] O. Masihzadeh, D.A. Ammar, M.Y. Kahook, and T.C. Lei. Coherent anti-Stokes Raman scattering (CARS) microscopy: A novel technique for imaging the retina. *Investigative Ophthalmology & Visual Science*, 54(5):3094–3101, 2013.

[92] X. Nan, E.O. Potma, and X.S. Xie. Nonperturbative chemical imaging of organelle transport in living cells with coherent anti-Stokes Raman scattering microscopy. *Biophysical Journal*, 91(2):728–735, 2006.

[93] C. Brackmann, J. Norbeck, M. Åkeson, D. Bosch, C. Larsson, L. Gustafsson, and A. Enejder. CARS microscopy of lipid stores in yeast: The impact of nutritional state and genetic background. *Journal of Raman Spectroscopy*, 40(7):748–756, 2009.

[94] R.K. Lyn, D.C. Kennedy, S.M. Sagan, D.R. Blais, Y. Rouleau, A.F. Pegoraro, X.S. Xie, A. Stolow, and J.P. Pezacki. Direct imaging of the disruption of hepatitis C virus replication complexes by inhibitors of lipid metabolism. *Virology*, 394(1):130–142, 2009.

[95] S. Niemelä, S. Miettinen, J.R. Sarkanen, and N. Ashammakhi. Adipose tissue and adipocyte differentiation: Molecular and cellular aspects and tissue engineering applications. In N. Ashammakhi, R. Reis, and F. Chiellini, editors, *Topics in Tissue Engineering*, volume 4. University of Oulu, 2008.

[96] A. Downes, R. Mouras, P. Bagnaninchi, and A. Elfick. Raman spectroscopy and CARS microscopy of stem cells and their derivatives. *Journal of Raman Spectroscopy*, 42(10):1864–1870, 2011.

[97] R. Mouras, P.O. Bagnaninchi, A.R. Downes, and A.P.D. Elfick. Label-free assessment of adipose-derived stem cell differentiation using coherent anti-Stokes Raman scattering and multiphoton microscopy. *Journal of Biomedical Optics*, 17(11):116011, 2012.

[98] Y.J. Lee, S.L. Vega, P.J. Patel, K.A. Aamer, P.V. Moghe, and M.T. Cicerone. Quantitative, label-free characterization of stem cell differentiation at the single-cell level by broadband coherent anti-Stokes Raman scattering microscopy. *Tissue Engineering Part C: Methods*, 2014.

[99] M. Paar, C. Jüngst, N.A. Steiner, C. Magnes, F. Sinner, D. Kolb, A. Lass, R. Zimmermann, A. Zumbusch, S.D. Kohlwein, and H. Wolinski. Remodeling of lipid droplets during lipolysis and growth in adipocytes. *The Journal of Biological Chemistry*, 287(14):11164–11173, 2012.

[100] D.L. Brasaemle, G. Dolios, L. Shapiro, and R. Wang. Proteomic analysis of proteins associated with lipid droplets of basal and lipolytically stimulated 3T3-L1 adipocytes. *Journal of Biological Chemistry*, 279(15):46835–46842, 2004.

[101] A. Marcinkiewicz, D. Gauthier, A. Garcia, and D.L. Brasaemle. The phosphorylation of Serine 492 of Perilipin A directs lipid droplet fragmentation and dispersion. *Journal of Biological Chemistry*, 281(17):11901–11909, 2006.

[102] T. Yamaguchi, N. Omatsu, E. Morimoto, H. Nakashima, K. Ueno, T. Tanaka, K. Satouchi, F. Hirose, and T. Osumi. CGI-58 facilitates lipolysis on lipid droplets but is not involved in the vesiculation of lipid droplets caused by hormonal stimulation. *Journal of Lipid Research*, 48(5):1078–1089, 2007.

[103] T. Hashimoto, H. Segawa, M. Okuno, H. Kano, H. Hamaguchi, T. Haraguchi, Y. Hiraoka, S. Hasui, T. Yamaguchi, F. Hirose, and T. Osumu. Active involvement of micro-lipid droplets and lipid droplet-associated proteins in hormone-stimulated lipolysis in adipocytes. *Journal of Cell Science*, 125(Pt 24):6127–6136, 2012.

[104] D.L. Brasaemle and N.E. Wolins. Packaging of fat: An evolving model of lipid droplet assembly and expansion. *The Journal of Biological Chemistry*, 287(4):2273–2279, 2012.

[105] T.C. Walther and R.V. Jr Farese. The life of lipid droplets. *Biochimica et Biophysica Acta*, 1791(6):459–466, 2009.

[106] M . Beller, K. Thiel, P.J. Thul, and H. Jäckle. Lipid droplets: A dynamic organelle moves into focus. *FEBS Letters*, 584(11):2176–2182, 2010.

[107] D.L. Brasaemle. Thematic review series: Adipocyte Biology. The perilipin family of structural lipid droplet proteins: stabilization of lipid droplets and control of lipolysis. *Journal of Lipid Research*, 48(12):2547–2559, 2007.

[108] P.E. Bickel, J.T. Tansey, and M.A. Welte. PAT proteins, an ancient family of lipid droplet proteins that regulate cellular lipid stores. *Biochimica et Biophysica Acta*, 1791(6):419–440, 2009.

[109] N.E. Wolins, D.L. Brasaemle, and P.E. Bickel. A proposed model of fat packaging by exchangeable lipid droplet proteins. *FEBS Letters*, 580(23):5484–5491, 2006.

[110] N.A. Ducharme and P.E. Bickel. Minireview: Lipid droplets in lipogenesis and lipolysis. *Endocrinology*, 149(3):942–949, 2008.

[111] M.A. Welte. Proteins under new management: lipid droplets deliver. *Trends in Cell Biology*, 17(8):363–369, 2007.

[112] I.W. Schie, L. Nolte, T.L. Pedersen, Z. Smith, J. Wu, I. Yahiatene, J.W. Newman, and T. Huser. Direct comparison of fatty acid ratios in single cellular lipid droplets as determined by comparative Raman spectroscopy and gas chromatography. *Analyst*, 138:6662–6670, 2013.

[113] E.A. Miles and P.C. Calder. Modulation of immune function by dietary fatty acids. *Proceedings of the Nutrition Society*, 57(2):277–292, 1998.

[114] L.H. Storlien, A.J. Hulbert, and P.L. Else. Polyunsaturated fatty acids, membrane function and metabolic diseases such as diabetes and obesity. *Current Opinion in Clinical Nutrition & Metabolic Care*, 1(6):559–563, 1998.

[115] H. Sampath and J.M. Ntambi. Polyunsaturated fatty acid regulation of gene expression. *Nutrition Reviews*, 62(9):333–339, 2004.

[116] M.N. Slipchenko, T.T. Le, H. Chen, and J.X. Cheng. High-speed vibrational imaging and spectral analysis of lipid bodies by compound Raman microscopy. *Journal of Physical Chemistry B*, 113(21):7681–7686, 2009.

[117] L. Hodson, C.M. Skeaff, and B.A. Fielding. Fatty acid composition of adipose tissue and blood in humans and its use as a biomarker of dietary intake. *Progress in Lipid Research*, 47(5):348–380, 2008.

[118] C. Di Napoli, I. Pope, F. Masia, P. Watson, W. Langbein, and P. Borri. Hyperspectral and differential CARS microscopy for quantitative chemical imaging in human adipocytes. *Biomedical Optics Express*, 5(5):1378–1390, 2014.

[119] D. Gachet, F. Billard, N. Sandeau, and H. Rigneault. Coherent anti-Stokes Raman scattering (CARS) microscopy imaging at interfaces: Evidence of interference effects. *Optics Express*, 15(16):10408–10420, 2007.

[120] A.M. Barlow, K. Popov, M. Andreana, D.J. Moffatt, A. Ridsdale, A.D. Slepkov, J.L. Harden, L. Ramunno, and A. Stolow. Spatial-spectral coupling in coherent anti-Stokes Raman scattering microscopy. *Optics Express*, 21(13):15298–15307, 2013.

[121] U. Schnell, F. Dijk, K.A. Sjollema, and B.N.G. Giepmans. Immunolabeling artifacts and the need for live-cell imaging. *Nature Methods*, 9(2):152–158, 2012.

[122] H. Ahmed. *Principles and reactions of protein extraction, purification, and characterization*, chapter Antibody labeling, antibody detection and immunochemical techniques, pages 324–328. CRC Press, 2004.

[123] C. Jüngst, M. Klein, and A. Zumbusch. Long-term live cell microscopy studies of lipid droplet fusion dynamics in adipocytes. *Journal of Lipid Research*, 54(12):3419–3429, 2013.

[124] J. Gong, Z. Sun, L. Wu, W. Xu, N. Schieber, D. Xu, G. Shui, H. Yang, R.G. Parton, and P. Li. Fsp27 promotes lipid droplet growth by lipid exchange and transfer at lipid droplet contact sites. *The Journal of Cell Biology*, 195(6):953–963, 2011.

[125] Z. Sun, J. Gong, H. Wu, W. Xu, L. Wu, D. Xu, J. Gao, J.W. Wu, H. Yang, M. Yang, and P. Li. Perilipin1 promotes unilocular lipid droplet formation through the activation of Fsp27 in adipocytes. *Nature Communications*, 4:1594, 2013.

[126] T.H.M. Grahn, Y. Zhang, M.J. Lee, A. Gianotti Sommer, G. Mostoslavsky, S.K. Fried, A.S. Greenberg, and V. Puri. FSP27 and PLIN1 interaction promotes the formation of large lipid droplets in human adipocytes. *Biochemical and Biophysical Research Communications*, 432(2):296–301, 2013.

[127] H. Stenmark and V.M. Olkkonen. The Rab GTPase family. *Genome Biology*, 2(5):reviews3007.1–3007.7, 2001.

[128] S. Martin and R.G. Parton. Characterization of Rab18, a lipid droplet-associated small GTPase. In Channing J. Der William E. Balch and Alan Hall, editors, *Small GTPases in Disease, Part A*, volume 438 of *Methods in Enzymology*, pages 109–129. Academic Press, 2008.

[129] S. Martin, K. Driessen, S.J. Nixon, M. Zerial, and R.G. Parton. Regulated localization of Rab18 to lipid droplets: Effects of lipolytic stimulation and inhibition of lipid droplet catabolism. *Journal of Biological Chemistry*, 280(51):42325–42335, 2005.

[130] R. Bartz, J. Seemann, J.K. Zehmer, G. Serrero, K.D. Chapman, R.G.W. Anderson, and P. Liu. Evidence that Mono-ADP-Ribosylation of CtBP1/BARS regulates lipid storage. *Molecular Biology of the Cell*, 18(8):3015–3025, 2007.

[131] C.H. Chien, W.W. Chen, J.T. Wu, and T.C. Chang. Investigation of lipid homeostasis in living Drosophila by coherent anti-Stokes Raman scattering microscopy. *Journal of Biomedical Optics*, 17(12):126001–1–7, 2012.

[132] N. Huang, M. Short, J. Zhao, H. Wang, H. Lui, M. Korbelik, and H. Zeng. Full range characterization of the Raman spectra of organs in a murine model. *Optics Express*, 19(23):22892–22909, 2011.

[133] M. Suzuki, Y. Shinohara, Y. Ohsaki, and T. Fujimoto. Lipid droplets: Size matters. *Journal of Electron Microscopy*, 60(1):S101–S116, 2011.

[134] P.O. Jr Kwiterovich, H.R. Sloan, and D.S. Fredrickson. Glycolipids and other lipid constituents of normal human liver. *Journal of Lipid Research*, 11(4):322–330, 1970.

[135] B.A. Neuschwander-Tetri. Fatty liver and the metabolic syndrome. *Current Opinion in Gastroenterology*, 23(2):193–8, 2007.

[136] N. Kaur, V. Chugh, and A.K. Gupta. Essential fatty acids as functional components of foods – A review. Journal of Food Science and Technology, March 2012.

Publications, Conferences, Proceedings and Academic Achievements

Publications

Parts of this work were published in the following articles:

1. **C. Di Napoli**, I. Pope, F. Masia, P. Watson, W. Langbein and P. Borri. Hyperspectral and differential CARS microscopy for quantitative chemical imaging in human adipocytes. *Biomedical Optics Express*, 5(5), 1378–1390, 2014.

2. **C. Di Napoli**, F. Masia, I. Pope, C. Otto, P. Watson, W. Langbein and P. Borri. Chemically-specific dual/differential CARS micro-spectroscopy of saturated and unsaturated lipid droplets. *Journal of Biophotonics*, 7(1–2), 68–76, 2014 (Published online in 2012).

Conferences and Proceedings

Parts of this work were presented at the following conferences:

1. **C. Di Napoli**, I. Pope, F. Masia, P. Watson, W. Langbein and P. Borri. Quantitative chemical analysis of CARS and D-CARS hyperspectral imaging on adipose-derived stem cells. *Poster presentation*. Bio-Nano-Photonics 2013, Cardiff, UK, 16 – 17 September 2013.

2. **C. Di Napoli**, I. Pope, F. Masia, P. Watson, W. Langbein and P. Borri. Differential CARS micro-spectroscopy of saturated and unsaturated lipid droplets in model and cellular systems. *Oral presentation*. European Conference on Nonlinear Optical Spectroscopy (ECONOS) and CARS Workshop 2013, Exeter, UK, 22 – 24 April 2013.

3. **C. Di Napoli**, I. Pope, W. Langbein, F. Masia, P. Watson and P. Borri. Quantitative CARS and D-CARS study of model lipid droplets. *Oral presentation*. Photon12, Durham, UK, 3 – 6 September 2012.

4. **C. Di Napoli**, I. Pope, W. Langbein, F. Masia, P. Watson and P. Borri. Quantitative CARS and D-CARS study of model lipid droplets. *Poster presentation*. International School of Physics "Enrico Fermi", Varenna, Italy, 12 - 22 July 2011; Bio-Nano-Photonics 2011, Cardiff, UK, 13 – 14 September 2011; Workshop on Applications of CRS Microscopy 2012, Exeter, UK, 23 – 24 April 2012.

5. W. Langbein, I. Rocha-Mendoza, F. Masia, **C. Di Napoli**, I. Pope, P. Watson and P. Borri. Differential CARS microscopy with linearly chirped femtosecond laser pulses. *Oral presentation*. SPIE Photonics West 2011, San Francisco, California, United States, 22 – 27 January 2011. Paper published in *Multiphoton Microscopy in the Biomedical Sciences XI*. Edited by Periasamy, Ammasi; König, Karsten; So, Peter T. C. Proceedings of the SPIE, 7903, 79031I–1-7, 2011.

Academic Achievements

1. Winner of the President's Research Ph.D. Scholarship, Cardiff University, 2010–2013.

2. Winner of the 2nd year Ph.D. poster competition for the "Molecular Biosciences" research division, Cardiff School of Biosciences, Cardiff University, 9 May 2012.

J. Biophotonics **7**, No. 1–2, 68–76 (2014) / **DOI** 10.1002/jbio.201200197

Journal of
BIOPHOTONICS

FULL ARTICLE

Chemically-specific dual/differential CARS micro-spectroscopy of saturated and unsaturated lipid droplets

Claudia Di Napoli[1], *Francesco Masia*[2], *Iestyn Pope*[1], *Cees Otto*[3], *Wolfgang Langbein*[2], *and Paola Borri*[*,1,2]

[1] Cardiff University School of Biosciences, Museum Avenue, Cardiff CF10 3AX, United Kingdom
[2] Cardiff University School of Physics and Astronomy, The Parade, Cardiff CF24 3AA, United Kingdom
[3] University of Twente, Faculty of Science and Technology, Drienerlolaan 5, 7500 AE Enschede, The Netherlands

Received 1 October 2012, revised 4 November 2012, accepted 6 November 2012
Published online 30 November 2012

Key words: Multiphoton microscopy, nonlinear optics, Coherent Antistokes Raman Scattering, lipids

We have investigated the ability of dual-frequency Coherent Antistokes Raman Scattering (D-CARS) micro-spectroscopy, based on femtosecond pulses (100 fs or 5 fs) spectrally focussed by glass dispersion, to distinguish the chemical composition of micron-sized lipid droplets consisting of different triglycerides types (poly-unsaturated glyceryl trilinolenate, mono-unsaturated glyceryl trioleate and saturated glyceryl tricaprylate and glyceryl tristearate) in a rapid and label-free way. A systematic comparison of Raman spectra with CARS and D-CARS spectra was used to identify D-CARS spectral signatures which distinguish the disordered poly-unsaturated lipids from the more ordered saturated ones both in the CH-stretch vibration region and in the fingerprint region, without the need for lengthy CARS multiplex acquisition and analysis. D-CARS images of the lipid droplets at few selected wavenumbers clearly resolved the lipid composition differences, and exemplify the potential of this technique for label-free chemically selective rapid imaging of cytosolic lipid droplets in living cells.

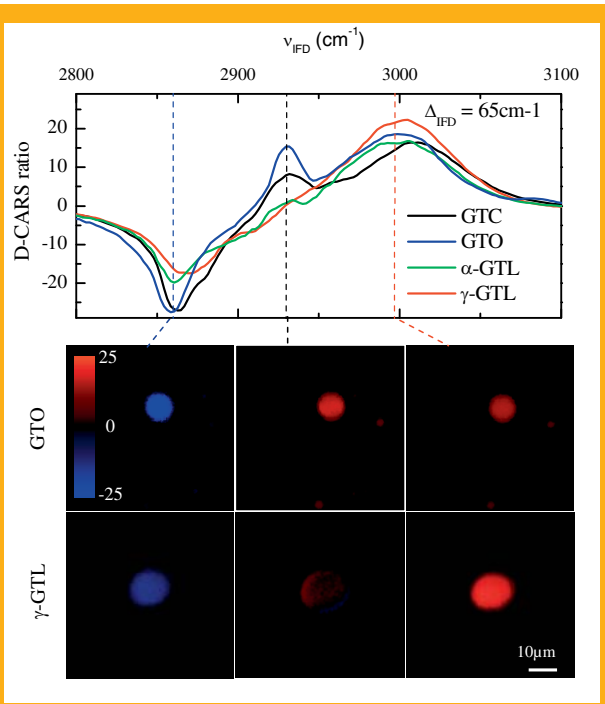

Measured D-CARS spectra in the CH-Strech region for lipid droplets (LDs) of different lipid composition as indicated. The bottom panels show images through the equatorial plane of LDs at wavenumbers indicated by the corresponding dashed lines.

* Corresponding author: e-mail: borrip@cardiff.ac.uk, Phone: +44 29 20879356

1. Introduction

Historically considered as inert fat particles, cytosolic lipid droplets (LDs) have been outside the focus of research until recently, but are now being recognized as dynamic organelles with complex and interesting biological functions, beyond mere energy storage, relevant for lipid homeostasis and the pathophysiology of metabolic diseases [1, 2]. LDs are found in most cell types, including plants, and consist of a hydrophobic core containing neutral lipids, mainly triglycerides and sterol esters, surrounded by a phospholipid monolayer. Among the several unanswered questions regarding LDs is their heterogeneity in size and composition and how this is regulated in cells. LDs show a large range of sizes from 0.1 μm to 100 μm, depending on the cell type, and there is increasing evidence that their lipid composition (e.g. saturated versus unsaturated acyl chains) varies between different droplets and even within a single droplet. Understanding the role of lipid composition in LDs could have implications in e.g. discovering the cellular mechanisms by which the quality of dietary fat influences our health.

Imaging LDs in cells using fluorescence staining of lipids is known to be prone to labeling artifacts, be unspecific, often require cell fixation [3], and suffer from photo-bleaching. A more specific technique to distinguish lipid composition uses electron dense osmium tetroxide which preferentially binds unsaturated fatty acid chains and is visible with electron microscopy, a method however limited by laborious sample preparation and not suitable for imaging living cells [4]. Coherent Antistokes Raman Scattering (CARS) microscopy has emerged in the last decade as a powerful multiphoton microscopy technique to image LDs label-free and with intrinsic three-dimensional spatial resolution in living cells [5–7]. In CARS two laser fields, pump and Stokes of frequencies ν_P and ν_S respectively, are used to coherently drive intrinsic molecular vibrations via their interference at the frequency difference $\nu_P - \nu_S$. In the two-pulse version, the pump field itself is used to probe the vibrations via the Anti-Stokes Raman scattering at $2\nu_P - \nu_S$. Compared to spontaneous Raman, CARS benefits from the constructive interference of the Raman scattered light of many identical bonds coherently driven in the focal volume. Therefore, the technique has proven to be especially advantageous to image cytosolic LDs of size $\gtrsim$0.5 μm in diameter (comparable or larger than the focal volume of a high numerical aperture objective) through the numerous CH bonds in the acyl chain of fatty acids.

To gain the degree of chemical specificity required to distinguish lipids of different chemical composition in CARS microscopy it is however not sufficient to resonantly drive a single frequency. For this purpose multiplex CARS micro-spectroscopy was implemented, where several vibrational frequencies are simultaneously excited and probed and a CARS spectrum carrying detailed information of the different vibrational components is recorded for every spatial point in the image. With this method, it was possible to image and quantitatively analyze the heterogeneous lipid composition of LDs in mouse adipocytes (3T3-L1 cells) [8]. The advantage of multiplex-CARS is that complex CARS spectra acquired over a sufficiently wide range can be quantitatively interpreted using fitting procedures (e.g. the maximum entropy method [9]) that allow reconstruction of the corresponding spontaneous Raman scattering spectra. The disadvantage of the method is however its low image speed, since the acquisition time for a single CARS spectrum is typically in the 10 ms range resulting in tens of minutes for the acquisition of spatially-resolved 3D images. Consequently, the work in Ref. [8] was performed on fixed cells, defeating the purpose of CARS microscopy as a live cell imaging technique.

We recently demonstrated a new method to perform dual-frequency/differential CARS (D-CARS) employing linearly chirped femtosecond laser pulses which simultaneously excite and probe two vibrational frequencies adjustable in center and separation. The resulting sum and difference CARS intensities are detected by a fast and efficient single photomultiplier (PMT), thus maintaining the high image speed of single-frequency CARS microscopy and offering at the same time improved chemical specificity and image contrast against the non-resonant CARS background [10, 11]. In the present work, we have applied this D-CARS method to a series of LD model systems (micron-sized LDs in agarose gel consisting of unsaturated, mono-saturated or poly-saturated triglycerides) and demonstrate its ability to distinguish between the different lipid types while maintaining rapid imaging speed. These results exemplify the potential of our D-CARS method for label-free chemically selective rapid imaging of cytosolic LDs in living cells.

2. Experimental

2.1 Spontaneous Raman spectroscopy set-up

Spontaneous Raman spectra were taken using two confocal micro-spectroscopy set-ups. Specifically, confocal Raman spectra of glyceryl tricaprylate and glyceryl tristearate LDs were taken using a Ti-U microscope stand with a 20 × 0.75 NA objective. The 532 nm laser excitation was filtered with a Semrock LL01-532 and coupled into the microscope by a di-

chroic mirror (Semrock LPD01-532RS), with a power of 10 mW at the sample. The Raman scattering was collected in epi-direction, filtered with a long pass filter (Semrock BLP01-532R), dispersed by an imaging spectrometer (Horiba iHR550) with a 600 lines/mm grating and detected with a CCD Camera (Andor Newton DU971N-BV) with a FWHM spectral resolution of 2.3 cm^{-1}. Raman spectra for the other lipids in this work were taken using the set-up described in details in Ref. [12] with a laser excitation at 647 nm, a 40×0.95 NA objective, a power of 35 mW onto the sample and a high-resolution spectrograph providing 2.25 cm^{-1} spectral resolution. All measurements were performed at room temperature.

2.2 CARS micro-spectroscopy set-up

For D-CARS micro-spectroscopy two set-ups were used. The first set-up is based on a 100 fs laser system and is described in Ref. [10, 13]. Briefly, a Ti : Sapphire laser source (Coherent Mira) delivering 100 fs Stokes pulses centered at 832.5 nm with $1/T = 76$ MHz repetition rate synchronously pumps an optical parametric oscillator (APE PP2) which is intracavity frequency doubled providing 100 fs pump pulses centered at 670 nm. Pump and Stokes pulses travel through a glass (SF57) block of 9 cm length, and the Stokes travels through an additional 8 cm of SF57. The chirp introduced by the remaining optics including the microscope objective was equivalent to 4 cm SF57. In this way, the linear chirp of pump and Stokes was adjusted to be similar to achieve spectral focussing and corresponded to an excitation spectral resolution of 30 cm^{-1} and a chirped pump pulse duration of 700 fs. This degree of linear chirp is a compromise between CARS spectral selectivity and signal strength [13]. The delay time t_0 between pump and Stokes controls their instantaneous frequency difference ν_{IFD}, enabling to measure CARS intensity spectra $I_{CARS}(\nu_{IFD}(t_0))$ by simply moving a delay line. To measure D-CARS, the pump-Stokes pair is divided into two orthogonally polarized pairs (Π_1, Π_2) with adjustable relative powers. Π_2 travels through an additional $d = 4$ mm thin SF57 glass element and is delayed by $T/2$ before being recombined with Π_1. This creates a periodic pulse sequence with Π_1 driving a vibrational resonance ν_{IFD1} tuneable via t_0 and Π_2 driving a shifted resonance ν_{IFD2} with the frequency difference $\Delta_{IFD} = \nu_{IFD1} - \nu_{IFD2} = 65\,cm^{-1}$ being determined by the additional thickness d. A home built microscope comprised a 1.2 numerical aperture (NA) water immersion objective (Leica HCX PL APO 63× W Corr CS) to focus the exciting beams and an identical objective to collect the CARS in transmission direction. The set-up provided xy beam and xyz sample scanning, where x, y are the transversal directions and z is the axial direction of the focussed beam. The CARS intensity generated by each pair is detected simultaneously using a single PMT and appropriate high-pass/low-pass frequency filtering of the PMT current and high-frequency detection electronics at the laser repetition rate (see Ref. [10]).

The second set-up is based on a single ultrafast laser source, similar to Ref. [11], except here we used a Ti : Sapphire laser (Venteon Pulse : One PE) delivering 5 fs pulses with a spectrum covering the range 660 nm to 970 nm above 10% peak intensity and a repetition rate of 80 MHz. By an appropriate sequence of dichroic beam splitters, the laser spectrum is split into a pump and a Stokes part centered at 682 nm and 806 nm with a bandwidth of 65 nm and 200 nm, respectively. The remaining infrared portion of the laser spectrum (930–970 nm) can be compressed to 30 fs pulses at the sample and used for two-photon fluorescence excitation and second harmonic generation simultaneously with CARS, but this option was not utilized here and will be discussed in a forthcoming work [14]. Pump and Stokes were linearly chirped using SF57 glass blocks similar to what discussed above, and enabled CARS spectroscopy by varying the delay time t_0 between pump and Stokes over the vibrational range of 1200–3500 cm^{-1}, with a spectral resolution of about 30 cm^{-1} in the 1200–2200 cm^{-1} range and about 15 cm^{-1} in the 2200–3500 cm^{-1} range. The former was limited by a non-perfect spectral focussing over the entire tuning range due to third-order glass dispersion (an effect which can be compensated by changing the SF57 glass length for the different spectral regions). D-CARS was performed as discussed above for the setup with 100 fs pulses, and two IFD differences were considered, namely $\Delta_{IFD} = 68\,cm^{-1}$ and $\Delta_{IFD} = 20\,cm^{-1}$. Pump and Stokes pulses were coupled into a commercial inverted microscope stand (Nikon Ti–U) via a home-built beam-scanning head. The microscope was equipped with a 20×0.75 NA dry objective (Nikon CFI Plan Apo λ) to focus the beams onto the sample and a 0.72 NA dry condenser for CARS collection in transmission direction. A motorized sample stage enabled xy sample movement and a motorized objective focussing enabled z movement. CARS was spectrally discriminated by appropriate band pass filters and detected by a PMT (Hamamatsu H7422-40). Noticeably this set-up is specifically designed for biological applications. CARS and D-CARS alignments are mostly hands-off via remote computer-controlled optics adjustments hence user-friendly. More details on the setup will be published in a forthcoming work [14]. All measurements were performed at room temperature.

2.3 *Lipid droplet samples*

Lipids were purchased from Sigma-Aldrich® (Zwijndrecht, the Netherlands) and from Nu-Chek Prep, Inc (Elysian, Minnesota, USA). The following five triglycerides were investigated: glyceryl tricaprylate (GTC) with C8:0 fatty acid saturated chains; glyceryl tristearate (GTS) with C18:0 fatty acid saturated chains; glyceryl trioleate (GTO) with C18:1 monounsaturated chains with *cis* double bond at the 9th position from the first carbon atom in the chain (*1,2,3-Tri(cis-9-octadecenoyl)glycerol*); α-glyceryl trilinolenate (α-GTL) with C18:3 fatty acid chains and all *cis* double bonds at 9, 12, and 15th position from the 1st carbon atom (*1,2,3-Tri-(cis,cis,cis-9,12,15-octadecatrienoyl)glycerol*); γ-glyceryl trilinolenate (γ-GTL) with C18:3 fatty acid chains all *cis* double bonds at the 6th, 9th and 12th position from the 1st carbon atom (*1,2,3-Tri-(cis,cis,cis-6,9,12-octadecatrienoyl)glycerol*).

At room temperature GTS is in solid phase, while the other lipids in liquid phase (melting temperatures are 9–10 °C for GTC, −5.5 °C for GTO, −24 °C for α-GTL, and 71–73 °C for GTS).

The samples consist of micron-sized lipid droplets suspended in a solution of 2% low melting temperature (65 °C) agarose powder and 98% water. Droplets were created by adding a given lipid type in the agar-water solution with a 1% volume-volume ratio and by sonicating the obtained emulsion for 15 minutes at 80 °C. 13 µL are pipetted inside a 120 µm thick imaging spacer (Grace™Bio-Lab SecureSeal™) glued on a glass coverslip in order to create a chamber, which is sealed afterwards by a second coverslip. Samples were stored in 100% humidity conditions in order to prevent drying of the agar emulsion.

3. Results and discussion

To characterize the Raman spectral features of the different lipid types investigated here and for comparison with CARS intensity spectra $I_{CARS}(\nu_{IFD})$, spontaneous Raman spectra were measured for all triglycerides LD samples. Additionally, spectra of LDs made of oleic acid (OA) were measured. All spectra are shown in Figure 1, normalized to the area in the CH-stretch region (2750–3050 cm^{-1}) which provides a good measure of the total lipid concentration [8]. Several bands are observed, with two spectral regions being characteristic for lipids with different molecular structures, namely the fingerprint (700–2000 cm^{-1}) and the CH-stretch regions. As discussed in literature [15, 16], the fingerprint region is characterized by a band between

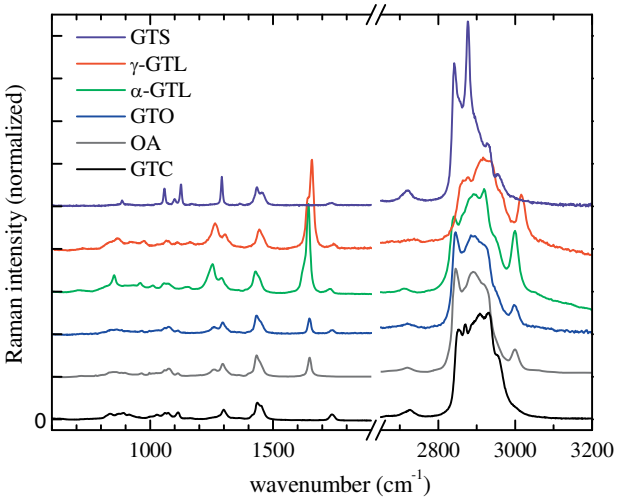

Figure 1 Raman spectra at room temperature of micron-sized lipid droplets in agarose gel made from different lipids as indicated. GTC: glyceryl tricaprylate. GTO: glyceryl trioleate. OA: oleic acid. $\alpha(\gamma)$-GTL: $\alpha(\gamma)$-glyceryl trilinolenate, GTS: glyceryl tristearate. Curves are vertically shifted for clarity.

1050 cm^{-1} and 1150 cm^{-1} due to the C–C stretch, a band around 1290 cm^{-1} due to CH_2 twist, and the band between 1400 cm^{-1} and 1500 cm^{-1} due to CH_2 and CH_3 deformations. In the unsaturated lipids (OA, GTO and GTL) the band around 1290 cm^{-1} broadens and splits into two bands around 1260 cm^{-1} and 1300 cm^{-1} attributed to =CH and CH_2 deformations respectively, with the relative intensity of the former increasing with increasing numbers of double bonds. A similar trend occurs for the band around 1660 cm^{-1} attributed to the C=C stretch, which is absent in saturated lipids (GTC and GTS), appears for GTO and OA and strengthens for GTL. The weak band around 1740 cm^{-1} is attributed to the C=O stretch from the ester bonds between glycerol and the fatty acids, and is indeed absent in the OA.

The CH stretch region is congested with several overlapping resonances complicating the attribution. The 2850 cm^{-1} band is due to the CH_2 symmetric stretch, shifting towards lower wavenumbers for saturated lipids in the solid phase (see spectrum of GTS). The 2880 cm^{-1} band is due to the CH_2 asymmetric stretch enhanced by the Fermi resonance interaction with the overtones of CH_2 and CH_3 deformations, especially prominent for lipids in the solid phase, such that the intensity ratio between the 2880 cm^{-1} and 2850 cm^{-1} bands can be used as a measure of the acyl chain order [8]. The 2930 cm^{-1} band is a combination of CH_3 stretch vibrations and CH_2 asymmetric stretch enhanced by the broadening and shift of the CH deformations in the liquid phase,

hence its intensity relative to the 2850 cm^{-1} band can be used as a measure of disorder. The =CH stretch gives rise to a band around 3010 cm^{-1}, with an intensity proportional to the number of carbon-carbon double bonds present in the main lipid chain, which is highest for GTL. GTS is solid at room temperature and exhibits the prominent 2880 cm^{-1} band while the other lipids which are liquid at room temperatures exhibit a significant band around [16] 2930 cm^{-1}. The band around 2730 cm^{-1} is likely [17, 18] due to a combination overtone of CH_2 scissor and wag, enhanced by the proximity of the Fermi resonance with the CH_2 stretch.

3.1 Single-pair CARS

It is well known that CARS intensity spectra do not resemble Raman spectra due to the interference between the resonant and non-resonant terms in the third-order susceptibility describing the CARS field [9]. For the application of D-CARS, our aim is to determine whether the *difference* between CARS intensities at suitable frequencies does provide a reliable information on the specific lipid type and can be directly used for rapid chemically-specific imaging, hence overcoming the drawback of slow acquisition speeds of multiplex CARS microscopy. For this purpose, we first measured the CARS intensity spectra $I_{CARS}(\nu_{IFD1})$ of the LD samples using the pulse pair Π_1 (see Section 2.2). Results are shown in Figure 2 using the 100 fs laser system and in Figure 3 using the 5 fs laser system. Figure 2a shows the CARS intensity $I_{CARS}(\nu_{IFD1}(t_0))$ measured as a function of the delay time t_0 between pump and Stokes pulses corresponding to ν_{IFD1} in the CH-stretch region [13, 19] on a GTO LD of 4 μm diameter taken at the LD center such that the focal volume was inside the LD. $I_{CARS}(x, t_0)$ (see inset in Figure 2a) for y, z in the center of the LD was acquired to determine the CARS intensity at the LD and in the surrounding agarose gel, as indicated by the dotted lines. The Gaussian shape of the CARS intensity spectrum in the agarose gel mainly reflects the pump-Stokes intensity cross-correlation when varying temporal overlap. However, due to the tail of the water resonance at ~3200 cm^{-1} this profile is not exactly equal to the non-resonant CARS response from the cross-correlation of the Gaussian pulses, as shown by the same measurement taken on the glass coverslip. To represent CARS spectral "strengths" independent of excitation/detection parameters, we normalize $I_{CARS}(\nu_{IFD1})$ to the non-resonant CARS intensity of glass $I^{NR}_{CARS}(\nu_{IFD1})$ resulting in the CARS ratio $\hat{I}_{CARS} = I_{CARS}/I^{NR}_{CARS}$ shown in Figure 2b, c. Corresponding Raman spectra are also shown for direct comparison in the same wavenumber range.

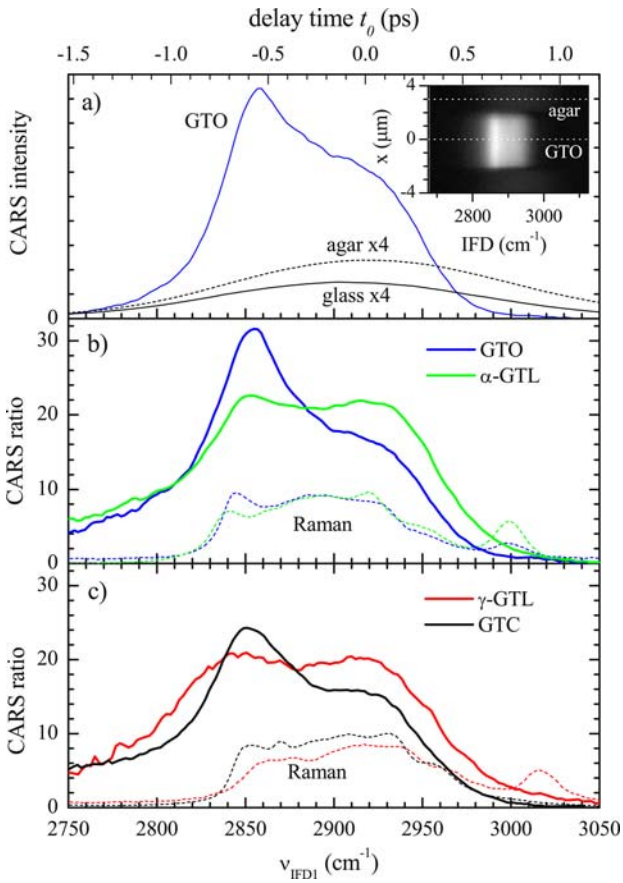

Figure 2 CARS measured with the 100 fs laser system. (**a**) I_{CARS} measured on a 4 μm LD of GTO, in the surrounding agarose gel and in the glass coverslip as a function of the delay time t_0 between pump and Stokes pulses and corresponding ν_{IFD1}. The inset shows a $I_{CARS}(x, t_0)$ for (y, z) at the center of the LD, with dotted lines indicating the x positions of GTO and agar. Pump power on the sample 7 mW, Stokes power 2 mW, objective 60 × 1.2 NA, 0.1 ms pixel dwell time, 75 nm pixel size. (**b**) and (**c**) CARS ratio $\hat{I}_{CARS}$ in LDs of different lipids as indicated. Raman spectra (dotted lines) are also shown for comparison.

Due to the interference between the resonant and non-resonant terms in the third-order susceptibility, low wavenumber edges are enhanced and high wavenumber edges are suppressed in CARS compared to spontaneous Raman, as seen here for the enhanced CH_2 symmetric stretch at 2850 cm^{-1}. Nevertheless, the relative intensity of the band at 2930 cm^{-1} with respect to the band at 2850 cm^{-1} follows the same trend as in spontaneous Raman, being higher for the more disordered poly-unsaturated GTL compared to the saturated and mono-unsaturated lipids. Similar results were obtained by measuring the CARS spectra in the CH-stretch region with the 5 fs laser system (see Figure 3 right panels), which enabled to address a broader spec-

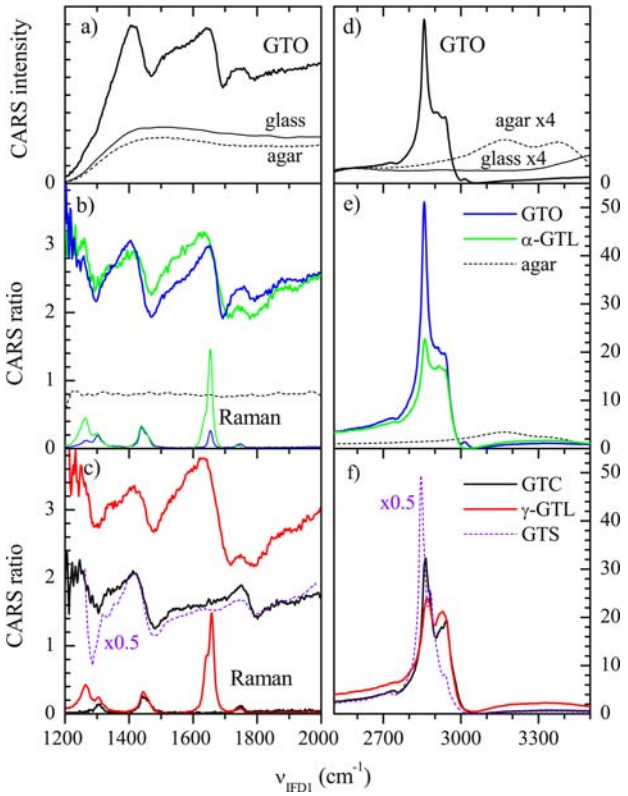

Figure 3 CARS measured with the 5 fs laser system in the fingerprint region (**a**–**c**) and in the CH-stretch region (**d**–**f**). (**a**) and (**d**) I_{CARS} measured on a $>2\,\mu$m lipid droplet of GTO, in the agarose gel and in the glass coverslip. (**b**) and (**c**) CARS ratio $\hat{I}_{\mathrm{CARS}}$ for different lipid types and agar as indicated, together with corresponding Raman spectra in the fingerprint region. (**e**) and (**f**) as (**b**) and (**c**), but for the CH-stretch region. Pump power on the sample 16 mW, Stokes power 8 mW, objective 20 × 0.75 NA.

tral range with a better spectral resolution (see Section 2.2).

With the 5 fs laser system we could also measure CARS spectra in the fingerprint region (see Figure 3 left panels). In this region the resonant CARS contribution is smaller than the non-resonant term and the spectral lineshape is dominated by the interference term [5, 11] $2\chi^{(3)}_{\mathrm{NR}}\Re\{\chi^{(3)}_R\}$ between the resonant part of the third-order susceptibility $\chi^{(3)}_R = R/(-\omega_\delta - i\Gamma)$ and the real non-resonant part $\chi^{(3)}_{\mathrm{NR}}$. Here ω_δ is the difference between vibrational excitation and resonance frequency [19], and Γ is the vibrational dephasing rate. This creates a dispersive lineshape $\Re\{\chi^{(3)}_R\} = -R\omega_\delta/(\omega_\delta^2+\Gamma^2)$ which is spectrally extended with tails $\propto\omega_\delta^{-1}$. Hence single-frequency CARS is less suited to create specific vibrational contrast than spontaneous Raman, which has a lineshape proportional to $\Im\{\chi^{(3)}_R\} = R\Gamma/(\omega_\delta^2+\Gamma^2)$. Nevertheless the presence of the C=C stretch band at around 1660 cm^{-1} is clearly visible in the CARS spectra of GTL and GTO and is absent in GTS and GTC as expected. GTO also exhibits a steeper slope between maximum and minimum in the dispersive spectrum, indicative of a sharper linewidth Γ of the 1660 cm^{-1} band compared to GTL consistent with the Raman spectra.

3.2 *Dual-pair differential CARS*

The concept of D-CARS is visualized in Figure 4 using the CARS spectrum measured in the CH-stretch region with the 100 fs laser system on GTO and α-GTL droplets. The D-CARS ratio $\hat{I}_{\mathrm{DCARS}} = \hat{I}_{\mathrm{CARS}}(\nu_{\mathrm{IFD2}}) - \hat{I}_{\mathrm{CARS}}(\nu_{\mathrm{IFD1}})$ is calculated from the CARS ratio of Π_1 using $\hat{I}_{\mathrm{CARS}}(\nu_{\mathrm{IFD2}}) = \hat{I}_{\mathrm{CARS}}(\nu_{\mathrm{IFD1}} - \Delta_{\mathrm{IFD}})$, i.e. the second pair Π_2 probes a vibrational resonance at a smaller frequency shifted by Δ_{IFD} compared to the first pair Π_1. The resulting D-CARS ratio spectrum is shown for $\Delta_{\mathrm{IFD}} = 65\,\mathrm{cm}^{-1}$ in Figure 4b, d. The differences

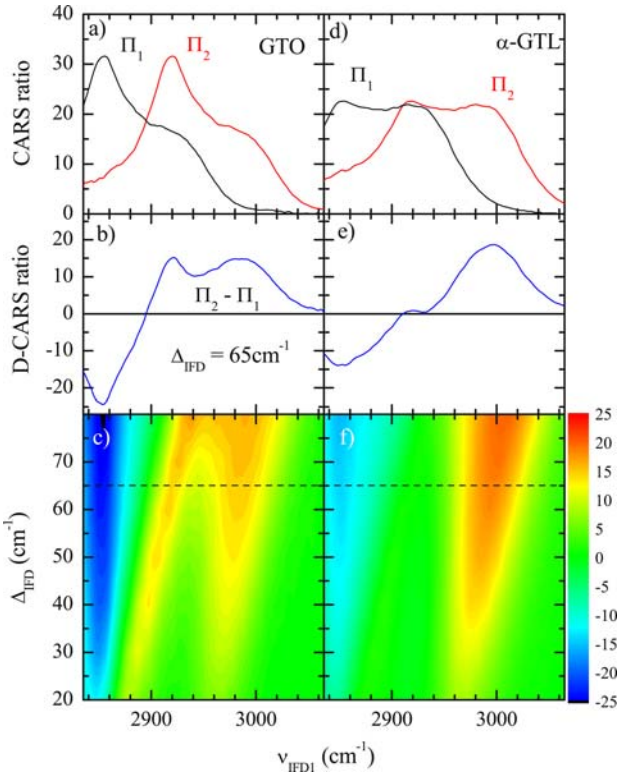

Figure 4 CARS and D-CARS ratio versus ν_{IFD1} calculated from the measured Π_1 CARS for GTO (**a**–**c**) and α-GTL (**d**–**f**). (**a**, **d**): CARS ratio $\hat{I}_{\mathrm{CARS}}$ of the two pairs $\Pi_{1,2}$ for $\Delta_{\mathrm{IFD}} = 65\,\mathrm{cm}^{-1}$. (**b**, **e**) D-CARS ratio $\hat{I}_{\mathrm{DCARS}}$ for $\Delta_{\mathrm{IFD}} = 65\,\mathrm{cm}^{-1}$. (**c**, **f**) D-CARS ratio $\hat{I}_{\mathrm{DCARS}}$ as function of Δ_{IFD} on a color scale as indicated.

between the single-pair CARS ratio of GTO, which has a pronounced peak at around 2850 cm^{-1} and a shoulder around 2930 cm^{-1}, and α-GTL which has a "flat-hat" lineshape with both bands equally intense, manifest as a D-CARS ratio which is nearly zero for α-GTL at 2930 cm^{-1} and significantly larger than zero for GTO. Figure 4c, f show the dependence of $\hat{I}_{DCARS}$ on Δ_{IFD}. Considering the limited bandwidth of the 100 fs laser system, the value $\Delta_{IFD} = 65\,cm^{-1}$ chosen for the D-CARS experiment represents a compromise between having a large difference in $\hat{I}_{DCARS}$ to distinguish GTO and GTL and maintaining sufficient temporal overlap of pump and Stokes in both pairs.

Measured D-CARS ratio spectra using both pairs are shown in Figure 5 in the CH-stretch range using both the 100 fs laser system (top panel) and the 5 fs system (center, bottom). They confirm the expected behavior from the simulations, with α-GTL and γ-GTL exhibiting $\hat{I}_{DCARS}$ (2930 cm^{-1}) ≈ 0 while GTC and GTO showing $\hat{I}_{DCARS}$ (2930 cm^{-1}) > 0, and all the lipids have a negative D-CARS at around 2850 cm^{-1} and a positive D-CARS at around 2990 cm^{-1}. The bottom panels in Figure 5 show the corresponding $\hat{I}_{DCARS}(x, y)$ images measured on the LDs, which reveal that D-CARS can be used to distinguish poly-unsaturated disordered lipids from more ordered unsaturated or mono-saturated ones by simply looking at $\hat{I}_{DCARS}$ at a specific $\nu_{IFD1,2}$. Note also the suppression of the non-resonant CARS background from the agarose gel surrounding each LD in D-CARS [10].

Measured D-CARS spectra are shown in Figure 6 in the fingerprint range using the 5 fs system with a $\Delta_{IFD} = 20\,cm^{-1}$ which is comparable to the spectral resolution and the Raman linewidth of the resonances in this range. Hence $\hat{I}_{DCARS}$ can be considered as the spectral derivative of $\hat{I}_{CARS}$, which for small resonant contributions is given by $\partial_{\omega_\delta}\Re\{\chi_R^{(3)}\} = R(\omega_\delta^2 - \Gamma^2)/(\omega_\delta^2 + \Gamma^2)^2$, and thus recover a lineshape similar to that of spontaneous Raman [11]. As expected, the C=C stretch at around 1660 cm^{-1} is absent in $\hat{I}_{DCARS}(\nu_{IFD1})$ of GTC and present for all other unsaturated lipids. The D-CARS images (bottom panels in Figure 6) measured on the LDs at the C=C stretch show the difference between the saturated GTC lipid ($\hat{I}_{DCARS} \approx 0$) and the unsaturated ones ($\hat{I}_{DCARS} > 0$), demonstrating that D-CARS at specific wavenumbers is a valuable tool to chemically distinguish saturated from unsaturated lipids. We note however that the values of $\hat{I}_{DCARS}$ from resonant contributions in the fingerprint wavenumber region are much lower than in the CH-stretch, hence small alignment artifacts due to e.g. non-perfect spatial overlap of Π_1 and Π_2 become critical. This is for example the case in the images shown for GTL where a spatial differential is visible. We also note that although GTL has three

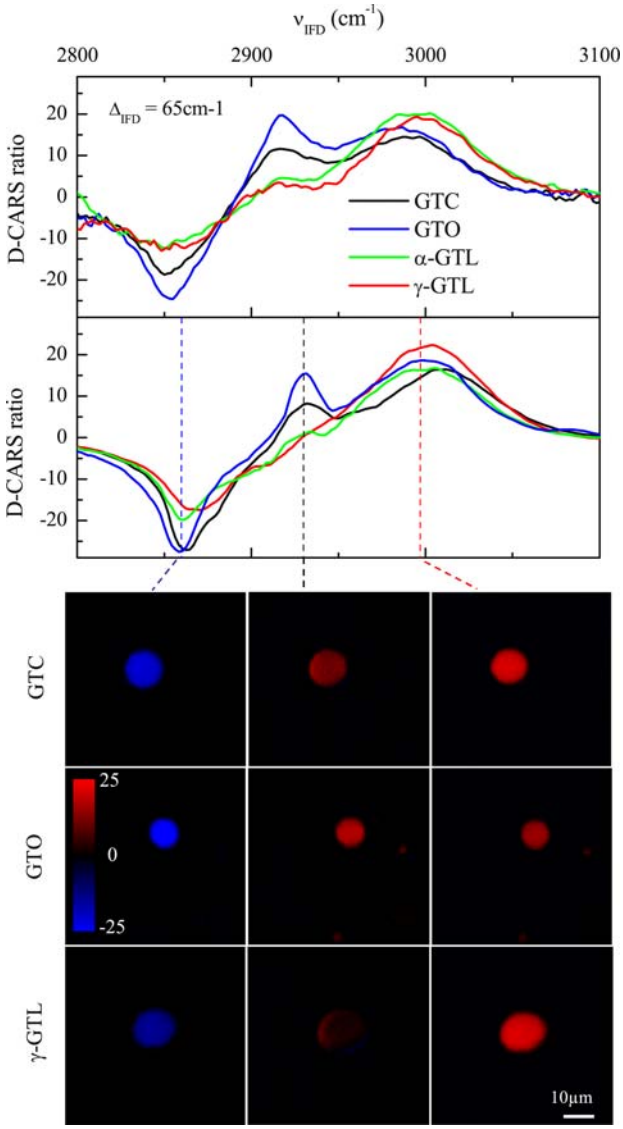

Figure 5 Measured $\hat{I}_{DCARS}$ spectra in the CH-stretch region at $\Delta_{IFD} \sim 65\,cm^{-1}$ for different lipids as indicated using the 100 fs laser system (top) and the 5 fs system (center, bottom). The bottom panels show $\hat{I}_{DCARS}(x, y)$ images through the center of LDs at ν_{IFD1}, indicated by corresponding dashed lines (blue 2860 cm^{-1}, black 2930 cm^{-1}, red 2997 cm^{-1}) on a color scale as shown. Pump power on each pair 16 mW, Stokes power on each pair 8 mW, objective 20 × 0.75 NA, 10 μs pixel dwell time, 0.3 μm pixel size.

double bonds, $\hat{I}_{DCARS}$ at around 1660 cm^{-1} for GTL even when scaled to the 1450 cm^{-1} resonance for relative comparison [8] remains comparable to that of GTO. This is attributed to the larger linewidth of the C=C resonance for GTL compared to GTO (see Figure 1) considering that at resonance $\hat{I}_{DCARS}$ is scaling as I_R/Γ.

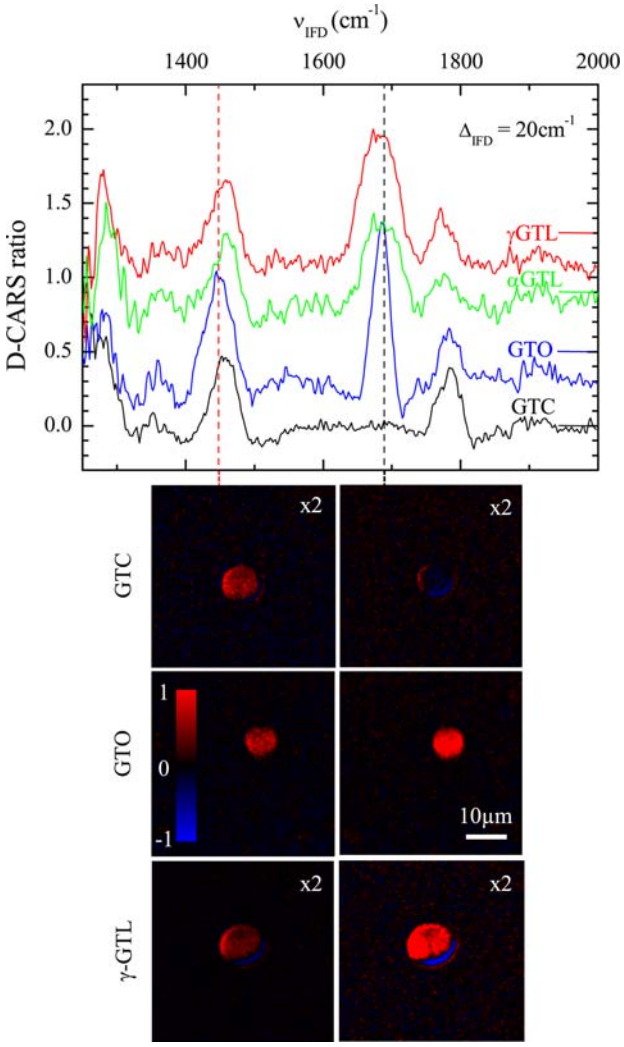

Figure 6 Measured $\hat{I}_{DCARS}$ in the fingerprint region with $\Delta_{IFD} = 20\,cm^{-1}$ for different lipids using the 5 fs system. Curves are vertically displaced for clarity, as indicated by offset lines. The bottom panels show $\hat{I}_{DCARS}(x, y)$ images of LDs on a color scale at the two ν_{IFD1} indicated by corresponding dashed lines (red 1448 cm^{-1}, black 1689 cm^{-1}). $\hat{I}_{DCARS}$ has been multiplied by two in the images for GTC and γ-GTL as indicated, in order to have comparable values at 1448 cm^{-1}. Pump power on each pair 16 mW, Stokes power on each pair 8 mW, objective 20 × 0.75 NA, 10 μs pixel dwell time, 0.3 μm pixel size.

4. Conclusions

In summary, we have demonstrated that differential-CARS microscopy using femtosecond pulses spectrally focussed by glass dispersion is able to distinguish poly-unsaturated glyceryl trilinolenate from the more ordered mono-unsaturated glyceryl trioleate and saturated glyceryl tricaprylate and glyceryl tristearate without the need of slow CARS multiplex acquisition and analysis. Spectral signatures of disorder which appear in the CH-stretch band of the Raman spectrum at around 2930 cm^{-1} correlate well with D-CARS measured as CARS intensity difference between the bands at around 2930 cm^{-1} and 2850 cm^{-1}. In particular poly-unsaturated glyceryl trilinolenate exhibit a "flat-hat" CARS spectrum with equally intense bands and hence zero D-CARS, while all other lipids exhibit a positive D-CARS. As a proof-of principle, D-CARS images were acquired on micron-sized lipid droplets at specific wavenumbers to directly distinguish glyceryl trilinolenate from the other lipids based solely on the D-CARS contrast. Similarly, spectral signatures of the degree of poly-unsaturation which appear in the fingerprint region of the Raman spectrum correlate with D-CARS spectra and images and enabled to distinguish the saturated glyceryl tricaprylate from the unsaturated lipids. Hence by overcoming the slow image acquisition of multiplex CARS and yet demonstrating sufficient chemical specificity to distinguish different lipid types, D-CARS has the potential to enable investigation of lipid composition of cytosolic lipid droplets, label-free, in living cells. We are presently evaluating this potential by imaging stem-cell derived human adipoctyes fed with saturated and unsaturated fatty acids to determine differences in lipid chemical contrast with D-CARS. The outcome of this study will be published in a future work.

Acknowledgements This work was funded by the UK BBSRC Research Council (grant n. BB/H006575/1). CDN acknowledges financial support by the President's Research Scholarship programme of Cardiff University, FM acknowledges financial support from the UK EPSRC Research Council (grant n. EP/H45848/1). PB acknowledges the UK EPSRC Research Council for her Leadership fellowship award (grant n. EP/I005072/1). The authors acknowledge the European Union COST action MP0603 "Chemical imaging by means of CARS microscopy (microCARS)" for supporting a short-term mission of IP to the University of Twente to perform some of the Raman spectroscopy shown in this work. The authors also acknowledge scientific discussions and support in LD sample preparation by Peter Watson.

Author biographies Please see Supporting Information online.

References

[1] M. Digel, R. Ehehalt, and J. Füllekrug, FEBS Letters **584**, 2168–2175 (2010).
[2] R. V. Farese and T. C. Walther, Cell **139**, 855 (2009).
[3] L. L. Listenberger and D. A. Brown, Curr. Protoc. Cell Biol. **24.2**, 24.2.1 (2007).

[4] J. Cheng, A. Fujita, Y. Ohsaki, M. Suzuki, Y. Shinohara, and T. Fujimoto, Histochem. Cell Biol. **132**, 281 (2009).
[5] M. Muller and A. Zumbusch, Chem. Phys. Chem. **8**, 2156 (2007).
[6] T. T. Le, S. Yue, and J.-X. Cheng, J. Lipid Res. **51**, 3091 (2010).
[7] J. P. Pezacki, J. A. Blake, D. C. Danielson, D. C. Kennedy, R. K. Lyn, and R. Singaravelu, Nat. Chem. Biol. **7**, 137 (2011).
[8] H. A. Rinia, K. N. J. Burger, M. Bonn, and M. Müller, Biophys. J. **95**, 4908 (2008).
[9] E. M. Vartiainen, H. A. Rinia, M. Müller, and M. Bonn, Opt. Express **14**, 3622 (2006).
[10] I. Rocha-Mendoza, W. Langbein, P. Watson, and P. Borri, Opt. Lett. **34**, 2258 (2009).
[11] W. Langbein, I. Rocha-Mendoza, and P. Borri, Appl. Phys. Lett. **95**, 081109 (2009).
[12] V. V. Pully, A. Lenferink, and C. Otto, J. Raman Spectrosc. **41**, 599–608 (2010).
[13] I. Rocha-Mendoza, W. Langbein, and P. Borri, Appl. Phys. Lett. **93**, 201103 (2008).
[14] I. Pope, W. Langbein, P. Watson, and P. Borri, unpublished.
[15] P. V. Joke De Gelder, Kris De Gussem, and L. Moens, J. Raman Spectrosc. **38**, 1133 (2007).
[16] S. P. Verma and D. F. Wallach, Biochim. Biophys. Acta **486**, 217 (1977).
[17] R. N. Jones and R. A. Ripley, Can. J. Chem. **42**, 305 (1964).
[18] J. Sebek, L. Pele, E. O. Potma, and R. Benny Gerber, Phys. Chem. Chem. Phys. **13**, 12724 (2011).
[19] W. Langbein, I. Rocha-Mendoza, and P. Borri, J. Raman Spectrosc. **40**, 800 (2009).

Biomedical Optics EXPRESS

Hyperspectral and differential CARS microscopy for quantitative chemical imaging in human adipocytes

Claudia Di Napoli,[1] Iestyn Pope,[1] Francesco Masia,[2] Peter Watson,[1] Wolfgang Langbein,[2] and Paola Borri[1,*]

[1] *School of Biosciences, Cardiff University, Cardiff CF10 3US, UK*
[2] *School of Physics and Astronomy, Cardiff University, Cardiff CF24 3AA, UK*
[*] *borrip@cf.ac.uk*

Abstract: In this work, we demonstrate the applicability of coherent anti-Stokes Raman scattering (CARS) micro-spectroscopy for quantitative chemical imaging of saturated and unsaturated lipids in human stem-cell derived adipocytes. We compare dual-frequency/differential CARS (D-CARS), which enables rapid imaging and simple data analysis, with broadband hyperspectral CARS microscopy analyzed using an unsupervised phase-retrieval and factorization method recently developed by us for quantitative chemical image analysis. Measurements were taken in the vibrational fingerprint region (1200-2000/cm) and in the CH stretch region (2600-3300/cm) using a home-built CARS set-up which enables hyperspectral imaging with 10/cm resolution via spectral focussing from a single broadband 5 fs Ti:Sa laser source. Through a ratiometric analysis, both D-CARS and phase-retrieved hyperspectral CARS determine the concentration of unsaturated lipids with comparable accuracy in the fingerprint region, while in the CH stretch region D-CARS provides only a qualitative contrast owing to its non-linear behavior. When analyzing hyperspectral CARS images using the blind factorization into susceptibilities and concentrations of chemical components recently demonstrated by us, we are able to determine vol:vol concentrations of different lipid components and spatially resolve inhomogeneities in lipid composition with superior accuracy compared to state-of-the art ratiometric methods.

OCIS codes: (180.5655) Raman microscopy; (300.6230) Spectroscopy, coherent anti-Stokes Raman scattering.

References and links

1. A. Zumbusch, W. Langbein, and P. Borri, "Nonlinear vibrational microscopy applied to lipid biology," Prog. Lipid Res. **52**, 615–632 (2013).
2. J. P. Pezacki, J. A. Blake, D. C. Danielson, D. C. Kennedy, R. K. Lyn, and R. Singaravelu, "Chemical contrast for imaging living systems: molecular vibrations drive cars microscopy," Nat. Chem. Biol. **7**, 137–145 (2011).
3. M. Digel, R. Ehehalt, and J. Füllekrug, "Lipid droplets lighting up: Insights from live microscopy," FEBS Lett. **584**, 2168–2175 (2010).
4. T. C. Walther and R. V. Farese Jr, "Lipid droplets and cellular lipid metabolism," Annu. Rev. Biochem. **81**, 687–714 (2012).
5. S. Fukumoto and T. Fujimoto, "Deformation of lipid droplets in fixed samples," Histochem. Cell Biol. **118**, 423–428 (2002).

#206105 - $15.00 USD Received 11 Feb 2014; revised 9 Mar 2014; accepted 9 Mar 2014; published 2 Apr 2014

6. X. Nan, J. X. Cheng, and X. S. Xie, "Vibrational imaging of lipid droplets in live fibroblast cells with coherent anti-stokes raman scattering microscopy," J. Lipid Res. **44**, 2202–2208 (2003).
7. Y. Ohsaki, Y. Shinohara, M. Suzuki, and T. Fujimoto, "A pitfall in using bodipy dyes to label lipid droplets for fluorescence microscopy," Histochem. Cell Biol. **133**, 477–480 (2010).
8. M. Paar, C. Jüngst, N. A. Steiner, C. Magnes, F. Sinner, D. Kolb, A. Lass, R. Zimmermann, A. Zumbusch, S. D. Kohlwein, and H. Wolinski, "Remodeling of lipid droplets during lipolysis and growth in adipocytes," J. Biol. Chem. **287**, 11164–11173 (2012).
9. E. M. Vartiainen, H. A. Rinia, M. Müller, and M. Bonn, "Direct extraction of raman line-shapes from congested cars spectra," Opt. Express **14**, 3622–3630 (2006).
10. Y. Liu, Y. J. Lee, and M. T. Cicerone, "Broadband cars spectral phase retrieval using a time-domain kramers-kronig transform," Opt. Lett. **34**, 1363–1365 (2009).
11. H. A. Rinia, K. N. J. Burger, M. Bonn, and M. Müller, "Quantitative label-free imaging of lipid composition and packing of individual cellular lipid droplets using multiplex cars microscopy," Biophys. J. **95**, 4908–4914 (2008).
12. I. Rocha-Mendoza, W. Langbein, P. Watson, and P. Borri, "Differential coherent anti-stokes raman scattering microscopy with linearly-chirped femtosecond laser pulses," Opt. Lett. **34**, 2258–2260 (2009).
13. W. Langbein, I. Rocha-Mendoza, and P. Borri, "Single source coherent anti-stokes raman microspectroscopy using spectral focusing," Appl. Phys. Lett. **95**, 081109 (2009).
14. I. Rocha-Mendoza, P. Borri, and W. Langbein, "Quadruplex cars micro-spectroscopy," J. Raman Spectr. **44**, 255–261 (2013).
15. C. Di Napoli, F. Masia, I. Pope, C. Otto, W. Langbein, and P. Borri, "Chemically-specific dual/differential cars micro-spectroscopy of saturated and unsaturated lipid droplets," J. Biophotonics **7**, 68–76 (2014 (2012 online)).
16. F. Masia, A. Glen, P. Stephens, P. Borri, and W. Langbein, "Quantitative chemical imaging and unsupervised analysis using hyperspectral coherent anti-stokes raman scattering microscopy," Anal. Chem. **85**, 10820–10828 (2013).
17. I. Pope, W. Langbein, P. Watson, and P. Borri, "Simultaneous hyperspectral differential-CARS, TPF and SHG microscopy with a single 5 fs ti:sa laser," Opt. Express **21**, 7096–7106 (2013).
18. T. Hellerer, A. M. Enejder, and A. Zumbusch, "Spectral focusing: High spectral resolution spectroscopy with broad-bandwidth laser pulses," Appl. Phys. Lett. **85**, 25–27 (2004).
19. I. Rocha-Mendoza, W. Langbein, and P. Borri, "Coherent anti-stokes raman microspectroscopy using spectral focusing with glass dispersion," Appl. Phys. Lett. **93**, 201103 (2008).
20. L. L. Listenberger and D. A. Brown, "Fluorescent detection of lipid droplets and associated proteins," Curr. Protoc. Cell Biol. **24.2**, 24.2.1–24.2.11 (2007).
21. L. Hodson, C. M. Skeaff, and B. A. Fielding, "Fatty acid composition of adipose tissue and blood in humans and its use as a biomarker of dietary intake," Progress in Lipid Research **47**, 348–380 (2008).
22. D. Gachet, F. Billard, N. Sandeau, and H. Rigneault, "Coherent anti-Stokes Raman scattering (CARS) microscopy imaging at interfaces: evidence of interference effects" Opt. Express **15**, 10408–10420 (2007).
23. A. M. Barlow, K. Popov, M. Andreana, D. J. Moffatt, A. Ridsdale, A. D. Slepkov, J. L. Harden, L. Ramunno, and A. Stolow, "Spatial-spectral coupling in coherent anti-Stokes Raman scattering microscopy" Opt. Express **21**, 15298–15307 (2013).

1. Introduction

Optical microscopy is an indispensable tool that is driving progress in cell biology, and is still the only practical means of obtaining spatial and temporal resolution within living cells and tissues. Coherent anti-Stokes Raman scattering microscopy has emerged in the last decade as a multiphoton technique able to image living cells label-free in real time with high three-dimensional spatial resolution and chemical specificity [1, 2]. CARS is a third-order nonlinear process where molecular vibrations are coherently driven by the interference between two optical fields (pump and Stokes) and a third field (the pump itself in a two-pulse CARS system) is used to generate anti-Stokes Raman scattering from the driven vibrations. Owing to the coherence of the driving process, CARS benefits, unlike spontaneous Raman, from the constructive interference of light scattered by spectrally overlapping vibrational modes within the focal volume, thus enabling fast acquisition at moderate powers compatible with live cell imaging. Being a nonlinear process, CARS is generated only in the focal volume where high photon densities are reached, allowing for an intrinsic 3D spatial resolution (optical sectioning) similar to other multiphoton microscopy techniques such as two-photon fluorescence and second-harmonic generation.

#206105 - $15.00 USD Received 11 Feb 2014; revised 9 Mar 2014; accepted 9 Mar 2014; published 2 Apr 2014

CARS microscopy has proven to be particularly successful in imaging unstained lipids especially when concentrated in vesicles such as cytosolic lipid droplets (LDs), owing to the large number of identical CH bonds in the lipid acyl chain. LDs are found in many cell types and consist of a hydrophobic core containing neutral lipids, mainly triglycerides and sterol esters, surrounded by a phospholipid monolayer. During the last two decades, it has become apparent that cytosolic LDs are highly dynamic organelles beyond static energy deposits, and are involved in the fine regulation of lipid metabolism and in turn the pathophysiology of metabolic diseases such as atherosclerosis, diabetes and obesity [3, 4]. The recent development of CARS micro-spectroscopy has further boosted this interest by opening the prospect to image LDs in living cells with an unprecedented intrinsic chemical specificity and without introducing staining artifacts. Such artifacts include for example cytosolic LD fusion artificially induced by standard staining protocols [5–7]. Recently, it became possible to gain detailed quantitative insights about the fusion behavior of unstained LDs in adipocytes with CARS time-course experiments over more than a week on the same cells without the limitation of marker bleaching [8].

Among the various technical implementations of CARS microscopy reported to date, hyperspectral CARS imaging is receiving increasing attention due to its superior chemical specificity compared to single-frequency CARS. In hyperspectral CARS, a CARS spectrum is measured at each spatial position, either by taking a series of spatially-resolved images at different vibrational frequencies, or by acquiring a spectrum at each spatial point following simultaneous excitation of several vibrations (the latter is also called multiplex CARS). Since the CARS intensity is proportional to the absolute square of the third-order susceptibility it contains the interference between vibrationally resonant and non-resonant terms and results in a non-trivial lineshape and dependence on the concentration of chemical components. In hyperspectral CARS, this limitation can be overcome by acquiring CARS intensity spectra over a sufficiently wide spectral range and analyzing them to retrieve Raman-like spectra linear in the concentration of chemical components [9, 10].

Multiplex CARS microscopy has previously been used to monitor the composition of LDs in differentiated mouse adipocytes (3T3-L1 cells) under different dietary conditions [11]. In Ref. [11], CARS spectra were analyzed using the maximum entropy method to derive the imaginary part of the CARS susceptibility resulting in Raman-like spectra. Ratios between amplitudes of these retrieved spectra at different vibrational resonances were then used to infer information about the acyl-chain order and the ratio between saturated and unsaturated fatty acids. This approach allowed the identification of variations in the composition of LDs in individual cells. However, measurements had to be taken on fixed cells since multiplex CARS typically requires acquisition times of ~ 10 ms per spectrum and in turn tens of minutes for the acquisition of spatially-resolved 3D images.

We recently demonstrated a method named dual-frequency/differential CARS (D-CARS) micro-spectroscopy where two vibrational frequencies are excited and probed simultaneously, and the sum and difference between the corresponding CARS intensities is detected by a single-channel fast photomultiplier using phase-sensitive frequency filtering [12–14]. This provides improved chemical specificity compared to single-frequency CARS and rejection of the spectrally-constant non-resonant CARS background without significant post-acquisition data analysis, while maintaining the high imaging speed of single-frequency CARS compatible with live cell imaging. We recently demonstrated the applicability of this method to distinguish in a rapid label-free way the chemical composition of micron-sized lipid droplet model systems consisting of pure triglycerides types (saturated and unsaturated) in an agarose gel [15]. However the question whether the technique would be able to distinguish different lipid compositions in a more complex chemical scenario such as LDs in cells remained open. We also recently demonstrated a novel method to analyze hyperspectral CARS microscopy images of organic

#206105 - $15.00 USD Received 11 Feb 2014; revised 9 Mar 2014; accepted 9 Mar 2014; published 2 Apr 2014

materials and biological samples resulting in an unsupervised and unbiased quantitative chemical analysis, which we named blind factorization into susceptibilities and concentrations of chemical components (FSC^3) [16].

In the present work, we have investigated the chemical composition of LDs in human adipose-derived stem cells (ADSCs) cultured with known supplemented mixtures of saturated and unsaturated fatty acids. We used both D-CARS and hyperspectral CARS microscopy in the vibrational fingerprint region (1200-2000/cm) and in the CH stretch region (2600-3300/cm) with FSC^3 data analysis, and quantitatively assessed and compared the capabilities of both techniques in this chemically-complex biologically relevant scenario.

2. Materials and methods

2.1. CARS micro-spectroscopy set-up

Hyperspectral CARS and D-CARS images were acquired with a home-built set-up based on a single Ti:Sapphire 5 fs broadband (660-970 nm) laser system as described in detail in Ref. [17]. Briefly, pump and Stokes components for the CARS excitation are obtained by spectrally separating the broadband laser output with an appropriate sequence of dichroic beam splitters, resulting in a pump (Stokes) with center wavelength at 682 nm (806 nm) and a bandwidth of 65 nm (200 nm). A spectral resolution of 10/cm is achieved through spectral focusing [18], namely an equal linear chirp applied to pump and Stokes in order to maintain a constant instantaneous frequency different (IFD) through the stretched pulse duration, using SF57 glass blocks of appropriate length [19]. We perform CARS spectroscopy rapidly without adjustments to the laser by simply changing the relative delay time t_0 between pump and Stokes pulses which results in a tuning of the IFD across the entire 1200-3800/cm vibrational range, owing to the large bandwidth of the Stokes pulse. D-CARS is implemented as described in our previous works [12, 17]. In this technique, the pump-Stokes pair is divided into two orthogonally polarized pairs, Π_1 and Π_2, with Π_2 travelling through an additional thin SF57 glass element and delayed by half the laser repetition period relative to Π_1. When the two pairs are recombined, a pulse sequence at twice the laser repetition rate is created where Π_1 excites the vibrational resonance ν_{IFD1} adjustable through t_0 and Π_2 excites the shifted resonance $\nu_{\mathrm{IFD2}} = \nu_{\mathrm{IFD1}} - \Delta_{\mathrm{IFD}}$ with the frequency difference Δ_{IFD} being determined by the thickness of the additional SF57 glass. By frequency analyzing the CARS signal, we can simultaneously detect the dc component proportional to the sum of the CARS intensity from Π_1 and Π_2 and the ac component at the pulse repetition rate proportional to the difference of the CARS intensity from Π_1 and Π_2. The excitation pulses were coupled into a commercial inverted microscope stand (Nikon Ti-U) via a home-built beam-scanning head. The microscope is equipped with a 20x 0.75 NA dry objective (Nikon CFI Plan Apochromat λ series) and the CARS signal is collected in forward direction with a 0.72 NA dry condenser, frequency selected by appropriate band-pass filters and detected by a photomultiplier tube (Hamamatsu H7422-40). The resulting CARS spatial resolution (FWHM of the intensity point-spread function) was measured to be 0.6 μm and 1.1 μm in the lateral (*xy*) and axial (*z*) direction, respectively [17]. A motorized sample stage enabled *xy* sample movement and a motorized objective focussing enabled *z* movement (Prior ProScan III).

The microscope stand was also equipped with differential interference contrast (DIC) optics and cells of interest were first identified with DIC. CARS hyperspectral *xy* images were acquired in the fingerprint region (1200-2000/cm) and in the CH region (2600-3300/cm) with 5/cm spectral steps. The reason for acquiring the two ranges separately is two-fold, as detailed in our previous work [17]. Firstly, non-linear chirp affecting the broadband Stokes pulse implies that the chirp on this pulse can be approximated as linear only for a limited wavelength range and thus requires different lengths of SF57 glass blocks to match the pump chirp at dif-

#206105 - $15.00 USD Received 11 Feb 2014; revised 9 Mar 2014; accepted 9 Mar 2014; published 2 Apr 2014

ferent Stokes centre wavelengths. Secondly, different detection bandwidth filters are needed for the two ranges, as shown in Table 1 in Ref. [17]. D-CARS *xy* images were acquired at wavenumbers maximizing the chemical contrast [15], as indicated in each figure. *xy* images were acquired using beam scanning with a pixel size of $0.3\times0.3\,\mu m^2$ and a pixel dwell time of $10\,\mu s$, resulting in 1.6 s acquisition time for a $120\times120\,\mu m^2$ single-frequency or D-CARS image. Correspondingly, a typical hyperspectral image stack with 100 spectral points required a total acquisition time of 160 s (less than 3 min). Images were acquired at a fixed *z* determined as the axial position for which most medium-sized (3-5 μm diameter) LDs are equatorially cut such that the lipid content of their inner core is optimally imaged. Non-resonant CARS spectra from glass were also recorded and used for normalization (i.e. measured CARS intensities in each sample were divided by the corresponding non-resonant CARS intensity in glass under the same excitation and detection conditions) in order to correct for the varying temporal overlap of pump and Stokes and to derive a CARS intensity ratio independent of excitation/detection parameters [15, 16]. All experiments were performed at room temperature.

2.2. Cell samples

Human ADSCs (Invitrogen) were cultured in low glucose Dulbecco's modified eagle medium and GlutaMAX™ supplemented with 10% mesenchymal stem cells qualified FBS, 75 μg/mL Gentamicin and 37.5 μg/mL Amphotericin. In order to induce differentiation into adipocytes, ADSCs were grown in StemPro® (Invitrogen) adipogenic differentiation media in accordance with the manufacturer's protocol. After 3 days, the medium was supplemented with a fatty acid-BSA complex resulting in 9.4 μg/mL of supplemented fatty acid in the final medium. Palmitic acid (PA) and α-linolenic acid (LA) complexes were prepared in house [20] with PA and LA purchased from Sigma-Aldrich. Structurally, PA is a saturated 16-carbon chain (*hexadecanoic acid*) and LA is a tri-unsaturated 18-carbon chain with *cis* double bonds at the 9, 12, and 15th position from the first carbon atom (*cis,cis,cis-9,12,15-octadecatrienoic acid*). Cells were grown for 3 additional days in the supplemented medium and then fixed in 4% formaldehyde-PBS solution. After fixation, coverslips containing cells were mounted onto standard glass slides using 120 μm thick imaging gaskets (Grace Bio-lab SecureSeal™) filled with water.

2.3. Data analysis

CARS and D-CARS images were background-corrected by subtracting an image measured under identical excitation/detection conditions but with pump and Stokes pulses out of time overlap. Note that, by simultaneous detection in the epi-direction [17], we could rule out the presence of a significant background arising from pump-Stokes two-photon absorption (which would be dependent on their time overlap) hence this background subtraction procedure is appropriate. Hyperspectral images were noise-filtered with a singular value decomposition (SVD) algorithm on the square root of the CARS intensity to retain only components above noise, as described in our recent work [16]. CARS intensity ratios were calculated by dividing the background-corrected CARS intensity by the corresponding non-resonant CARS intensity measured in glass under the same excitation and detection conditions. The phase-corrected Kramers-Kronig method [16] (PCKK) was used to retrieve from the CARS intensity ratio the complex CARS third-order susceptibility (normalized to the non-resonant value in glass) which is linear in the concentration of chemical components, and in particular its imaginary part $\Im(\tilde{\chi})$. We then used non-negative matrix factorization applied to the imaginary part and the non-resonant real part of the susceptibility with an additional concentration constraint (blind factorization into susceptibilities and concentrations of chemical components -FSC^3 method) to obtain susceptibility spectra of independently varying chemical components and their vol-

#206105 - $15.00 USD Received 11 Feb 2014; revised 9 Mar 2014; accepted 9 Mar 2014; published 2 Apr 2014

ume concentration [16]. As well as representing the full spatial distribution of CARS intensity ratios, the retrieved $\Im(\tilde{\chi})$ and the associated spatial maps of independently varying chemical components, we also calculated LD mean spectra by averaging spectra over more than 100 LDs for each group of cells fed with the same fatty acids (each group containing at least 6 differentiated cells). In this case only LDs with a diameter above $2\,\mu$m were considered, and the spectrum of each LD was taken by averaging over the LD core spatial region of constant CARS intensity, to take into account only regions completely filled with lipids.

3. Results and discussion

3.1. Hyperspectral CARS

Hyperspectral images of CARS intensity ratios and the corresponding phase-retrieved imaginary part $\Im(\tilde{\chi})$ are shown in Fig. 1 for human ADSCs grown in media supplemented with either saturated (palmitic) or unsaturated (α-linolenic) fatty acids. Images are shown at characteristic wavenumbers, and full spectra are given as averages over more than 100 LDs of spatially well resolved size. The CARS intensity ratio has a spectral shape affected by the interference between the resonant vibrational contribution and the non-resonant electronic contribution to the CARS susceptibility resulting in a dispersive lineshape in the fingerprint region and a spectral shape only qualitatively resembling a Raman spectrum in the CH stretch region. A Raman-like spectrum is recovered in the retrieved $\Im(\tilde{\chi})$ exhibiting the characteristic vibrational bands typical of neutral lipids [15]. In the fingerprint region bands are observed at around 1450/cm due to CH_2 and CH_3 deformations and at 1660/cm due to the C=C stretch vibration which is absent in saturated lipids. The weak band around 1740/cm is attributed to the C=O stretch from the ester bonds between glycerol and the fatty acids and demonstrates the storage of lipids in the form of triglycerides [15]. The CH stretch region is more congested with several overlapping resonances. The most prominent features are the band at around 2850/cm from the CH_2 symmetric stretch vibrational resonance and the broad shoulder at around 2930/cm which is a combination of CH_3 stretch vibrations and CH_2 asymmetric stretch enhanced by the broadening and shift of the CH deformations in the liquid phase. Polyunsaturated lipids which are liquid at room temperature exhibit a significant band around 2930/cm. The =CH stretch gives rise to a band around 3010/cm. We clearly observe that cells fed with LA which is poly-unsaturated have on average much more prominent bands at 1660/cm, 2930/cm and 3010/cm characteristic of the presence of unsaturated bonds compared to cells fed with PA. Noticeably, the retrieved spectrum of $\Im(\tilde{\chi})$ for these cells has a similar shape to the Raman spectrum of pure α-glyceryl trilinolenate [15] (particularly the relative amplitude between the 1660/cm and 1450/cm bands) indicating an efficient uptake and storage of LA in these samples. This is consistent with other findings in the literature indicating that the different fatty-acid composition in the medium does change the chemical composition of LDs in adipocytes [11]. Conversely, cells fed with PA still show the presence of unsaturated bonds. The average LD spectrum in these cells is similar to that measured for oleic acid [15, 16] which appears to be the main fatty acid component of the differentiation medium (cells grown in a medium supplemented with oleic acid also showed very similar spectra, data not shown). This suggests that under our experimental conditions, human ADSCs incorporate LA much more efficiently than PA. This point is discussed in greater detail in a following section.

3.2. Dual-frequency differential CARS

In a previous work we demonstrated that D-CARS, measuring the difference between the CARS intensity at suitable wavenumbers, is a tool to suppress the non-resonant background and perform chemically-discriminative imaging with fast acquisition speeds on LD model sys-

#206105 - $15.00 USD Received 11 Feb 2014; revised 9 Mar 2014; accepted 9 Mar 2014; published 2 Apr 2014

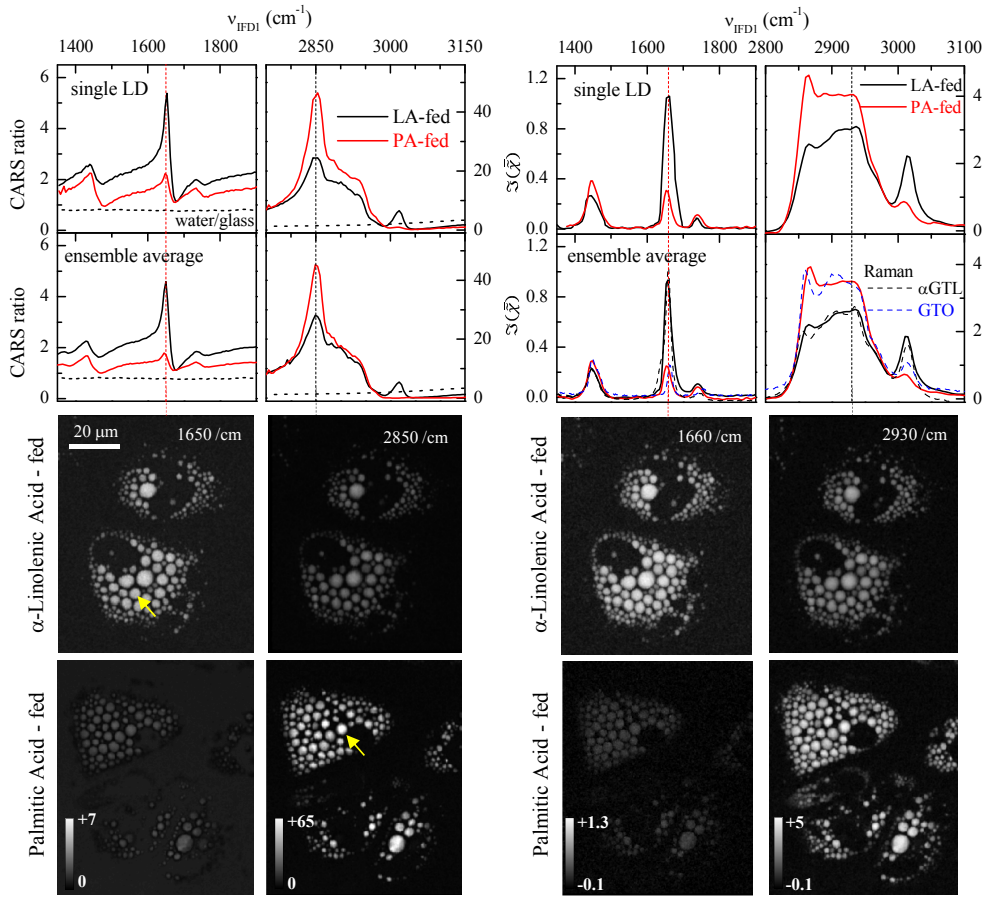

Fig. 1. CARS intensity ratio (left) and phase-retrieved imaginary part of the normalized susceptibility $\Im(\bar{\chi})$ (right). Images (lower panels) as well as spectra (upper panels) averaged over more than 100 LDs, and for the individual droplet indicated by the yellow arrow, are shown for human adipose-derived stem cells fed with palmitic acid (PA) and α-linolenic acid (LA). Raman spectra of α-glyceryl trilinolenate (αGTL) and glyceryl trioleate (GTO) are shown for comparison (dashed lines). In the CARS intensity ratio, the spectrum of the water to glass ratio is also shown. Images of the CARS intensity ratio are shown at 1650/cm and 2850/cm, as indicated by the vertical dotted lines in the spectra. Images of the imaginary part of the normalized susceptibility are shown at 1660/cm and 2930/cm. Linear grey scales are indicated. The pump power on the sample was 20 mW (14 mW) and the Stokes power was 10 mW (7 mW) for the fingerprint region (CH region); 10 μs pixel dwell time, 0.3 μm pixel size.

tems [15]. The purpose of this study is to investigate the validity of this technique in a more physiologically relevant but chemically complex case such as cytosolic LDs in adipocytes.

The D-CARS results corresponding to Fig. 1 are given in Fig. 2. The upper panel shows simulated D-CARS spectra constructed using the single-pair CARS intensity ratio of Fig. 1 and the experimental value of the wavenumber shift Δ_{IFD}. As described in detail in Ref. [15], we construct a shifted spectrum to represent the effect of the second pulse pair in the D-CARS experiment and calculate the difference accordingly. These calculations agree well with ex-

#206105 - $15.00 USD Received 11 Feb 2014; revised 9 Mar 2014; accepted 9 Mar 2014; published 2 Apr 2014

perimentally measured D-CARS spectra [15]. The experimental D-CARS images measured at selected wavenumbers are shown in the lower panels of Fig. 2.

In the fingerprint region, D-CARS images were measured for $\Delta_{\mathrm{IFD}} = 34$/cm. This value was chosen to provide the maximum D-CARS contrast since it is comparable to the wavenumber distance from the peak to the dip in the dispersive lineshape of the CARS ratio at around 1450/cm and 1660/cm. The simulated D-CARS spectra have a maximum at around 1470/cm and 1680/cm for which D-CARS images were acquired. The peak at 1680/cm is a measure of the abundance of the C=C stretch band in the LDs of cells fed with α-linolenic acid.

In the more congested CH region, D-CARS images were measured using $\Delta_{\mathrm{IFD}} = 65$/cm which enables distinction of saturated from poly-unsaturated triglycerides based on their different CARS intensity lineshapes and relative importance of the peak at 2850/cm and the broad shoulder at around 2930/cm, as discussed in details in Ref. [15]. Simulated D-CARS spectra have a maximum at around 2920/cm, which is more pronounced for cells fed with PA consistent with the presence of more saturated or mono-unsaturated fatty acids compared to cells fed with LA. D-CARS images are shown at 2920/cm and at 2990/cm for relative comparison (with D-CARS at 2990/cm being a measure of the amplitude of the broad shoulder in the CARS intensity spectrum, see sketch in Fig. 2). For the CARS intensity peak around 3010/cm characteristic of the =CH bond, D-CARS was acquired using $\Delta_{\mathrm{IFD}} = 27$/cm comparable to the linewith of this peak. Simulated D-CARS spectra show a maximum at 3045/cm proportional to the amplitude of this CARS intensity peak. Corresponding D-CARS images measured at 3045/cm show the presence of this peak for cells fed with LA.

We note that, although it might appear cumbersome to use different Δ_{IFD} in the D-CARS technique, the choice of which might not be straightforward without an a priori knowledge of the substance to be investigated, an approach which can be taken as a general rule for D-CARS is to use Δ_{IFD} comparable to the resonance linewidth.

3.3. Ratiometric analysis

As shown by Rinia *et al.* [11] a ratiometric analysis can be used to quantitatively determine the degree of C=C polyunsaturation and the order of lipids (i.e. their fluidity) in cytosolic LDs. In particular, the ratio of the phase-retrieved $\Im(\tilde{\chi})$ between 1660/cm and 1450/cm was shown to provide a quantitative measure for the degree of lipid-chain unsaturation. The ratio of $\Im(\tilde{\chi})$ between the band at around 2930/cm and the CH_2 symmetric stretch resonance at 2850/cm can be used as a measure of the disorder [15]. In Fig. 3 we show this ratiometric analysis performed both for D-CARS and the phase-retrieved $\Im(\tilde{\chi})$. Human ADSCs were fed with media supplemented with PA, LA and their mixtures. For each group of cells fed with one type of lipid-supplemented medium, the ratio was calculated on more than 100 LDs of resolved diameter and the average ratio together with its standard deviation in the statistics are shown as symbols and error bars in Fig. 3.

In the fingerprint region, the ratio measured using D-CARS coincides within errors with the ratio using $\Im(\tilde{\chi})$ and scales proportionally to the LA volume fraction used in the experiments (the dashed line in Fig. 3 shows the linear dependence proportional to the LA volume fraction). Since $\Im(\tilde{\chi})$ is linear in the concentration of chemical components [16], this result demonstrates that i) on average the cellular uptake of LA in the lipid droplets of ADSCs follows the LA relative concentration in the supplemented medium and ii) D-CARS is equally able to quantitatively determine the degree of C=C poly-unsaturation in cytosolic LDs, circumventing hyperspectral CARS measurements and data analysis. In the CH stretch region, $\Im(\tilde{\chi})$ ratios scale linearly with the LA volume fraction used in the experiments (see dashed lines), as expected from the linearity of the phase-retrieved imaginary part of the susceptibility. Conversely, D-CARS ratios are different from $\Im(\tilde{\chi})$ ratios and whilst showing a qualitatively similar trend to $\Im(\tilde{\chi})$ as a

#206105 - $15.00 USD Received 11 Feb 2014; revised 9 Mar 2014; accepted 9 Mar 2014; published 2 Apr 2014

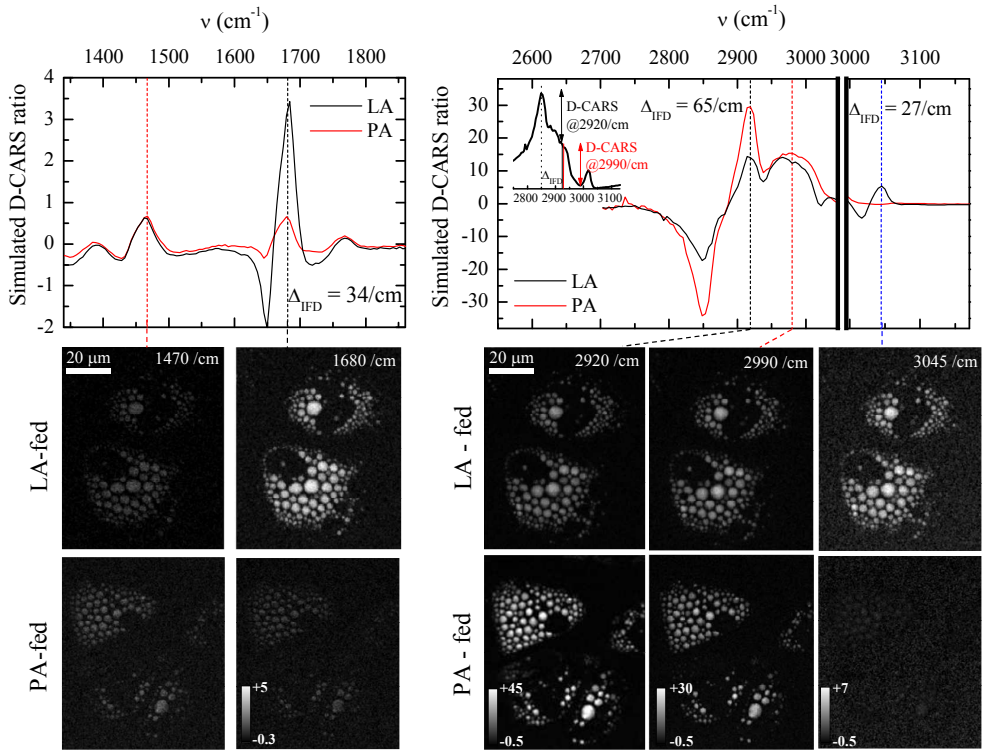

Fig. 2. D-CARS imaging in the fingerprint and CH region of human ADSCs fed with different fatty acids as given in Fig. 1. Top: D-CARS spectra calculated from the measured CARS intensity ratios shown in Fig. 1 with Δ_{IFD} as indicated. In the CH stretch region, the inset schematically shows D-CARS amplitudes (vertical arrows) at 2920/cm and 2990/cm in relation to the CARS intensity linshape. Bottom: D-CARS images of adipocytes measured at the wavenumbers indicated by corresponding dotted lines (1470 and 1680/cm in the fingerprint region; 2920, 2990 and 3045/cm in the CH region) on a grey scale as shown. Pump power on each pair 16 mW, Stokes power on each pair 8 mW, 10 μs pixel dwell time, 0.3 μm pixel size.

function of the lipid mixture they exhibit significant quantitative deviations. This is due to the non-linear concentration dependence of CARS which is retained in D-CARS in the CH stretch region.

3.4. Quantitative chemical analysis using FSC^3

A key point in CARS micro-spectroscopy is the determination of the spatial distribution of chemical components. Hence, beside calculating D-CARS and $\Im(\tilde{\chi})$ as average values over many LDs as shown in Fig. 3, we want to address the question of what is the spatially-resolved chemical composition of LDs even within cells fed with one type of lipid. The error bars in the ratios of $\Im(\tilde{\chi})$ in Fig. 3 give us a measure of the distribution width in the degree of unsaturation and lipid order in the investigated LD ensembles, and suggest fairly homogeneous distributions in most cases. They also include measurement noise, which is however not significant for the observed distribution width, also due to the noise filtering [16] with SVD. A much more detailed picture is obtained using the FSC^3 method [16].

#206105 - $15.00 USD Received 11 Feb 2014; revised 9 Mar 2014; accepted 9 Mar 2014; published 2 Apr 2014

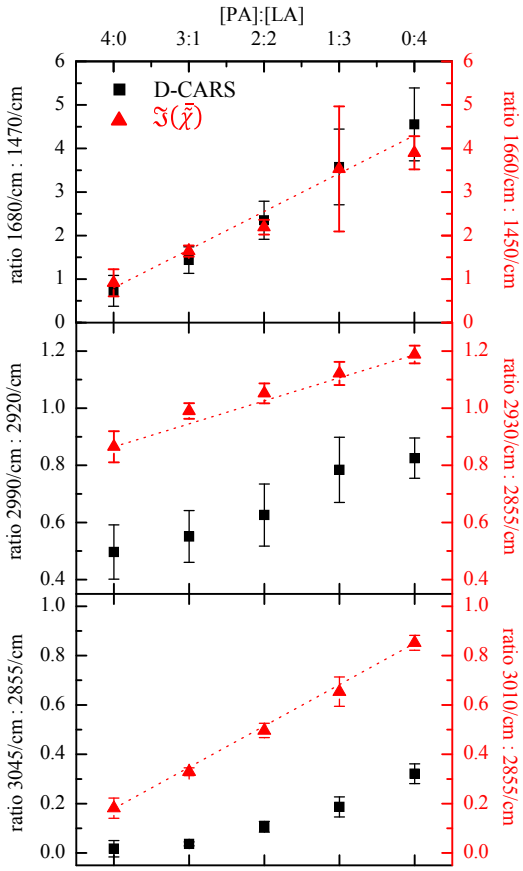

Fig. 3. Ratiometric analysis of measured D-CARS ratio and phase-retrieved $\Im(\bar{\chi})$ in human ADSCs fed with mixtures of palmitic acid and α-linolenic acid with a vol:vol ratio as indicated. Black squares give average D-CARS intensity ratios, red triangles give average ratios of $\Im(\bar{\chi})$. The errors bars show the standard deviation over the analyzed droplets ensemble. Dotted lines are the calculated linear dependencies according to the mixture ratio from the values with pure PA and LA. Top: D-CARS ratio between 1680/cm and 1470/cm and corresponding ratio of $\Im(\bar{\chi})$ at 1660/cm and 1450/cm. Middle: D-CARS intensity ratio between 2990/cm and 2920/cm and corresponding ratio of $\Im(\bar{\chi})$ at 2930/cm and 2855/cm. Bottom: D-CARS intensity ratio between 3045/cm and 2855/cm and corresponding ratio of $\Im(\bar{\chi})$ at 3010/cm and 2855/cm.

Fig. 4 shows the FSC^3 results on the investigated human ADSCs fed with PA, LA and the equal volume mixture of both. In this analysis we considered 5 chemical components which was the minimum number needed to well represent the chemical composition of all samples. Their spectral profile and spatial distribution in volume concentration units is shown in the figure. The component number 1 with the highest volume fraction in all samples is water (shown in Fig. 4 for cells fed with LA). The main lipid component of medium-large sized cytosolic LDs appears as component 4 in the analysis and has the same characteristic spectrum as shown in Fig. 1. Its spatial distribution is color–coded in red in the red–green–blue (RGB) overlay of Fig. 4. Moreover, a chemical component spatially located in the cytosol and the nucleus is distinguished (component 3, spatial distribution color–coded in blue), with a spectrum having a

#206105 - $15.00 USD Received 11 Feb 2014; revised 9 Mar 2014; accepted 9 Mar 2014; published 2 Apr 2014

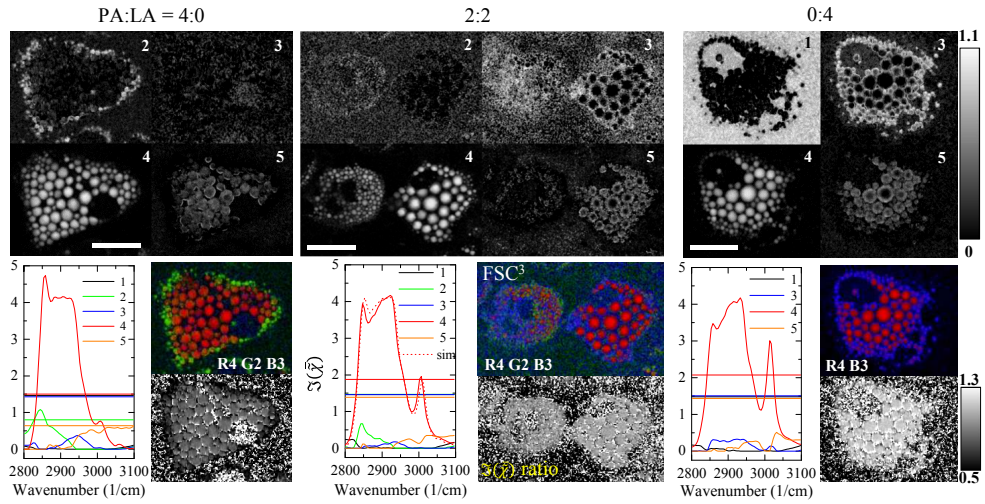

Fig. 4. Results of FSC^3 on the phase-retrived $\Im(\bar{\tilde{\chi}})$ in human ADSCs fed with PA, LA and an equal mixture (vol:vol) of PA and LA. Top: Spatial distributions of the volume concentration on a gray scale from 0 (black) to 1.1 (white) for the 5 components considered in the analysis. Bottom: spectra of $\Im(\bar{\tilde{\chi}})$ and its real part (horizontal lines) for the corresponding components. In the spectra for the PA:LA mixture the thin dotted line is an equally weighted superposition from component 4 of cells fed with PA and LA only. RGB overlays show the spatial distribution of the concentration for specific components as indicated. Below the RGB overlays, the spatial distribution of the $\Im(\bar{\tilde{\chi}})$ ratio between 2930/cm and 2855/cm is shown on a gray scale, as indicated. The scale bars indicate 20 μm.

pronounced band at around 2930/cm characteristic of proteins and nucleic acids (partly mixed with lipid resonances for cells fed with LA) [16]. We also distinguish a component 5 located at or near the LDs with a spectral shape which is not of straightforward interpretation, and might be a result of image artifacts at the LDs. Indeed, distortions of the excitation fields by spatial refractive index structures lead to a modulation of the CARS intensity as discussed in [22] and might give rise to artifacts in the retrieved concentrations. As discussed in detail in our recent work [16], the error of the factorization in the FSC^3 analysis is quantified by the relative spectral error $\mathbf{E}_\mathrm{S}$ and the relative concentration error $\mathbf{E}_\mathrm{C}$. These are shown in Fig. 5 for the analysis reported in Fig. 4. The spectral error $\mathbf{E}_\mathrm{S}$ is a measure of the residual in the factorization of the phase-retrieved data set into the product of a matrix of concentrations and a non-negative matrix of spectra of the chemical components. The maximum relative spectral error in Fig. 5 is around 30% and is localized at large lipid droplets. The concentration error is defined as $\mathbf{E}_\mathrm{C} = \left\{ (\sum_{k=1}^{K} c_p^{\{k\}}) - 1 \right\}$ where $c_p^{\{k\}}$ is the non-negative relative volume concentration of the k-th chemical component at voxel p. Fig. 5 shows the spatial distribution of $\mathbf{E}_\mathrm{C}$, with largest relative errors located at the large lipid droplets and correlating with component 5, possibly due to distortions of the excitation fields by the spatial refractive index structure [22]. Note that the spatial-spectral coupling effects of the type described in [23] are expected to be weak if the resonant CARS contribution is much larger than the non-resonant one, which is the case in the CH stretch region and for droplets comparable or larger than the focal volume.

Interestingly, in cells fed with PA, smaller LDs (which tend to be located in the outer periphery of differentiated cells) exhibit a distinct lipid spectrum more resembling that of a saturated lipid such as PA (component 2 in the analysis, spatial distribution color–coded in green). Con-

#206105 - $15.00 USD Received 11 Feb 2014; revised 9 Mar 2014; accepted 9 Mar 2014; published 2 Apr 2014

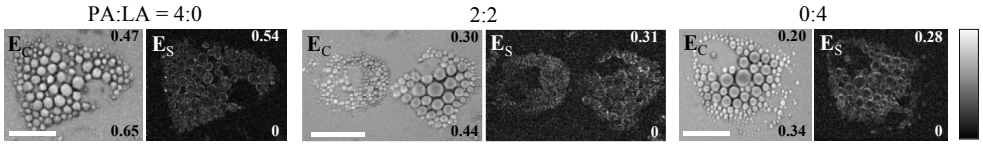

Fig. 5. Relative spectral error $\mathbf{E}_S$ and relative concentration error $\mathbf{E}_C$ for the same cells analyzed with FSC^3 in Fig. 4. The grey scale is indicated, with the range given for each image. The scale bars are 20 μm.

versely, large LDs formed during stem cell differentiation (also via LD fusion) and located toward the inner part of the cell appear to be filled with lipids from the differentiation media (mostly oleic acid). This finding suggests that PA in the supplemented medium is not easily transported across LDs during differentiation (possibly because of its lower fluidity, the melting temperature of PA is 63°) and remains located into smaller LDs. It is also interesting to see that the main lipid component in cells fed with the PA:LA mixture is well reproduced by an equally weighted combination of the LD spectrum of cells fed with LA and PA. As discussed above, the main lipid component in medium-large LDs of cells fed with PA appears to be the oleic-acid lipid present in the differentiation medium. Since both LA and oleic acid are liquid at room temperature, it is reasonable that they mix into a spatially homogeneous compound recognized as a single substance in the FSC^3 analysis. We also distinguish a more saturated lipid component in cells fed with the PA:LA mixture which is located in smaller LDs, similar to what observed in cells fed with PA only. No such component is observed in cells fed with LA only (which in fact are fully represented by 4 chemical components). As a side remark, we note that palmitic acid is the second most present fatty acid in human adipose tissue (21.5 %) after oleic acid (43.5 %), while α-linolenic acid is far less abundant (0.8 %) [21]. Despite being not so commonly present, our data suggest that α-linolenic acid is actually efficiently incorporated and stored in human adipocytes. Furthermore, the analysis of component 3 which appears more pronounced around LDs in cells fed with LA might suggest that LDs of different chemical composition have different protein coatings. This might be related to protein targeting mechanisms which are lipid specific. Indeed, how proteins target LDs is not yet well understood [4] and deserves more detailed studies.

For comparison, on the lower part of Fig. 4 we show the spatial distribution of the LD chemical content from a simple ratiometric analysis following the method by Rinia *et al.* [11]. We used the ratio of $\Im(\tilde{\bar{\chi}})$ between 2930/cm and 2855/cm representative of the lipid chemical composition through the degree of lipid disorder (which correlates with the degree of lipid chain unsaturation) as shown in Fig. 3 in the CH stretch region. The analysis shows the general trend of an increased degree of unsaturation going from cells fed with PA to cells fed with LA, but it offers far worse spatially-resolved chemical contrast than the results obtained with FSC^3.

4. Conclusions

In this work we have compared the performances of fast dual-frequency CARS imaging, requiring only minimal data analysis, with hyperspectral CARS imaging analyzed with phase-retrieval and an unsupervised factorization into concentrations of chemical components (FSC^3), for quantitative chemical imaging on human stem-cell derived adipocytes fed with saturated and poly-unsaturated fatty acids. We find that D-CARS is equally able to quantify the degree of poly-unsaturation when used in the fingerprint region. It is however less quantitative when used in the congested CH stretch region but still provides a qualitatively similar result as hyperspectral CARS. Hyperspectral CARS is specifically powerful when combined with FSC^3,

#206105 - $15.00 USD Received 11 Feb 2014; revised 9 Mar 2014; accepted 9 Mar 2014; published 2 Apr 2014

extracting the spatial distribution of chemical components with superior contrast compared to state-of-the-art ratiometric methods.

In view of the recently renewed interest in lipid droplet cell biology, these results pave the way towards label-free imaging of LDs with an unprecedented combination of subcellular spatial resolution, live cell dynamics and quantitative chemical sensitivity. This has the potential to answer many open questions on the fundamental molecular mechanisms of lipid metabolism in cells which might be of key importance to tackle metabolic disease, such as obesity and diabetes, which greatly effect today's modern societies.

Acknowledgment

This work was funded by the UK BBSRC Research Council (grant n. BB/H006575/1) and the UK EPSRC Research Council (grant n. EP/H045848/1). CDN acknowledges financial support by the President's Research Scholarship programme of Cardiff University and by the UK EPSRC Research Council (grant n. EP/I016260/1). PB acknowledges the UK EPSRC Research Council for her Leadership fellowship award (grant n. EP/I005072/1). FM acknowledges financial support from the European Union (Marie Curie Grant Agreement No. PERG08- GA-2010-276807).

#206105 - $15.00 USD Received 11 Feb 2014; revised 9 Mar 2014; accepted 9 Mar 2014; published 2 Apr 2014